Analysis and simulation of vector controlled bearingless induction motors

by Ungku Anisa Ungku Amirulddin,
BEng (Honours)

Thesis submitted to the University of Nottingham for the degree of Doctor of Philosophy, June 2005

Abstract

The concept of bearingless motors, which combine both motoring and rotor bearing capabilities, is appealing especially in high speed and high power machine applications. Although extensive research has been carried out on permanent magnet and reluctance types of bearingless motors, studies on the induction motor type are less successful. This thesis addresses the bearingless induction motor based on the concept of dual-pole windings, one controlling the motor torque and the other the generated radial forces. A modelling approach is undertaken to investigate the effect of induction machine design on radial force generation and motor levitation under both steady state and transient conditions. The simulation is based on the dynamic reluctance mesh model embedded in vector control systems for the decoupled control of torque, flux and radial force. This is achieved through modification of a previously developed computer software for modelling induction motors in order to model the control of bearingless induction motors.

Both the squirrel cage and wound rotor induction motors are investigated and their suitability for generating controlled bearing relief forces assessed. Vector control schemes for the bearingless cage and wound rotor induction motors were also designed and simulated. A mixed field oriented vector control scheme, which incorporates the simple rotor field orientation for motoring control and an airgap field orientation for rotor levitation control, is introduced and found to be advantageous in bearingless induction motor control. Apart from investigating totally bearingless conditions, the study also investigates bearing relief capabilities for a vector controlled cage and wound rotor induction motor in which the rotor movement is restricted by bearings but with the bearing load cancelled by suitably directed radial force. The effects of real winding topologies, stator and rotor slotting and iron saturation on the performance of bearing relief and bearingless induction motors are also presented.

Finally, suggestions for future work is included in order to further investigate bearingless induction motors and its applications.

Acknowledgements

Firstly, I would like to express my sincerest gratitude to Professor Greg Asher and Professor Phil Sewell for their invaluable assistance and guidance during my study at the University of Nottingham. Special thanks are extended to Dr. Keith Bradley for his numerous advice and support during the past three and a half years. Support from Newage AVK SEG, UK is also gratefully acknowledged.

I would also like to thank all the staff and students at the School of Electrical Engineering, University of Nottingham, especially to the PEMC research group, for their encouragement, support and friendship throughout the years. In particular Li Yao and Chris Gerada, with whom I have had countless useful discussions that have provided various ideas and clarification in tackling problems related to my research.

Lastly, I would like to express earnest appreciation to my family who have relentlessly supported me in every possible way throughout the past seven years of my study in the UK. Most importantly, my utmost gratitude goes to my husband, Norshah Hafeez Shuaib, to whom I am indebted to for all the love, patience and support he has given me throughout the good and bad times we had to go through in completing my PhD.

Table of contents

List of symbols

Characterisation by style of writing:

ω_r^*, F_y^*	reference value
$\hat{\theta}_r, \hat{\theta}_o$	estimated or controller variable
$\theta_r^{DFT}, B_4^{DFT}$	variables obtained from spatial discrete Fourier transform (DFT)

Symbols:

$A = wd$	area of airgap reluctance element
$\mathbf{A(x)}$	matrix of state equations solved by the DCM software
B	coefficient of friction
B_{gap}	flux density due to the airgap reluctance element
B_o^M	M-pole peak airgap flux density
B_F^N	N-pole peak airgap flux density
B_{Fy}^N, B_{Fx}^N	N-pole peak airgap flux densities associated with F_y and F_x
$B_o^M(\theta,t)$	M-pole flux density distribution
$B_o^{M'}(\theta,t)$	M-pole flux density distribution due to a perturbed rotor
$B_f^N(\theta,t)$	N-pole flux density distribution
$B_f^{M'}(\theta,t)$	N-pole flux density distribution due to a perturbed rotor
d	depth of reluctance element
D	rotor diameter
E	magnetic energy stored in an airgap reluctance element
f	supply frequency
f_i	MMF at node i
F_{mmf}	value of MMF source associated with each stator or rotor slot
F_{rad}	radial force
F_{tan}	tangential force
F_y, F_x	y- and x- directed force acting on the rotor

$F_y^{'}, F_x^{'}$	y- and x- directed force acting on a perturbed rotor
$\Delta F_y, \Delta F_x$	force due to rotor perturbation in the y- and x- direction
i_{sq-con}^N	N-pole q- axis stator current responsible for field orientation
$i_{sq-orient}^N$	N-pole q- axis stator current responsible for F_x production
I_{rated}	machine rated phase current
I_{sa}, I_{sb}, I_{sc}	stator phase currents
I_{ra}, I_{rb}, I_{rc}	rotor phase currents
$I_{sa}^M, I_{sb}^M, I_{sc}^M$	main stator winding phase currents
$I_{sa}^N, I_{sb}^N, I_{sc}^N$	levitation stator winding phase currents
J	rotor moment of inertia
k_{ws}^M	winding factor of the main stator winding
k_{ws}^N	winding factor of the levitation stator winding
l	length of reluctance element
l_g	length of airgap reluctance element
l_{g0}	airgap length of the motor when the rotor is centred
$l_g(\theta)$	airgap length at position θ when the rotor is perturbed from the centre
l_z	rotor length
$l_r^{'}$	referred rotor leakage inductance
L_o	magnetizing inductance
$L_r^{'}$	referred rotor inductance
L_s	stator inductance
M_r	rotor mass
$M(m)$	number of poles (pole pair) for main winding
$N(n)$	number of poles (pole pair) for levitation winding
$Nnode$	total number of nodes in the reluctance mesh
$Nbar$	number of rotor bars in a squirrel cage rotor
N_{ts}^M	total number of series turns per phase of the main stator winding

N_{ts}^{N}	total number of series turns per phase of the levitation winding
r	rotor radius
r_{mesh}	meshing radius
$R_r^{'}$	referred rotor resistance
R_s	stator phase resistance
S_s, S_r	number of stator and rotor slots
t	time
tol_{NR}	tolerance parameter of Newton Raphson iteration loop
tol_{solver}	tolerance parameter of linear equation solver
Δt	simulation time step
Δt_{max}	maximum time step allowed in simulation
T	torque generated by the motor
T_{load}	applied load torque
T_{rated}	machine rated torque
w	width of reluctance element
$\mathbf{x}$	matrix of state variables, x_i
$\mathbf{x}_t$	matrix of state variables at time t
$\Delta y, \Delta x$	rotor perturbation in the positive y- and x- direction
bid_s, bid_r	stator and rotor back iron depth
bd_s, bd_r	stator and rotor bridge depth
sd_s, sd_r	stator and rotor slot depth
tw_s, tw_r	stator and rotor tooth width
$\Re$	reluctance of an element
ϕ_{ij}	flux flowing in a reluctance element connected by nodes i and j
μ_0	permeability of vacuum
μ_r	relative permeability
$\mu = \mu_0 \mu_r$	permeability of an element
$\hat{\theta}$	estimated angle of field oriented flux vector
θ, θ_{mech}	rotor mechanical angular coordinate

θ^M	flux orientation angle of M-pole winding vector control scheme
θ^N	flux orientation angle of N-pole winding vector control scheme
θ_o^{air}	angle obtained from DFT of airgap element flux density samples
θ_o^{tip}	angle obtained from DFT of rotor tooth tip element flux density samples
ω, ω_e	synchronous speed (electrical)
$\omega_{r\,mech}$	rotor mechanical rotational speed
ω_r	rotor rotational speed (electrical)
ω_{sl}	slip speed (electrical)
$\underline{\psi}_s$	stator flux linkage vector
$\underline{\psi}_r$	rotor flux linkage vector
$\underline{\psi}_o$	airgap flux linkage vector

Subscripts:

$\underline{i}_{s\alpha\beta}, \underline{v}_{s\alpha\beta}$	αβ denotes variables in the fixed αβ reference frame
$\underline{i}_{sdq}, \underline{v}_{sdq}$	dq denotes variables in the rotating dq reference frame

Superscripts:

B_o^M, I_{sa}^M	M denotes variables associated with the main stator winding
B_F^M, I_{sa}^N	N denotes variables associated with the levitation stator winding

Chapter 1

Introduction

1.1. Bearingless motor

Alternating current (AC) motor drives are reaching power and speed ranges exceeding that of direct current (DC) drives due to developments in inverter and control strategies. High speed and high power impose problems of lubrication on conventional rolling element bearings. AC drives may incorporate magnetic bearings as they provide support of rotors without any physical contact offering the following advantages (Matsumura *et al.*, 1997):

- frictionless operation
- reduced frictional wear
- low vibration
- high rotational speed capability
- use in special environments such as vacuum, ultra-low temperature and toxic or flammable atmosphere
- low maintenance

This enables the use of AC drives for high speed and high power applications. Applications include for high-speed spindles for machine tools, turbomolecular pumps, liquid helium pumps and turbogenerators (Dussaux, 1990; Matsumura *et al.*, 1997; Brown, 1999). However, there are still many problems in AC drives with magnetic bearings. One problem is where there is a long axial shaft length required by bearings. This reduces the critical speed of the shaft (Fukao, 2000). Furthermore, long shaft lengths operating at high speeds create flexible shafts that require increased attention to control (Knospe and Collins, 1996). A problem in small, high speed rotating machinery

is the magnetic bearing design which is limited in terms of its size and mass. Constraint in the former is usually due to a limited operating space whereas the latter is to avoid adverse effects to shaft dynamics (Maslen *et al.*, 1988).

One of the possible solutions to reduce the problems associated with magnetic bearings in high speed motor applications is to use bearingless motors which are capable of producing both motoring operation and rotor levitation without the presence of separate magnetic bearing systems. All desirable properties of separate magnetic bearing systems are achievable by the bearingless motors (Bleuler, 1992). Therefore, most applications involving the former are applicable to the latter.

According to Chiba (1994), any electric machine that can be made equivalent to a DC machine through coordinate transformation can act as a bearingless motor. Successful operation has been reported for several bearingless motor types; for example the permanent-magnet (PM) motor (Bichsel, 1992; Oshima *et al.*, 1996), reluctance motor (Chiba *et al.*, 1991(a)) and induction motor (Chiba *et al.*, 1991(b)). In the proposed bearingless motors, the main M-pole (m pole pair) winding is augmented by an auxiliary N-pole (n pole pair) levitation winding, in such a way that the interaction between the M- and N-pole fields generates radial forces that can levitate the rotor. A general theory of pole number combination for the main and levitation windings of a permanent magnet synchronous type or an induction motor type bearingless motor was carried out by Okada *et al.* (1995) and Ohishi *et al.* (1995) showing that the condition $M - N = \pm 2$ ($m - n = \pm 1$) produces a constant radial force acting on the rotor. Bearingless motors utilising only a single set of windings have also been put forward by Salazar and Stephan (1993), Osama and Lipo (1999), Santisteban and Stephen (1999) and Khoo *et al.* (2002).

In this thesis only the induction type motor is considered for bearingless motor investigations. This is due both to the widespread use of induction motors in domestic and industry applications and the fact that there has been less successful research into using this short airgap type of machine for rotor levitation. Furthermore, induction type bearingless motors have been found to be capable of producing a stronger levitation

force when compared to bearingless PM and reluctance motors (Okada *et al.*, 1996; Fengxiang *et al.*, 2001).

1.2. Literature review on bearingless induction motors

Research into induction type bearingless motors having a 4-pole main winding and 2-pole levitation winding has experimentally studied the possibility of controlled radial forces suitable for levitation both under no load (Chiba *et al.*, 1995) and load conditions (Chiba *et al.*, 1997). These experiments used a vertical rig with one end of the shaft held by bearings. No true levitation of a bearingless induction machine has been reported. The problem is a challenging one, the radial force produced varies under load. There are two reasons for this. The first reason is due to reduction in the main magnetising current and consequently the main 4-pole field caused by the 4-pole currents induced in the rotor. Furthermore, a phase delay is introduced which causes force interactions between two perpendicular axes (y- and x- axes). Thus, information of the amplitude and orientation of the revolving magnetic field is necessary for control of a bearingless induction motor in order to ensure the radial force produced is in agreement with the reference radial force. Therefore, field-oriented vector control schemes for the induction type bearingless motors have also been introduced by Schöb and Bichsel (1994), Chiba *et al.* (1997), Suzuki *et al.* (2000) and Deng *et al.* (2002).

Secondly, the reduction in the force magnitudes and a phase delay with respect to the radial force command also occurs in the bearingless induction motors operating under load due to the 2-pole levitation currents induced in the squirrel cage (Nomura *et al.*, 1993). In order to overcome the effects of the 2-pole rotor currents, phase-lead compensation was introduced in the levitation winding controllers (Nomura *et al.*, 1993) or else the rotor cage was modified such that only 4-pole currents were allowed to flow (Chiba *et al.*, 1996; Chiba and Fukao, 1998). An alternative is through a wound rotor.

Successful finite element modelling of a bearingless wound rotor induction motor under transient conditions has been reported by Cai and Henneberger (2001). Force production comparison between a cage rotor and wound rotor type bearingless IM was also investigated by Cai and Henneberger (2001). They have found that the force

production in the cage rotor type motor is weakened due to the cage rotor inducing not only a 4-pole but also a 2-pole field which tries to oppose the airgap field asymmetry responsible for force production. This behaviour does not occur in the wound rotor type motor investigated by them since the rotor has the same pole number as the motoring winding. Hence, Cai and Henneberger (2001) have shown that the bearingless wound rotor IM is more efficient in building radial forces compared to the cage rotor type. A decoupled motoring and levitation control system for the wound rotor type motor was also proposed by Cai and Henneberger (2001) but no modelling results of a controlled bearingless motor was reported.

Effects of rotor eccentricity on a finite element model of bearingless induction motors have been presented by Yahia and Henneberger (1998) and Baoguo and Fengxiang (2001). Both papers report that the force produced by the motor increases as the levitation winding current is increased. Furthermore, rotor eccentricities were also observed to cause an increase in the force produced for a fixed value of levitation winding current. This is due to the unbalance magnetic pull of the eccentric rotor (Yahia and Henneberger, 1998). Analytical force expressions of a bearingless induction motor with rotor eccentricity are also presented by (Baoguo and Fengxiang, 2001).

1.3. Dynamic reluctance mesh modelling of an induction motor

The literature review on bearingless induction motors has shown that no successful experimental levitation has been reported. Therefore, this thesis intends to employ the use of a modelling approach to investigate the problems associated with true bearingless induction motors. This will build a foundation from which others can develop experimental test rigs with confidence. Furthermore, a modelling approach is considered as it allows various machine designs and control schemes to be considered easily without incurring the time consuming and costly aspects associated with experimentation.

There are basically four approaches to modelling electrical machines, namely the simple equivalent circuit, dq- representation, dynamic reluctance mesh modelling (DRMM) and finite element modelling (FEM). The characteristics of these modelling techniques

are summarised in Table 1.1. As the name suggests, the simple equivalent circuit modelling technique is based on employing the equivalent circuit of electric machines to investigate its performance. However, this only enables steady state conditions to be investigated. This modelling technique uses the least amount of computation time compared to the other methods but because it only provides an approximate model of the machine, it is the least accurate of all. The dq- representation modelling technique models the machine based on a two-axis lumped parameter circuit in which circuit equations and variables are transformed to represent separately its effect on the direct and quadrature axes of the machine. This enables the machine to be modelled dynamically and is equally applicable to steady-state conditions.

Simple equivalent circuit	Dq-representation	DRMM	FEM
• steady state conditions	• dynamic and steady state conditions	• dynamic and steady state conditions	• dynamic and steady state conditions
• approximate machine model	• poor machine model	• good machine model	• difficult system model
• fast - simplistic calculations	• good system model • fast computation	• good system model • relatively fast computation	• good field model • relatively slow computation

seconds ← Computation time → days

Less accurate ← Accuracy → Most accurate

Table 1.1: Electrical machine modelling techniques.

The FEM method of modelling electric machines is based on meshing the machine using triangular or rectangular elements within which the energy in each element is minimized based on predefined boundary conditions. This method of modelling is able to provide the most accurate results when compared to the other methods. However, the computation time required is long since generally dense meshes are required. On the other hand, the DRMM technique of modelling electrical machines is based on the simple concept of reluctance meshes, as an alternative to finite elements of the FEM technique. In the DRMM technique, the magnetic field behaviour in the machine is mapped onto an equivalent lumped circuit network which is then coupled to the

electrical circuits. The modelling of an induction motor using the DRMM technique has been developed by Abdel-Kader (1979), Amin (1982), Ostovic (1986 and 1988) and Sewell *et al.* (1999) whereas modelling of a permanent magnet and switched reluctance motors have also been reported by Roisse *et al.* (1998) and Nakamura *et al.* (2005) respectively.

As the study in this thesis requires a dynamic magnetic field model of the machine embedded in a vector-controlled system, the use of the simple equivalent circuit technique is ruled out. The dq- representation and DRMM methods of modelling an induction motor are chosen for the investigations presented in this thesis. The former modelling technique is chosen since it provides convenience in incorporating field oriented control strategies proposed for the bearingless induction motors. On the other hand, the choice of the DRMM technique as opposed to FEM is discussed here.

Finite element models are considered inappropriate due to the very long computation times associated with the problem dynamics. Although FEM provides a better field model of an electrical machine, the DRMM method incorporates user experience to model the most important flux paths in the machine since the qualitative direction and spatial variation of the fields in the machine are predictable with sufficiently good accuracy. Hence, the resulting lumped equivalent circuit mesh may be coarse in comparison with a conventional FEM mesh whilst still yielding good results. The DRMM approach includes all of the sources of key operating problems in induction motors, which are winding MMF harmonics, slotting effects, skew, saturation of main flux paths, and saturation of leakage flux paths. It can be argued that a coarse FEM mesh can produce relatively comparable computation time to that of DRMM mesh, however this requires the user to develop their own FEM package. However, the DRMM approach will always have fewer nodes, and therefore reduced computation time when compared to even the sparsest FEM mesh. Furthermore, it is much simpler to mesh the airgap of electrical machines using the DRMM method compared to a coarse FEM mesh since the use of narrow triangle mesh elements in the latter should be avoided to ensure accurate and stable solutions (Silvester and Ferrari, 1996).

The DRMM method provides speed of computation which is crucial when small time steps are required to incorporate control and/or power electronic schemes for electrical machines. These features are essential for the bearingless induction motor studies of this thesis. Generally, FEM simulations of induction motors require large time steps which can cause discrepancies between the actual FE model and the incorporated control and/or power electronic schemes. Currently, there are few commercially available packages which combine FE and system modelling and those that are available are slow. In a project such as this one, understanding the behaviour of the machine and control is more important than absolute precision of calculation and this requires a large problem space to be examined in a relatively short period of research.

Based on the discussion stated above, the DRMM method was chosen to model the bearingless induction motors investigated in this thesis as the method creates a machine model that is complex enough to model the most significant flux paths accurately within reasonable computation time. Furthermore, since the study presented here is intended to study the feasibility of bearingless induction motors, only a relatively good field model is required which is provided by the DRMM. In future, with advances in computing abilities, FEM analysis of bearingless induction motors is favourable compared to DRMM. For the moment, the DRMM method is employed.

1.4. Thesis overview

This thesis employs the use of a modelling approach to investigate the performance of vector controlled bearingless induction motors. Therefore, in Chapter 2, a computationally efficient simulation software (from here onwards referred to as the Dynamic Circuit Modelling (DCM) software) for modelling induction machines based on the dynamic reluctance mesh modelling (DRMM) technique is introduced. The state variables, state equations and numerical solution techniques employed in the software are also presented. Further modifications and improvements to the software in order to model a bearingless induction motor for this study are also reviewed.

In Chapter 3, derivations of the force expressions in an induction motor containing an M-pole motoring winding and an N-pole levitation winding are carried out. The force

expressions are derived for two cases; one for a motor having its rotor fixed by conventional bearings and the second for a motor having a rotor perturbed from the axial centre line of the machine. The former force derivations will be useful in studying bearing relief capability of induction motors whereas the latter will be useful when designing position control for a totally bearingless induction motor.

The forces created in a bearingless induction motor arise from interactions between the main motoring and the levitation fields. This leads to the use of field-oriented vector control schemes to control a levitated induction motor. Chapter 4 proposes control schemes for bearingless induction motors having two different rotor structures; one having a cage rotor while the other contains a rotor that does not allow any N-pole rotor currents to be induced. The reason for having the second type of rotor will be apparent in Chapter 6. Three vector control schemes are proposed in Chapter 4 for each of the two bearingless IM types; namely based on indirect rotor field orientation (IRFO), indirect airgap field orientation (IAFO) and mixed field orientation (MFO). It will be shown that the IRFO vector control scheme for the cage rotor type motor will always produce a force in the x- direction even when unwanted since the force produced is dependent on the airgap field which is not kept constant in the rotor frame. Therefore, an indirect airgap field oriented (IAFO) control scheme is also proposed. Finally, the mixed field oriented (MFO) scheme, in which the M-pole winding is rotor field oriented whereas the N-pole field is oriented onto the M-pole airgap flux, is put forward since no extra advantage is gained by having the torque (M-pole winding) being airgap field oriented.

In Chapter 5, the electrical parameters of a 4-pole cage and 4-pole wound rotor induction motor are derived. These motors will provide the motoring field in the bearingless induction motors investigated in this thesis. The levitation field in the bearingless motors is provided by an additional 2-pole winding added into the stator of each of the 4-pole motors. Therefore, Chapter 5 will also describe the design and parameter derivation of the 2-pole levitation winding. With the 4+2 pole cage and wound rotor induction motors, the vector control schemes proposed in Chapter 4 for the bearingless cage rotor motor and a motor with no N-pole levitation rotor circuit, respectively, will be simulated to investigate the levitation and lateral force produced in

these motors. This simulation is carried out in MATLAB Simulink using a two-axis lumped parameter circuit model of the bearingless IM. Before presenting the simulation results, Chapter 5 also includes the controller design for both the 4- and 2-pole winding required for the vector control scheme simulations.

The study of bearingless induction motors in this thesis also includes a study on bearing relief capabilities. The term bearing relief means that the rotor movement is still restricted by conventional bearings but with the bearing load being cancelled by suitably directed radial forces created in the motor by the incorporation of the N-pole levitation winding. In Chapter 6, DCM simulations of a linear iron bearing relief cage rotor motor under direct on-line start and MFO vector control conditions are presented. It will be shown that the cage rotor will cause the 2-pole levitation field to experience a very high slip. This high slip introduces leakages effects that cause lower then expected force values to be produced by the motor. Therefore, in order to generate the required radial force in the motor, considerably higher 2-pole currents are required than predicted from the force expressions derived in Chapter 3. Hence, the possibility of reducing the high slip leakage effects through the suppression of induced N-pole currents in the rotor will be examined in Chapter 7.

The suppression of the induced N-pole currents due to the levitation winding is achieved using the 4+2 pole wound rotor bearingless IM since the rotor is wound with the same number of poles as the motoring field. Therefore, in Chapter 7, simulation of a direct on-line start 4+2 pole linear wound rotor IM under bearing relief conditions is carried out using the DCM software. This is to investigate the radial force production in the wound rotor type motor which will be compared with the cage rotor type motor. The chapter will also present results from a DCM simulation of the same linear iron motor controlled using the MFO vector control scheme. Finally, the effects of non-linear iron on the performance of the wound rotor motor under direct on-line start and vector control conditions will also be investigated.

Chapter 8 discusses the results of an MFO vector controlled bearingless wound rotor IM modelled using the DRMM technique by way of the DCM software. However, due to ability of the rotor to move freely in the bearingless motor, the x- and y- direction

position controllers required in the simulation will first be designed. A verification of the force expressions derived for a perturbed rotor motor in Chapter 3 is also discussed thorough comparison with DCM simulation results investigating the effect of unbalance magnetic pull force due to rotor displacements in a motor supplied only with the motoring field.

The numerical solution technique used within the DCM software is controlled by key parameters to ensure that convergence and accuracy is achieved in all the simulations carried out. Therefore, Chapter 9 will discuss the numerical effects associated with the parameter choices on the results of the DCM simulations presented in thesis.

Finally in Chapter 10, a conclusion to the study of bearingless induction motors including the main findings of the work of this thesis is presented. Possible areas in which future work can be directed will also be proposed.

Chapter 2

Dynamic Circuit Modelling (DCM) software

2.1 Introduction

The time consuming and costly aspects of experimentation faced by designers in search of enhanced machine performance have resulted in the creation of computer simulation software capable of considering many design variations. Although simulation software for machine design purposes (such as finite element based packages) produces accurate and detailed results of machine performance, designers are often forced to compromise the simulation undertaken by considering either two-dimensional approximations or steady state conditions in order to manage the computational intensity. This is a consequence of the large number of variables necessary to accurately characterise the state of the machine and the very long computation times associated with the problem dynamics. Restriction to the two-dimensional case and/or steady state operation undermines the utility of the simulations, especially when transient analysis and three-dimensional effects such as skew are important.

Therefore, another approach to modelling electrical machines based on the simple concept of reluctance meshes, as an alternative to finite elements, was developed by Abdel-Kader (1979), Amin (1982), Ostovic (1986 and 1988) and Sewell *et al.* (1999) in which the magnetic field behaviour in the machine is mapped onto an equivalent lumped circuit network. A computer simulation software employing the dynamic reluctance mesh modelling technique was also developed by Sewell *et al.* (1999) to model three-dimensional induction motors in transient and steady state conditions. The key to the efficiency of this approach is the fact that in most parts of the machine, the qualitative direction and spatial variation of the magnetic field are predictable with

sufficiently good accuracy from experience, and hence well approximated by the behaviour of a simple lumped circuit element. Therefore, the resulting lumped equivalent circuit mesh may be coarse in comparison with conventional finite element mesh, as mentioned in Section 1.2, whilst still yielding good results. This provides a significant saving in both computational time and memory consumption. In fact, the results obtained from the reluctance mesh model of a conventional induction motor have previously shown excellent agreement with experimental results (Sewell *et al.*, 1999).

In this chapter, a brief description of this computationally efficient dynamic reluctance mesh modelling technique is presented. The Dynamic Circuit Modelling (DCM) computer simulation program initially developed by Sewell *et al.* (1999) and further enhanced in this work is introduced in this chapter. Details of both the modifications and its use to produce the results presented in Chapters 5, 6, 7 and 8 of this thesis are discussed. First, this chapter will look at how an induction motor is modelled using the reluctance mesh approach before introducing the state variables, state equations and numerical solution techniques employed in the DCM program. However, comparison between the results of the DCM simulation of a conventional induction motor and experimental results will not be presented here as the basic algorithm and code have already been extensively validated by Sewell *et al.* (1999).

2.2 Creating the reluctance mesh

In this model, a typical induction machine stator and rotor geometry is discretised into a number of cells in which the flux may be realistically considered to flow perpendicularly to the inter-cell boundaries as shown in Figure 2.1(a). At each boundary, a node is defined, at which point the MMF is sampled. Each cell is represented by a reluctance element of width, w, length, l, and depth, d, which connects two nodes, as shown in Figure 2.2, and is physically consistent with flux flowing along the element and uniformly distributed in its cross-section. Given the geometry of the stator and rotor laminations, a segment for both the stator and rotor reluctance mesh is created as shown in Figure 2.1(b) with the dimensions of each reluctance element in the

segment being determined from the lamination geometry as shown in Table 2.1. The stator element node numbers seen in Figure 2.1(b) start from 1000, for coding reasons.

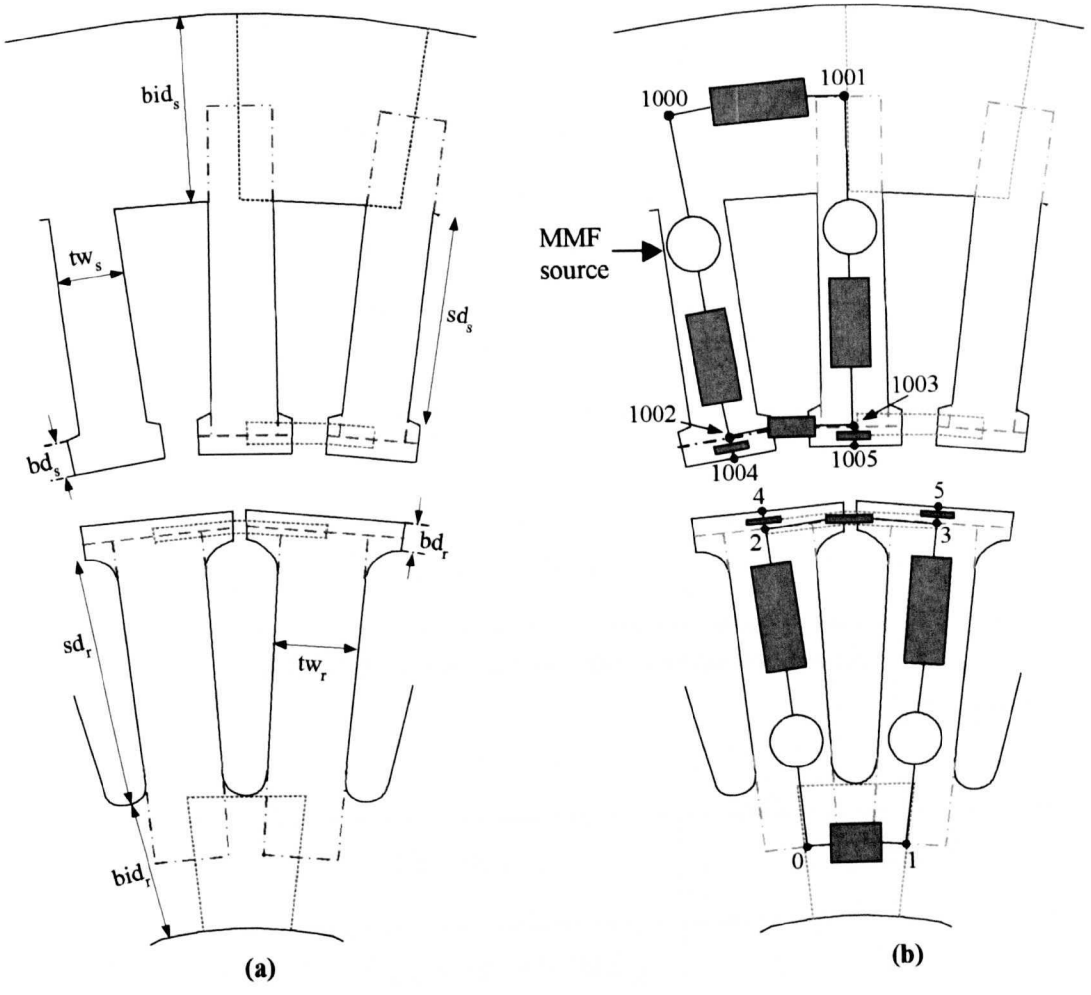

Figure 2.1: Discretisation of stator or rotor teeth into reluctance cells.

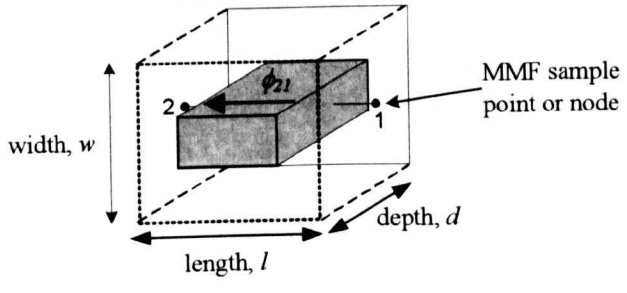

Figure 2.2: A reluctance element cell.

Node number		Length, l	Width, w
0	1	$\left(2\pi/S_r\right)(r_{mesh} - sd_r - 0.5bid_r)$	bid_r
0	2	$0.5bid_r + (sd_r - 0.5bd_r)$	tw_r
1	3	$0.5bid_r + (sd_r - 0.5bd_r)$	tw_r
2	4	$0.5bd_r$	$\left(2\pi/S_r\right)(r_{mesh} - sd_r - 0.5bid_r)$
3	5	$0.5bd_r$	$\left(2\pi/S_r\right)(r_{mesh} - sd_r - 0.5bid_r)$
2	3	$\left(2\pi/S_r\right)(r_{mesh} - 0.5bd_r)$	$0.5bd_r$

Table 2.1(a): Dimensions of rotor reluctance elements.

Node number		Length, l	Width, w
1000	1001	$\left(2\pi/S_s\right)(r_{mesh} + sd_s + 0.5bid_s)$	bid_s
1000	1002	$0.5bid_s + (sd_s - 0.5bd_s)$	tw_s
1001	1003	$0.5bid_s + (sd_s - 0.5bd_s)$	tw_s
1002	1004	$0.5bd_s$	$\left(2\pi/S_s\right)(r_{mesh} + sd_s + 0.5bid_s)$
1003	1005	$0.5bd_s$	$\left(2\pi/S_s\right)(r_{mesh} + sd_s + 0.5bid_s)$
1002	1003	$\left(2\pi/S_s\right)(r_{mesh} + 0.5bd_s)$	$0.5bd_s$

Table 2.1(b): Dimensions of stator reluctance elements.

Each reluctance element is designated to be of type 'linear' iron, 'non-linear' iron or 'air'. In the case of non-linear iron, a suitable experimental B-H curve defines the permeability, otherwise an appropriate relative permeability value μ_r= constant, is given. The slots on both the stator and rotor side can be left open or semi-closed by modelling the reluctance element between the teeth as an 'air' element. The placement of MMF sources on each stator and rotor tooth were chosen using Ampere's law to correctly model the location of both the stator and rotor bar currents (Sewell *et al.*, 1999). The reluctance of each element in the mesh is obtained by

$$\Re = \frac{l}{\mu w d} \tag{2.1}$$

where μ is the permeability of the element determined by its given type. As stated above, this assumes uniform flux flow in each element, although, if required, the reluctance of any element in the model can be defined more generally in terms of the MMF difference between the end of the element nodes, possibly obtained from pre-processing simulations of flux flows in the motor using a local finite element analysis.

Therefore, assuming uniform flux flow, the flux flowing through a reluctance element, shown in Figure 2.2, is calculated using

$$\phi_{21} = \frac{f_2 - f_1}{\Re} \tag{2.2}$$

where f_2 is the MMF at node 2, f_1 is the MMF at node 1 and $\Re$ is the reluctance of the element as given by (2.1). If the reluctance element is in series with an MMF source,

$$\phi_{21} = \frac{f_2 + F_{mmf} - f_1}{\Re} \tag{2.3}$$

where F_{mmf} is the potential of the MMF source.

After a segment of the stator and rotor is discretised and represented as an equivalent reluctance element lumped circuit, the node numbers, dimensions and type of each reluctance element are put into two data files. At the start of the DCM program, these data files together with a data file representing the 'non-linear' type B-H curve, and a

file containing the motor's physical and running parameters are loaded. As the stator and rotor teeth are symmetrical, the program then replicates both segments, from the data files, according to the number of stator and rotor bar slots respectively to create a complete slice, or axial section, of the induction motor.

Correctly modelling the reluctance mesh of the airgap is crucial in a dynamic simulation. In this model, flux is assumed to flow radially across the airgap at all times, as shown by the inset figure in Figure 2.3. Therefore, the airgap reluctance elements are allocated on the basis of the overlap area between pairs of rotor and stator tooth tips. As the rotor rotates the overlaps between rotor and stator teeth change. Hence, the airgap reluctance element values and the reluctance mesh vary depending on the instantaneous position of the rotor as shown in Figure 2.3. In the DCM program, these elements are dynamically created at each time step. For this reason, these airgap reluctance elements are referred to as dynamic reluctance elements while all other reluctance elements will be regarded as fixed elements.

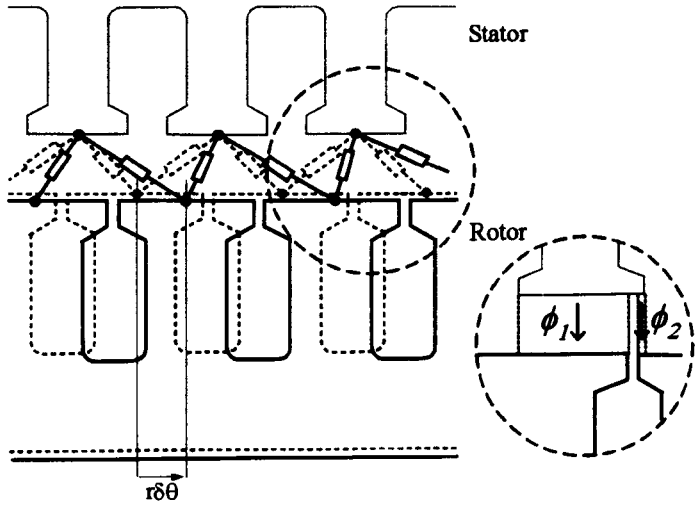

Figure 2.3: Creation of airgap elements based on overlap between stator and rotor tooth. As the rotor moves by rδθ, a new set of airgap elements are created (solid lines). The set of rotor teeth after the movement is drawn slightly lower than before the movement (dashed lines) for clarity.

The stator and rotor slots are filled by a three-phase winding and a squirrel cage bar respectively. The model is capable of modelling a fractional or full pitch double layer stator winding. Figure 2.4 illustrates part of the reluctance mesh created by the DCM program for a bearingless induction motor.

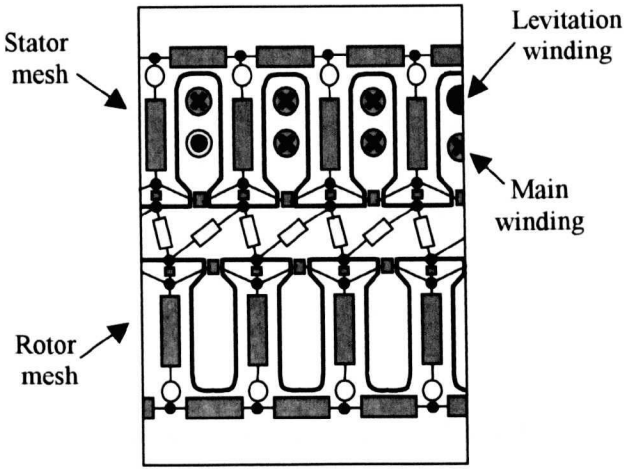

Figure 2.4: Reluctance mesh model.

In order to obtain experimentally verifiable simulations, the model is made quasi-3D to allow for rotor skew along its axis. The motor is divided into a number of axial sections with each section of the rotor being offset from its predecessor by a small angle to model the skew. Adjacent axial sections are only coupled through the rotor and stator electrical circuits as it is assumed that axially directed flux is negligible which is a physically realistic assumption. This dramatically improves the computational efficiency of the model. Therefore, after creating a slice or axial section from the stator and rotor segments, the DCM program then replicates the slice or section according to the user-defined number of sections with each rotor section being offset by

$$\text{skew offset} = \frac{\text{skew angle in mechanical degrees}}{\text{number of sections}}$$

The incorporation of skew in the DCM simulation program is an advantage when compared to two-dimensional finite element simulations of an induction motor in which skew is not taken into account.

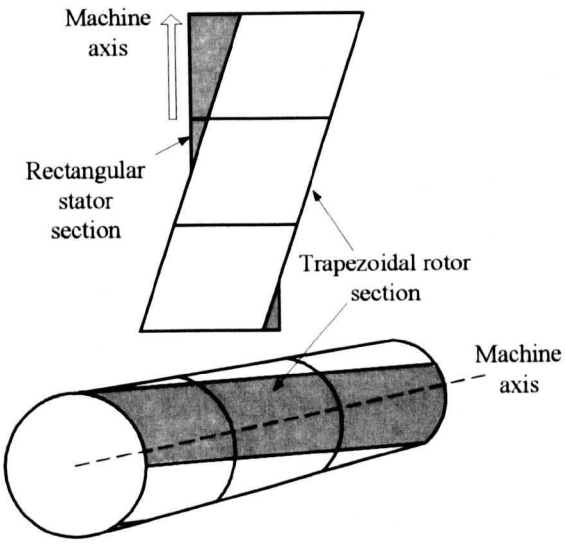

Figure 2.5: Modelling rotor skew.

Generally, in an unskewed machine, the area of each rotor tooth in contact with the airgap would be reasonably considered to be rectangular. However, in this reluctance element model, the area is defined to be trapezoidal, as in Figure 2.5, to account for the skew. This also has important numerical consequences when calculating the torque generated in the motor from the virtual work principle as it relies upon the rate of change of the dynamic airgap elements with rotor position. This rate of change is continuous when the rotor tip elements are defined as trapezoidal shaped elements and this avoids any unrealistic steps in torque, unlike the case of rectangular shaped elements. Furthermore, a trapezoidal area takes into account zigzag leakage paths more realistically.

2.3 State variables and state equations solved

The model enforces conservation of the rate of change of flux entering each node *i*, (for example see Figure 2.4)

$$\sum_j \frac{\partial}{\partial t}\phi_{ij}\left(f_i, f_j\right) = 0 \tag{2.4}$$

As there are a total of *Nnode* nodes in the reluctance-mesh, a set of equations is recovered linking together all the nodal MMFs, f, in the simulation. The magnetic

model is coupled to the stator and rotor electrical models by applying Ampere's and Faraday's laws. Satisfaction of Ampere's law requires placing MMF sources in the teeth of both the rotor and stator as shown in Figure 2.1. Each of the three phase windings on the stator and the wound rotor comprise three independent phase loops and knowledge of the winding distribution allows the appropriate current to be used to determine each tooth MMF source. In the case of the cage rotor, each bar current is regarded as an independent quantity. Faraday's law is enforced for each independent electrical loop in the motor. These loops comprise each of the phases of the stator winding. For the cage rotor, the independent electrical loops consist of pairs of adjacent rotor bars. Having identified the electrical loops, the teeth fluxes which couple with each of them is clear from the winding distribution of the stator and the pairing of rotor bars. Hence, an equation of the form

$$V_{loop}(t) - R_{loop} I_{loop}(t) - N_{turns} \frac{d}{dt} \sum_{teeth} \phi(t) = 0 \tag{2.5}$$

is formed. V_{loop} is either the imposed stator voltage or 0 for the cage rotor loops, and R_{loop} and N_{turns} are known from the machine specification.

Finally, the rotor dynamics are encapsulated by

$$\omega_{r\,mech} - \frac{d\theta}{dt} = 0 \tag{2.6}$$

$$T - J \frac{d\omega_{r\,mech}}{dt} - B\omega_{r\,mech} - T_{load} = 0 \tag{2.7}$$

In (2.7), the torque T generated by the motor is calculated in the model using the virtual work principle on each airgap reluctance element. Based on this principle, the torque is calculated from the change of magnetic energy due to a virtual perturbation of the rotor in the θ direction (Mizia *et al*, 1988). Therefore,

$$T = \sum \frac{\partial E}{\partial \theta} \tag{2.8}$$

where E is the magnetic energy stored in each airgap reluctance element and is given by

$$E = \frac{B_{gap}^2}{2\mu_0} A l_g \tag{2.9}$$

To summarise, the state variables being solved by the model are the nodal MMFs, the MMF sources due to the rotor bar currents, the stator winding's phase current and the position and velocity of the rotor

$$\mathbf{x} = \left[f_0, f_1, \ldots, f_{Nnode-1}, F_{Rmmf,0}, F_{Rmmf,1}, \ldots, F_{Rmmf,Nbar-1}, I_{sa}, I_{sb}, I_{sc}, \theta_{mech}, \omega_{r\,mech} \right]^T \tag{2.10}$$

where *Nbar* is the number of rotor bars. The model employs the MMF sources due to the rotor bar currents $F_{Rmmf,i}$ as state variables as it is more convenient to use than the bar currents themselves since according to Ampere's law the current flowing through rotor bar i is given by

$$I_{r,i} = F_{Rmmf,i+1} - F_{Rmmf,i} \tag{2.11}$$

A matrix **A(x)** consisting the set of state equations constructed from (2.4), (2.5), (2.6) and (2.7) in which

$$\mathbf{A}(\mathbf{x}) = \begin{bmatrix} Nnode \times \text{conservation of flux rate equations, eq. (2.4)} \\ n \times \text{electrical loop equations, eq. (2.5)} \\ \text{2 dynamic equations, eq. (2.6) and (2.7)} \end{bmatrix} \tag{2.12}$$

where $n = 3 + Nbar - 1$.

2.4 Solving the model

The model is simulated directly in the time domain which is better for non-linear conditions and in the presence of control schemes, when compared to simulations in the frequency domain. Determining the state variables $\mathbf{x}_{t+\Delta t}$ at time $t + \Delta t$, given the values of the state variables $\mathbf{x}_t$ at time t, involves linearising the state equations using the well-known multi-variable Newton Raphson method for non-linear systems of

equations (Press, 2002). As the state equations are in the form of first order differential equations, the Crank-Nicolson approach of approximating the state variables $\mathbf{x}$ is also adopted in the solving process in which

$$x_i\big|_{t+\Delta t/2} = (1-\alpha)x_{i,t+\Delta t} + \alpha x_{i,t} \tag{2.13}$$

$$\left.\frac{dx_i}{dt}\right|_{t+\Delta t/2} = \frac{x_{i,t+\Delta t} - x_{i,t}}{\Delta t} \tag{2.14}$$

where $\alpha \leq 0.5$ for stability with 0.5 giving the most accurate results. The Crank-Nicolson method is an implicit scheme which generally allows larger time step Δt values to be utilised and provides greater stability compared to explicit schemes. Therefore, although several other approximation techniques can be employed, the Crank-Nicolson approach was chosen due to its well-proven efficiency and reliability.

Once the equations are linearised, the matrix $\mathbf{A}$ obtained is sparse and relatively large. Therefore, the model solves for the variables $\mathbf{x}_{t+\Delta t}$ at time $t+\Delta t$ using a linear conjugate gradient solver (Van Der Vorst, 1992) exploiting efficient sparse matrix operations. The conjugate gradient technique is iterative and in order to initiate the solution $\mathbf{x}_{t+\Delta t}$ at time $t+\Delta t$, a simple linear prediction scheme is employed based on the previous two solutions $\mathbf{x}_t$ and $\mathbf{x}_{t-\Delta t}$ as given by

$$\mathbf{x}^p_{t+\Delta t} = \mathbf{x}_t + (\mathbf{x}_t - \mathbf{x}_{t-\Delta t}) \tag{2.15}$$

where $\mathbf{x}^p_{t+\Delta t}$ is the prediction of the solution at time $t+\Delta t$.

Furthermore, the conjugate gradient technique also requires preconditioning for robust operations whereby the solution of

$$\mathbf{A}\mathbf{x}^p_{t+\Delta t} = \mathbf{b} \tag{2.16}$$

is reformulated as

$$\tilde{\mathbf{A}}^{-1}\mathbf{A}\mathbf{x}^p_{t+\Delta t} = \tilde{\mathbf{A}}^{-1}\mathbf{b} \tag{2.17}$$

where $\tilde{\mathbf{A}}^{-1}$ is an approximation to the inverse of $\mathbf{A}$, i.e. $\tilde{\mathbf{A}}^{-1}\mathbf{A} = \mathbf{I}$. In the DCM software, the preconditioning is achieved using an incomplete LU decomposition with partial fill based on a 'threshold' criterion, allowing for control over the trade off between memory usage and computation time. If a small value of 'threshold' is used, the solver requires more memory but the time taken to solve is reduced. A zero or negative value of threshold implies the use of a full LU decomposition for solving the matrix.

In practise, the conjugate gradient solver will perform reliably if a sensible prediction and reasonable preconditioning is available. Without reasonable preconditioning the iterative routine will stall unless the prediction $\mathbf{x}^{p}_{t+\Delta t}$ is very close to the solution $\mathbf{x}_{t+\Delta t}$, thus requiring very small time steps. However, the prediction and preconditioning method utilised in the DCM software was proven to produce reasonable results with acceptable computational time when a large time step Δt is used. Even so, the time step Δt in the software is adaptive. If the residual error during the Newton Raphson cycle at time $t + \Delta t$ increases compared with that in the previous time step or the linear equation solver fails to solve the linear equations within a predefined number of iterations, the time step Δt is halved. If the halved time step provides successful convergence, the time step is doubled, subject to it being below the predefined maximum value $\Delta t_{\max}$, in preparation for the next solving process. Successful convergence of the linear solver is obtained when its rms error is less than the solver tolerance tol_{solver} ($\sqrt{\sum \text{error}_i^2} < tol_{solver}$) whereas successful solving of a particular time step is achieved when the rms residual error from the Newton Raphson loop is less than the Newton Raphson (NR) tolerance tol_{NR}. The flow chart of the DCM software developed by Sewell *et al.* (1999) is shown in Figure 2.6.

In the reluctance mesh model, a large part of the mesh corresponding to the fixed reluctance elements remains the same during the linear solver iteration at a particular time step. This provides scope for improving the preconditioner by allowing certain parts of the matrix (relating to the fixed reluctance elements) to be reused. There is also a possibility of further improving the adaptive time step control loop in order to provide

a more efficient solving technique for the software. However, this was not explored in this thesis since the aim here is to utilise and modify the DCM software sufficiently enough to simulate a bearingless induction motor and not to optimise the software to the possible limits of the solver.

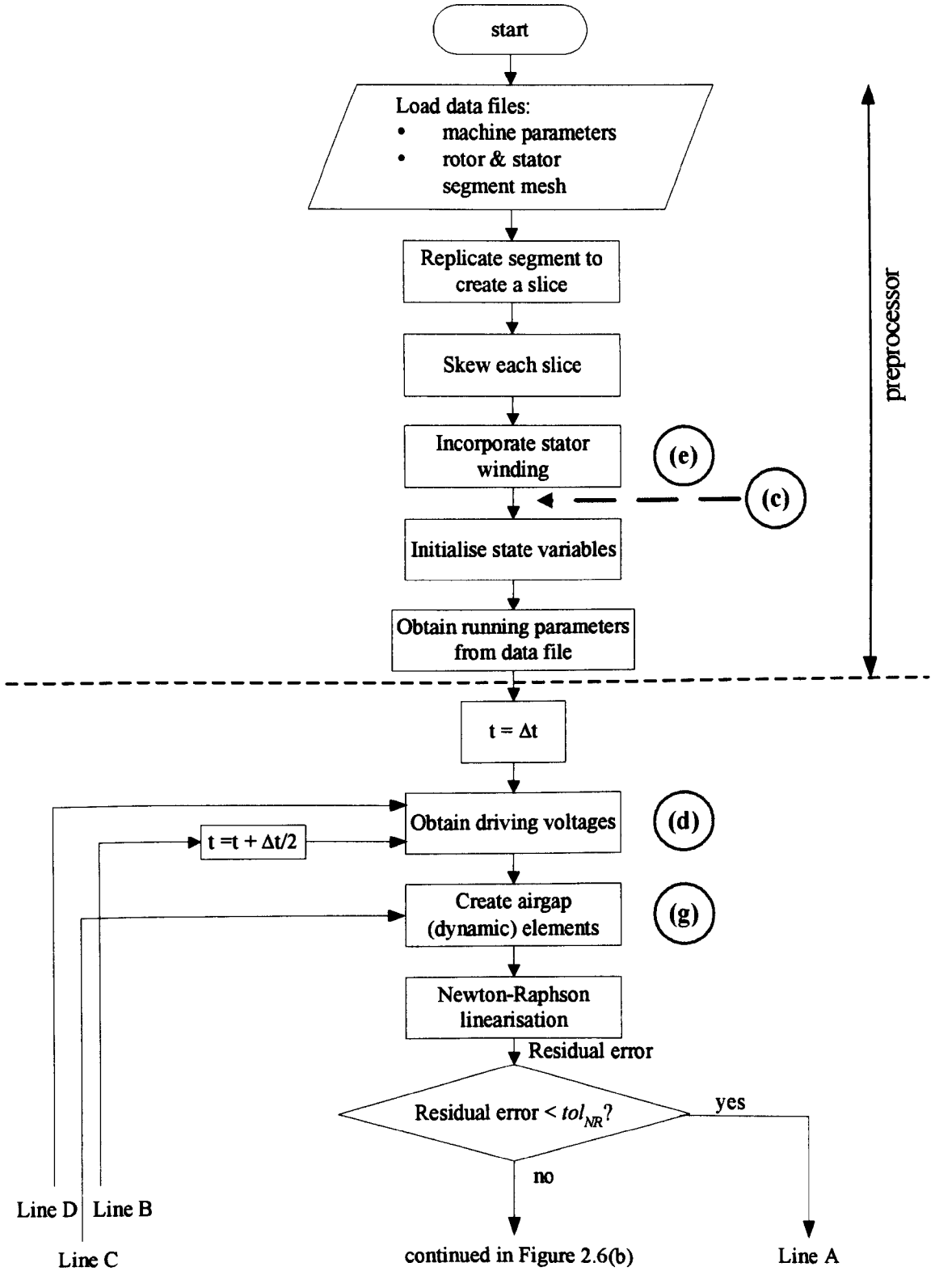

Figure 2.6(a): Flow chart of DCM software.

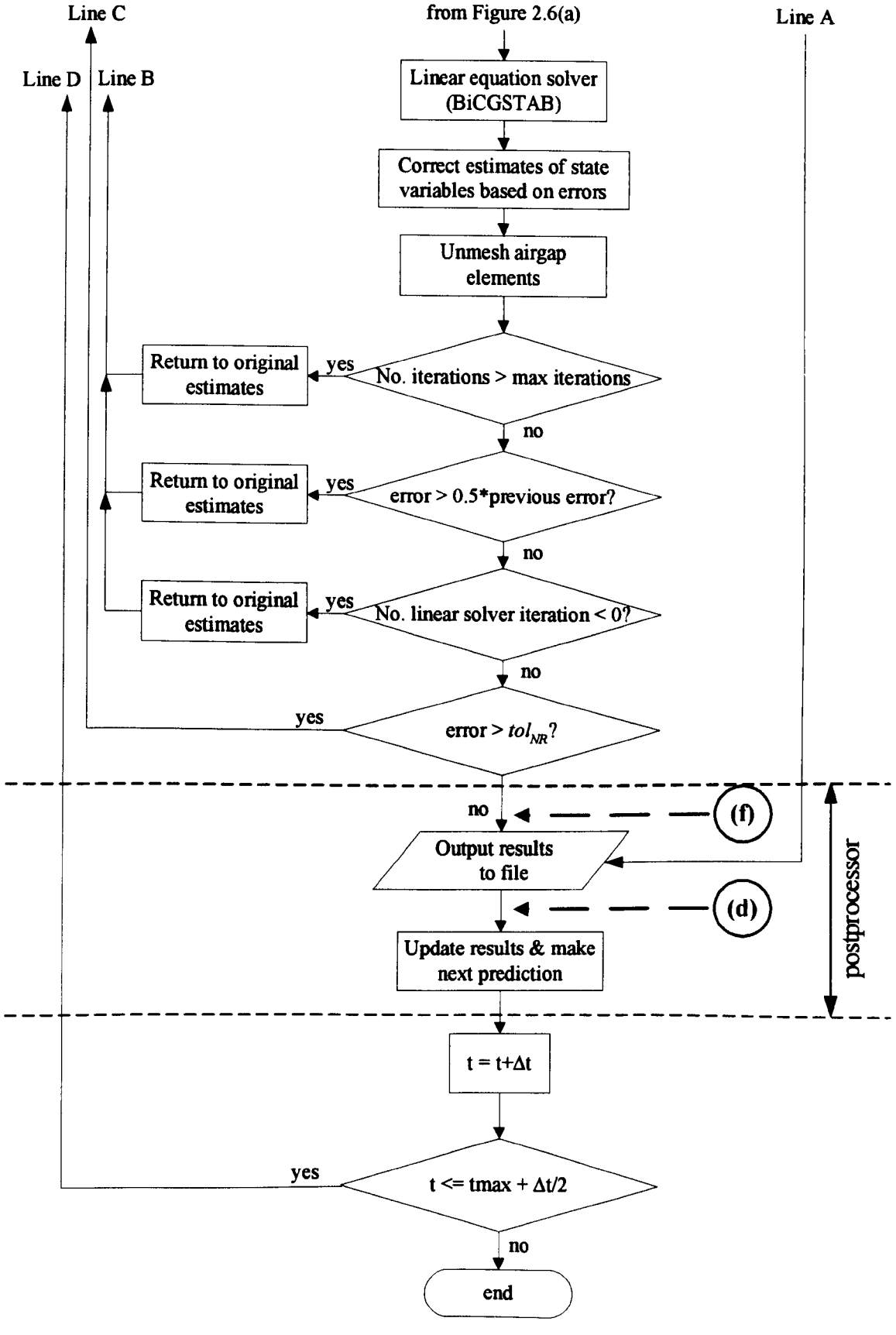

Figure 2.6(b): Flow chart of DCM software (continued).

2.5 Program developments

The DCM software introduced above only models a squirrel cage induction motor. In order to use the DCM software to model and simulate a bearingless induction motor, several modifications were made to the original code which will be presented here. It is noted that all modifications listed in this section (a-g) are by no means optimised to the maximum limit but to the extent of providing reasonable computation time and memory usage for all simulation conditions presented in Chapters 5 to 8.

a) Improvements to linear equation solver

Several changes were made to the preconditioner of the linear equation solver to improve its memory efficiency. However, this causes a slight increase in the computational time. Therefore, the solving section of the software was recoded to speed up the computation. The end result of the modification is a solver that utilises significantly less memory compared to the original code but with the same computational time per simulation run. The changes applied to the solver in this software were done such that the memory usage and computational time required to simulate the vector controlled bearingless induction motor with the free moving rotor (presented in Chapter 8) is reasonable on a typical PC. For example, the simulation of the vector controlled non-linear bearingless wound rotor IM with the free moving rotor, presented in Section 8.5, was completed in 95 minutes and required a maximum memory usage of 3.26M bytes.

b) Solving for conservation of flux equations

As mentioned in Section 2.3, the DCM software solves for conservation of rate of change of flux equation on each node in the reluctance mesh model. This was in order to be consistent with physics whereby reluctance elements being magnetic storage elements in magnetic circuits are analogous to capacitances in electric circuits. However, when implementing the conservation of rate of change of flux with time, as in equation (2.4), on each node numerically in the software, rounding errors are produced

due to the non-existence of a grounding point. This causes residual flux at each node which in turn causes offsets in the three-phase rotor flux linkages as observed in the simulation of a vector controlled 4-pole wound rotor IM shown in Figure 7.5.

Therefore, the DCM software was modified such that conservation of flux, entering and leaving, on each node was solved instead of rate of change of flux using the following equation

$$\sum_j \phi_{ij}(f_i, f_j) = 0 \tag{2.18}$$

This ensures that no residual flux exists in any node. Hence, the matrix of state equations to be solved by the DCM software becomes

$$\mathbf{A}(\mathbf{x}) = \begin{bmatrix} Nnode \times \text{conservation of flux equations, eq. (2.18)} \\ n \times \text{electrical loop equations, eq. (2.5)} \\ 2 \text{ dynamic equations, eq. (2.6) and (2.7)} \end{bmatrix} \tag{2.19}$$

with $n = 3 + Nbar - 1$.

All the simulations presented in Chapters 5, 6, 7 and 8, performed using the DCM software, were simulated based on solving for conservation of flux equation at each node in the model, i.e. using equation (2.18), except in Sections 6.2 and 7.2 in which simulations solving for both conservation of rate of change of flux and conservation of flux equations were presented to demonstrate the effects of residual flux observed when the former state equations are solved for.

c) Modelling a wound rotor

Bearingless induction motors with two different rotor structures, cage and wound rotor, will be investigated in this thesis. As the original DCM software is only capable of modelling motors with a cage rotor, modifications were added to the code to include modelling of a three-phase wound rotor. The subroutine written to incorporate the rotor winding is called after the stator winding incorporation subroutine is called, as indicated by '(c)' in Figure 2.6(a). The subroutine enables the DCM software to model a fractional or full pitch double layer rotor winding. Similar to the stator winding, for each of the

three-phase rotor windings, three independent phase loops are identified to create three extra state equations of the form shown in equation (2.5) in which V_{loop} is set to zero to model the short-circuited rotor windings. Hence, with the wound rotor IM, the state variables being solved by the model are the nodal MMFs, the three rotor winding phase currents, the stator winding phase currents and the position and velocity of the rotor, i.e.

$$\mathbf{x} = \left[f_0, f_1, \ldots, f_{Nnode-1}, I_{ra}, I_{rb}, I_{rc}, I_{sa}, I_{sb}, I_{sc}, \theta_{mech}, \omega_{r\,mech}\right]^T \tag{2.20}$$

where I_{rabc} are the phase currents of the three-phase rotor winding. Consequently, the matrix **A(x)** consisting of the set of state equations is now given by

$$\mathbf{A(x)} = \begin{bmatrix} Nnode \times \text{conservation of flux equations, eq. (2.18)} \\ 6 \times \text{electrical loop equations, eq. (2.5)} \\ 2 \text{ dynamic equations, eq. (2.6) and (2.7)} \end{bmatrix} \tag{2.21}$$

when the motor contains a wound rotor. Therefore, by comparing the set of state variables and state equations of the cage rotor motor, given by equations (2.10) and (2.12), to that of the wound rotor motor, the latter DCM modelled motor type has a total of $Nbar - 3$ less state variables and state equations to solve and thus reduces the amount of memory usage and computation time for each simulation run.

d) Addition of vector control

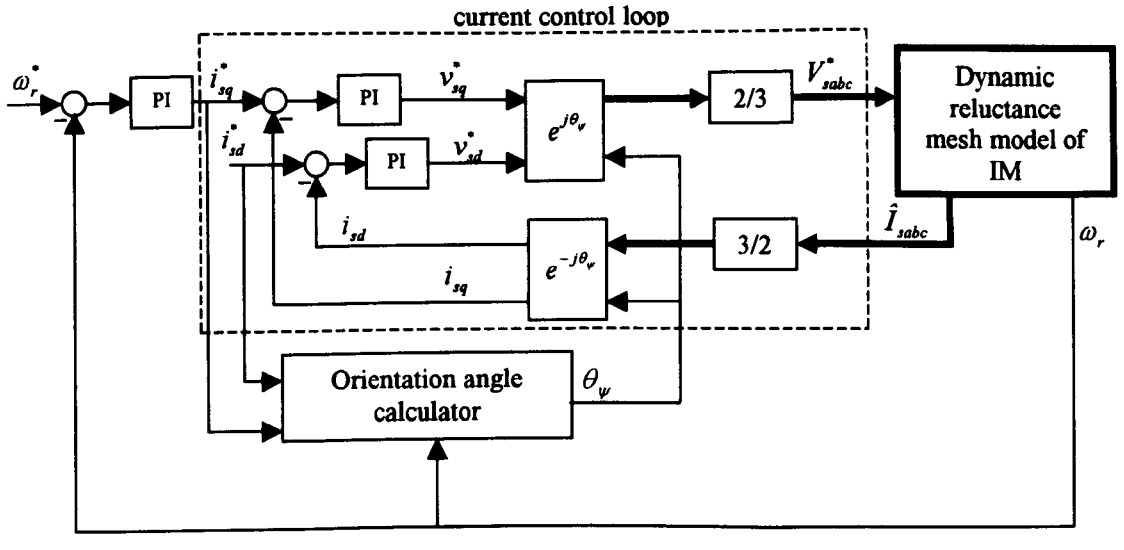

Figure 2.7: Vector control of a conventional induction motor.

The DCM software was also modified to include vector control of a conventional as well as a bearingless induction motor. The objective of the vector control subroutine is to obtain the values of driving voltages V_{abc} of the stator winding for the next simulation time step. Therefore, in the DCM software, the vector control subroutine is called in the postprocessor section of the software just before calling the subroutine that updates the state variables and makes the prediction of the state variables for the next simulation time is called, as indicated by '(d)' in Figure 2.6(b). The vector control routine is also called at the start of the simulation, replacing the 'obtain driving voltages' block shown in Figure 2.6(a), to obtain the stator winding terminal voltages at the start.

The vector control scheme for a conventional motor involves two control loops, consisting of an inner current control loop and an outer speed control loop as shown in Figure 2.7, with the control being performed in the dq- rotating frame. Therefore, the inputs of the control loops (for example the feedback stator currents) have to be transformed from the three-phase quantities into their equivalent dq quantities. This is achieved by, firstly, transforming the three-phase quantities (x_a, x_b and x_c) into the equivalent two-phase quantities ($x_{s\alpha}$ and $x_{s\beta}$) in the stator frame (denoted by 's' in the subscript) using the rms convention given by

$$\begin{bmatrix} x_{s\alpha} \\ x_{s\beta} \end{bmatrix} = \begin{bmatrix} 1/\sqrt{2} & 0 & 0 \\ 0 & 1/\sqrt{6} & 1/\sqrt{6} \end{bmatrix} \begin{bmatrix} x_a \\ x_b \\ x_c \end{bmatrix} \tag{2.22}$$

where x can be the stator phase currents or flux linkages in the motor depending on the controlled variable. Then, the fixed two-phase quantities ($x_{s\alpha}$ and $x_{s\beta}$) are transformed into the dq- rotating frame quantities (x_{sd} and x_{sq}) using

$$\begin{bmatrix} x_{sd} \\ x_{sq} \end{bmatrix} = \begin{bmatrix} \cos\theta_\psi & \sin\theta_\psi \\ -\sin\theta_\psi & \cos\theta_\psi \end{bmatrix} \begin{bmatrix} x_{s\alpha} \\ x_{s\beta} \end{bmatrix} \tag{2.23}$$

where θ_ψ is the angle of the flux vector used for the vector control orientation. Consequently, the output of the control loops (for example the stator driving voltages)

will have to be transformed back from the dq- rotating frame to the three-phase quantities, via the fixed two-phase quantities, using the following equations:

$$\begin{bmatrix} x_{s\alpha} \\ x_{s\beta} \end{bmatrix} = \begin{bmatrix} \cos\theta_{\psi} & -\sin\theta_{\psi} \\ \sin\theta_{\psi} & \cos\theta_{\psi} \end{bmatrix} \begin{bmatrix} x_{sd} \\ x_{sq} \end{bmatrix} \tag{2.24}$$

$$\begin{bmatrix} x_a \\ x_b \\ x_c \end{bmatrix} = \begin{bmatrix} \sqrt{2} & 0 \\ -1/\sqrt{2} & \sqrt{3/2} \\ -1/\sqrt{2} & -\sqrt{3/2} \end{bmatrix} \begin{bmatrix} x_{s\alpha} \\ x_{s\beta} \end{bmatrix} \tag{2.25}$$

In the DCM software, within the vector control subroutine, four separate subroutines were written to compute the transformations from the three-phase quantities into their equivalent dq quantities, and back, using equations (2.22) to (2.25). However, before being able to transform the currents I_{sabc} into the feedback currents i_{sdq} when modelling the current control, any circulating zero sequence current has to be eliminated. This is achieved in the vector control subroutine by constructing the respective line currents $I_{line-sabc}$ from the three stator phase currents I_{sabc}, using equation (2.26), before reconstructing the phase currents $\hat{I}_{sabc}$ from the line currents, using equation (2.27), to be used in the vector control.

$$\begin{aligned} I_{line-sa} &= I_{sa} - I_{sb} \\ I_{line-sb} &= I_{sb} - I_{sc} \\ I_{line-sc} &= I_{sc} - I_{sa} \end{aligned} \tag{2.26}$$

$$\begin{aligned} \hat{I}_{sa} &= (I_{line-sa} - I_{line-sb})/3 \\ \hat{I}_{sb} &= (I_{line-sb} - I_{line-sc})/3 \\ \hat{I}_{sc} &= (I_{line-sc} - I_{line-sa})/3 \end{aligned} \tag{2.27}$$

The PI controllers are modelled in the DCM software by difference equations obtained from the digital equivalent of the controllers designed in the continuous *s*-plane. The digital equivalent controllers were achieved through the Bilinear Transform (Franklin *et al.*, 1998) with a sampling time chosen such that the sampling frequency ratio (i.e. f_{samp} / controller bandwidth) exceeds 15. Therefore, the DCM software requires the user to input the PI controller parameters as well as the sampling times t_{samp-i},

associated with the current control loop, and $t_{samp-\omega}$, associated with the speed control loop, into a data file.

If the simulation time $t + \Delta t$ exceeds the sampling time for the controller, the inputs to the current control loop (I_{sabc}) and speed control loop (ω_r) are linearly interpolated to obtain the stator phase currents and rotor speed values at the sampling time using the following relationship

$$x_{inter} = x_t + \left[\frac{t_{samp} - t}{\Delta t}\right](x_{t+\Delta t} - x_t) \tag{2.28}$$

where x represents either the individual stator phase currents I_{sabc} or the rotor speed ω_r and t_{samp} is the sampling time and is a multiple of t_{samp-i} and $t_{samp-\omega}$. Figure 2.8 shows the flow chart of the vector control subroutine written for the DCM software.

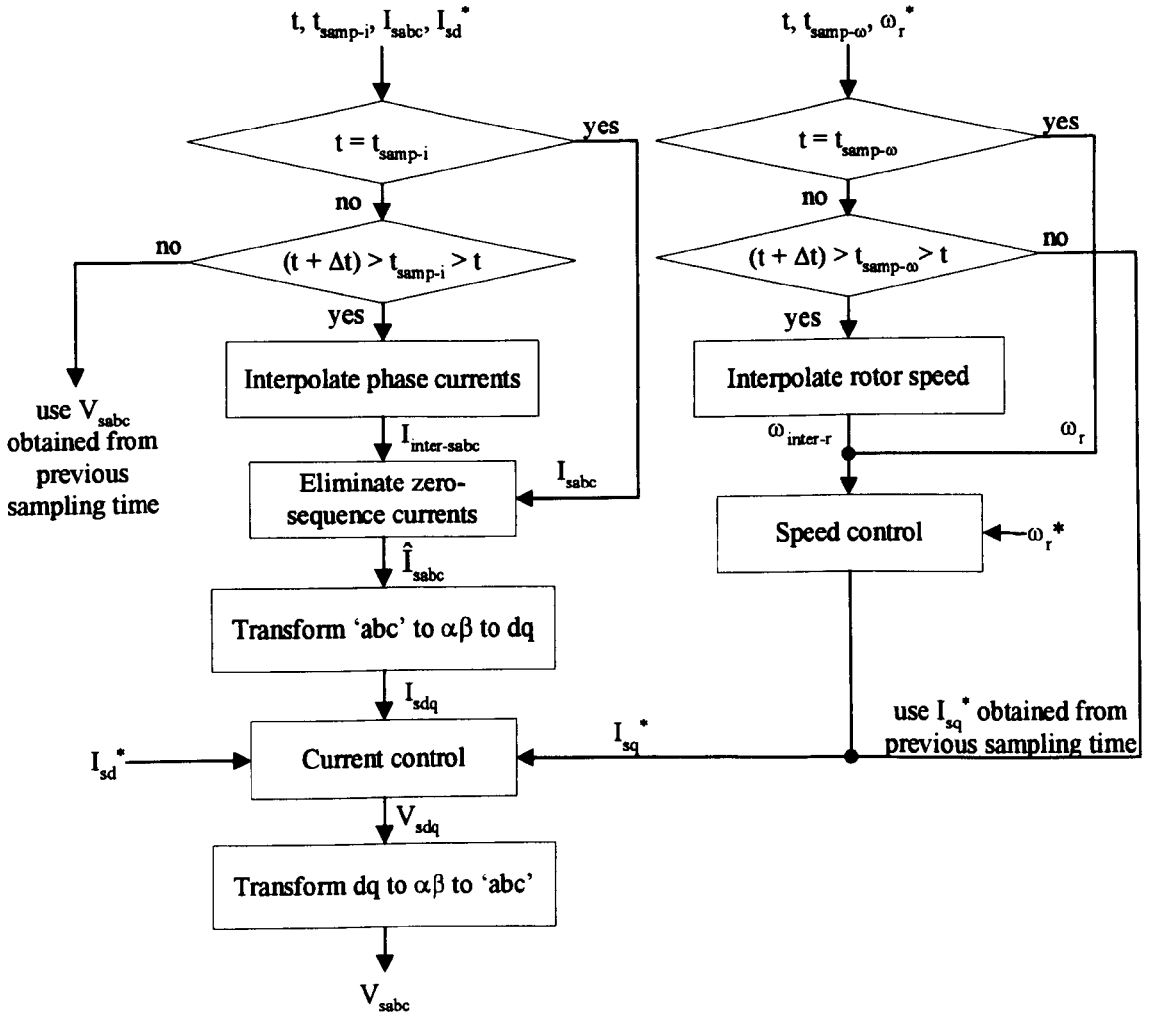

Figure 2.8: Flow chart of vector control subroutine for the DCM software.

e) Incorporation of levitation winding

The forces required to levitate the rotor in a bearingless motor are generated by incorporating an extra set of windings on the stator. Therefore, the DCM software was modified to enable a second set of double-layer stator winding, wound in either fractional or full-pitch configuration, to be modelled. The additional code written in the DCM software to incorporate the second set of stator winding is added to the original subroutine written to incorporate the first set of stator winding as indicated by '(e)' in Figure 2.6(a). The addition of the levitation stator winding increases the number of state variables and state equations to be solved by three. Therefore, for a cage rotor type bearingless motor

$$\mathbf{x} = \lfloor f_0, f_1, \cdots, f_{Nnode-1}, F_{Rmmf,0}, F_{Rmmf,1}, \cdots, F_{Rmmf,Nbar-1}, I_{sa}^{M}, I_{sb}^{M}, I_{sc}^{M}, I_{sa}^{N}, I_{sb}^{N}, I_{sc}^{N}, \theta_{mech}, \omega_{r\,mech} \rfloor^{T} \tag{2.29}$$

whereas for the wound rotor type motor

$$\mathbf{x} = \lfloor f_0, f_1, \cdots, f_{Nnode-1}, I_{ra}, I_{rb}, I_{rc}, I_{sa}^{M}, I_{sb}^{M}, I_{sc}^{M}, I_{sa}^{N}, I_{sb}^{N}, I_{sc}^{N}, \theta_{mech}, \omega_{r\,mech} \rfloor^{T} \tag{2.30}$$

where I_{sabc}^{M} and I_{sabc}^{N} are the phase currents of the M-pole main and N-pole levitation stator windings, respectively. The matrix **A(x)** of the set of state equations in the bearingless motor is then defined as

$$\mathbf{A}(\mathbf{x}) = \begin{bmatrix} Nnode \times \text{conservation of flux equations, eq. (2.18)} \\ n \times \text{electrical loop equations, eq. (2.5)} \\ 2 \text{ dynamic equations, eq. (2.6) and (2.7)} \end{bmatrix} \tag{2.31}$$

where $n = \begin{cases} 6 + Nbar - 1, & \text{for cage rotor} \\ 9 & \text{, for wound rotor} \end{cases}$.

f) Force calculations

After solving the state variables in the bearingless induction motor, the forces acting on the rotor are evaluated by the postprocessor. Similar to the torque calculation, the forces are determined using the virtual work principle on each airgap reluctance element. Based on this principle, the radial force due to an airgap reluctance element is obtained from the change of magnetic energy E stored in the element due to a virtual change in its length in the radial direction. Therefore, radial force due to airgap element 'i' is given by

$$F_{rad,i} = \frac{\partial E_i}{\partial l_g} \tag{2.32}$$

where E_i is the magnetic energy E stored in the element and is obtained from equation (2.9). On the other hand, the tangential force is obtained from the change of magnetic energy E stored in each airgap element due to a virtual movement of the rotor in the tangential direction, which is given by

$$F_{\tan,i} = \frac{1}{r}\frac{\partial E_i}{\partial \theta} \tag{2.33}$$

The y- and x- directed forces acting on each rotor tooth ($F_{y,r}$ and $F_{x,r}$ respectively) are then obtained by resolving the sum of the radial and tangential forces due to all the airgap elements connected to the rotor tooth using the following equation

$$\begin{bmatrix} F_{y,r} \\ F_{x,r} \end{bmatrix} = \begin{bmatrix} \cos\left(\theta_{rt} + \theta_{skew}^{mech}/2\right) & -\sin\left(\theta_{rt} + \theta_{skew}^{mech}/2\right) \\ \sin\left(\theta_{rt} + \theta_{skew}^{mech}/2\right) & +\cos\left(\theta_{rt} + \theta_{skew}^{mech}/2\right) \end{bmatrix} \begin{bmatrix} \sum_i F_{rad,i} \\ \sum_i F_{\tan,i} \end{bmatrix} \tag{2.34}$$

where θ_{rt} is the mechanical angular position of the rotor tooth relative to the 0° axis and θ_{skew}^{mech} is the skew angle of the rotor in mechanical degrees. Hence, the total forces acting on the rotor F_y and F_x are given by the summation of the individual forces acting on each rotor tooth, i.e.

$$\begin{bmatrix} F_y \\ F_x \end{bmatrix} = \begin{bmatrix} \sum_r F_{y,r} \\ \sum_r F_{x,r} \end{bmatrix} \tag{2.35}$$

A subroutine was written to evaluate the forces acting on the rotor in the DCM software based on the equations stated above. This subroutine is called just before the simulation results are written to an output file at each time step, as indicated by '(f)' in Figure 2.6(b).

g) Modelling a free-moving rotor

In Chapter 8, simulations of a bearingless wound rotor induction motor will be presented. In the bearingless motor simulated, the rotor is free to move. Therefore, to accurately simulate the motor, a model of the free-moving rotor in the DCM software is essential. When the rotor is held fixed by bearings, the length of all the airgap reluctance elements is equal to the airgap length, l_{g0}. However, when the rotor is allowed to move, the length of each airgap reluctance element 'i' is evaluated every time it is created using the following equation

$$l_{g,i} = l_{g0} - \Delta y \cos\theta_i - \Delta x \sin\theta_i \tag{2.36}$$

with Δy and Δx being the displacements experienced by the rotor in the y- and x-directions, respectively. In equation (2.36), θ_i is the angular position of each airgap reluctance element 'i'. It is assumed that the displacements of the rotor are small such that the stator and rotor teeth are still considered to be parallel as they pass each other. A subroutine was written in the software to calculate the angular position of each airgap element and it is called each time equation (2.36) is used to obtain the length of each airgap reluctance element created at every time step in the simulation, part '(g)' indicated in Figure 2.6(a).

The additional state variables to be solved by the DCM software, due to the modelling of a free-moving rotor, are the displacements Δy and Δx as well as the velocities $\dot{y}$ and

$\dot{x}$. The state equations related to the four new state variables are obtained from the mechanical equations of movement in the y- and x- direction in which

$$\dot{y} - \frac{dy}{dt} = 0 \tag{2.37}$$

$$F_y - M_r \frac{d\dot{y}}{dt} - D\dot{y} - Ky - F_{load-y} = 0 \tag{2.38}$$

$$\dot{x} - \frac{dx}{dt} = 0 \tag{2.39}$$

$$F_x - M_r \frac{d\dot{x}}{dt} - D\dot{x} - Kx - F_{load-x} = 0 \tag{2.40}$$

where M_r is the mass of the rotor, D represents the friction and K represents the stiffness. In equations (2.38) and (2.40), F_{load-y} and F_{load-x} are the load forces acting on the motor in the y- and x- directions respectively. The forces F_y and F_x in the above equations are the forces produced by the motor obtained from the virtual work principle using equation (2.35). Hence, for the bearingless wound rotor IM, the vector of state equations to solve is given by

$$\mathbf{x} = \left[f_0, f_1, \cdots, f_{Nnode-1}, I_a^R, I_b^R, I_c^R, I_a^M, I_b^M, I_c^M, I_a^N, I_b^N, I_c^N, \theta_{mech}, \omega_{r\,mech}, y, \dot{y}, x, \dot{x} \right]^T \tag{2.41}$$

with the matrix **A(x)** of the set of state equations defined as

$$\mathbf{A(x)} = \begin{bmatrix} Nnode \times \text{conservation of flux equations, eq. (2.18)} \\ 6 \times \text{electrical loop equations, eq. (2.5)} \\ \text{2 dynamic equations, eq. (2.6) and (2.7)} \\ \text{equation (2.37)} \\ \text{equation (2.38)} \\ \text{equation (2.39)} \\ \text{equation (2.40)} \end{bmatrix} \tag{2.42}$$

Chapter 3

Force production in a self-levitating motor

3.1. Introduction

In a bearingless motor, both the main M-pole torque production winding and the levitation N-pole winding produces a particular rotating airgap flux density, which will interact to produce a non-uniformly distributed airgap flux density. It is this non-uniform flux density distribution which will produce Maxwell forces acting on the rotor. In previous research, a reluctance-type (Chiba *et al.*, 1991(a)) and induction-type (Chiba *et al.*, 1991(a), 1995 and Chiba *et al.*, 1997) bearingless motor had been proposed in which both motors consisted of an additional two-pole winding wound onto the stator having an existing four-pole torque producing winding. The choice of pole number for both the stator windings were specifically chosen by Chiba *et al.* based on their ability of producing an imbalance in the airgap magnetic field at certain places in the airgap, as shown in Figure 3.1, which creates levitation forces.

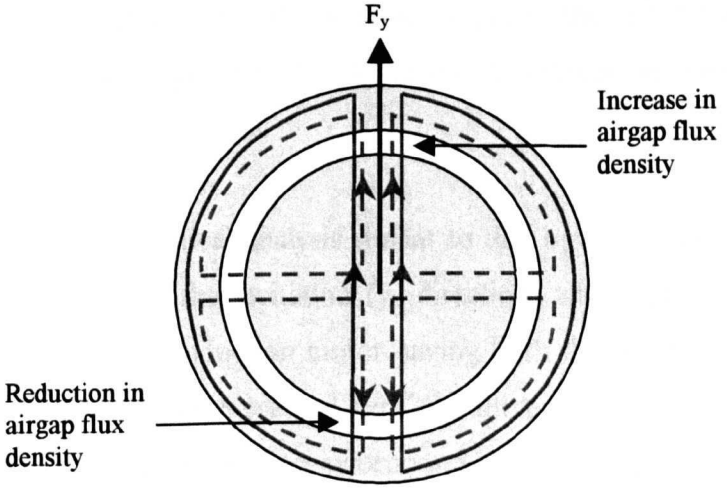

Figure 3.1: Imbalance in airgap field due to interaction between the 4-pole field (dashed lines) and the 2-pole field (solid lines).

However, no mathematical justification or general theory of pole number combination between the main torque production winding and the levitation winding was presented by Chiba *et al.*

A general theory on the choices of pole number combination for a permanent magnet synchronous type and induction type bearingless motors was, however, carried out by Okada *et al.* (1995). It was shown that a levitation winding having a pole number of plus or minus two of the motoring winding pole number was able to produce constant radial force acting on the rotor. The force expression was obtained by adding up the force contributions ΔF on each infinitesimal area ΔS due to the airgap flux density, B given by

$$\Delta F(\theta) = \frac{B^2}{2\mu_0}\Delta S$$

For the permanent magnet type motor, Okada *et al.* (1995) obtained the airgap flux density B, used in the force equation above, by adding up the flux density contributions due to the permanent magnet rotor and the levitation winding wound onto the stator. In the case of the induction motor type, the airgap flux density B was obtained by adding up the field contributions of both the main and levitation winding stator currents together with the field contributions due to the rotor currents induced by the two stator fields. By separating the field contributions of each winding into their corresponding stator and induced rotor fields, the analysis required the use of induced coefficient. Therefore, in order to implement the equations, knowledge of the induced coefficient value is required.

In this chapter, a mathematical analysis similar to that by Okada *et al.* (1995) is utilised to obtain expressions for the levitation (y- direction) and lateral (x- direction) forces acting on the rotor of an induction motor having both the main and levitation winding on the stator. In the analysis presented here, the force expressions will be derived from field distributions that is assumed to incorporate both the contributions from the stator winding and the induced rotor currents, i.e. without the use of induced coefficients. Furthermore, the force equations derived in this chapter are believed to be more

consistent with vector control concepts, as compared to those derived by Okada *et al.* Firstly, in Section 3.2, the force expressions will be derived for an induction motor having a uniform airgap length. This will be used to model an induction motor having bearing relief capabilities, which will be simulated in this thesis in Chapters 5, 6 and 7. Secondly, the force expressions for an induction motor with a non-uniform airgap length, in which the rotor is assumed to be subjected to a perturbation from its centre, will be derived in Section 3.3. This will be useful when designing position control for a totally bearingless induction motor, which will be presented in Chapter 8. Before the force expressions are derived the airgap flux density distribution due to the N-pole (n pole pair) levitation winding is first obtained for both the fixed and perturbed rotor conditions in the respective sections.

3.2. Forces acting on a rotor fixed by bearings

3.2.1. Flux distribution of levitation winding

The N-pole (n pole pair) levitation winding is assumed to be modelled as a current sheet of units A/rad, which has the following current distribution

$$I_f(\theta,t) = I_F \sin(\omega t - n\theta - \phi) \tag{3.1}$$

where ϕ is the phase difference in mechanical radians between the peak of the main winding current and the peak of the radial force winding current. The flux density distribution arising from this stator current distribution can be obtained by way of Ampere's Law,

$$\oint_c \mathbf{H} \cdot \mathbf{dl} = I_{enc} \tag{3.2}$$

where $\mathbf{H}$ is the magnetic intensity, c is the closed path along which the line integral is taken and I_{enc} is the current enclosed by the closed path. In order to perform this calculation it is assumed that the iron in the stator and rotor are infinitely permeable. Hence, the contribution to the line integral, for the closed loop path, c, through the rotor and stator are negligible and only the flux density in the airgap will be considered.

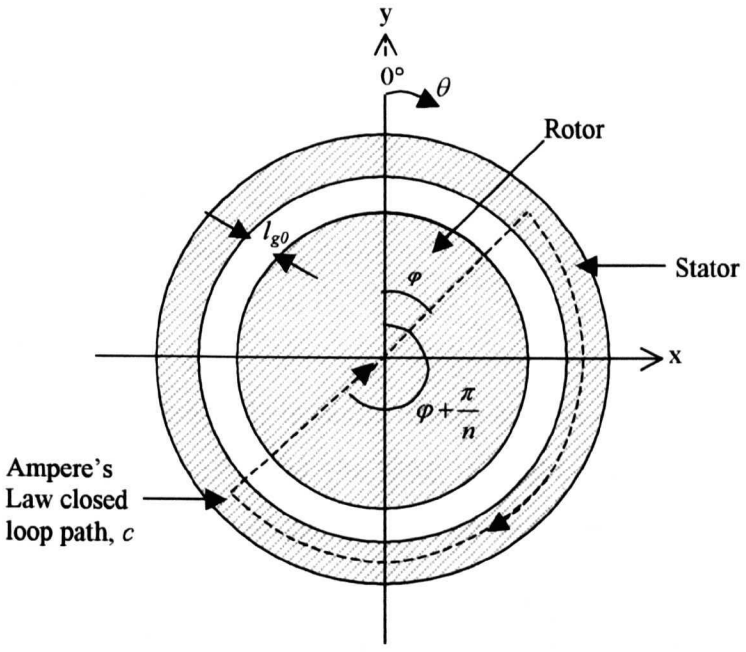

Figure 3.2: Ampere's Law path.

As in Figure 3.2, the line integral crosses the airgap at φ and $\varphi+\pi/n$. Due to symmetry, the flux density at the two airgap crossings of the closed path, c, will be identical in value but opposite in direction. Therefore, equation (3.2) reduces to

$$\oint_c \mathbf{H}\cdot\mathbf{dl} = I_{enc}$$
$$2B_f(\varphi,t)l_{g0} = \mu_0 \cdot NI \tag{3.3}$$

where $B_f(\varphi,t)$ is the flux density at angle φ, l_{g0} is the airgap length, μ_0 is the permeability of vacuum and NI is the total current enclosed by the closed loop path, c. The term NI in this equation is obtained by integrating equation (3.1), which models the current sheet of the levitation winding, over the range φ and $\varphi+\pi/n$. Hence,

$$\begin{aligned}
2B_f(\varphi,t)l_{g0} &= \mu_0 \int_{\varphi}^{\varphi+\frac{\pi}{n}} I_F \sin(\omega t - n\theta - \phi)d\theta \\
&= \frac{\mu_0}{n}\left\{I_F \cos\left(\omega t - n(\varphi+\frac{\pi}{n}) - \phi\right) - I_F \cos(\omega t - n\varphi - \phi)\right\} \\
&= -\frac{2\mu_0}{n}\{I_F \cos(\omega t - n\varphi - \phi)\}
\end{aligned}$$

Therefore, the flux density distribution of the radial force winding is given as

$$B_f(\varphi,t) = -B_F \cos(\omega t - n\varphi - \phi) \tag{3.4}$$

for an arbitrary angle φ, where

$$B_F = \frac{\mu_o}{nl_{g0}} I_F \tag{3.5}$$

It is helpful to rewrite equation (3.1) in terms of two current components, one having a peak in the y- direction ($\theta = 0°$) and the other at right angles to it, i.e. in the x-direction. By separating the current distribution due to the levitation winding into the two components, an alternative expression for its flux density distribution could be derived which will assist in deriving the forces acting on the rotor in the y- and x-directions. Therefore, equation (3.1) then becomes

$$I_f(\theta,t) = I_{F1} \sin(\omega t - n\theta) - I_{F2} \cos(\omega t - n\theta) \tag{3.6}$$

where $I_{F1} = I_F \cos\phi$ and $I_{F2} = I_F \sin\phi$ are the peak currents of the two components in the current sheet of the N-pole radial force winding. As before, the flux density distribution arising from the stator current distribution of equation (3.6) can again be obtained using Ampere's Law (equation (3.3)), whereby

$$\begin{aligned} 2B_f(\varphi,t)l_{g0} &= \mu_0 \int_{\varphi}^{\varphi+\frac{\pi}{N}} I_{F1} \sin(\omega t - n\theta) - I_{F2} \cos(\omega t - n\theta) d\theta \\ &= -\frac{2\mu_0}{n} \{I_{F1} \cos(\omega t - n\varphi) + I_{F2} \sin(\omega t - n\varphi)\} \end{aligned}$$

Hence, the flux density distribution of the radial force winding can also be written as

$$B_f(\varphi,t) = -B_{F1} \cos(\omega t - n\varphi) - B_{F2} \sin(\omega t - n\varphi) \tag{3.7}$$

for an arbitrary angle φ, where

$$B_{F1} = \frac{\mu_o}{nl_{g0}} I_{F1} \text{ and } B_{F2} = \frac{\mu_o}{nl_{g0}} I_{F2} \tag{3.8}$$

It is evident that equation (3.7) is the flux density distribution due to the levitation winding current distribution given by equation (3.1) since the former can be obtained from expanding the cos( ) term of equation (3.4) to give $B_{F1} = B_F \cos\phi$ and $B_{F2} = B_F \sin\phi$. Having derived the flux density distribution due to the N-pole levitation winding, i.e. equation (3.4) and its alternative representation given by equation (3.7), the forces acting on the rotor in the y- and x- direction can be derived.

3.2.2. Derivation of force expressions

The flux density acting on the surface of the rotor due to the main M-pole (m pole pair) winding stator current and induced M-pole rotor current is assumed to be sinusoidal and given by

$$B_o^M(\theta,t) = B_o^M \cos(\omega t - m\theta) \tag{3.9}$$

where B_o^M is the peak magnetic flux density and θ is the mechanical angular coordinate. It is also assumed that this flux density is equal to the airgap field.

As derived in section 3.2.1, the additional N-pole winding in the stator produces a sinusoidal flux density distribution given by

$$B_f^N(\theta,t) = -B_F^N \cos(\omega t - n\theta - \phi) \tag{3.10}$$

where B_F^N is the peak flux density of the N-pole flux distribution and ϕ is the phase difference between the peak of the M-pole flux density distribution to that of the N-pole flux density distribution. Similar to the flux density due to the main winding, it is assumed that equation (3.10) acts on the surface of the rotor, which is assumed equal to the airgap field, and is due to the N-pole winding stator current and induced N-pole rotor current.

Therefore, the magnetic flux density distribution in the airgap of the induction motor can be obtained through the superposition of equations (3.9) and (3.10) and expressed as

$$\begin{aligned} B(\theta,t) &= B_o^M(\theta,t) - B_f^N(\theta,t) \\ &= B_o^M \cos(\omega t - m\theta) + B_F^N \cos(\omega t - n\theta - \phi) \end{aligned} \tag{3.11}$$

This airgap flux density is responsible of producing an attractive force on a surface element of the rotor, ΔS, which can be written as

$$\Delta F(\theta) = \frac{B^2}{2\mu_0}\Delta S \tag{3.12}$$

Hence, the x- and y- direction forces produced in the motor are obtained by resolving equation (3.12) into its horizontal and vertical components and integrating it over the surface of the rotor, of length l_z, as shown below.

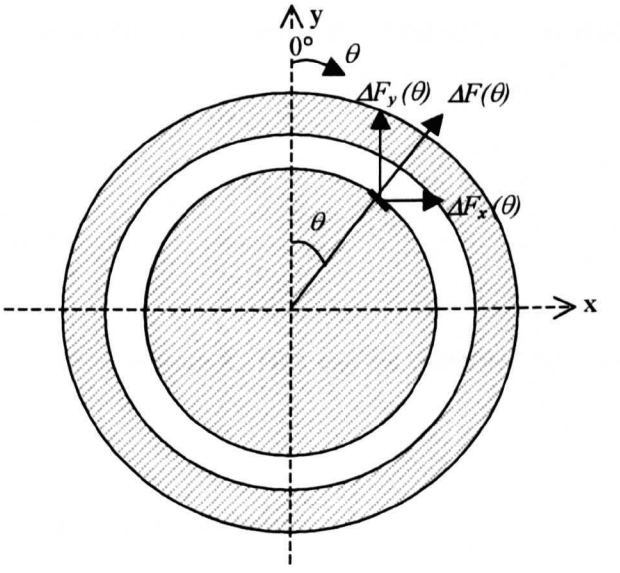

Figure 3.3: Horizontal and vertical forces on the rotor.

$$F_y = \int_0^{2\pi} \int_0^{l_z} \Delta F(\theta)\cos\theta \tag{3.13}$$

$$F_x = \int_0^{2\pi} \int_0^{l_z} \Delta F(\theta)\sin\theta \tag{3.14}$$

3.2.2.1. Levitation force

The levitation or y-direction force exerted on the rotor is given by equation (3.13) and by substituting equation (3.12) this becomes,

$$F_y = \frac{rl_z}{2\mu_0}\int_0^{2\pi} B(\theta,t)^2 \cos\theta \, d\theta$$

The equation above is then solved by further substituting equation (3.11),

$$F_y = \frac{rl_z}{2\mu_0}\int_0^{2\pi} \left\{ \begin{array}{l} B_o^{M\,2}\cos^2(\omega t - m\theta) \\ + B_F^{N\,2}\cos^2(\omega t - n\theta - \phi) \\ + 2B_o^M B_F^N \cos(\omega t - m\theta)\cos(\omega t - n\theta - \phi) \end{array} \right\} \cos\theta \, d\theta \qquad (3.15)$$

where m and n are positive integers larger than or equal to 1. The limits of the integral and the periodicity of the integrand in equation (3.15) results in certain terms within the integral to be zero, when expanded, due to the terms reducing to integrals of the form,

$$\int_0^{2\pi} a\cos(b - k\theta)\, d\theta = 0 \qquad (3.16)$$

$$\int_0^{2\pi} a\sin(b - k\theta)\, d\theta = 0 \qquad (3.17)$$

for all values of b and non-zero integers k. This can be observed by solving each term in equation (3.15) in turn.

The first term integrates to zero as shown below,

$$\begin{aligned} &\frac{rl_z}{2\mu_0}\int_0^{2\pi} B_o^{M\,2}\cos^2(\omega t - m\theta)\cos\theta \, d\theta \\ &= \frac{rl_z}{2\mu_0}\int_0^{2\pi} \frac{B_o^{M\,2}}{2}\left[1 + \cos(2\omega t - 2m\theta)\right]\cos\theta \, d\theta \qquad (3.18) \\ &= \frac{rl_z}{2\mu_0}\int_0^{2\pi} \frac{B_o^{M\,2}}{2}\left[\cos\theta + \frac{1}{2}\cos(2\omega t - (2m+1)\theta) + \frac{1}{2}\cos(2\omega t - (2m-1)\theta)\right] d\theta \\ &= 0 \end{aligned}$$

since all cos( ) terms are of the form given in equation (3.16). The second term of equation (3.15) also reduces to zero because it is similar to the first term with $B_o^{M^2}$ replaced by $B_F^{N^2}$ and m replaced by n in the $\cos^2(\ )$ term.

The integration of the final term in equation (3.15) is given by equation (3.19) below.

$$\begin{aligned}
&\frac{rl_z}{2\mu_0}\int_0^{2\pi} 2B_o^M B_F^N \cos(\omega t - m\theta)\cos(\omega t - n\theta - \phi)\cos\theta\, d\theta \\
&= \frac{rl_z}{2\mu_0}\int_0^{2\pi} \frac{B_o^M B_F^N}{2}\begin{bmatrix}\cos(-(m-n+1)\theta+\phi)+\cos(-(m-n-1)\theta+\phi) \\ +\cos(2\omega t-(m+n+1)\theta-\phi) \\ +\cos(2\omega t-(m+n-1)\theta-\phi)\end{bmatrix} d\theta \\
&= 0, \text{ when } m\text{-}n \neq \pm 1
\end{aligned} \tag{3.19}$$

However, when $m-n=\pm 1$, the above equation integrates to give

$$\begin{aligned}
&\frac{rl_z}{2\mu_0}\int_0^{2\pi} \frac{B_o^M B_F^N}{2}\begin{bmatrix}\cos(-(m-n+1)\theta+\phi)+\cos(-(m-N-1)\theta+\phi) \\ +\cos(2\omega t-(m+n+1)\theta-\phi) \\ +\cos(2\omega t-(m+n-1)\theta-\phi)\end{bmatrix} d\theta \\
&= \frac{rl_z}{2\mu_0}\int_0^{2\pi} \frac{B_o^M B_F^N}{2}\cos(0+\phi)\, d\theta \\
&= \frac{rl_z}{2\mu_0} B_o^M B_F^N \pi\cos\phi
\end{aligned} \tag{3.20}$$

which is the only non-zero term in equation (3.15).

Hence, the levitation force expression, given by equation (3.15), reduces to a constant force,

$$F_y = \frac{rl_z \pi B_o^M}{2\mu_0} B_F^N \cos\phi \tag{3.21}$$

when the difference between the main winding pole number, M, and the levitation winding pole number, N, is ± 2.

3.2.2.2. Lateral force

Equation (3.14) represents the lateral or x- direction force acting on the rotor, which upon substitution of equation (3.12) becomes:

$$F_x = \frac{rl_z}{2\mu_0}\int_0^{2\pi} B(\theta,t)^2 \sin\theta \, d\theta$$

As for the levitation force, the expression for $B(\theta,t)$, as given in equation (3.11), was substituted into the above equation to give,

$$F_x = \frac{rl_z}{2\mu_0}\int_0^{2\pi}\left\{\begin{array}{l} B_o^{M\,2}\cos^2(\omega t - m\theta) \\ + B_F^{N\,2}\cos^2(\omega t - n\theta - \phi) \\ + 2B_o^M B_F^N \cos(\omega t - m\theta)\cos(\omega t - n\theta - \phi) \end{array}\right\}\sin\theta \, d\theta \qquad (3.22)$$

The similar method employed to solve for the levitation force will be employed here where each term of equation (3.22) will be solved in turn.

The first term does not contribute to the x- direction force as shown below

$$\begin{aligned} &\frac{rl_z}{2\mu_0}\int_0^{2\pi} B_o^{M\,2}\cos^2(\omega t - m\theta)\sin\theta \, d\theta \\ &= \frac{rl_z}{2\mu_0}\int_0^{2\pi}\frac{B_o^{M\,2}}{2}[1+\cos(2\omega t - 2m\theta)]\sin\theta \, d\theta \qquad (3.23) \\ &= \frac{rl_z}{2\mu_0}\int_0^{2\pi}\frac{B_o^{M\,2}}{2}\left[\sin\theta + \frac{1}{2}\sin(2\omega t - (2m-1)\theta) - \frac{1}{2}\sin(2\omega t - (2m+1)\theta)\right]d\theta \\ &= 0 \end{aligned}$$

as all $\sin(\,)$ terms in this integration are of the form given in equation (3.17). Likewise, the second term of equation (3.22) also reduces to zero because it is similar to the first term, in which $B_o^{M\,2}$ is replaced by $B_F^{N\,2}$ and m replaced by n in the $\cos^2(\,)$ term.

The final term to be considered from equation (3.22) also integrates to zero as shown in equation (3.24).

$$\frac{rl_z}{2\mu_0}\int_0^{2\pi} 2B_o^M B_F^N \cos(\omega t - m\theta)\cos(\omega t - n\theta - \phi)\sin\theta\, d\theta$$

$$= \frac{rl_z}{2\mu_0}\int_0^{2\pi} \frac{B_o^M B_F^N}{2}\left[\begin{array}{r}\sin\left(-(m-n-1)\theta+\phi\right)-\cos\left(-(m-n+1)\theta+\phi\right)\\ +\sin\left(2\omega t-(m+n-1)\theta-\phi\right)\\ -\sin\left(2\omega t-(m+n+1)\theta-\phi\right)\end{array}\right]d\theta \qquad (3.24)$$

$= 0$, when $m\text{-}n \neq \pm 1$

However, if $m-n=\pm 1$, this final term becomes

$$\frac{rl_z}{2\mu_0}\int_0^{2\pi} \frac{B_o^M B_F^N}{2}\left[\begin{array}{r}\sin\left(-(m-n-1)\theta+\phi\right)-\sin\left(-(m-n+1)\theta+\phi\right)\\ +\sin\left(2\omega t-(m+n-1)\theta-\phi\right)\\ +\sin\left(2\omega t-(m+n+1)\theta-\phi\right)\end{array}\right]d\theta$$

$$= \frac{rl_z}{2\mu_0}\int_0^{2\pi} \pm\frac{B_o^M B_F^N}{2}\sin(0+\phi)\,d\theta \qquad (3.25)$$

$$= \pm\frac{rl_z}{2\mu_0} B_o^M B_F^N \pi\sin\phi$$

Therefore, the lateral force expression reduces to,

$$F_x = \pm\frac{rl_z\pi B_o^M}{2\mu_0} B_F^N \sin\phi, \text{ when } m-n=\pm 1 \qquad (3.26)$$

However, unlike the levitation force, equation (3.26) clearly illustrates that the direction of the lateral force is dependent on the relationship between the main winding pole number, M and the levitation control winding pole number, N.

Based on equations (3.21) and (3.26), an induction motor, with a motoring M-pole stator winding, is capable of producing magnetic bearing forces when an additional winding having a pole number N = M ± 2 is wound onto the stator. The magnitude of this force is obtained from

$$|F| = \sqrt{F_y^2 + F_x^2} = \frac{rl_z\pi B_o^M}{2\mu_0} B_F^N \qquad (3.27)$$

where F_y and F_x are given by equations (3.21) and (3.26).

Despite equations (3.21) and (3.26), the force expressions become much more useful if it is derived using a levitation winding flux density distribution $B_f(\theta,t)$ which is separated into two separate components lying along the y- and x- axis respectively. Therefore equation (3.10), could be separated into two separate components to give

$$B_f^N(\theta,t) = -B_{Fy}^N \cos(\omega t - n\theta) - B_{Fx}^N \sin(\omega t - n\theta) \tag{3.28}$$

where $B_{Fy}^N = B_F^N \cos\phi$ and $B_{Fx}^N = B_F^N \sin\phi$ are the peak flux densities of the two components aligned with the y- and x- axis respectively when B_o^M is aligned with the y-axis as shown in Figure 3.4. It is important to note that equation (3.28) is identical to equation (3.7) derived in section 3.2.1 with B_{F1} being replaced by B_{Fy}^N and B_{F2} by B_{Fx}^N.

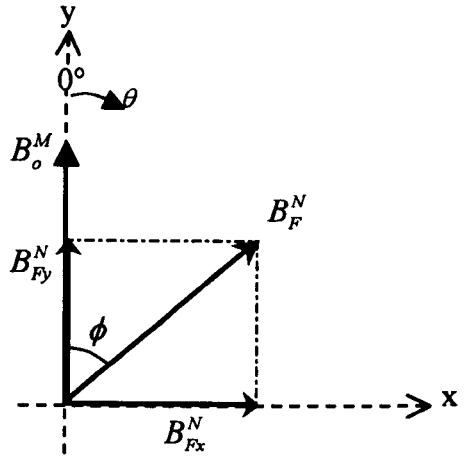

Figure 3.4: Graphical representation of the peak airgap flux densities due to the M-pole main winding and N-pole levitation winding.

Therefore, the terms $B_F^N \cos\phi$ and $B_F^N \sin\phi$ in the levitation and lateral force expressions given by equations (3.21) and (3.26) respectively could be rewritten as

$$F_y = \frac{rl_z \pi B_o^M}{2\mu_0} B_{Fy}^N \tag{3.29}$$

$$F_x = \pm \frac{rl_z \pi B_o^M}{2\mu_0} B_{Fx}^N \tag{3.30}$$

when M – N = ±2 or m – n = ±1.

Equations (3.29) and (3.30) are much more useful in comparison to equations (3.21) and (3.26) because it clearly illustrates that the levitation and lateral forces acting on the rotor could be directly controlled by the peak magnitudes of the levitation winding flux density components B_{Fy}^{N} and B_{Fx}^{N} respectively. However, in order for the equations to be applicable, the flux density component B_{Fy}^{N} must be aligned with the peak airgap flux density of the main winding B_{o}^{M} with B_{Fx}^{N} lying in quadrature.

Equations (3.29) and (3.30) correspond with the findings of Okada *et al.* (1995) for a permanent magnet type bearingless motor. However, unlike the results presented by Okada *et al.* (1995), it is clear from the derivation above that the direction of the lateral force F_x is dependant on the M-N pole combination, that is F_x acts in the positive x-direction when M – N = +2 and is negative when M – N = -2. In the case of an induction type motor, the force relationship derived by Okada *et al.* (1995) utilised a formulation based on separating the flux density distributions in terms of contributions from the stator currents and from their induced rotor currents, in which induced coefficients were involved in the formulation. This introduces an additional term dependant upon the induced coefficients to be multiplied with equations (3.29) and (3.30), which increases the complexity in calculating the forces since a value of the induced coefficients is required. Furthermore, force expressions for the induction motor derived in this section are believed to be more consistent with vector control concepts, as compared to those derived by Okada *et al.*

3.3. Forces acting on a perturbed rotor

The force expressions derived in the previous section are only relevant for machines with rotors fixed by conventional bearings, thus making it relevant for bearing relief applications. In a totally bearingless machine, however, the interaction between the flux densities of the main winding and the additional stator winding will produce radial forces acting on a free moving rotor. This will cause the rotor to experience perturbations from its central position. Expressions for the radial forces acting on the

rotor due to the perturbations experienced will be derived in this section. These expressions are thought to be useful when designing the position control compensator for a totally bearingless induction motor, which will be presented in this thesis in Chapter 8. However, it is crucial to comprehend that the rotor perturbations will also result in a change in the airgap flux density distribution in the machine, which will be looked into firstly.

3.3.1. Flux distribution of the levitation winding due to a perturbed rotor

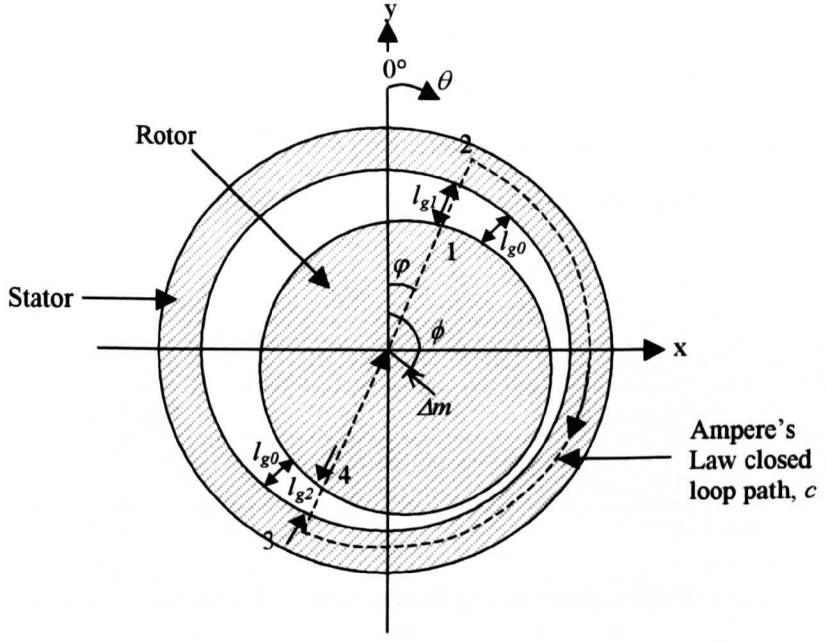

Figure 3.5: Ampere's Law path for a perturbed rotor machine.

Assuming that the rotor has been perturbed in the ϕ direction by a distance Δm, a non-uniform airgap length is created between the rotor and the stator as shown in Figure 3.5. The airgap length in the machine at a general mechanical angle θ can then be expressed as

$$l_g(\theta) = l_{g0}\left[1 - \frac{\Delta m}{l_{g0}}\cos(\theta - \phi)\right] \tag{3.31}$$

where l_{g0} is the airgap length when the rotor is centred. It is also assumed that the perturbation is small, thus making first order approximations applicable in the derivations wherever necessary. Equation (3.31) can also be expressed in terms of small perturbations, Δx and Δy, in the direction of the positive x- and positive y- axis respectively,

$$l_g(\theta) = l_{g0}\left[1 - \frac{\Delta y}{l_{g0}}\cos\theta - \frac{\Delta x}{l_{g0}}\sin\theta\right] \tag{3.32}$$

In order to obtain an expression for the airgap flux density due to the N-pole winding in a perturbed rotor machine, Ampere's Law is again considered. Figure 3.5 shows the Ampere's Law closed loop path for the perturbed motor machine. The same closed loop path is also shown in Figure 3.6, but with the stator and rotor being rolled out.

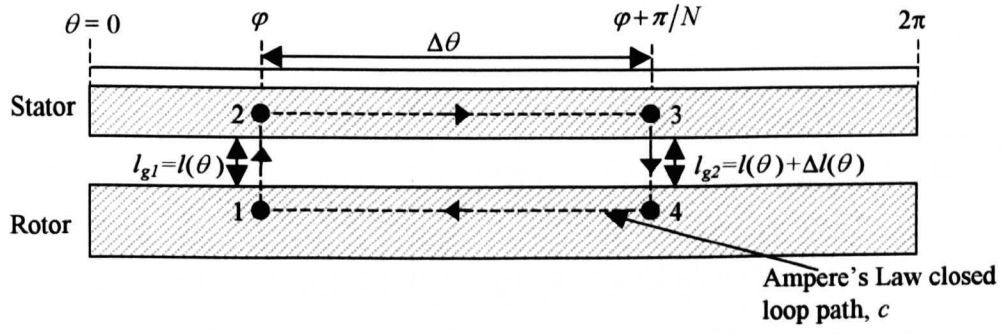

Figure 3.6: Ampere's Law path for a perturbed rotor machine with the stator and rotor rolled out.

Therefore, assuming that the rotor and stator iron are infinitely permeable, Ampere's Law requires:

$$\oint_c \mathbf{H}\cdot\mathbf{dl} = I_{enc}$$

$$\int_1^2 H_1 l_{g1} + \int_3^4 H_2 l_{g2} = \int_{\varphi}^{\varphi+\frac{\pi}{N}} I(\theta,t)d\theta \tag{3.33}$$

$$H(\theta,t)l(\theta) - [H(\theta,t) + \Delta H(\theta,t)][l(\theta) + \Delta l(\theta)] = I(\theta,t)\Delta\theta$$

$$H(\theta,t)\Delta l(\theta) + l(\theta)\Delta H(\theta,t) = -I(\theta,t)\Delta\theta$$

If the last line of equation (3.33) was divided by $\Delta\theta$ and the limit of $\Delta\theta$ is taken as it approaches zero,

$$\begin{aligned}
\lim_{\Delta\theta\to 0}\left[H(\theta,t)\frac{\Delta l(\theta)}{\Delta\theta}+l(\theta)\frac{\Delta H(\theta,t)}{\Delta\theta}\right] &= -I(\theta,t)\\
H(\theta,t)\frac{\partial l(\theta)}{\partial\theta}+l(\theta)\frac{\partial H(\theta,t)}{\partial\theta} &= -I(\theta,t)\\
\frac{\partial}{\partial\theta}[H(\theta,t)l(\theta)] &= -I(\theta,t)
\end{aligned} \tag{3.34}$$

Hence, an expression for the airgap flux density $B_f^{N'}(\theta,t)$ due to the N-pole winding in the perturbed rotor can be obtained from the last line of equation (3.34) with the knowledge that $B = \mu_0 H$ and that the expression for $I(\theta,t)$ is given by equation (3.6). Therefore,

$$\frac{\partial}{\partial\theta}[B_f^{N'}(\theta,t)l(\theta)] = -\mu_0 I_f(\theta,t) \tag{3.35}$$

and by substituting equation (3.6) into equation (3.35) and integrating both sides,

$$\begin{aligned}
B_f^{N'}(\theta,t)l_g(\theta) &= -\mu_0\int I_{F1}\sin(\omega t-n\theta)-I_{F2}\cos(\omega t-n\theta)d\theta\\
&= -\frac{\mu_0}{n}[I_{F1}\cos(\omega t-n\theta)+I_{F2}\sin(\omega t-n\theta)]
\end{aligned}$$

Hence,

$$\begin{aligned}
B_f^{N'}(\theta,t) &= -\frac{\mu_0}{nl_g(\theta)}[I_{F1}\cos(\omega t-n\theta)+I_{F2}\sin(\omega t-n\theta)]\\
&= -\frac{\mu_0}{nl_{g0}\left[1-\frac{\Delta y}{l_{g0}}\cos\theta-\frac{\Delta x}{l_{g0}}\sin\theta\right]}[I_{F1}\cos(\omega t-n\theta)+I_{F2}\sin(\omega t-n\theta)]\\
&= \frac{B_f(\theta,t)}{\left[1-\frac{\Delta y}{l_{g0}}\cos\theta-\frac{\Delta x}{l_{g0}}\sin\theta\right]}
\end{aligned}$$

As the perturbation is assumed to be small and first order approximations apply, the airgap flux density distribution of the N-pole winding due to a perturbed rotor can be simplified to be:

$$B_f^{N'}(\theta,t) \approx B_f^N(\theta,t)\left[1+\frac{\Delta y}{l_{g0}}\cos\theta+\frac{\Delta x}{l_{g0}}\sin\theta\right] \tag{3.36}$$

where $B_f^N(\theta,t)$ is the airgap flux density distribution of a centred rotor due to the N-pole winding, as in equation (3.28).

The effect of rotor eccentricity on the airgap field of a non-salient pole machine had been investigated previously by Swann (1963) by means of a mathematical analysis employing conformal transformation. Swann proved that an approximate calculation of the airgap flux density distribution on a perturbed rotor using Ampere's Law was able to yield results which were in good agreement to those derived through the mathematical analysis. Hence, the use of equation (3.36) as the airgap flux density distribution due to the levitation winding for a perturbed rotor (derived from Ampere's Law) throughout this thesis is justified.

The effect of the rotor perturbation on the flux density distribution due to main M-pole winding is similar to that derived for the N-pole levitation winding. Hence, the airgap flux density distribution of the M-pole winding due to a perturbed rotor can also simplified to

$$B_o^{M'}(\theta,t) \approx B_o^M(\theta,t)\left[1+\frac{\Delta y}{l_{g0}}\cos\theta+\frac{\Delta x}{l_{g0}}\sin\theta\right] \tag{3.37}$$

with $B_o^M(\theta,t)$ being the airgap flux density distribution of a centred rotor due to the M-pole winding, as given in equation (3.9).

3.3.2. Force derivations for the perturbed rotor case

In order to derive the force expressions for the perturbed rotor condition, the total airgap flux density distribution is required and it is obtained from

$$B'(\theta,t) = B_o^{M'}(\theta,t) - B_f^{N'}(\theta,t)$$
$$= B_o^M(\theta,t)\left[1+\frac{\Delta y}{l_{g0}}\cos\theta+\frac{\Delta x}{l_{g0}}\sin\theta\right] - B_f^N(\theta,t)\left[1+\frac{\Delta y}{l_{g0}}\cos\theta+\frac{\Delta x}{l_{g0}}\sin\theta\right] \quad (3.38)$$

where $B_o^M(\theta,t) = B_o^M\cos(\omega t - m\theta)$ and

$B_f^N(\theta,t) = -B_{Fy}^N\cos(\omega t - n\theta) - B_{Fx}^N\sin(\omega t - n\theta)$

are the airgap flux density distributions of the unperturbed rotor due to the main and levitation windings respectively.

With this, the expression for the forces acting on the perturbed rotor can be obtained as in Section 3.2.2 but with the airgap flux density now given by equation (3.38), where

$$F_y' = \frac{rl_z}{2\mu_0}\int_0^{2\pi} B'(\theta,t)^2\cos\theta\, d\theta \quad (3.39)$$

$$F_x' = \frac{rl_z}{2\mu_0}\int_0^{2\pi} B'(\theta,t)^2\sin\theta\, d\theta \quad (3.40)$$

However, before proceeding with the integration, it would be worthwhile to look further at the expression for $B'(\theta,t)^2$.

From equation (3.38),

$$B'(\theta,t)^2 = B_o^{M'}(\theta,t)^2 - 2B_o^{M'}(\theta,t)B_f^{N'}(\theta,t) + B_f^{N'}(\theta,t)^2 \quad (3.41)$$

which can be simplified by employing first order approximations whereby

$$\left[1+\frac{\Delta y}{l_{g0}}cos\theta+\frac{\Delta x}{l_{g0}}sin\theta\right]^2 \approx \left[1+2\frac{\Delta y}{l_{g0}}cos\theta+2\frac{\Delta x}{l_{g0}}sin\theta\right] \quad (3.42)$$

Therefore, through substitution of (3.36) and (3.37) and application of (3.42), equation (3.41) becomes:

$$B'(\theta,t)^2 = \left(B_o^M(\theta,t)^2 - 2B_o^M(\theta,t)B_f^N(\theta,t) + B_f^N(\theta,t)^2\right)\left[1+2\frac{\Delta y}{l_{g0}}\cos\theta + 2\frac{\Delta x}{l_{g0}}\sin\theta\right]$$

$$= B(\theta,t)^2\left[1+2\frac{\Delta y}{l_{g0}}\cos\theta + 2\frac{\Delta x}{l_{g0}}\sin\theta\right]$$

$$= B(\theta,t)^2 + 2B(\theta,t)^2\left[\frac{\Delta y}{l_{g0}}\cos\theta + \frac{\Delta x}{l_{g0}}\sin\theta\right] \tag{3.43}$$

In the equation above,

$B(\theta,t) = B_o^M\cos(\omega t - m\theta) + B_{Fy}^N\cos(\omega t - n\theta) + B_{Fx}^N\sin(\omega t - n\theta)$

which is the total airgap flux density of the unperturbed rotor due to both M- and N-pole windings. Therefore, the levitation and lateral force due to the perturbed rotor can now be obtained by substituting equation (3.43) into equations (3.39) and (3.40).

3.3.2.1. Levitation force

The perturbed rotor levitation force, obtained from (3.39) and (3.43) is given by

$$F_y' = \frac{rl_z}{2\mu_0}\int_0^{2\pi}\left\{B(\theta,t)^2 + 2B(\theta,t)^2\left[\frac{\Delta y}{l_{g0}}\cos\theta + \frac{\Delta x}{l_{g0}}\sin\theta\right]\right\}\cos\theta\, d\theta$$

$$= \frac{rl_z}{2\mu_0}\int_0^{2\pi}B(\theta,t)^2\cos\theta\, d\theta + \frac{rl_z}{\mu_0}\int_0^{2\pi}B(\theta,t)^2\left[\frac{\Delta y}{l_{g0}}\cos\theta + \frac{\Delta x}{l_{g0}}\sin\theta\right]\cos\theta\, d\theta \tag{3.44}$$

$$= F_y + \Delta F_y$$

where F_y is the unperturbed levitation force, as given by equation (3.29), when $m-n=\pm1$. Thus, the only term of equation (3.43) left to be considered is the levitation force due to the perturbations in the x and y direction,

$$\Delta F_y = \frac{rl_z}{\mu_0 l_{g0}}\int_0^{2\pi}B(\theta,t)^2\left[\Delta y\cos\theta + \Delta x\sin\theta\right]\cos\theta\, d\theta \tag{3.45}$$

In order to simplify the integration of equation (3.45), the terms inside the integral are taken in two separate groups.

Firstly, the term $B(\theta,t)^2$ is given by

$$\begin{aligned} B(\theta,t)^2 &= \left[B_o^M \cos(\omega t - m\theta) + B_{Fy}^N \cos(\omega t - n\theta) + B_{Fx}^N \sin(\omega t - n\theta)\right]^2 \\ &= B_o^{M\,2} \cos^2(\omega t - m\theta) + B_{Fy}^{N\,2} \cos^2(\omega t - n\theta) + B_{Fx}^{N\,2} \sin^2(\omega t - n\theta) \\ &\quad + 2B_o^M \cos(\omega t - m\theta) B_{Fy}^N \cos(\omega t - n\theta) + 2B_o^M \cos(\omega t - m\theta) B_{Fx}^N \sin(\omega t - n\theta) \\ &\quad + 2B_{Fy}^N \cos(\omega t - n\theta) B_{Fx}^N \sin(\omega t - n\theta) \end{aligned} \tag{3.46}$$

which expands into the following five terms:

A. $B_o^M B_{Fy}^N [\cos(-(m-n)\theta) + \cos(2\omega t - (m+n)\theta)]$

B. $B_o^M B_{Fx}^N [\sin(2\omega t - (m+n)\theta) - \sin(-(m-n)\theta)]$

C. $\dfrac{B_o^{M\,2}}{2} + \dfrac{B_{Fy}^{N\,2}}{2} + \dfrac{B_{Fx}^{N\,2}}{2}$ (3.47)

D. $\dfrac{B_o^{M\,2}}{2}\cos(2\omega t - 2m\theta) + \left[\dfrac{B_{Fy}^{N\,2}}{2} - \dfrac{B_{Fx}^{N\,2}}{2}\right]\cos(2\omega t - 2n\theta)$

E. $B_{Fy}^N B_{Fx}^N \sin(2\omega t - 2n\theta)$

The second group of terms in the integral of equation (3.45), when expanded becomes

$$[\Delta y \cos\theta + \Delta x \sin\theta]\cos\theta = \frac{\Delta y}{2}(1 + \cos 2\theta) + \frac{\Delta x}{2}\sin 2\theta \tag{3.48}$$

Therefore ΔF_y can be obtained from the integral over the range of 0 to 2π of the five terms in equation (3.47), taken in turn, multiplied by equation (3.48),

$$\Delta F_y = \frac{rl_z}{\mu_0 l_{g0}} \int_0^{2\pi} (A + B + C + D + E)\left[\frac{\Delta y}{2}(1 + \cos 2\theta) + \frac{\Delta x}{2}\sin 2\theta\right] d\theta \tag{3.49}$$

Firstly, the integration of A and B of (3.47) with (3.48) integrates to zero

$$\frac{rl_z}{\mu_0 l_{g0}} \int_0^{2\pi} (A + B)\left[\frac{\Delta y}{2}(1 + \cos 2\theta) + \frac{\Delta x}{2}\sin 2\theta\right] d\theta = 0 \tag{3.50}$$

since it gives rise to terms of the form $\cos(k\omega t-(m\pm n\pm c)\theta)$ and $\sin(k\omega t-(m\pm n\pm c)\theta)$ which integrate to zero over the limits considered, with $k = 0$ or 2, $c = 0$ or 2 and m - n = ± 1. Furthermore, since m, n ≥ 1, thus m + n ≥ 3.

Secondly equation (3.49) also consists of,

$$\frac{rl_z}{\mu_0 l_{g0}}\int_0^{2\pi}(D+E)\left[\frac{\Delta y}{2}(1+\cos 2\theta)+\frac{\Delta x}{2}\sin 2\theta\right]d\theta \tag{3.51}$$

which upon expansion and simplification becomes

$$\frac{rl_z}{\mu_0 l_{g0}}\int_0^{2\pi}\left\{\begin{aligned}&\left(\frac{B_{Fy}^N B_{Fx}^N \Delta x}{4}+\frac{\Delta y\left(B_{Fy}^{N\,2}-B_{Fx}^{N\,2}\right)}{8}\right)\cos(2\omega t-2(n+1)\theta)\\&+\left(-\frac{B_{Fy}^N B_{Fx}^N \Delta x}{4}+\frac{\Delta y\left(B_{Fy}^{N\,2}-B_{Fx}^{N\,2}\right)}{8}\right)\cos(2\omega t-2(n-1)\theta)\\&+\left(\frac{B_{Fy}^N B_{Fx}^N \Delta y}{4}+\frac{\Delta x\left(B_{Fy}^{N\,2}-B_{Fx}^{N\,2}\right)}{8}\right)\sin(2\omega t-2(n-1)\theta)\\&+\left(\frac{B_{Fy}^N B_{Fx}^N \Delta y}{4}-\frac{\Delta x\left(B_{Fy}^{N\,2}-B_{Fx}^{N\,2}\right)}{8}\right)\sin(2\omega t-2(n+1)\theta)\end{aligned}\right\}d\theta \tag{3.52}$$

The pole number N, and hence the pole pair number n, of the levitation windings is a non-zero positive integer, therefore

$$\int_0^{2\pi}\mathrm{trig}(2\omega t-2(n-1)\theta)d\theta=\begin{cases}2\pi\times\mathrm{trig}(2\omega t), & n=1\\ 0, & n>1\end{cases}$$

where trig( ) represents either cos( ) or sin( ). Hence, (3.52) integrates to

$$\frac{rl_z\pi}{4\mu_0 l_{g0}}\left\{\begin{aligned}&2B_{Fy}^N B_{Fx}^N(\Delta y\sin 2\omega t-\Delta x\cos 2\omega t)\\&+\left(B_{Fy}^{N\,2}-B_{Fx}^{N\,2}\right)(\Delta y\cos 2\omega t+\Delta x\sin 2\omega t)\end{aligned}\right\} \tag{3.53}$$

when n = 1 and zero when n > 1. Finally,

$$\begin{aligned}&\frac{rl_z}{\mu_0 l_{g0}}\int_0^{2\pi} C\left[\frac{\Delta y}{2}(1+\cos 2\theta)+\frac{\Delta x}{2}\sin 2\theta\right]d\theta \\ &=\frac{rl_z}{\mu_0 l_{g0}}\int_0^{2\pi}\left(\frac{B_o^{M\,2}}{2}+\frac{B_{Fy}^{N\,2}}{2}+\frac{B_{Fx}^{N\,2}}{2}\right)\left[\frac{\Delta y}{2}(1+\cos 2\theta)+\frac{\Delta x}{2}\sin 2\theta\right]d\theta \\ &=\frac{rl_z}{\mu_0 l_{g0}}\frac{\Delta y}{2}\pi\left(B_o^{M\,2}+B_{Fy}^{N\,2}+B_{Fx}^{N\,2}\right)\end{aligned} \tag{3.54}$$

since the integral of $\cos(2\theta)$ and $\sin(2\theta)$ over the considered range is zero.

Therefore, from the contribution of equations (3.50), (3.53) and (3.54) to equation (3.49), the levitation force due to the perturbation, ΔF_y, when $n = 1$ becomes

$$\Delta F_y=\frac{rl_z\pi}{4\mu_0 l_{g0}}\left\{\begin{aligned}&2B_o^{M\,2}\Delta y+B_{Fy}^{N\,2}\Delta y(2+\cos 2\omega t)+B_{Fx}^{N\,2}\Delta y(2-\cos 2\omega t)\\&+\left(B_{Fy}^{N\,2}-B_{Fx}^{N\,2}\right)\Delta x\sin 2\omega t\\&+2B_{Fy}^{N}B_{Fx}^{N}(\Delta y\sin 2\omega t-\Delta x\cos 2\omega t)\end{aligned}\right\} \tag{3.55}$$

However, when n > 1, equation (3.53) becomes zero, and thus,

$$\Delta F_y=\frac{rl_z}{\mu o l_{g0}}\frac{\Delta y}{2}\pi\left(B_o^{M\,2}+B_{Fy}^{N\,2}+B_{Fx}^{N\,2}\right) \tag{3.56}$$

As in equation (3.44), the levitation force acting on a perturbed rotor, with a main and levitation winding pole combination of M – N = ±2, can be expressed as

$$F_y^{'}=F_y+\Delta F_y$$

where

$$F_y=\frac{rl_z\pi B_o^M B_{Fy}^N}{2\mu_0},\ \text{when } M-N=\pm 2 \text{ or } m-n=\pm 1$$

and ΔF_y is as given in equations (3.55) or (3.56) depending on the value of n.

It can be observed that with a perturbed rotor, the levitation force is now dependent on both B_{Fy}^{N} and B_{Fx}^{N}. Furthermore, when n = 1, the levitation force will no longer be constant but will experience oscillations due to the terms $\cos(2\omega t)$ and $\sin(2\omega t)$.

3.3.2.2. Lateral force

Similar to the levitation force, by substituting equation (3.43) into (3.40), the lateral force acting on the perturbed rotor is obtained

$$\begin{aligned} F_x' &= \frac{rl_z}{2\mu_0}\int_0^{2\pi}\left\{B(\theta,t)^2 + 2B(\theta,t)^2\left[\frac{\Delta y}{l_{g0}}\cos\theta + \frac{\Delta x}{l_{g0}}\sin\theta\right]\right\}\sin\theta\, d\theta \\ &= \frac{rl_z}{2\mu_-}\int_0^{2\pi} B(\theta,t)^2\sin\theta\, d\theta + \frac{rl_z}{\mu_0}\int_0^{2\pi} B(\theta,t)^2\left[\frac{\Delta y}{l_{g0}}\cos\theta + \frac{\Delta x}{l_{g0}}\sin\theta\right]\sin\theta\, d\theta \\ &= F_x + \Delta F_x \end{aligned} \tag{3.57}$$

with F_x being the unperturbed lateral force experienced by the bearingless machine when m – n = ±1, as in (3.30).

Again, the remaining term to be considered is the lateral force due to the perturbations, ΔF_x, given by

$$\begin{aligned} \Delta F_x &= \frac{rl_z}{\mu_0 l_{g0}}\int_0^{2\pi} B(\theta,t)^2\left[\Delta y\cos\theta + \Delta x\sin\theta\right]\sin\theta\, d\theta \\ &= \frac{rl_z}{\mu_0 l_{g0}}\int_0^{2\pi}\left(A+B+C+D+E\right)\left[\frac{\Delta y}{2}\sin 2\theta + \frac{\Delta x}{2}(1-\cos 2\theta)\right]d\theta \end{aligned} \tag{3.58}$$

with the terms A, B, C, D and E representing the expansion of the term $B(\theta,t)^2$, as in (3.47).

The integral of the above equation will, again, be done in turn starting with

$$\frac{rl_z}{\mu_0 l_{g0}}\int_0^{2\pi}\left(A+B\right)\left[\frac{\Delta y}{2}\sin 2\theta + \frac{\Delta x}{2}(1-\cos 2\theta)\right]d\theta = 0 \tag{3.59}$$

Equation (3.59) integrates to zero because the expansion of the integrand gives rise to terms of the form $\cos(k\omega t-(m\pm n\pm c)\theta)$ and $\sin(k\omega t-(m\pm n\pm c)\theta)$ which integrate to zero in the limits considered, where $k = 0$ or 2, $c = 0$ or 2 and $m - n = \pm 1$ with $m - n \geq 3$ due to m and n being positive non-zero integers.

The next part of (3.58) to be considered is

$$\frac{rl_z}{\mu_0 l_{g0}}\int_0^{2\pi}(D+E)\left[\frac{\Delta y}{2}\sin 2\theta+\frac{\Delta x}{2}(1-\cos 2\theta)\right]d\theta \tag{3.60}$$

which integrates to give

$$\frac{rl_z\pi}{4\mu_0 l_{g0}}\left\{\begin{array}{l}-2B_{Fy}^{N}B_{Fx}^{N}(\Delta y\cos 2\omega t+\Delta x\sin 2\omega t)\\+\left(B_{Fy}^{N\,2}-B_{Fx}^{N\,2}\right)(\Delta y\sin 2\omega t-\Delta x\cos 2\omega t)\end{array}\right\} \tag{3.61}$$

when n = 1 and zero when n > 1.Lastly,

$$\begin{aligned}&\frac{rl_z}{\mu_0 l_{g0}}\int_0^{2\pi}C\left[\frac{\Delta y}{2}\sin 2\theta+\frac{\Delta x}{2}(1-\cos 2\theta)\right]d\theta\\&=\frac{rl_z}{\mu_0 l_{g0}}\int_0^{2\pi}\left(\frac{B_o^{M\,2}}{2}+\frac{B_{Fy}^{N\,2}}{2}+\frac{B_{Fx}^{N\,2}}{2}\right)\left[\frac{\Delta y}{2}\sin 2\theta+\frac{\Delta x}{2}(1-\cos 2\theta)\right]d\theta\\&=\frac{rl_z}{\mu_0 l_{g0}}\frac{\Delta x}{2}\pi\left(B_o^{M\,2}+B_{Fy}^{N\,2}+B_{Fx}^{N\,2}\right)\end{aligned} \tag{3.62}$$

By considering equations (3.59), (3.61) and (3.62), there exists two possible solutions to the lateral force, ΔF_x, exerted on the rotor due to the perturbation.

When $n = 1$,

$$\Delta F_x=\frac{rl_z\pi}{4\mu_0 l_{g0}}\left\{\begin{array}{l}2B_o^{M\,2}\Delta x+B_{Fy}^{N\,2}\Delta x(2-\cos 2\omega t)+B_{Fx}^{N\,2}\Delta x(2+\cos 2\omega t)\\+\left(B_{Fy}^{N\,2}-B_{Fx}^{N\,2}\right)\Delta y\sin 2\omega t\\-2B_{Fy}^{N}B_{Fx}^{N}(\Delta y\cos 2\omega t+\Delta x\sin 2\omega t)\end{array}\right\} \tag{3.63}$$

However, when n > 1, the contribution of (3.60) to (3.58) becomes zero, and thus,

$$\Delta F_x = \frac{rl_z}{\mu_0 l_{g0}} \frac{\Delta x}{2} \pi \left(B_o^{M\,2} + B_{Fy}^{N\,2} + B_{Fx}^{N\,2} \right) \tag{3.64}$$

Finally, the total lateral force acting on a perturbed rotor, with a main and levitation winding pole combination of M – N = ±2, can be expressed as

$$F_x' = F_x + \Delta F_x$$

where

$$F_x = \pm \frac{rl_z \pi B_o^M B_{Fx}^N}{2\mu_0}, \text{ when } M - N = \pm 2 \text{ or } m - n = \pm 1$$

and ΔF_x is dependant on the value of n, as shown in (3.63) and (3.64).

From the analysis carried out in this chapter, it can be concluded that the forces acting on the rotor of a bearingless motor, in conditions of constant or varying airgap length, are dependant on the peak flux density due to the main M-pole winding in the stator B_o^M as well as the flux densities due to the N-pole levitation winding B_{Fy}^N and B_{Fx}^N. If the magnitude and position of these peak flux densities can be ascertained in the motor, then a suitable force control scheme could be designed to maintain levitation of the rotor.

Chapter 4

Vector control of a bearingless induction motor

4.1. Introduction

In Chapter 3, the expression for the forces acting on a fixed rotor of a bearingless IM having an M-pole torque production stator winding and an N-pole levitation stator winding was derived as

$$F_y = \frac{rl_z \pi B_o^M B_{Fy}^N}{2\mu_o} \tag{4.1}$$

$$F_x = \pm \frac{rl_z \pi B_o^M B_{Fx}^N}{2\mu_o} \tag{4.2}$$

when M – N = ±2. From these equations, it is clear that the forces are dependent on the peak field on the rotor surface due to the M-pole winding, B_o^M, and the peak of the N-pole winding fields, B_{Fy}^N and B_{Fx}^N. It is assumed that B_o^M corresponds to the net airgap flux linkage vector, $\underline{\psi}_o^M$, and B_{Fy}^N and B_{Fx}^N correspond to the net airgap flux linkage vector of the N-pole winding, $\underline{\psi}_o^N$. Therefore, a field-oriented vector control scheme leads to the control of a levitated induction motor. It is a requirement that, in order for (4.1) and (4.2) to be valid, the peaks B_o^M and B_{Fy}^N must lie in the same radial direction, measured in electrical radians, at all instants in time, whilst B_{Fx}^N lies in quadrature. Therefore, in the vector control schemes both B_o^M and B_{Fy}^N are required to be aligned with the d- axis of the rotating frame with B_{Fx}^N aligned with the q-axis.

The vector control schemes introduced in this chapter will be designed for induction motors having two types of rotor structures. Section 4.3, considers a vector control scheme for a motor with squirrel cage rotor whereas Section 4.4 considers a control scheme for an induction motor without any induced N-pole rotor currents, for example a wound rotor having an M-pole winding. For each type of bearingless IM, three different vector control schemes will be proposed. The first scheme involves an indirect rotor field orientation (IRFO) in which both M- and N- pole winding quantities are oriented onto the M-pole rotor flux. However, it will be shown that in the IRFO control of the cage type motor a force in the x- direction F_x will always be produced, even when unwanted, since B_{Fx}^N is aligned on ψ_{oq}^N which is non-zero in the rotor frame. Therefore, to ensure that F_x is present only when required, both the M- and N- pole winding quantities must be oriented onto the M-pole airgap flux. Hence, an indirect airgap field oriented (IAFO) vector control scheme will also be proposed in Sections 4.3 and 4.4. Finally, a mixed field oriented (MFO) scheme, in which the M-pole winding is rotor field oriented whereas the N-pole field is oriented onto the M-pole airgap flux, will also be designed for the bearingless motor having either a cage rotor or a rotor that does not induce any N-pole currents. The MFO scheme will be shown to be beneficial, as it has a simpler design compared to the IAFO scheme since the torque (M-pole winding) control of the motor can be rotor field oriented without compromising the efficiency of the force (N-pole winding) control.

However, before considering the various vector control schemes for the bearingless induction motor, a relationship between forces acting on the rotor and the airgap flux linkage vectors $\underline{\psi}_o^M$ and $\underline{\psi}_o^N$ will first be derived.

4.2. Relationship between the forces acting on the rotor and the airgap flux linkage vectors

This relationship will be derived in two parts. First, an expression relating the peak airgap flux linkage $\hat{\psi}_o$ to the peak airgap field $\hat{B}_o$ is obtained which is applicable to

both the main winding and levitation winding. This expression is then used to relate the x- and y- direction forces to the airgap flux vectors $\underline{\psi}_o^M$ and $\underline{\psi}_o^N$.

4.2.1. Relationship between peak $\hat{\psi}_o$ and peak B_o

The relationship between the peak airgap flux density, $\hat{\psi}_o$, to the peak airgap field, $\hat{B}_o$, is obtained using the basic equations relating the airgap flux, flux linkage and flux density in a rotating ac machine.

For a P-pole (p pole pair) machine, the flux linkage spans an area

$$A = \frac{\pi D l_z}{2p} \tag{4.3}$$

where D is the diameter and l_z is the length of the rotor. The flux density in the airgap of the machine is assumed to be sinusoidal, hence the average flux density, B_{av}, is given by

$$\begin{aligned} B_{av} &= \frac{1}{\pi}\int_{\theta=0}^{\pi} \hat{B}_o \sin\theta d\theta \\ &= \frac{2\hat{B}_o}{\pi} \end{aligned} \tag{4.4}$$

where θ is in electrical degrees.

The relationship between the average airgap flux density and the maximum flux in the airgap is known to be

$$\hat{\phi}_o = B_{av} \cdot A$$

upon which substitution of equations (4.3) and (4.4), can be expressed as

$$\hat{\phi}_o = \frac{\hat{B}_o D l_z}{p} \tag{4.5}$$

Hence, the maximum airgap flux linkage in the machine is given by

$$\hat{\psi}_o = N_{eff}\hat{\phi}_o = N_{eff}\frac{\hat{B}_o 2rl_z}{p} \tag{4.6}$$

where r is the radius of the rotor. In equation (4.6), N_{eff} is the effective fundamental turns, which, for a machine having N_t number of total turns in series per phase, can be expressed as

$$N_{eff} = k_w N_t \tag{4.7}$$

with k_w being the winding factor (Chapman, 1999).

Therefore, a relationship between the peak flux density in the airgap and the peak flux linkage is available from (4.6),

$$\hat{B}_o = \frac{p\hat{\psi}_o}{2rl_z k_w N_t} \tag{4.8}$$

The peak airgap field could also be related to the terminal voltage applied to the windings of the induction motor. Figure 4.1 shows the per phase equivalent circuit of an induction machine.

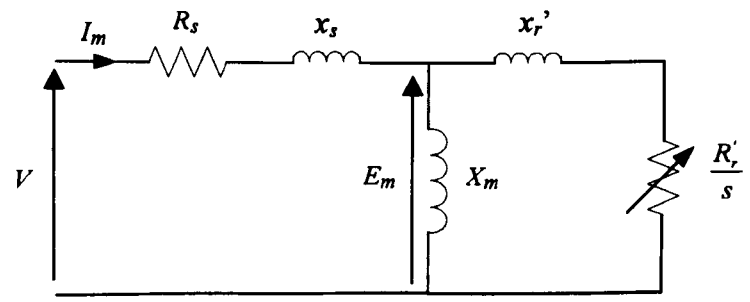

Figure 4.1: Per phase equivalent circuit of an induction motor.

The back emf stator voltage induced in the machine is represented in the equivalent circuit as E_m. The peak of this voltage can also be written as

$$\hat{E}_m = N_{eff}\frac{d\phi_o}{dt} = \omega N_{eff}\hat{\phi}_o \tag{4.9}$$

where $\omega = 2\pi f$ for a machine operating with a frequency, f.

In the induction motor, E_m is assumed to be approximately equal to the rms terminal voltage, V. Therefore, by substituting equation (4.5) and (4.7) into equation (4.9),

$$\hat{E}_m = V\sqrt{2} = \omega k_w N_t \frac{\hat{B}_o 2rl_z}{p}$$

Hence,

$$V = \frac{4\pi f}{\sqrt{2}} k_w N_t \frac{\hat{B}_o r l_z}{p} \tag{4.10}$$

Equation (4.10) now relates the rms terminal voltage applied to the machine to the peak flux density in the airgap. Therefore, by rearranging, the peak flux density in the airgap of the machine can also be expressed as

$$\hat{B}_o = \frac{V\sqrt{2}p}{4\pi f k_w N_t r l_z} \tag{4.11}$$

This final expression is useful when calculating the amount of rms terminal voltage required to produce a certain value of peak airgap flux density. However, currently the most useful expression will be equation (4.8).

A relationship between the forces acting on the rotor and the airgap flux linkage vectors $\underline{\psi}_o^M$ and $\underline{\psi}_o^N$ can now be derived by employing the relationship between peak airgap flux density, $\hat{\psi}_o$, and the peak airgap field, $\hat{B}_o$ given by (4.8).

4.2.2. Relationship between F_y, F_x and the airgap flux vectors

In the vector control schemes considered in this chapter and throughout this thesis, all the three-phase (a, b, and c) quantities of the motor are transformed into an equivalent two-phase stationary αβ quantity through the rms convention. For example, applying the rms convention on the three phase stator currents implies that the magnitude of the stator current vector $\underline{i}_s$ is equal to the rms phase current i_{ph}, i.e. $|\underline{i}_s| = \sqrt{i_{s\alpha}^2 + i_{s\beta}^2} = i_{ph}$. Therefore, using this convention,

$$\begin{bmatrix} x_\alpha \\ x_\beta \end{bmatrix} = \begin{bmatrix} 1/\sqrt{2} & 0 & 0 \\ 0 & 1/\sqrt{6} & -1/\sqrt{6} \end{bmatrix} \begin{bmatrix} x_a \\ x_b \\ x_c \end{bmatrix} \tag{4.12}$$

where x represents either the stator voltage v_s, stator current i_s or the flux linkages in the motor ψ. These 2-phase αβ quantities are then transformed onto the dq reference frame, rotating at the synchronous speed ω_e, using the following relationship

$$\underline{x}_{dq} = e^{-j\omega_e} \underline{x}_{\alpha\beta} \tag{4.13}$$

Therefore, based on the rms convention, the equivalent dq axis flux linkage components are related to the peak magnitude of the airgap flux vectors $\left|\underline{\psi}_o^M\right|$ and $\left|\underline{\psi}_o^N\right|$ by

$$\frac{\left|\underline{\psi}_o^M\right|}{\sqrt{2}} = \frac{\psi_o^M}{\sqrt{2}} = \sqrt{\psi_{od}^{M\,2} + \psi_{oq}^{M\,2}} \tag{4.14}$$

$$\frac{\left|\underline{\psi}_o^N\right|}{\sqrt{2}} = \frac{\psi_o^N}{\sqrt{2}} = \sqrt{\psi_{od}^{N\,2} + \psi_{oq}^{N\,2}} \tag{4.15}$$

Therefore, from (4.8) and (4.14), the peak field, B_o^M for the main M-pole winding of the bearingless induction motor can be expressed as

$$B_o^M = \frac{\sqrt{2}m\sqrt{\psi_{od}^{M\,2} + \psi_{oq}^{M\,2}}}{2rl_z k_{ws}^M N_{ts}^M} \tag{4.16}$$

where k_{ws}^M and N_{ts}^M are the winding factor and the total number of turns in series per phase of the main stator winding, respectively.

Similarly, for the N-pole levitation winding,

$$B_F^N = \sqrt{B_{Fy}^{N\,2} + B_{Fx}^{N\,2}} = \frac{\sqrt{2}n\sqrt{\psi_{od}^{N\,2} + \psi_{oq}^{N\,2}}}{2rl_z k_{ws}^N N_{ts}^N} \tag{4.17}$$

Therefore, B_{Fy}^N and B_{Fx}^N can be expressed as

$$B_{Fy}^N = B_{od}^N = \frac{\sqrt{2}n\psi_{od}^N}{2rl_z k_{ws}^N N_{ts}^N} \tag{4.18}$$

$$B_{Fx}^N = B_{oq}^N = \frac{\sqrt{2}n\psi_{oq}^N}{2rl_z k_{ws}^N N_{ts}^N} \tag{4.19}$$

Equation (4.1) shows that the y- direction force, F_y is related to the peak airgap fields B_o^M and B_{Fy}^N, whereas equation (4.2) relates the x- direction force, F_x to B_o^M and B_{Fx}^N. Therefore, B_{Fy}^N and B_{Fx}^N will be used to control the amount of force produced in the motor.

Through substitution of (4.18) and (4.19) into (4.1) and (4.2), the x- and y- direction forces acting on the rotor are expressed as

$$\begin{bmatrix} F_y \\ F_x \end{bmatrix} = \frac{\pi B_o^M n}{2\sqrt{2}\mu_o k_{ws}^N N_{ts}^N} \begin{bmatrix} \psi_{od}^N \\ \psi_{oq}^N \end{bmatrix} \tag{4.20}$$

with B_o^M given by (4.16). This equation can now be inverted to determine the value of $\psi_{od}^{N\,*}$ and $\psi_{oq}^{N\,*}$ required to achieve the reference forces F_y^* and F_x^* needed to levitate the rotor:

$$\begin{bmatrix} \psi_{od}^{N\,*} \\ \psi_{oq}^{N\,*} \end{bmatrix} = \frac{2\sqrt{2}\mu_o k_{ws}^N N_{ts}^N}{\pi B_o^M n} \begin{bmatrix} F_y^* \\ F_x^* \end{bmatrix} \tag{4.21}$$

4.3. Vector control schemes for a bearingless cage rotor IM

The vector control schemes considered in this section are designed for a bearingless squirrel cage induction motor in which both the main M-pole rotor current as well as the levitation N-pole rotor current are induced. Three different vector control schemes are proposed for the cage rotor type bearingless IM. The first scheme involves an indirect rotor field orientation (IRFO) in which both M- and N- pole winding quantities are oriented onto the M-pole rotor flux. However, it will be shown in Section 4.3.1 that a force in the x- direction F_x will always be produced, even when unwanted, in the motor since B_{Fx}^N is aligned on ψ_{oq}^N which is non-zero in the rotor flux frame. Therefore, to ensure that F_x is present only when required, both the M- and N- pole winding quantities must be oriented onto the M-pole airgap flux. Hence, an indirect airgap field oriented (IAFO) vector control scheme will also be proposed in Sections 4.3.2. However, there is no extra advantage of having the torque (M-pole winding) control of the rotor to be airgap field oriented. Hence, a mixed field oriented (MFO) scheme, in which the M-pole winding is rotor field oriented whereas the N-pole field is oriented onto the M-pole airgap flux, will also be designed for a cage rotor motor.

4.3.1. Indirect Rotor Field Orientation (IRFO)

Vector control schemes rely on orientation to a vector. In a rotor flux orientation scheme, the d-axis of the reference frame rotating at synchronous speed, ω_e, is aligned with the rotor flux vector. Therefore,

$$\psi_{rq} = 0 \tag{4.22}$$

Hence, equations (A.11) to (A.14) governing the behaviour of an induction motor in the dq rotating frame, as derived in Appendix A, reduce to

$$v_{sd} = R_s i_{sd} + \sigma L_s \frac{d}{dt} i_{sd} - \omega_e \sigma L_s i_{sq} + \frac{L_o}{L_r} \frac{d}{dt} \psi_{rd} \tag{4.23}$$

$$v_{sq} = R_s i_{sq} + \sigma L_s \frac{d}{dt} i_{sq} + \omega_e \sigma L_s i_{sd} + \omega_e \frac{L_o}{L_r} \psi_{rd} \tag{4.24}$$

$$0 = \frac{R_r}{L_r} \psi_{rd} + \frac{d}{dt} \psi_{rd} - \frac{L_o}{L_r} R_r i_{sd} \tag{4.25}$$

$$0 = -\frac{R_r}{L_r} L_o i_{sq} + \omega_{sl} \psi_{rd} \tag{4.26}$$

where

$$\sigma L_s = \frac{L_s L_r - L_o^2}{L_r} \tag{4.27}$$

$$\omega_{sl} = \omega_e - \omega_r \tag{4.28}$$

The rotor flux due to the motoring M-pole winding, ψ_{rd}^M, is controlled by i_{sd}^M, since equation (4.25) rearranges to give

$$\psi_{rd}^M = L_o^M i_{mrd}^M \tag{4.29}$$

where

$$i_{mrd}^M = \frac{1}{s\tau_r^M + 1} i_{sd}^M \tag{4.30}$$

with s representing the derivative operator, $\frac{d}{dt}$, and $\tau_r^M = \frac{L_r^M}{R_r^M}$ is the rotor time constant of the main motoring winding.

The force acting on the rotor is dependent on the peak field on the rotor surface due to the main M-pole motoring winding, B_o^M, which in turn is proportional to $\sqrt{\psi_{od}^{M\,2} + \psi_{oq}^{M\,2}}$ as in equation (4.16). The flux linkages, ψ_{odq}^M can be related to ψ_{rdq}^M through

$$\psi_{od}^M = \frac{L_r^M}{L_o^M} \psi_{rd}^M + (L_r^M - L_o^M) i_{sd}^M \tag{4.31}$$

$$\psi_{oq}^{M} = (L_r^M - L_o^M) i_{sq}^M \tag{4.32}$$

which was derived from the manipulation of the following flux linkage equations

$$\psi_{rdq} = L_r i_{rdq} + L_o i_{sdq} \tag{4.33}$$

$$\psi_{odq} = L_o i_{rdq} + L_o i_{sdq} \tag{4.34}$$

As in a normal vector control scheme, i_{sq}^M controls the main torque produced by the motor. The main flux orientation angle, θ_r^M, measured in electrical radians, is obtained from the integration of the synchronous speed, ω_e, which is the sum of the electrical slip speed of the main rotor flux, ω_{sl}^M, and the electrical rotational speed of the rotor, ω_r^M. Therefore,

$$\theta_r^M = \int (\omega_{sl}^M + \omega_r^M) dt \tag{4.35}$$

with

$$\omega_{sl}^M = \frac{1}{\tau_r^M i_{mrd}^M} i_{sq}^M \tag{4.36}$$

as obtained from (4.26). This gives the standard indirect rotor field orientation (IRFO) scheme.

The main assumption governing the vector control scheme of the bearingless induction motor is that the N-pole levitation winding field rotates at the same electrical synchronous speed, relative to the stator, as the M-pole main field. Hence, the electrical orientation angle of the N-pole field is defined as

$$\theta_r^N = \theta_r^M \tag{4.37}$$

Therefore, in order to implement the vector control scheme for both the M- and N-pole windings which is restrained by (4.37), an expression for the electrical slip speed of the N pole field, ω_{sl}^{N}, is required.

Both the M and N pole fields are rotating at the same electrical angular speed, ω_e, thus the rotor will then rotate at a mechanical speed of

$$\omega_{r\,mech} = \frac{\omega_e - \omega_{sl}^{M}}{m} \tag{4.38}$$

The electrical slip speed between the N pole field and the rotor is then given as

$$\omega_{sl}^{N} = n\left[\frac{\omega_e}{n} - \omega_{r\,mech}\right] \tag{4.39}$$

Hence, by substituting (4.38),

$$\omega_{sl}^{N} = \left(\frac{m-n}{m}\right)\omega_e + \frac{n}{m}\omega_{sl}^{M} \tag{4.40}$$

Similar to the main winding currents, it is assumed that i_{sd}^{N} controls ψ_{rd}^{N} with

$$\psi_{rd}^{N} = L_o^{N} i_{mrd}^{N} \tag{4.41}$$

and

$$i_{mrd}^{N} = \frac{1}{s\tau_r^{N} + 1} i_{sd}^{N} \tag{4.42}$$

where $\tau_r^{N} = \frac{L_r^{N}}{R_r^{N}}$.

It is important to note that the levitation winding N-pole field will sweep past the rotor with a large slip in which slip currents are consequently induced in the rotor. Therefore, due to the rotor field orientation scheme, a component of i_{sq}^{N} must exist, as a direct outcome of equation (4.26). This can be expressed as

$$i_{sq-orient}^{N} = \omega_{sl}^{N} \cdot \tau_{r}^{N} i_{mrd}^{N} \tag{4.43}$$

This component of q-axis current is termed $i_{sq-orient}^{N}$ as it is required to synchronise the orientation of the N-pole field to the M-pole field. In order to introduce a lateral, or x-directional, force an extra i_{sq}^{N} component represented as i_{sq-con}^{N} is required. Therefore,

$$i_{sq}^{N} = i_{sq-orient}^{N} + i_{sq-con}^{N} \tag{4.44}$$

This i_{sq}^{N} will cause an N-pole torque, T^{N}, to be produced which could be fed forward onto the main motoring torque controlled by i_{sq}^{M} where

$$T^{N} = k^{N} i_{sd}^{N} i_{sq}^{N} \tag{4.45}$$

with $k^{N} = 3n\frac{L_{o}^{N^2}}{L_{r}^{N}}$ and the value of $\sqrt{i_{sd}^{N^2} + i_{sq}^{N^2}}$ equals the phase rms magnitude of the N-pole winding stator current.

As derived in Chapter 3, the x- and y- direction forces acting on the rotor are controlled by the peak airgap flux densities, B_{Fy}^{N} and B_{Fx}^{N}, of the N-pole winding respectively. These flux density peaks are related to the airgap flux linkage vector, $\underline{\psi}_{o}^{N}$. Therefore, we can choose:

$$B_{Fy}^{N} \propto \psi_{od}^{N} \tag{4.46}$$

$$B_{Fx}^{N} \propto \psi_{oq}^{N} \tag{4.47}$$

as this will ensure that both flux density peaks B_{o}^{M} and B_{Fy}^{N} occur in the same direction in order for the y- direction force expression previously derived in Chapter 3 to be valid. From (4.37), the N-pole rotor field is also oriented on the d-axis of the rotating reference frame to give

$$\psi_{rq}^{N} = 0 \tag{4.48}$$

This implies that

$$\psi_{oq}^{N} = (L_r^N - L_o^N) i_{sq}^{N} \tag{4.49}$$

which is obtained by rearranging equations (4.33) and (4.34) in terms of the N-pole winding inductances and its dq axis components of rotor flux linkage, airgap flux linkage and stator currents. The consequence of (4.47) and (4.49) is that when i_{sq-con}^{N}, the current responsible for F_x, is zero and only $i_{sq-orient}^{N}$ is present, ψ_{oq}^{N} will also be present. Thus an unwanted F_x will be produced by $i_{sq-orient}^{N}$. Figure 4.2 illustrates the rotor field oriented vector control scheme for the bearingless induction motor with no field weakening.

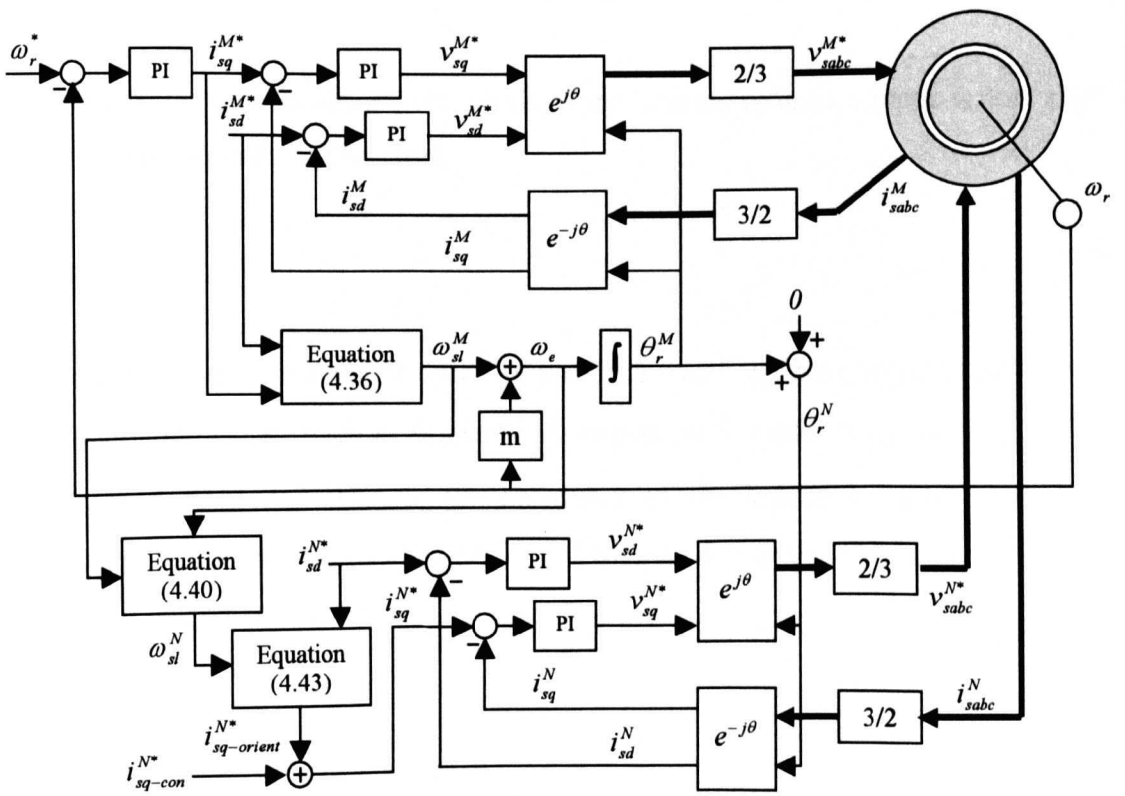

Figure 4.2: Indirect rotor field orientation (IRFO) vector control for a bearingless squirrel cage induction motor.

The N-pole stator winding current references, i_{sd}^{N*} and i_{sq-con}^{N*} will be derived from the feedback control of ψ_{od}^{N} and ψ_{oq}^{N} based on respective reference values obtained using equation (4.21) from given values of F_y^* and F_x^*. Customarily, in a totally bearingless induction motor, F_y^* and F_x^* are obtained from positional feedback of the rotor vertical and horizontal displacements respectively. However, F_y^* and F_x^* could also be given constant values or step references for bearing relief purposes in which conventional bearings are still present at either end of the rotor.

4.3.2. Indirect Airgap Field Orientation (IAFO)

As previously seen, the IRFO vector control scheme designed will always produce a force in the x-direction even when it is not required. This was a direct consequence of a non-zero N-pole airgap flux linkage ψ_{oq}^{N} component. Therefore, an airgap field oriented vector control scheme would be able to overcome this problem.

With this vector control design, the d-axis of the rotating reference frame is now aligned to the airgap flux vector. Therefore,

$$\psi_{oq} = 0 \tag{4.50}$$

Before proceeding, it is thought useful to have the equations governing the behaviour of an induction motor, as given in Appendix A, expressed in terms of i_{sdq} and ψ_{odq}. This is derived in Section A.2. Hence, the behaviour of the induction motor can also be represented by equations (A.20) to (A.23). However, due to the airgap field orientation, these equations reduce to

$$v_{sd} = R_s i_{sd} + \left[\sigma L_s - \frac{L_o}{L_r}(L_r - L_o)\right]\left(\frac{d}{dt} i_{sd} - \omega_e i_{sq}\right) + \frac{d}{dt}\psi_{od} \tag{4.51}$$

$$v_{sq} = R_s i_{sq} + \left[\sigma L_s - \frac{L_o}{L_r}(L_r - L_o)\right]\left(\frac{d}{dt} i_{sq} + \omega_e i_{sd}\right) + \omega_e \psi_{od} \tag{4.52}$$

$$0 = \frac{R_r}{L_o}\psi_{od} + \frac{L_r}{L_o}\frac{d}{dt}\psi_{od} - R_r i_{sd} - (L_r - L_o)\left[\frac{d}{dt}i_{sd} - \omega_{sl} i_{sq}\right] \tag{4.53}$$

$$0 = -R_r i_{sq} - (L_r - L_o)\frac{d}{dt}i_{sq} + \omega_{sl}\left[\frac{L_r}{L_o}\psi_{od} - (L_r - L_o)i_{sd}\right] \tag{4.54}$$

The implementation of the airgap field orientation vector control scheme for a bearingless induction motor is not too different from the rotor field orientation scheme discussed in the previous section.

In the rotor field orientation, ψ_{rd}^M is controlled only by i_{sd}^M. However, with the airgap field orientation, ψ_{od}^M is related to both i_{sd}^M and i_{sq}^M as obtained from (4.53) where

$$\psi_{od}^M = \frac{1}{s\tau_r^M + 1}\left[L_o i_{sd} + \frac{L_o}{L_r}(L_r - L_o)\left(s i_{sd} - \omega_{sl}^M i_{sq}^M\right)\right] \tag{4.55}$$

Since the force acting on the rotor is dependent on ψ_{od}^M, this has to remain constant in order to develop a constant force. However, from (4.55), it is clear that ψ_{od}^M will change with i_{sq}^M for a constant i_{sd}^M. Hence, for this vector control scheme, ψ_{od}^M has to be kept constant through flux linkage control.

The main torque produced by the motor is still controlled by i_{sq}^M. Similarly, the main flux orientation angle, θ_o^M, is again obtained from the integration of the synchronous speed, ω_e, which is the sum of the electrical slip speed of the main airgap flux, ω_{sl}^M, and the electrical rotational speed of the rotor, ω_r^M as in (4.35).

However, since the airgap flux vector is considered and not the rotor flux, the expression for the electrical ω_{sl}^M is now obtained from (4.54) to give

$$\omega_{sl}^{M} = \frac{R_r i_{sq}^{M} + (L_r - L_o)\frac{d}{dt} i_{sq}^{M}}{\left[\frac{L_r}{L_o}\psi_{od} - (L_r - L_o) i_{sd}\right]} \tag{4.56}$$

As with the rotor field orientation, the N-pole levitation winding field rotates at the same synchronous speed as the M-pole main field. Thus, the electrical orientation angle of the N pole field, θ_o^N, is defined to be equal to the M-pole field orientation angle θ_o^M, i.e. $\theta_o^N = \theta_o^M$. Consequently, the expression for the electrical slip speed of the N-pole field, ω_{sl}^N, given by equation (4.40) is still valid.

Despite the airgap field vector orientation scheme, $i_{sq-orient}^N$ must exist in the motor in order to maintain the orientation of the N pole field. Therefore, from equation (4.54) we have:

$$i_{sq-orient}^N = \frac{\omega_{sl}^N \cdot \left[\frac{L_r}{L_o}\psi_{od} - (L_r - L_o) i_{sd}\right]}{R_r + (L_r - L_o)s} \tag{4.57}$$

Even though $i_{sq-orient}^N$ exists, this does not imply the existence of a B_{Fx}^N field in the motor. This is because B_{Fx}^N, and consequently the x- directional force acting on the rotor, is zero since

$$B_{Fy}^N \propto \psi_{od}^N \tag{4.58}$$

$$B_{Fx}^N \propto \psi_{oq}^N \tag{4.59}$$

and

$$\psi_{oq}^N = 0 \tag{4.60}$$

due to the airgap field orientation. Hence, in order to introduce a lateral, or x- directed, force the control field B_{Fx}^{N} has to be applied. This is achieved by creating a ψ_{oq}^{N} component relative to ψ_{od}^{N} orientated by the angle θ_{o}^{N}. The straightforward method of attaining this is through i_{sq-con}^{N}, as was seen in the IRFO scheme.

This airgap field oriented vector control scheme for a bearingless induction motor with no field weakening is represented in Figure 4.3. The values for i_{sd}^{N*} and i_{sq-con}^{N*} are obtained in the same manner as in the IRFO vector scheme described in Section 4.3.1. Comparing Figure 4.2 and Figure 4.3 shows that the difference between the IAFO scheme and the IRFO scheme mainly lies in the expressions for ω_{sl}^{N} and $i_{sq-orient}^{N*}$ together with the addition of a ψ_{od}^{M} control loop required to produce the correct i_{sd}^{M*}. The feedback signal for the ψ_{od}^{M} control loop is obtained using equation (4.55).

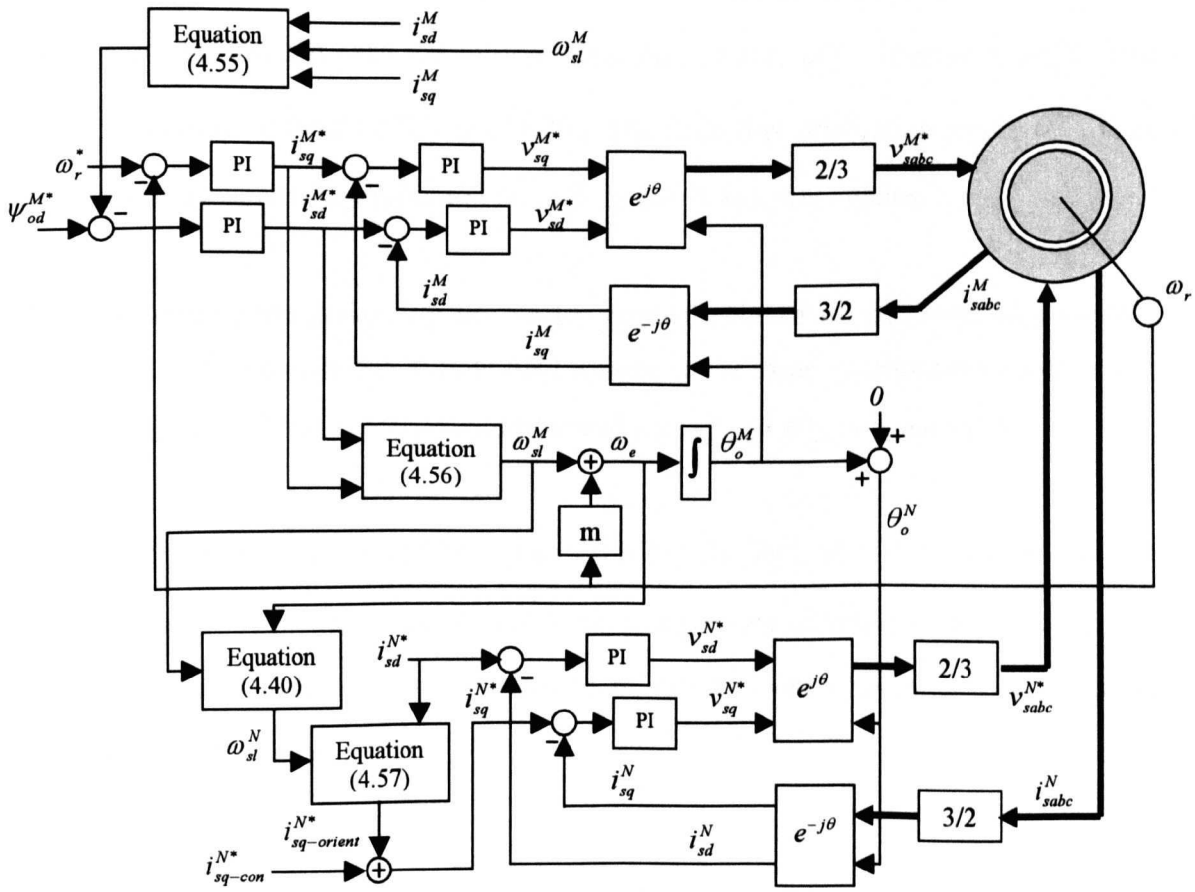

Figure 4.3: Indirect airgap field orientation (IAFO) vector control for a bearingless squirrel cage induction motor.

4.3.3. Mixed Field Orientation (MFO)

When IRFO is used for both the M- and N-pole windings, an x- direction force will always be produced in the bearingless induction motor when $i^N_{sq-orient}$ is non-zero. When an IAFO scheme is used for both windings, the control of the M-pole main winding requires an extra ψ^M_{od} control loop and a more complicated M-pole field slip speed, ω^M_{sl}, equation. However, the unwanted x-direction force seen in the IRFO scheme could be theoretically eliminated. Therefore, it is clear that for the N-pole radial force winding, the d- axis rotating frame has to be oriented on the M-pole airgap field in order to produce the levitation forces acting on the rotor. However, there is no extra advantage on having an airgap field orientation control on the main M-pole winding.

In this section, the M-pole winding d- axis components of voltage, currents and flux linkages are all oriented onto the M-pole rotor flux vector, $\underline{\psi}^M_r$. Therefore, ψ^M_{rq} is zero and ψ^M_{rd} is obtained from (4.29) and (4.30). The main flux orientation angle, θ^M_r, is as given by (4.35) where the expression for ω^M_{sl}, from (4.36), still applies.

The main assumption governing the vector control scheme of the levitated induction motor still holds whereby the N-pole field rotates at the same synchronous speed as the M-pole main field. Thus, the expression derived for ω^N_{sl}, (4.40), is again valid.

However, the electrical orientation angle of the N pole field, θ^N, is no longer equal to θ^M_r. This is due to the fact that all the *d*-axis components of voltage, currents and flux linkages of the N pole winding, now has to be oriented onto the main M-pole airgap field vector, $\underline{\psi}^M_o$. Therefore,

$$\theta^N_o = \theta^M_r + \tan^{-1}\left(\frac{\psi^M_{oq}}{\psi^M_{od}}\right) \tag{4.61}$$

where ψ^M_{od} and ψ^M_{oq} are as given by (4.31) and (4.32).

Equation (4.61) ensures an airgap field orientation for the N-pole winding whereby ψ_{oq}^{N} is now zero. This N-pole field experiences slip and introduces $i_{sq-orient}^{N}$, which must exist in the motor, obtained from equation (4.57) as in the IAFO scheme of section 4.3.2. As explained in the previous section, $i_{sq-orient}^{N}$ does not imply the existence of a B_{Fx}^{N} field in the motor since B_{Fx}^{N} is proportional to ψ_{oq}^{N}. Hence, i_{sq-con}^{N} is again used to introduce a ψ_{oq}^{N} component in order to obtain an x-directional force. This vector control scheme combining an IRFO scheme for the M-pole main field and an IAFO scheme for the N-pole levitation field will be termed mixed field orientation (MFO) and is as shown in Figure 4.4.

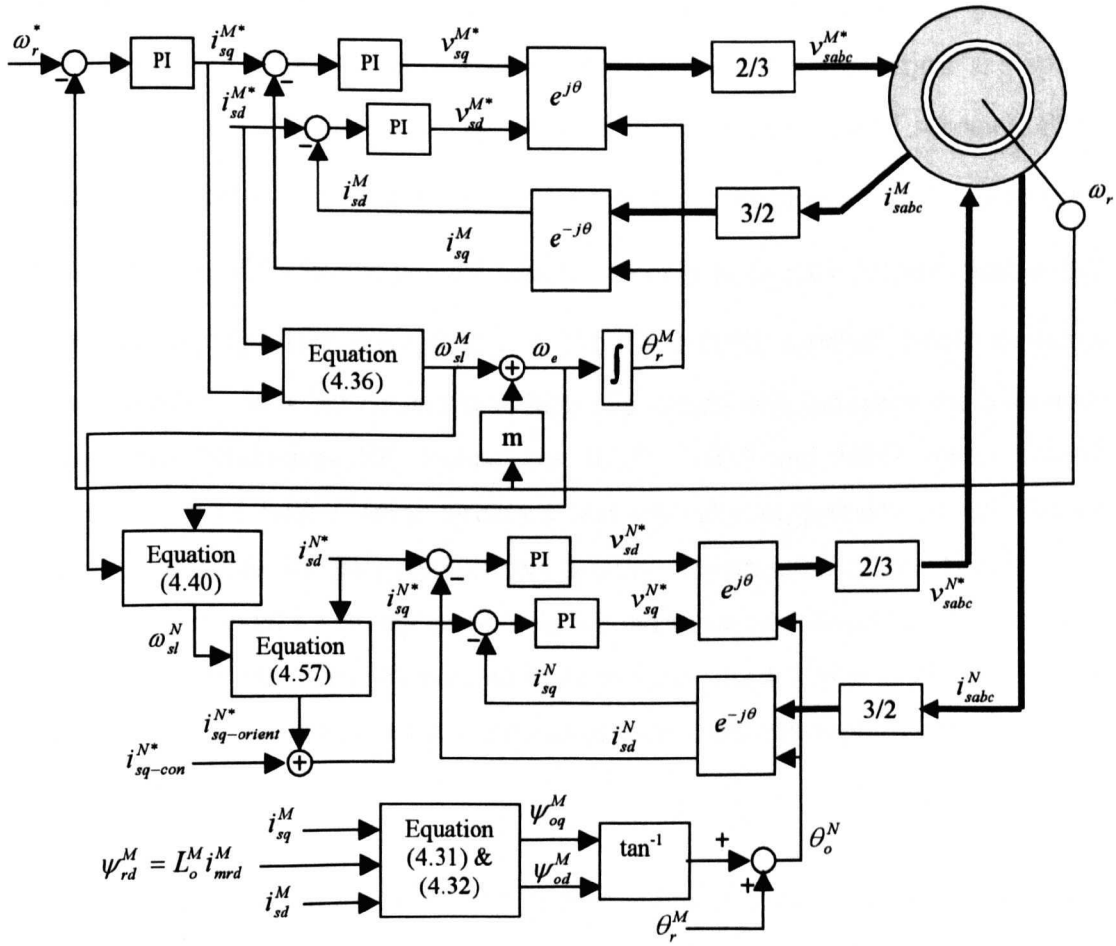

Figure 4.4: Mixed field orientation (MFO) vector control for a bearingless squirrel cage induction motor.

As in the two other vector control schemes, the N-pole stator winding current references, i_{sd}^{N*} and i_{sq-con}^{N*} are to be derived from the feedback control of ψ_{od}^{N} and ψ_{oq}^{N}

based on their respective reference values obtained from F_y^* and F_x^* using equation (4.21). Furthermore, in a totally bearingless induction motor, F_y^* and F_x^* is then obtained from positional feedback of the rotor's vertical and horizontal displacements respectively.

4.4. Vector control implementations for a bearingless IM without N- pole secondary circuit

In section 4.3, three different vector control schemes were introduced for a bearingless squirrel cage induction motor. In the cage rotor motor, both M- and N-pole rotor currents are induced in the rotor. Therefore, expressions for the electrical slip speed, ω_{sl}^N and $i_{sq-orient}^N$ of the N-pole winding are vital in the vector control schemes. From equations (4.43) and (4.57), a large $i_{sq-orient}^N$ current will be present in the cage rotor motor, irrespective of its vector control scheme, since it is directly proportional to ω_{sl}^N which can be very high (for example ω_{sl}^N = 25Hz in a 50Hz supplied 2-pole levitation winding). Therefore, it is anticipated that high slip effects will influence the behaviour of a cage rotor bearingless IM. Hence, the IRFO, IAFO and MFO vector control schemes for a motor with a rotor structure that provides suppression of any N-pole induced rotor currents are proposed in this section. Suppression of the N-pole rotor currents can be achieved by having an M-pole wound rotor or a custom-built cage rotor structure which will only allow M-pole currents to be induced. Chiba *et al.* (1996) have previously proposed several cage rotor structures which provide suppression of induced N-pole rotor currents.

If the bearingless induction motor has no N-pole induced rotor currents, or no N-pole secondary circuit, the vector control scheme would be less complicated. The main point to stress is that without the N-pole secondary circuit, only the vector control scheme involving the levitation winding will change. The vector control for the main M-pole winding established previously would remain the same. Secondly, the changes associated with the absence of the N-pole secondary circuit applies to both the rotor and airgap field vector control schemes.

The key assumption governing the vector control scheme of the levitated induction motor still holds whereby the N-pole field rotates at the same synchronous speed as the M-pole main field. Furthermore, the electrical orientation angle of the N-pole field θ^N is still defined to be equal to θ_r^M or θ_o^M depending on whether the motor is rotor field or airgap field orientated respectively. However, for the mixed field orientation scheme, θ^N is given by (4.61).

In the new vector control scheme, without the N-pole secondary circuit present, i_{rdq}^N and ψ_{rdq}^N no longer exist. Therefore, the rotor equations associated with the N-pole winding no longer exist and ω_{sl}^N has no meaning. Previously, in all the cage rotor vector control schemes, i_{sq}^N consisted of two components, $i_{sq-orient}^N$ and i_{sq-con}^N, as given by (4.44). The first component, $i_{sq-orient}^N$, arose from the slip experienced by the N-pole field whereas the second component, i_{sq-con}^N, was responsible for producing a lateral force in the motor. Nevertheless, in the subsequent vector control schemes, $i_{sq-orient}^N$ does not exist since ω_{sl}^N is no longer applicable. Therefore, only i_{sq-con}^N is left. Henceforth, in the vector control schemes to be considered, the current responsible for producing a lateral force in the motor will no longer be termed i_{sq-con}^N but will just be represented by i_{sq}^N.

Furthermore since,

$$\psi_{odq}^N = L_o^N i_{sdq}^N \tag{4.62}$$

a direct relationship is obtained between the forces acting on the rotor and the N-pole stator winding currents i_{sd}^N and i_{sq}^N. Through substitution of equation (4.62) into equation (4.20):

$$\begin{bmatrix} F_y \\ F_x \end{bmatrix} = \frac{\pi B_o^M n L_o^N}{2\sqrt{2}\mu_o k_{ws}^N N_{ts}^N} \begin{bmatrix} i_{sd}^N \\ i_{sq}^N \end{bmatrix} \tag{4.63}$$

Therefore, the N-pole stator winding current references i_{sd}^{N*} and i_{sq}^{N*} can now be directly related to F_y^* and F_x^* by inverting equation (4.63) to give

$$\begin{bmatrix} i_{sd}^{N*} \\ i_{sq}^{N*} \end{bmatrix} = \frac{2\sqrt{2}\mu_o k_w^N N_t^N}{\pi B_o^M n L_o^N} \begin{bmatrix} F_y^* \\ F_x^* \end{bmatrix} \tag{4.64}$$

As before, F_y^* and F_x^* can be obtained from positional feedback of the rotor vertical and horizontal displacements respectively, or from step references depending on whether the motor is totally bearingless or the forces are created for bearing relief purposes.

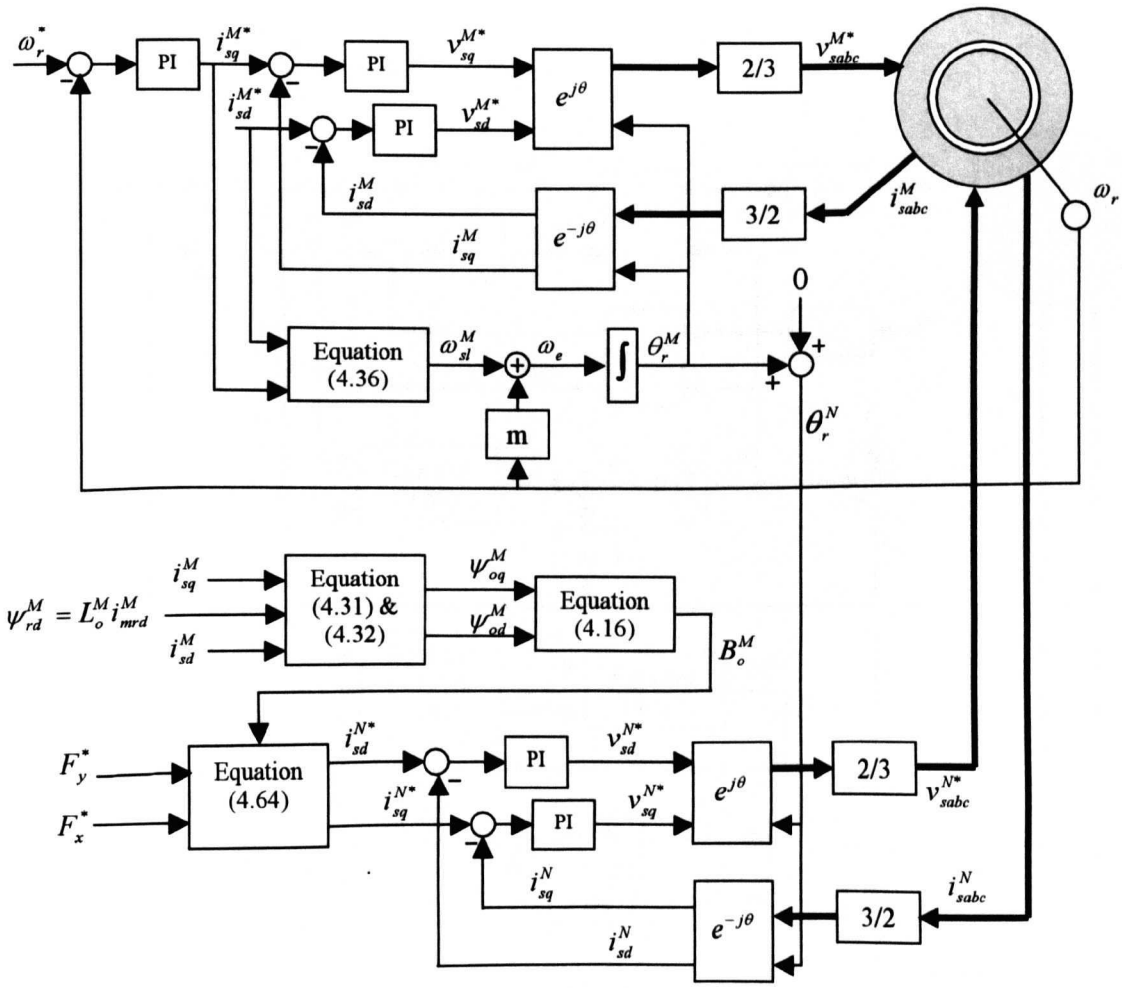

Figure 4.5: IRFO vector control for a bearingless induction motor without an N-pole secondary circuit.

An indirect rotor field oriented vector control scheme for the bearingless induction motor without an N-pole secondary circuit is shown in Figure 4.5. In the caged rotor scheme, an unwanted F_x was anticipated to be produced by $i^N_{sq-orient}$. However, this will not become a problem in the IRFO scheme of Figure 4.5, since $i^N_{sq-orient}$ is no longer relevant.

If equation (4.56) is used, instead of equation (4.36), to calculate ω^M_{sl} the bearingless induction motor would instead be airgap field oriented. However, as mentioned in Section 4.3.2, an additional ψ^M_{od} control loop, with a feedback signal obtained using equation (4.55), is required to produce i^{M*}_{sd}. Figure 4.6 illustrates the new indirect airgap field oriented vector control scheme for the bearingless induction motor.

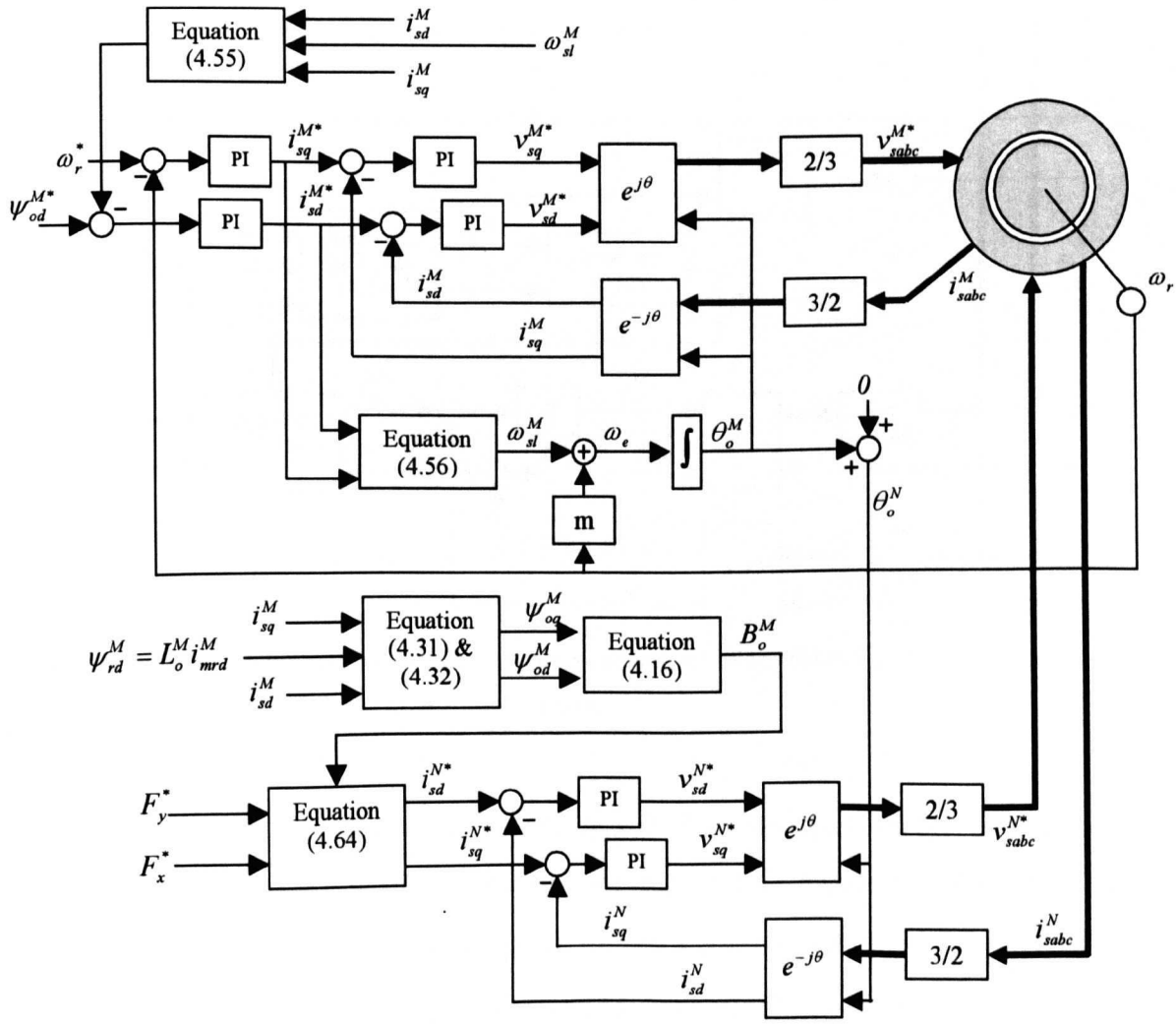

Figure 4.6: IAFO vector control for a bearingless induction motor without an N-pole secondary circuit.

The mixed field orientation vector control scheme consists of an indirect rotor field orientation vector control for the M-pole winding and an airgap field oriented control scheme for the N-pole winding. This mixed field oriented vector control scheme for the bearingless induction motor without an N-pole secondary circuit is shown in Figure 4.7.

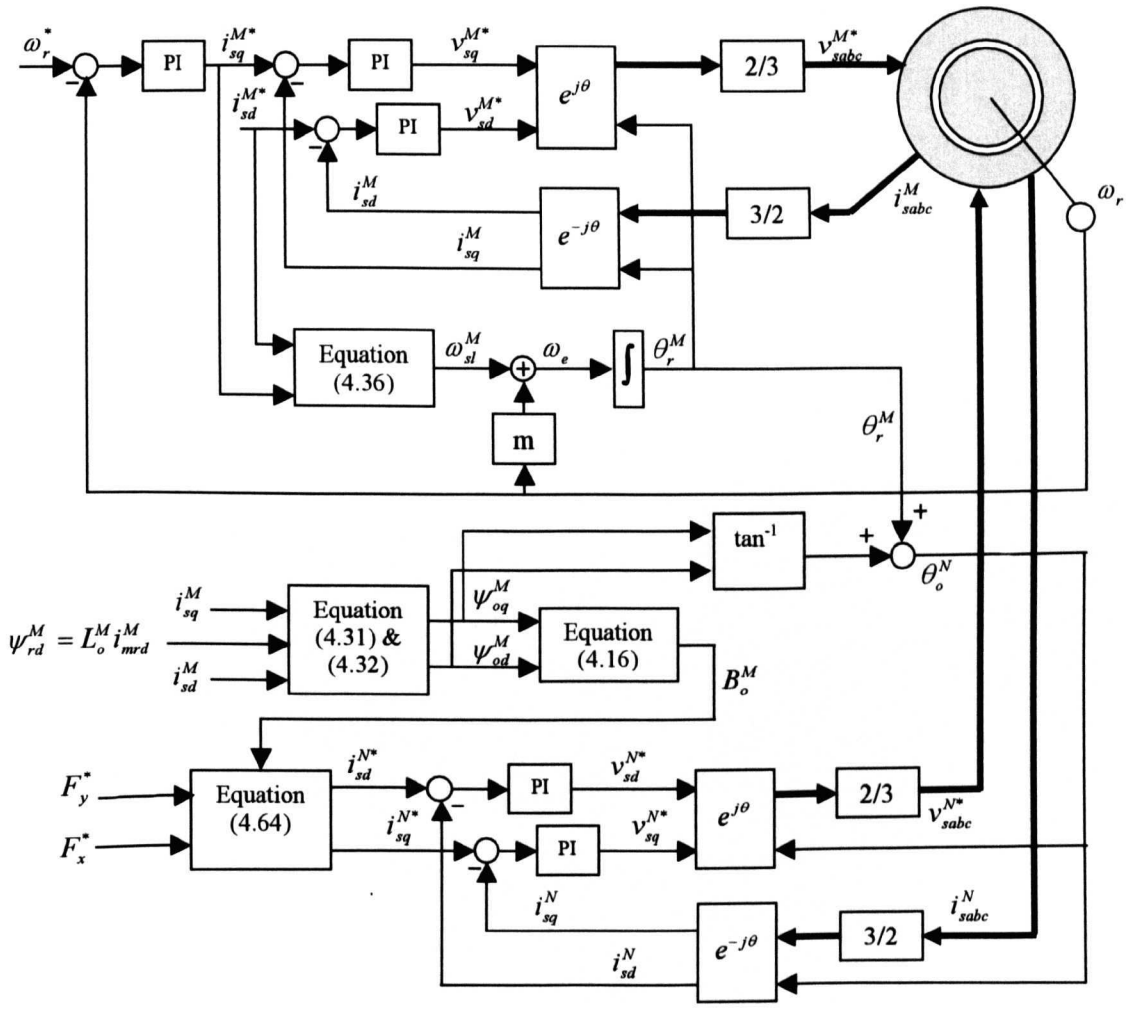

Figure 4.7: MFO vector control for a bearingless induction motor without an N-pole secondary circuit.

In the cage rotor bearingless motor, the mixed field oriented vector control was preferred because it gave a simpler control for the M-pole winding compared to the IAFO scheme and it was also able to ensure no extra contribution to F_x is produced by the existence of $i^N_{sq-orient}$ as was seen in the IRFO scheme. However, for the bearingless induction motor without an N-pole secondary circuit, there seem to be no great

advantage towards the performance of the mixed field orientation vector control scheme when compared with the equivalent indirect rotor field orientation scheme.

The vector control schemes for the bearingless induction motor, with squirrel cage rotor or a rotor without an N-pole rotor circuit, introduced in this chapter will be simulated using MATLAB Simulink in the following chapter.

Chapter 5

Simulation of vector control methods for generating levitation and lateral forces

5.1. Introduction

Chapter 4 proposes vector control schemes for bearingless induction motors with two different rotor structures; one having a cage rotor while the other rotor suppresses any N-pole induced rotor currents. The latter type of rotor can be achieved using a wound rotor having the same pole number as the main M-pole winding, since it does not allow any N-pole currents to flow, resulting in a bearingless motor with no N-pole rotor circuit. In this thesis, the motoring field of the two bearingless motors investigated is provided by a 4-pole cage and a 4-pole wound rotor induction motor. The levitation field of the motor is provided by an additional 2-pole winding added to the stator of each of the 4-pole motors. Both the 4+2 pole cage and wound rotor bearingless IM together with their respective vector control schemes proposed in Chapter 4 will be computationally simulated in this chapter using MATLAB Simulink.

Before presenting the simulation results of the vector controlled bearingless induction motors, the equivalent circuit parameters of the 4-pole (M = 4) cage and wound rotor induction motors are evaluated in Section 5.2. Then, the 2-pole (N = 2) levitation winding is designed and its equivalent circuit parameters calculated. In order to implement the vector control schemes proposed in Chapter 4, the current, speed and flux control compensators for both the 4 and 2-pole windings will also be designed. Finally, with the designed levitation winding and compensators, all the vector control schemes proposed in Chapter 4 will be simulated for both rotor structures.

5.2. Derivation of the 4-pole machine parameters

In this section the equivalent circuit parameters of the 4-pole cage rotor and wound rotor motors chosen to provide the motoring capabilities of the bearingless induction motors studied in this thesis are evaluated.

5.2.1. Squirrel cage induction motor

The cage induction motor is based on a Brook Crompton, 4-pole, Δ- connected three-phase induction motor having a 48/40 slot combination and the following data:

Rated power	15kW
Rated frequency	50Hz
Rated line voltage (rms)	415V
Rated line current (rms)	27.08A
Rated speed	1450
Rated torque, T_{rated}	99.5Nm
Rotor moment of inertia, J	0.071kgm^2
Total number of turns per phase, N_{ts}^M	176
Winding factor, k_{ws}^M	0.958

Table 5.1: Machine parameters of the 4-pole Brook Crompton induction motor.

The drawings of the stator and rotor laminations of the motor were utilised to create the reluctance mesh employed to model the motor as presented in Section 2.2. The values of the stator phase resistance R_s of 1.04Ω and the referred rotor resistance R_r' of 0.76Ω were obtained from the data sheet provided by Brook Crompton for the motor. The equivalent circuit inductances of this motor were evaluated by performing no load and locked rotor tests (Alger, 1995) using direct on-line (DOL) start simulations with the DCM software. The resistance and derived parameters of the cage motor is summarised in Table 5.2 assuming equal split in leakage inductance between the stator and rotor.

R_s^M	1.04Ω (from data sheet)
$R_r^{M'}$	0.76Ω (from data sheet)
L_s^M	267.75mH
L_r^M	267.75mH
L_o^M	264.20mH

Table 5.2: Equivalent circuit parameters of the squirrel cage induction motor.

A DOL start DCM simulation for this induction motor was then compared to a DOL start simulation performed in Simulink based on the parameters of Table 5.2. In both simulations, load torque equal to T_{rated} (see Table 5.1) is applied to the motor at 1s. The comparison between the two simulation results is presented in Figure 5.1. It was found that during transient conditions there is a slight difference between the two simulations as observed in the torque variation shown in Figure 5.1(b). This is due to the fact that the Simulink model is unable to show slotting effects in the machine since it relies on a lumped parameter circuit to model the cage induction motor. The DCM simulation, however, is able to show these slotting effects during transient conditions and can be considered to produce a more reliable result. Once the motor reached steady state, the results between the DCM and Simulink simulations were found to be consistent with each other even under full load.

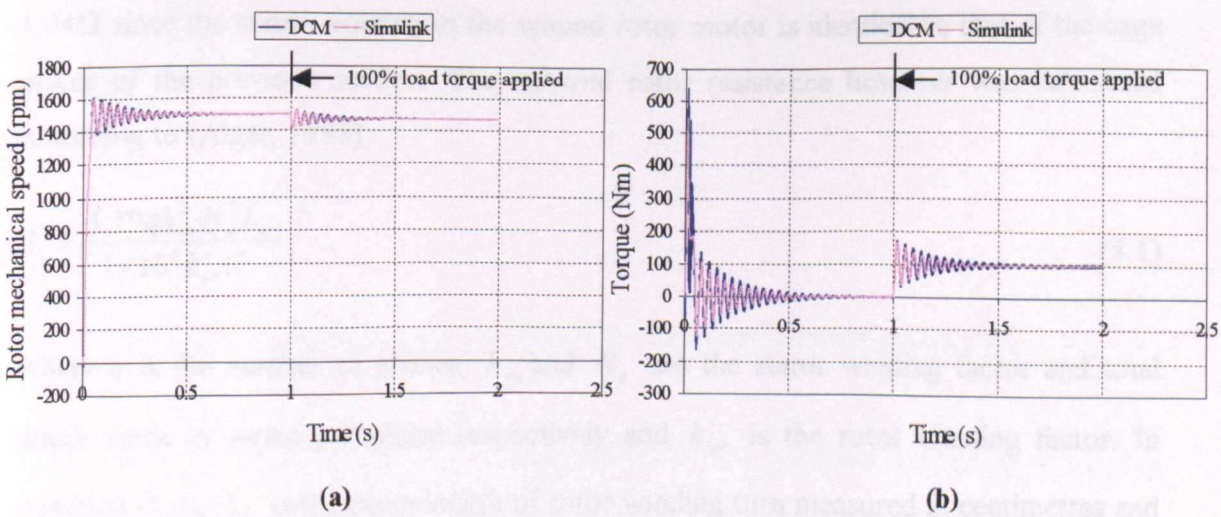

(a) (b)

Figure 5.1: Comparison of DCM and Simulink simulations for a DOL start of cage IM under load:

(a) speed

(b) torque (DCM results exhibit high frequency slotting effects during transient)

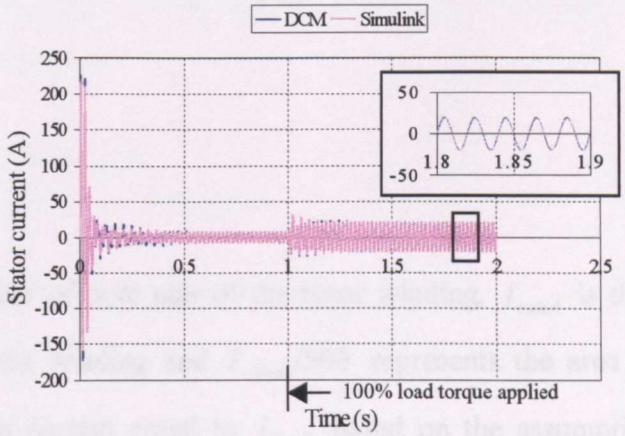

(c)

Figure 5.1: Comparison of DCM and Simulink simulation for a DOL start cage IM under load:
(c) stator phase current

5.2.2. Wound rotor induction motor

The wound rotor induction motor considered for the bearingless motor is also based on the same Brook Crompton, 4-pole induction motor introduced in the previous section. However, instead of having shorted aluminium bars, the rotor slots are filled with a short-circuited 4-pole three-phase winding. In order to be able to accommodate the winding, the number of rotor slots was reduced from 40 to 36 with the rotor tooth widths and slot openings reduced proportionally. The total number of series rotor turns per phase was chosen to be 180. The stator phase resistance value was maintained at 1.04Ω since the stator winding in the wound rotor motor is identical to that of the cage motor of the previous section. The referred rotor resistance however was calculated according to (Alger, 1995):

$$R_r' = \frac{4.19 q k_{ws}^2 N_s^2 L_{tr}}{1\times 10^6 k_{wr}^2 C_r} \tag{5.1}$$

where q is the number of phases, k_{ws} and N_s are the stator winding factor and total stator turns in series per phase respectively and k_{wr} is the rotor winding factor. In equation (5.1), L_{tr} is the mean length of rotor winding turn measured in centimetres and C_r is the total cross section of copper of all phases in the rotor slots stated in square centimetres. The equations used to calculate L_{tr} and C_r are:

$$L_{tr} = 2l_z + \frac{\pi}{p}r \tag{5.2}$$

$$C_r = \left(\frac{I_{rated}}{500}\right)2N_r \tag{5.3}$$

where p is the number of pole pair of the rotor winding, I_{rated} is the peak rated phase current flowing in the winding and $I_{rated}/500$ represents the area occupied by a coil carrying a maximum current equal to I_{rated} based on the assumption that the current density in the induction motor is taken as 5A/mm^2. With $p = 2$, I_{rated} equal to the stator winding rated current and $N_r = 180$, the values of L_{tr} and C_r for the 4-pole rotor winding can be calculated from equations (5.2) and (5.3). Therefore, given $k_{ws}^M = 0.958$ and $N_{ts}^M = 176$ (from Table 5.1), $k_{wr}^M = 0.96$, and the calculated values of L_{tr} and C_r, equation (5.1) computes to give $R_r^{M'} = 0.99\Omega$.

As for the cage motor, the remaining equivalent circuit parameters for the wound rotor motor were evaluated by performing no load and locked rotor tests with direct on-line (DOL) start simulations using the DCM program, assuming equal split in leakage inductance between the stator and rotor. The results are:

R_s^M	1.04Ω
$R_r^{M'}$	0.99Ω
L_s^M	269.73mH
L_r^M	269.73mH
L_o^M	265.36mH

Table 5.3: Equivalent circuit parameters of the wound rotor induction motor.

The DCM simulation of the wound rotor motor, having full load applied after 1s, was compared with the results from Simulink under the same load conditions with the Simulink motor modelled by the parameters of Table 5.3. As in the cage motor, the results shown in Figure 5.2 show dissimilarity between the two results during transient

conditions mostly due to the slotting effects modelled by the DCM software but are not present in the Simulink model.

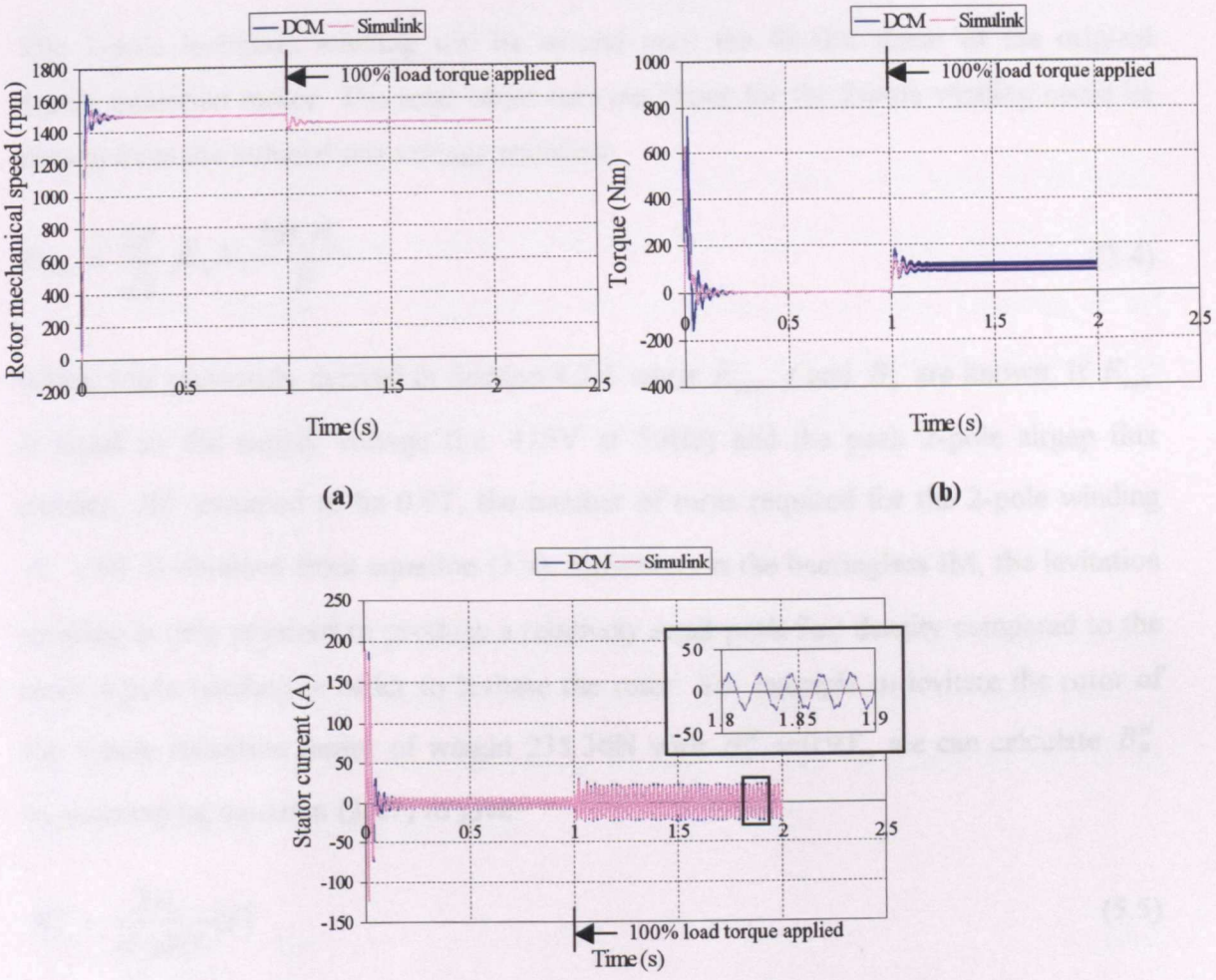

Figure 5.2: Comparison of DCM and Simulink simulations for a DOL start of wound rotor IM under load:

(a) speed

(b) torque (DCM results exhibit high frequency slotting effects during transient)

(c) stator phase current

5.3. Design and parameter derivation of the levitation winding

The constant forces required to levitate the rotor of a bearingless induction motor is a result of interaction between the main M-pole winding and a second N-pole winding where $M - N = \pm 2$. Therefore, the two 4-pole motors introduced in Section 5.2 are

supplemented with a 2-pole second winding wound on the stator. A 6-pole levitation winding is also possible. This will be discussed in Chapter 7.

The 2-pole levitation winding will be wound onto the 48-slot stator of the original 4-pole induction motor. The total series turn per phase for the 2-pole winding could be chosen from the induced rms voltage equation:

$$E_{rms} = \frac{2\pi}{\sqrt{2}} f k_w N_t \frac{2B_o r l_z}{P} \tag{5.4}$$

which was previously derived in Section 4.2.1 when E_{rms}, f and B_o are known. If E_{rms} is equal to the supply voltage (i.e. 415V at 50Hz) and the peak 2-pole airgap flux density, B_F^N assumed to be 0.9T, the number of turns required for the 2-pole winding $N_t = 90$ is obtained from equation (5.4). However, in the bearingless IM, the levitation winding is only required to produce a relatively small peak flux density compared to the main 4-pole winding in order to levitate the rotor. For example to levitate the rotor of the 4-pole induction motor of weight 235.36N with $B_o^M = 0.9\text{T}$, we can calculate B_F^N by rearranging equation (3.27) to give:

$$B_F^N = \frac{2\mu_0}{r l_z \pi B_o^M} |F| \tag{5.5}$$

Using this equation and $|F| = 235.36\text{N}$, B_F^N computes to give 17.4mT. This means that the required 2-pole levitation winding supply voltage is much less than 415V and the selection of the total series turn per phase for the 2-pole winding N_t is rather arbitrary. Hence, the total series turn per phase was chosen to be 48 instead of 90. The value 48 was chosen to reduce the space occupied by the levitation winding in the stator slots but this choice is by no means optimised in terms of space utilisation.

The stator phase resistance, R_s of the 2-pole winding was calculated using

$$R_s = \frac{4.19 q N_s^2 L_{ts}}{1\times10^6 C_s} \tag{5.6}$$

obtained from Alger (1995) where q is the number of phases and $N_s = 48$ is the 2-pole stator winding turns in series per phase. In equation (5.6), L_{ts} and C_s are the stator winding equivalence of L_{tr} and C_r given by equations (5.2) and (5.3). Hence, R_s of the 2-pole winding was found to be 0.83Ω.

Two motors are considered in this thesis and in both motors the stator is identical. Therefore, R_s of the 2-pole winding calculated above applies to both motors. The 2-pole levitation winding rotor resistance, on the other hand, would vary depending on the rotor structure of the motor. In the cage IM, 2-pole currents will be induced. The referred rotor resistance for a cage rotor is given by (Alger, 1995)

$$R_r^{'} = \frac{4.19qk_{ws}^2 N_s^2}{1\times 10^6} \times a \tag{5.7}$$

where a is a constant dependant on the dimensions of the cage rotor. However, because the cage rotor supports equivalent 4-pole and the 2-pole three-phase windings ($q = 3$), the referred rotor resistance of the 2-pole winding $R_r^{N'}$ can be related to that of the 4-pole $R_r^{M'}$ by the following equation:

$$R_r^{N'} = \frac{k_{ws}^{N\,2} N_{ts}^{N\,2}}{k_{ws}^{M\,2} N_{ts}^{M\,2}} \times R_r^{M'} \tag{5.8}$$

With $k_{ws}^N = 0.956$, $N_{ts}^N = 48$ turns per phase and k_{ws}^M, N_{ts}^M and $R_r^{M'}$ obtained from Tables 5.1 and 5.2 respectively, $R_r^{N'}$ calculates to 0.057Ω. The remaining parameters of the 2 pole winding equivalent circuit for the squirrel cage motor was then obtained from simulating no load and locked rotor conditions using the DCM program with the 4-pole currents removed. The equivalent circuit parameter values for the 2-pole levitation winding of the cage rotor bearingless motor are as shown in Table 5.4(b).

On the other hand, the 2-pole levitation winding of the wound rotor type bearingless motor will not have any rotor circuit since the rotor is wound with a 4-pole winding. Therefore, in the wound rotor motor, the referred rotor resistance $R_r^{N'}$ and rotor inductance L_r^N of the 2-pole stator winding do not exist. The stator inductance L_s^N can

be derived from the no load test. Due to the fact that the 2-pole winding is to be wound onto the same stator as the 4-pole wound rotor motor of Section 5.2.2, the no load DCM simulation was performed with a 4-pole wound rotor in place to emulate the bearingless induction motor to be designed without the 4-pole stator winding present. However, in order to obtain the magnetizing inductance L_o^N of the 2-pole winding, the value of the stator leakage inductance l_s^N is required. This is obtained by performing a locked rotor test of the 2-pole stator winding motor having a 2-pole wound rotor. The parameters of the 2-pole winding in the wound rotor induction motor is summarised in Table 5.4.

Total stator series turn per phase, N_{ts}^N	48
Stator winding factor, k_{ws}^N	0.956

(a)

	Squirrel cage motor	Wound rotor motor
R_s^N	0.83Ω	0.83Ω
$R_r^{N'}$	0.057Ω	-
L_s^N	58.30mH	58.76mH
L_r^N	58.30mH	-
L_o^N	58.12mH	58.57mH

(b)

Table 5.4: Parameters of the 2-pole levitation winding.

5.4. Vector control simulations for sustained levitation of induction motors

As mentioned at the start of this chapter, the vertical and lateral force control of two vector controlled bearingless induction motors having different rotor structures will be simulated using MATLAB Simulink. The first type has a squirrel cage rotor and a stator having both a main 4-pole winding and a 2-pole levitation winding with respective equivalent circuit parameters given in Tables 5.2 and 5.4. The second motor type contains a 4-pole wound rotor with an identical stator to that of the first type. The

equivalent circuit parameters for this motor are as given in Tables 5.3 and 5.4. The current, speed and flux controllers of the proposed vector control schemes of Chapter 4 are designed from the equivalent circuit parameters presented in the previous two sections.

5.4.1. Compensator design for the 4-pole and 2-pole windings

5.4.1.1. Current control loops

In all the vector control schemes, two inner fast current control loops are required for each stator winding of the bearingless induction motor, one for each d- and q- axis current of the main and levitation winding. Due to symmetry, the current controls of the d- and q- axis currents of each stator winding are controlled by an identical PI controller.

For the main 4-pole winding, the transfer function between $\underline{i}_{sdq}^{M}$ and $\underline{v}_{sdq}^{M}$ required for the control design is derived from equations (5.9) and (5.10) which govern the behaviour of the induction motor in the dq rotating frame with the coupling terms introduced after the control.

$$v_{sd} = R_s i_{sd} + \sigma L_s \frac{d}{dt} i_{sd} - \omega_e \sigma L_s i_{sq} + \frac{L_o}{L_r} \frac{d}{dt} \psi_{rd} \tag{5.9}$$

$$v_{sq} = R_s i_{sq} + \sigma L_s \frac{d}{dt} i_{sq} + \omega_e \sigma L_s i_{sd} + \omega_e \frac{L_o}{L_r} \psi_{rd} \tag{5.10}$$

Thus, the 4-pole current control plant transfer function is given by

$$\frac{\underline{i}_{sdq}^{M}(s)}{\underline{v}_{sdq}^{M}(s)} = \frac{1/R_s^M}{s\tau_s^M + 1} \tag{5.11}$$

where $\tau_s^M = \sigma^M L_s^M / R_s^M$. The values of R_s^M and τ_s^M are obtained from either Table 5.2, for the cage rotor motor, or Table 5.3, for the wound rotor motor.

From equation (5.11), the controller was designed in the continuous s-plane, by way of root locus, with the objective of obtaining a high bandwidth while maintaining the damping factor ς at a value of approximately 0.8. The parameters of the designed PI current controller, with a transfer function given by

$$G_c = \frac{k_i^M \left(s + a_i^M\right)}{s} \tag{5.12}$$

for both the squirrel cage and wound rotor 4 pole induction motor is as shown in Table 5.5.

	Squirrel cage IM	Wound rotor IM
Proportional gain, k_i^M	27.39	33.85
Controller zero, a_i^M	1630.67	1619.24

Table 5.5: PI current controller parameters designed for the 4-pole winding current control of the bearingless induction motor.

This design gives a nominal closed loop bandwidth of 400Hz.

A PI controller is designed for the current loops of the 2-pole levitation winding. As the 2-pole winding also induces rotor currents in the cage rotor, the transfer function between $\underline{i}_{sdq}^N$ and $\underline{v}_{sdq}^N$ can also be obtained from equations (5.9) and (5.10) with the introduction of the corresponding coupling terms. Hence, from the parameters in Table 5.4 for the squirrel cage motor, the 2-pole current control plant transfer function is given by

$$\frac{\underline{i}_{sdq}^N(s)}{\underline{v}_{sdq}^N(s)} = \frac{1.204}{0.435 \cdot 10^{-3} s + 1} \tag{5.13}$$

Employing similar methods as that used for the 4-pole current controller design, the transfer function of the PI controller for the 2-pole winding currents is given in Table 5.6 and yields a nominal closed loop bandwidth of 400Hz with a damping ratio ς of approximately 0.8.

For the wound rotor bearingless induction motor, the transfer function between $\underline{i}_{sdq}^{N}$ and $\underline{v}_{sdq}^{N}$ in the current loop of the 2-pole winding is derived from equations (5.14) and (5.15)

$$v_{sd} = R_s i_{sd} + L_s \frac{d}{dt} i_{sd} - \omega_e L_s i_{sq} \tag{5.14}$$

$$v_{sq} = R_s i_{sq} + L_s \frac{d}{dt} i_{sq} + \omega_e L_s i_{sd} \tag{5.15}$$

since the rotor is wound with a 4-pole winding which prohibits any 2-pole induced rotor currents. Hence, from the parameters in Table 5.4, the 2-pole current control plant transfer function is

$$\frac{\underline{i}_{sdq}^{N}(s)}{\underline{v}_{sdq}^{N}(s)} = \frac{1}{58.757 \cdot 10^{-3} s + 0.8304} \tag{5.16}$$

The PI controller is designed to achieve a nominal closed loop bandwidth of 100Hz at $\varsigma = 0.8$ and is given in Table 5.6. The bandwidth of 100Hz was chosen instead of 400Hz (i.e. similar to that of the squirrel cage type motor) because when the controller with the 400Hz bandwidth was used in the vector control scheme, the results obtained in the DCM simulations produced higher noise effects compared to the 100Hz bandwidth controller. The current controller parameters designed for the 2-pole winding current control loop is summarised in Table 5.6.

	Squirrel cage IM	Wound rotor IM
Proportional gain, k_i^N	0.63	58.24
Controller zero, a_i^N	3616.43	398.29

Table 5.6: PI current controller parameters for the 2-pole winding current control of the bearingless induction motor.

5.4.1.2. Speed control loop

The q- axis stator current demand of the main 4-pole winding i_{sq}^{M*} is responsible for controlling the main torque produced in the motor. Hence, as in normal vector control

schemes, i_{sq}^{M*} is derived from the speed loop. This loop is closed by a PI controller in order to obtain zero steady state error. In addition, the PI controller is designed to have a limited output and an anti-windup mechanism due to the large mechanical time constant and the limit imposed on the magnitude of the stator currents in practical situations. The high bandwidths of the current control loops enables its closed loop dynamics to be neglected. Thus, the plant dynamics for the speed loop is dominated by the mechanical dynamics of the motor. Therefore, the mechanical transfer function is given by

$$G_p(s) = \frac{k_t}{Js + B} \tag{5.17}$$

with J being inertia of the rotor, B representing the mechanical friction and k_t the torque constant calculated using

$$k_t = 3m\frac{L_o^{M\,2}}{L_r^M} \tag{5.18}$$

In both the cage and wound rotor IM, L_o^M and L_r^M (given by Table 5.2 or 5.3) are almost identical. Therefore, the value of k_t for the both motor types was calculated to be 1.6. Hence, the plant for the speed loop is given by

$$G_p(s) = \frac{1.6}{0.0713s} \tag{5.19}$$

when the mechanical friction, B, is neglected. A PI controller is designed to obtain a closed loop bandwidth of 5Hz at a damping factor of 0.8 to yield an s-plane controller of

$$G_c(s) = \frac{0.61(s + 19.63)}{s} \tag{5.20}$$

5.4.1.3. Flux linkage control loops

As stated in Section 4.3.2 of Chapter 4, the airgap field oriented vector control scheme proposed for the two bearingless IM types require a flux linkage control in order that

i_{sd}^{M*} maintains a constant ψ_{od}^{M}. This is because the force acting on the rotor is dependent on ψ_{od}^{M}, thus it has to remain constant in order to produce a constant force. This airgap flux linkage control loop contains the dynamics of the current control loop and another given by the transfer function between i_{sd}^{M} and ψ_{od}^{M} in the feedback path, which is

$$\frac{\psi_{od}^{M}(s)}{i_{sd}^{M}(s)} = \frac{L_o^M}{s\tau_r^M + 1} \tag{5.21}$$

where $\tau_r^M = L_r^M / R_r^M$. Due to the high bandwidth of the inner current control loop, the plant dynamics for the flux linkage loop is dominated by equation (5.21). A PI controller is designed for the ψ_{od}^{M} control loop for both motor types to achieve a nominal closed loop bandwidth of 9Hz. The parameters of the designed PI controller are as shown in Table 5.7.

	Squirrel cage IM	Wound rotor IM
Proportional gain, k_i^N	116.55	88.77
Controller zero, a_i^N	36.49	36.84

Table 5.7: PI current controller parameters for the ψ_{od}^{M} control of the bearingless induction motor.

Flux linkage control is also required in order to produce $\underline{i}_{sdq}^{N*}$ of the 2-pole winding which will in turn produce the appropriate $\underline{\psi}_{odq}^{N}$ values and achieve the correct levitation forces. This control is only necessary in the cage type bearingless motor because there is no direct relationship between F_{xy}^{*} and $\underline{i}_{sdq}^{N*}$ as found in the wound rotor type. Similar to the flux linkage control loop of the main 4-pole winding, the plant dynamics for the flux linkage loop is dominated by the airgap flux dynamics since the inner current control loop has a high bandwidth. The transfer function between $\underline{i}_{sdq}^{N}$ and $\underline{\psi}_{odq}^{N}$, is given by

$$\frac{\underline{\psi}_{odq}^{N}(s)}{\underline{i}_{sdq}^{N}(s)} = \frac{L_o^N}{s\tau_r^N + 1} = \frac{58.116 \cdot 10^{-3}}{1.03s + 1} \tag{5.22}$$

where $\tau_r^N = L_r^N / R_r^N$ and is obtained from the parameters of the 2-pole squirrel cage equivalent circuit in Table 5.4.

A PI controller is designed for the $\underline{\psi}_{odq}^N$ control loops to achieve a nominal closed loop bandwidth of 9Hz. The controller transfer function is

$$G_c(s) = \frac{1584.06(s+35.73)}{s} \tag{5.23}$$

Now that all the compensators required for the proposed vector control schemes for both motor types have been designed, the vertical and lateral force control of the motors can be simulated in MATLAB Simulink to achieve sustained levitation.

5.4.2. Indirect Rotor Field Orientation (IRFO)

In this section, the force simulation results of the IRFO vector control schemes for the two machine types will be presented. At the start of the simulation, an i_{sd}^{M*} value of 4.90A, for both types of motors, is applied in order to allow the main 4-pole flux to build up. In both simulations, a step rotor speed reference ω_r^* of 1500rpm is applied to the speed control loop at 3s. Finally at 4s, a load torque equal to 90% of the rated torque T_{rated} is given. An external load having inertia equal to the motor inertia of 0.0713kgm^2 as well as a linear friction of $0.1T_{rated}$ at 1500 rpm was also applied throughout the simulation.

Cage rotor

The y- and x- direction force reference values F_y^* and F_x^* required to levitate the cage rotor are 235.36N and 0N respectively. Therefore, at 2s, a ψ_{od}^{N*} value of 13.56mWb and ψ_{oq}^{N*} value of zero was applied to the d- and q- axis flux linkage control loop of the 2-pole winding in the cage type motor respectively. This value of ψ_{od}^{N*} and ψ_{oq}^{N*} was calculated from equation (4.21) and rewritten here for convenience,

$$\begin{bmatrix} \psi_{od}^{N*} \\ \psi_{oq}^{N*} \end{bmatrix} = \frac{2\sqrt{2}\mu_o k_{ws}^N N_{ts}^N}{\pi B_o^M n} \begin{bmatrix} F_y^* \\ F_x^* \end{bmatrix} \tag{5.23}$$

This is assuming that the magnitude of the main flux density $B_o^M = 0.9\text{T}$. The IRFO control scheme for the cage rotor type motor to be simulated is shown in Figure 5.3.

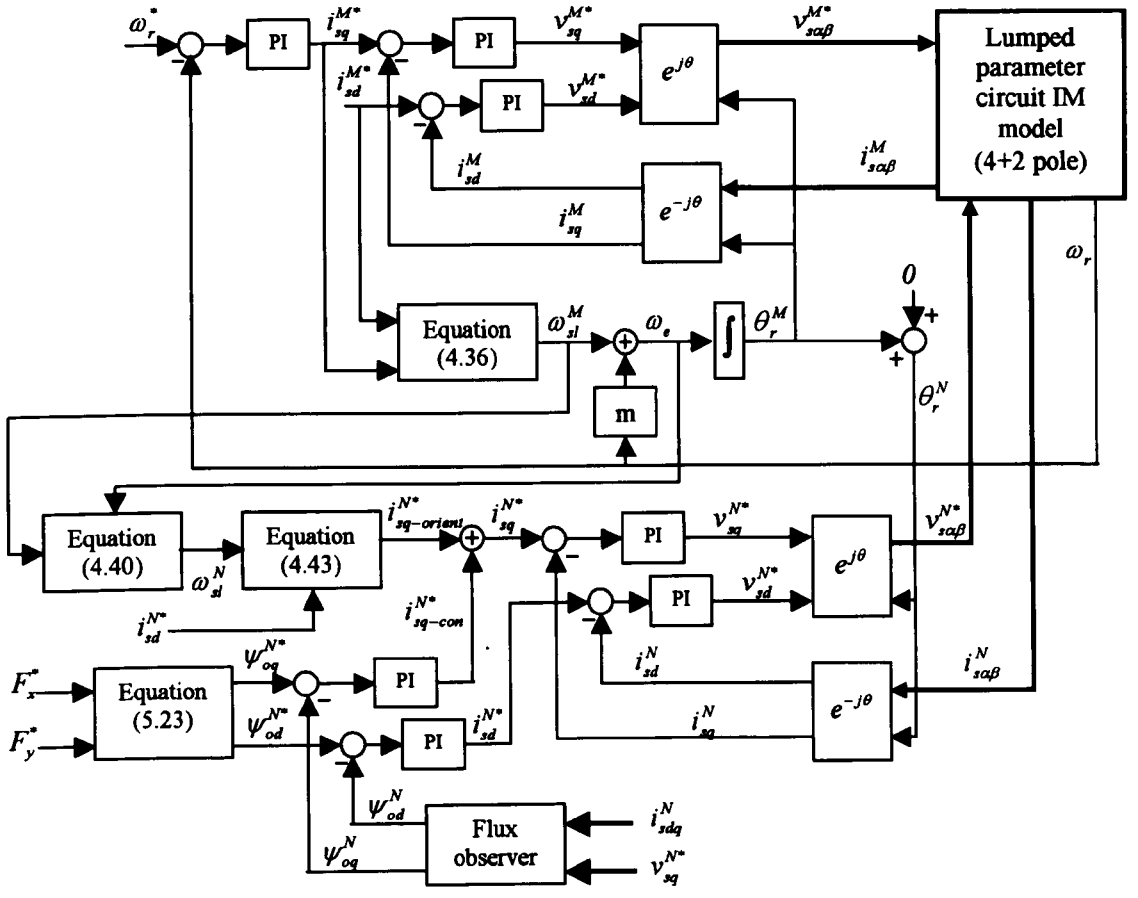

Figure 5.3: IRFO control scheme for the 4+2 pole cage rotor type motor simulated in Simulink.

Wound rotor

For the wound rotor type motor, a reference F_y^* value equal to the rotor weight of 253.36N and a zero reference F_x^* is also applied at 2s. This will then derive a value for i_{sd}^{N*} and i_{sq}^{N*} of 0.23A and 0A according to the relationship given in Chapter 4 (equation (4.64)), which is again repeated here for convenience

$$\begin{bmatrix} i_{sd}^{N*} \\ i_{sq}^{N*} \end{bmatrix} = \frac{2\sqrt{2}\mu_o k_{ws}^N N_{ts}^N}{\pi B_o^M n L_o^N} \begin{bmatrix} F_y^* \\ F_x^* \end{bmatrix} \tag{5.24}$$

with the same assumption that $B_o^M = 0.9\text{T}$. Figure 5.4 illustrates the IRFO control scheme for the wound rotor type motor.

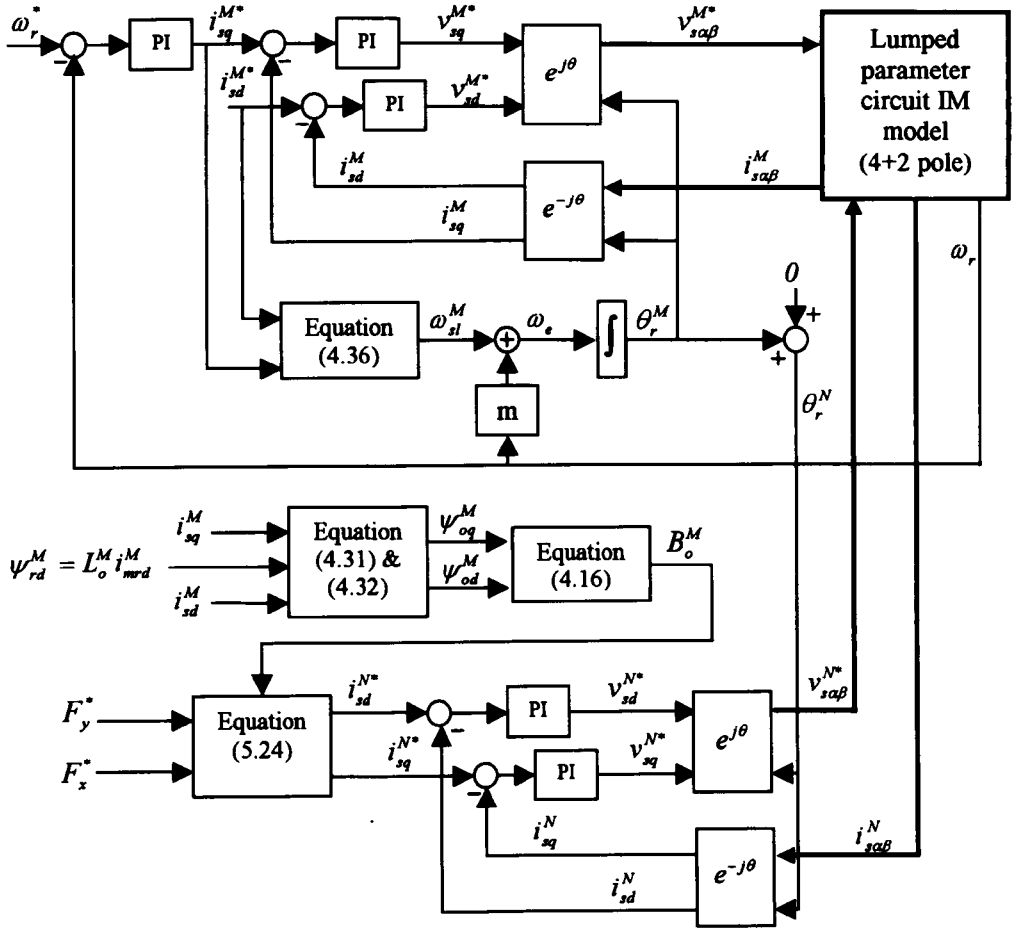

Figure 5.4: IRFO control scheme for the 4+2 pole wound rotor type motor simulated in Simulink.

In all the MATLAB Simulink simulations, the force produced in the bearingless motor is obtained using equations (3.29) and (3.30):

$$\begin{bmatrix} F_y \\ F_x \end{bmatrix} = \frac{rL\pi B_o^M}{2\mu_o} \begin{bmatrix} B_{od}^N \\ B_{oq}^M \end{bmatrix} \tag{5.25}$$

with B_o^M derived from $\underline{\psi}_{odq}^M$ (using equation (4.16)) and $\underline{B}_{odq}^N$ derived from $\underline{\psi}_{odq}^N$ using equations (4.18) and (4.19) respectively. These flux linkages, on the other hand, are derived from the stator currents and voltages as shown in Figure 5.5. Figure 5.5 also applies to the wound rotor type motor when the N-pole 'flux observer' block is replaced by equation (4.62). This is because in the wound rotor bearingless motor $\underline{\psi}_{odq}^N$ can be directly obtained from $\underline{i}_{sdq}^N$ due to no induced 2-pole rotor currents.

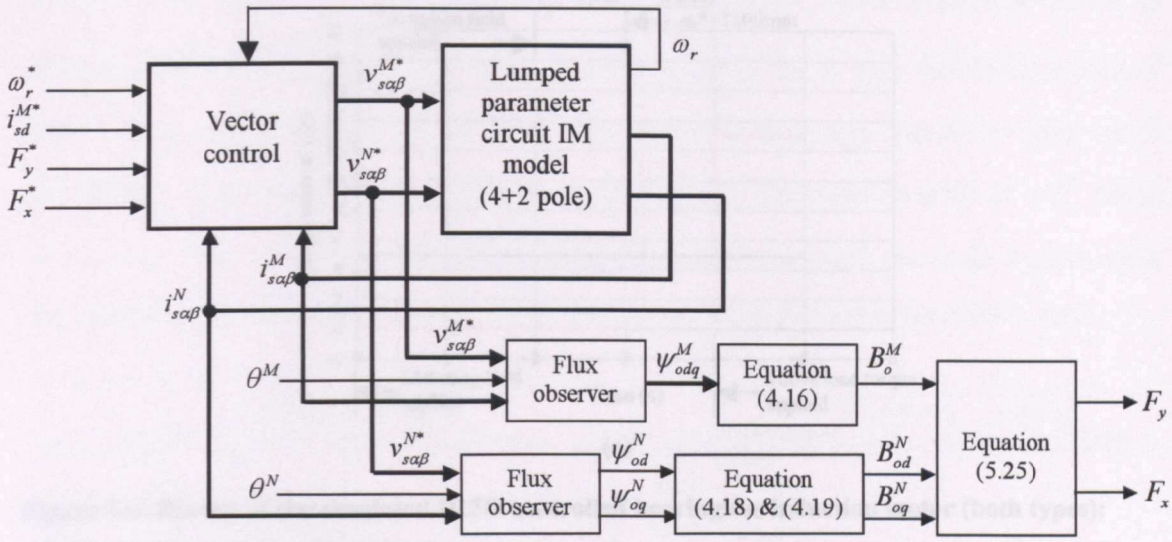

Figure 5.5: Block diagram of the vertical and lateral force control of the vector controlled bearingless cage rotor IM simulated in Simulink.

Results for both motors

The rotor mechanical speed, torque and i_{sdq}^{M} for both types of machine are shown in Figures 5.6(a), (b) and (c) respectively. The 2-pole currents i_{sdq}^{N} are present in both motors from 2s onwards. It is evident in Figures 5.6 (a)-(c) that the presence of i_{sdq}^{N} has no effect on the speed, torque and stator current of the 4-pole main winding waveforms.

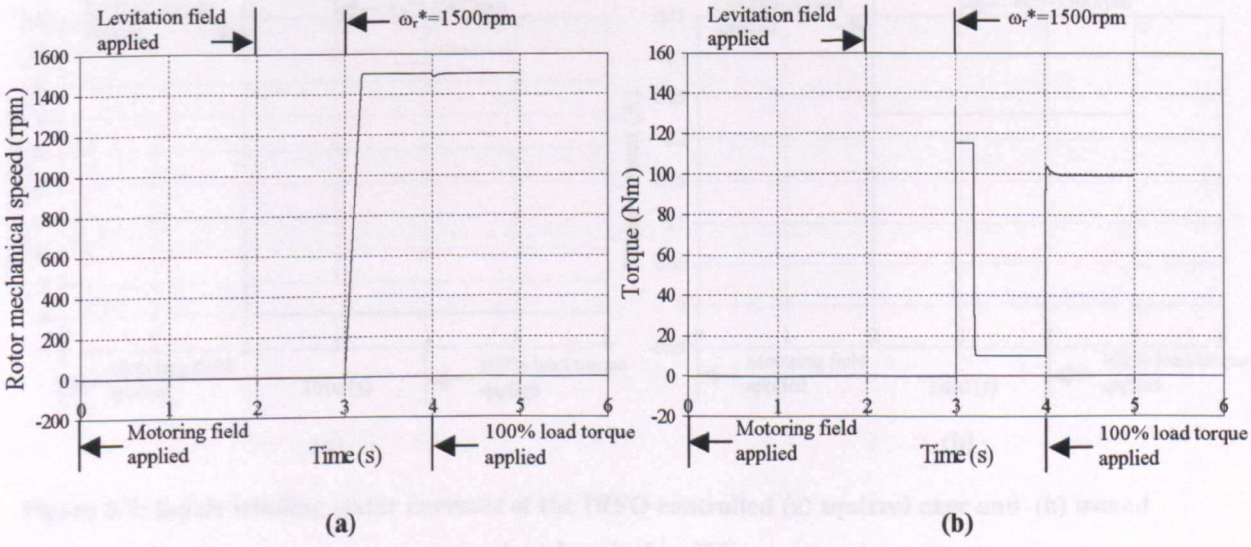

(a) (b)

Figure 5.6: Results of the simulated IRFO controlled bearingless induction motor (both types):

(a) speed

(b) torque

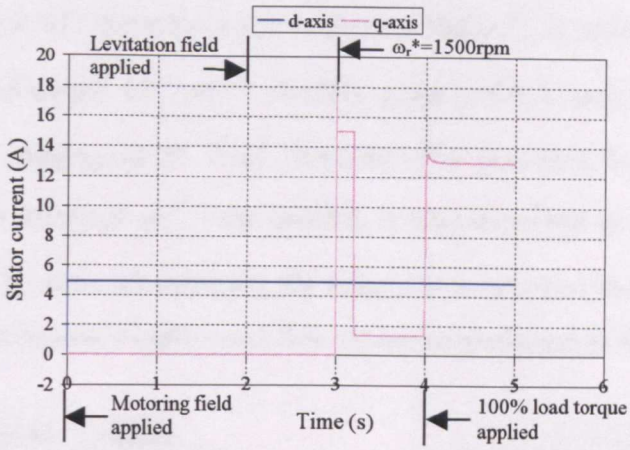

(c)`

Figure 5.6: Results of the simulated IRFO controlled bearingless induction motor (both types):
(c) 4-pole winding dq- axis stator currents

The behaviour of the 2-pole winding stator currents between the two machines is dissimilar. The 2-pole levitation winding stator currents of the squirrel cage and wound rotor type bearingless induction motors are as shown in Figures 5.7(a) and (b) respectively. For the wound rotor type motor, the 2-pole winding current controller is able to maintain the levitation winding stator current values according to the applied reference values i_{sd}^{N*} and i_{sq}^{N*} of 0.23A and 0A respectively from the moment the force references F_y^* and F_x^* were applied at 2s.

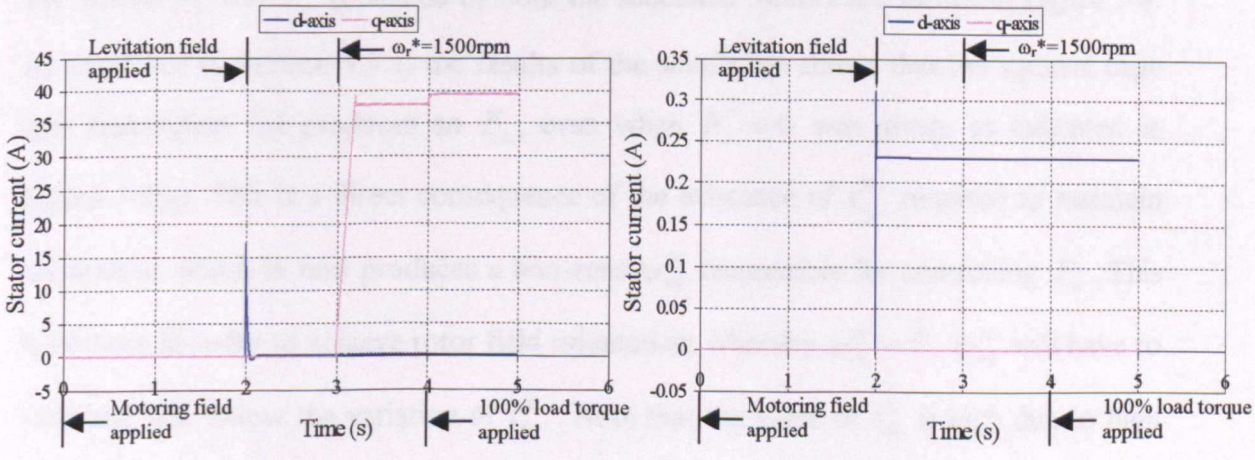

(a) (b)

Figure 5.7: 2-pole winding stator currents of the IRFO controlled (a) squirrel cage and (b) wound rotor type bearingless IM.

In the case of the squirrel cage type motor (Figure 5.7(a)), i_{sd}^{N} is maintained at 0.23A, as expected, from the reference ψ_{od}^{N*} of 13.56mWb given to the d- axis flux linkage control loop of the 2-pole winding at 2s. The existence of a non-zero 2-pole q- axis stator current i_{sq}^{N}, from the moment ψ_{od}^{N*} was applied, is also expected in spite of ψ_{oq}^{N*} being set to zero. This is in order to maintain the orientation between the main 4-pole rotor flux vector and the levitation 2-pole rotor flux vector as explained in Section 4.3.1.

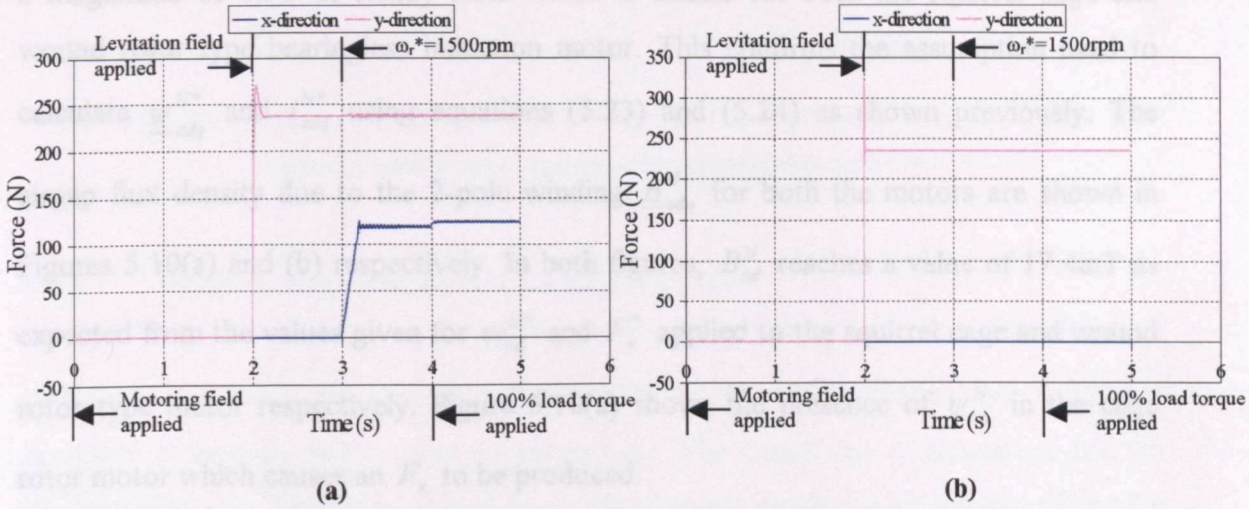

Figure 5.8: Force variation of the IRFO controlled (a) squirrel cage and (b) wound rotor type bearingless induction motor.

The forces F_y and F_x produced by both the simulated motors are shown in Figure 5.8. As explained in Section 4.3.1, the results of the simulation shows that the squirrel cage type bearingless IM produces an F_x, even when $F_x^* = 0$ was given, as indicated in Figure 5.8(a). This is a direct consequence of the existence of i_{sq}^{N}, required to maintain orientation, which in turn produces a non-zero ψ_{oq}^{N} responsible for controlling F_x. This is because in order to achieve rotor field orientation, whereby $\psi_{rq}^{N} = 0$, ψ_{oq}^{N} will have to exist and will follow the variation of i_{sq}^{N}. Note that the value of i_{sq}^{N} is high due to high slip between the 2-pole field and the rotor speed. This can be reduced only by choosing high M and N values. This is a natural disadvantage of having a cage rotor in which N-pole currents can flow. Even so, the cage rotor type motor is able to achieve the required F_y to counteract the rotor weight. In comparison, Figure 5.8(b) shows that

even with a rotor field orientation the wound rotor type bearingless induction motor is successful in producing a stable F_y even during acceleration and load conditions as required. There is also no force produced in the x- direction since ψ_{oq}^{N} remains zero at all times due to the zero i_{sq}^{N} as shown in Figure 5.7(b).

The airgap flux density due to the 4-pole winding B_o^M is shown in Figure 5.9 indicating a magnitude of 0.9T in steady state which is similar for both the squirrel cage and wound rotor type bearingless induction motor. This confirms the assumption used to calculate $\underline{\psi}_{odq}^{N*}$ and $\underline{i}_{sdq}^{N*}$ using equations (5.23) and (5.24) as shown previously. The airgap flux density due to the 2-pole winding $\underline{B}_{odq}^{N}$ for both the motors are shown in Figures 5.10(a) and (b) respectively. In both figures, B_{od}^{N} reaches a value of 17.4mT as expected from the values given for ψ_{od}^{N*} and F_y^* applied to the squirrel cage and wound rotor type motor respectively. Figure 5.10(a) shows the presence of ψ_{oq}^{N} in the cage rotor motor which causes an F_x to be produced.

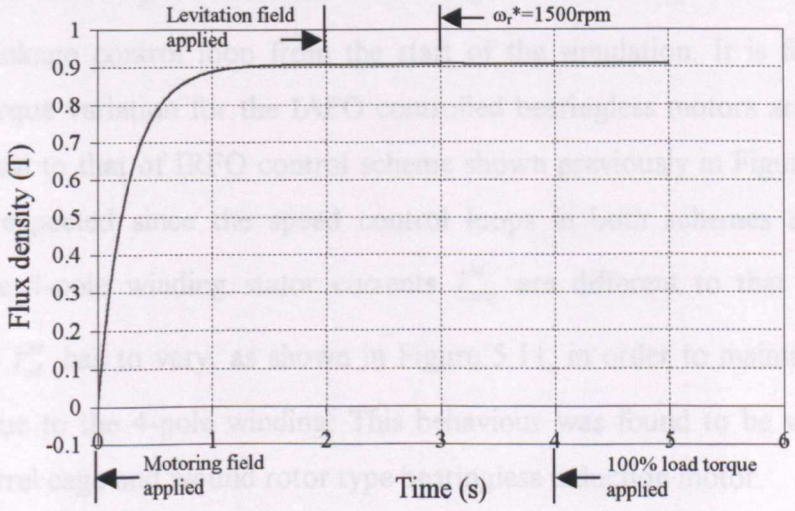

Figure 5.9: Observed 4-pole winding airgap flux density in the IRFO controlled bearingless induction motor (both types).

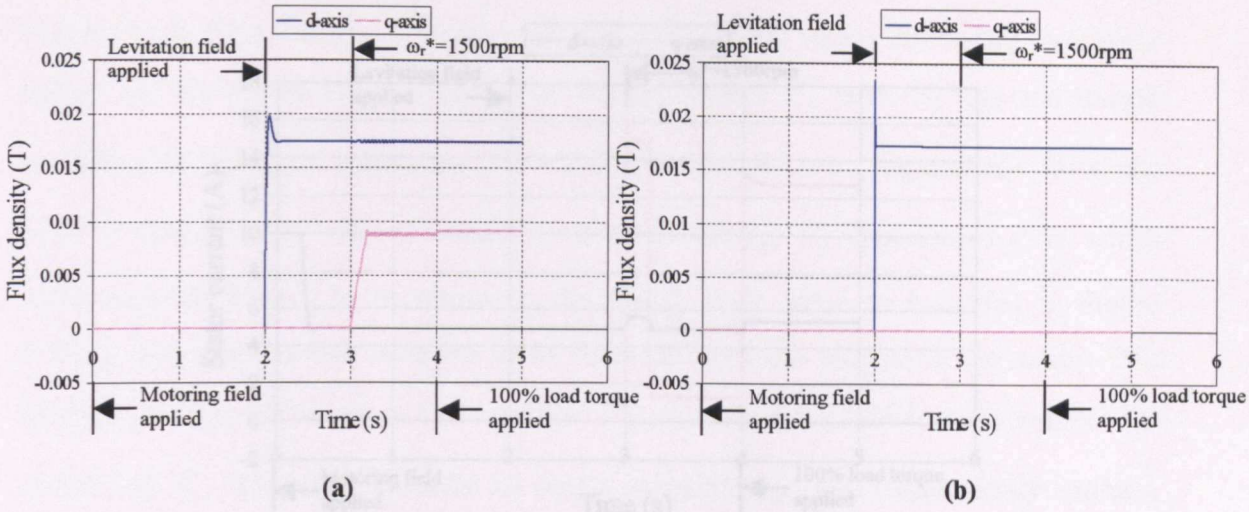

Figure 5.10: Observed 2-pole winding airgap flux density of the IRFO controlled (a) squirrel cage and (b) wound rotor type bearingless induction motor.

5.4.3. Indirect Airgap Field Orientation (IAFO)

Both motor types were also simulated based on the IAFO vector control scheme proposed in Sections 4.3.2 and 4.4, respectively. The conditions of simulation and the PI controllers are exactly as described in the previous section with the inclusion of a ψ_{od}^{M} control to obtain i_{sd}^{M*}. A constant flux linkage reference ψ_{od}^{M*} of 1.3Wb is applied to the flux linkage control loop from the start of the simulation. It is found that the speed and torque variation for the IAFO controlled bearingless motors are found to be almost identical to that of IRFO control scheme shown previously in Figures 5.6(a) and (b). This is expected since the speed control loops in both schemes are the same. However, the 4-pole winding stator currents $\underline{i}_{sdq}^{M}$ are different to that of the IRFO scheme since i_{sd}^{M} has to vary, as shown in Figure 5.11, in order to maintain a constant airgap flux due to the 4-pole winding. This behaviour was found to be very similar in both the squirrel cage and wound rotor type bearingless induction motor.

As in the IRFO scheme, the airgap field oriented 2-pole winding current i_{sq}^{N} must also be present in the cage rotor type motor in order to maintain the orientation between the 4-pole and the 2-pole fields.

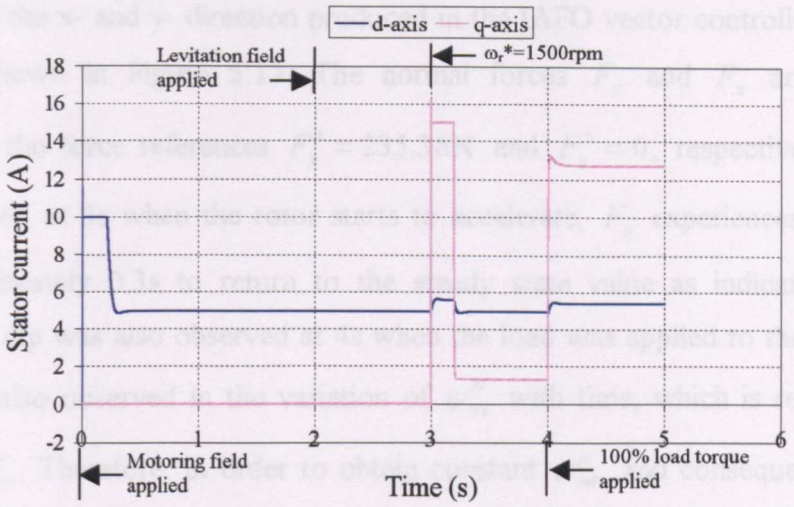

Figure 5.11: 4-pole winding stator currents of the IAFO controlled bearingless induction motor (for events see Section 5.4.2).

However, unlike in the IRFO scheme, i_{sd}^{N} is no longer constant. This is because in order to maintain ψ_{od}^{N} constant using the flux linkage control loop, i_{sd}^{N*} has to vary as shown in Figure 5.12(a). Figure 5.12(b) illustrates the 2-pole winding stator currents in the wound rotor type motor. The PI current controllers are able to maintain the current values according to the applied reference values $\underline{i}_{sdq}^{N*}$ which are derived from the force references F_y^* and F_x^* as seen in the IRFO scheme of the previous section.

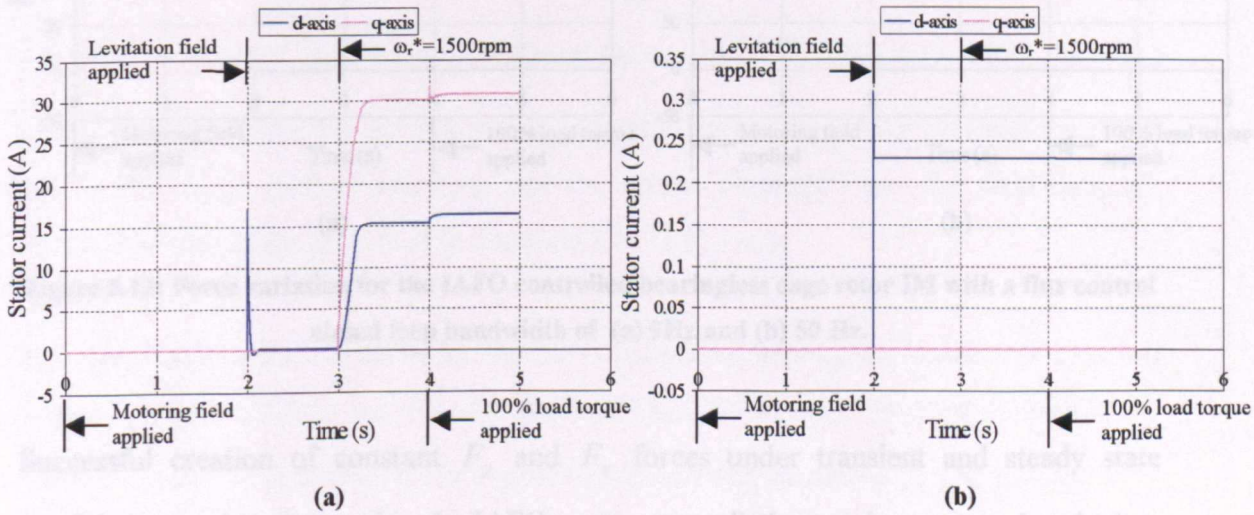

Figure 5.12: 2-pole winding stator currents in the IAFO controlled (a) squirrel cage and (b) wound rotor type bearingless induction motor.

The forces in the x- and y- direction produced in the IAFO vector controlled cage rotor motor are shown in Figure 5.13. The normal forces F_y and F_x are maintained according to the force references $F_y^* = 235.36\text{N}$ and $F_x^* = 0$, respectively, in steady state. However, at 3s when the rotor starts to accelerate, F_y experiences a dip which takes approximately 0.3s to return to the steady state value as indicated in Figure 5.13(a). This dip was also observed at 4s when the load was applied to the motor. This behaviour is also observed in the variation of ψ_{od}^N with time, which is responsible for controlling F_y. Therefore, in order to obtain constant ψ_{od}^N, and consequently constant F_y, the closed loop bandwidth of the flux linkage control loop has to be increased from the present value of 9Hz. Figure 5.13(b) shows the time variation of F_y when the flux linkage control loop bandwidth is increased to 50Hz. As seen in Figure 5.12, no F_x is produced since $\psi_{oq}^N = 0$ at all times due to the airgap field orientation, unlike that seen in the IRFO controlled motor.

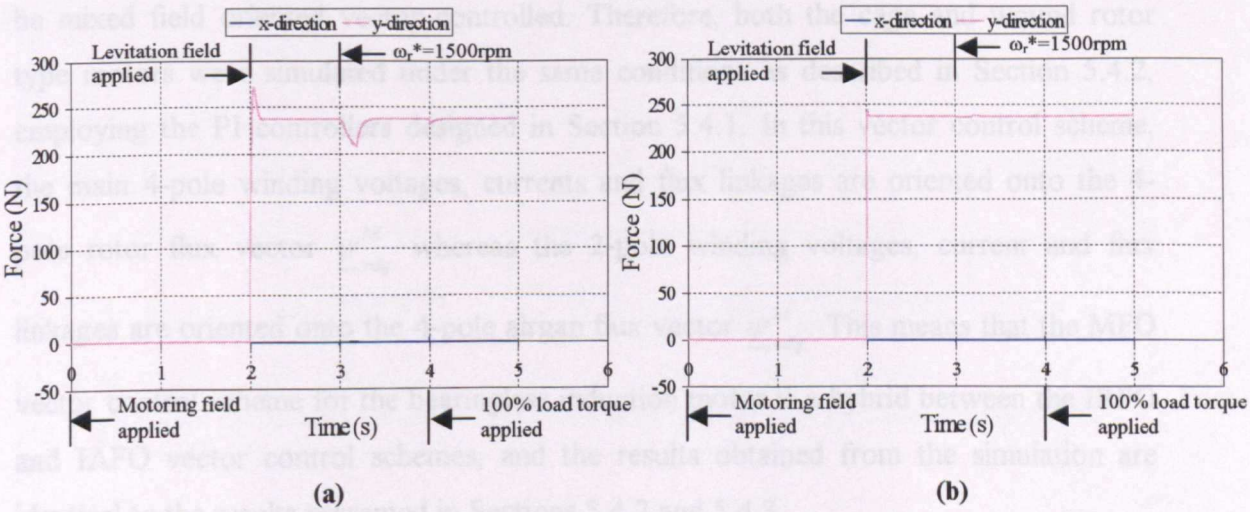

Figure 5.13: Force variation for the IAFO controlled bearingless cage rotor IM with a flux control closed loop bandwidth of (a) 9Hz and (b) 50 Hz.

Successful creation of constant F_y and F_x forces under transient and steady state conditions are also observed in the IAFO vector controlled wound rotor type bearingless induction motor as indicated in Figure 5.14.

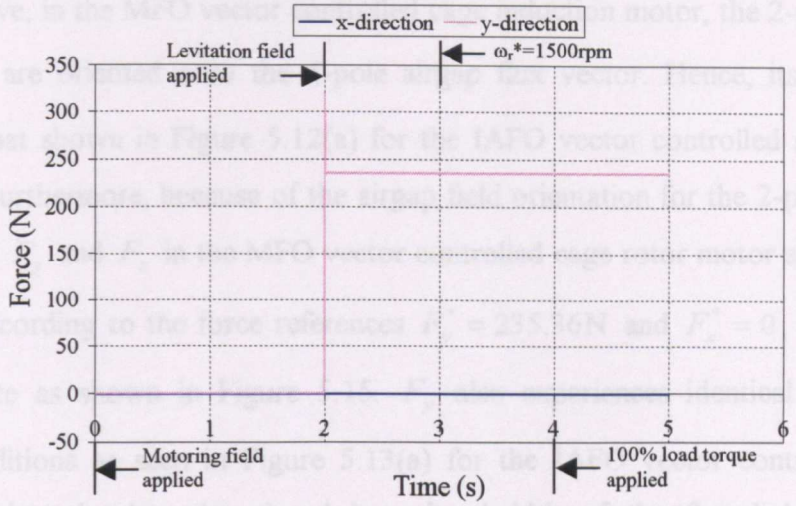

Figure 5.14: Force variation for the IAFO controlled wound rotor type bearingless induction motor.

5.4.4. Mixed Field Orientation (MFO)

As proposed in Sections 4.3.3 and 4.4, both the cage and wound rotor type motors can be mixed field oriented vector controlled. Therefore, both the cage and wound rotor type motors were simulated under the same conditions as described in Section 5.4.2, employing the PI controllers designed in Section 5.4.1. In this vector control scheme, the main 4-pole winding voltages, currents and flux linkages are oriented onto the 4-pole rotor flux vector $\underline{\psi}^{M}_{rdq}$ whereas the 2-pole winding voltages, current and flux linkages are oriented onto the 4-pole airgap flux vector $\underline{\psi}^{M}_{odq}$. This means that the MFO vector control scheme for the bearingless induction motor is a hybrid between the IRFO and IAFO vector control schemes, and the results obtained from the simulation are identical to the results presented in Sections 5.4.2 and 5.4.3.

The speed and torque variation for the MFO controlled bearingless motors are identical to that in Figures 5.6(a) and (b) obtained from the IRFO vector controlled bearingless induction motor. Furthermore, the 4-pole winding stator currents $\underline{i}^{M}_{sdq}$ are also found to be similar to that of the IRFO scheme shown previously in Figure 5.6(c).

As stated above, in the MFO vector controlled cage induction motor, the 2-pole winding currents $\underline{i}_{sdq}^{N}$ are oriented onto the 4-pole airgap flux vector. Hence, its variation is identical to that shown in Figure 5.12(a) for the IAFO vector controlled squirrel cage type motor. Furthermore, because of the airgap field orientation for the 2-pole field, the normal forces F_y and F_x in the MFO vector controlled cage rotor motor are able to be maintained according to the force references $F_y^* = 235.36\text{N}$ and $F_x^* = 0$, respectively, at steady state as shown in Figure 5.15. F_y also experiences identical dips during transient conditions as seen in Figure 5.13(a) for the IAFO vector controlled motor which is eliminated when the closed loop bandwidth of the flux linkage loop is increased. In addition, no F_x is produced since the 2-pole winding is airgap flux vector oriented despite the main 4-pole winding being rotor field oriented.

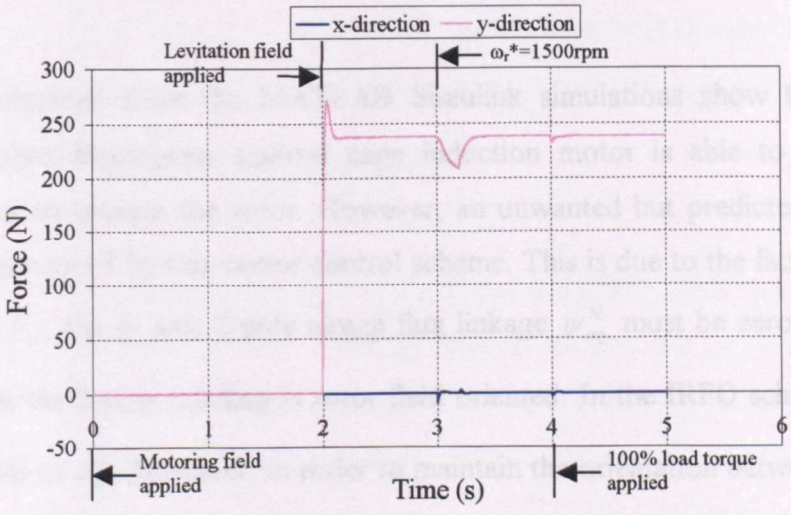

Figure 5.15: Force variation in the MFO controlled squirrel cage type bearingless motor.

On the other hand, the time variation of $\underline{i}_{sdq}^{N}$ for the MFO vector controlled wound rotor type motor is found to be exactly the same as that of the IAFO vector control scheme demonstrated in Figure 5.12(b). Consequently, constant F_y and F_x forces under transient and steady state conditions are observed in this vector control scheme as shown in Figure 5.16 which is identical to that of the IAFO vector controlled wound rotor type motor (Figure 5.14).

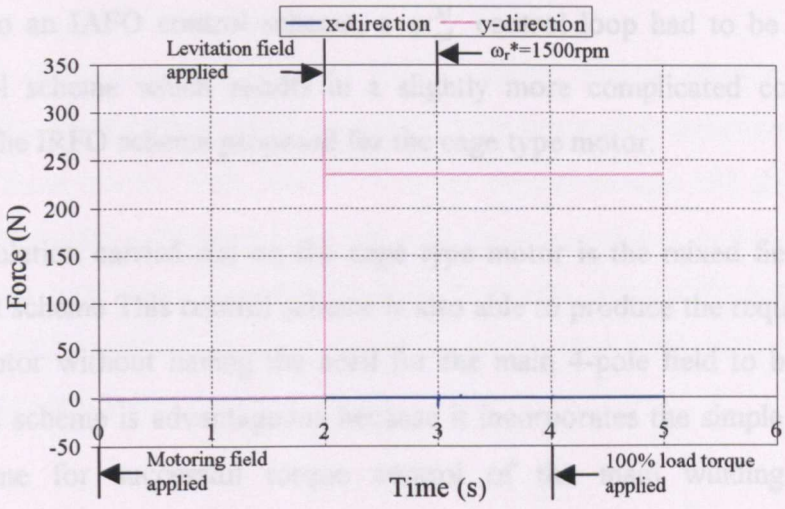

Figure 5.16: Force variation in the MFO controlled bearingless wound rotor motor.

5.5. Chapter summary and discussion

The results obtained from the MATLAB Simulink simulations show that an IRFO vector controlled bearingless squirrel cage induction motor is able to achieve a y-direction force to levitate the rotor. However, an unwanted but predicted x- direction force is also produced by this vector control scheme. This is due to the fact that in order to have zero F_x, the q- axis 2-pole airgap flux linkage ψ_{oq}^N must be zero, which is not the case when the 2-pole winding is rotor field oriented. In the IRFO scheme, ψ_{oq}^N will be proportional to i_{sq}^N. However, in order to maintain the orientation between the 4-pole and 2-pole rotor fields, a large i_{sq}^N was present in the motor due to the large slip speed of the 2-pole field as explained in Section 4.3.2.

When the cage type motor is controlled using the IAFO vector control scheme, successful normal forces are obtained. An F_y equal to the rotor weight is produced which remains constant even during transient conditions provided that ψ_{od}^N is very closely controlled as indicated in Figure 5.13. Furthermore, a zero F_x is produced since ψ_{oq}^N is successfully controlled at zero by the q-axis flux linkage control despite the existence of the orientation component of i_{sq}^N. However, because the 4-pole field was

also subject to an IAFO control scheme, a ψ_{od}^{M} control loop had to be added to the vector control scheme which results in a slightly more complicated control scheme compared to the IRFO scheme proposed for the cage type motor.

The final simulation carried out on the cage type motor is the mixed field orientation vector control scheme This control scheme is also able to produce the required forces to levitate the rotor without having the need for the main 4-pole field to be airgap field oriented. This scheme is advantageous because it incorporates the simple IRFO vector control scheme for successful torque control of the main winding as well as incorporating the IAFO control scheme required for the 2-pole levitation winding in order to ensure no unwanted F_x is produced despite the existence of the orientation i_{sq}^{N}. However, as observed in Figure 5.15, the force obtained in the MFO vector control scheme experiences a dip during transient conditions in an identical manner to that of the IAFO scheme (see Figure 5.13). Therefore, the MFO control scheme for the squirrel cage type motor also requires a closely controlled $\underline{\psi}_{odq}^{N}$ control loop in order to maintain constant F_y and F_x during transient conditions.

The simulation of the wound rotor type motor under the IRFO, IAFO and MFO vector control schemes all showed that constant normal forces are achieved under all conditions as required by the force references. However, under the IRFO vector control scheme both the 4-pole and 2-pole winding currents, voltages and flux linkages are oriented onto $\underline{\psi}_{r}^{M}$ which means that when the torque current i_{sq}^{M} is present, B_{o}^{M} will no longer be aligned with B_{od}^{N} and will not be in quadrature with B_{oq}^{N}. Therefore, the forces F_y and F_x will no longer be constant since in order for the constant forces to be produced and governed by equation (5.25), the peak flux densities B_{od}^{N} and B_{o}^{M} must be aligned with each other. Hence, the IAFO and MFO vector control schemes are the only control schemes suitable for the wound rotor type motor. Even so, as observed for the control of the cage rotor motor, the MFO vector control scheme is at an advantage since it incorporates a simpler IRFO control for the main 4-pole winding whilst still being able to produce the necessary forces via the IAFO control scheme required for the 2-pole levitation winding.

In conclusion, the mixed field oriented (MFO) vector control scheme is chosen to control both the squirrel cage and wound rotor type bearingless induction motors. The simulation of these motors under the MFO vector control scheme will also be repeated using the DCM model in Chapter 6 for the cage rotor type motor, and in Chapter 7 for the wound rotor type motor. A comparison of the results obtained from the MATLAB Simulink and DCM simulations of these MFO vector controlled motors will also be discussed in the appropriate chapters.

Chapter 6

Dynamic circuit modelling (DCM) of a bearing relief cage rotor induction motor

6.1. Introduction

The study of bearingless induction motors in this thesis also entails a study on bearing relief capabilities in which the rotor movement is still restricted by conventional bearings. However, the bearing load is cancelled by suitably directed radial forces created in the motor through the incorporation of the N-pole levitation windings. In this chapter, the simulation of a bearing relief cage rotor motor will be presented, as it is the most common type of induction motor. The motor consists of two stator windings in which the main torque production winding is of a 4-pole nature and the levitation winding is a 2-pole winding. The parameters of both windings are given in Sections 5.2.1 and 5.3. An uncontrolled simulation of the 4+2 pole bearing relief motor, in which both stator windings are started directly on-line, will be presented in Section 6.3. This is to investigate the radial force production and to verify the theory of bearingless induction motors.

A vector controlled simulation of the same motor will be discussed in Section 6.4. In this simulation, the bearing relief motor is controlled in a mixed field oriented (MFO) frame whereby the main 4-pole winding is rotor field oriented and the 2-pole levitation winding is 4-pole airgap field oriented. This vector control scheme was chosen based on the successful MATLAB Simulink simulations for the 4+2 pole cage rotor motor under the MFO vector control scheme and based on a two-axis lumped parameter model of the motor (refer Section 5.4.4). A comparison between the DCM and the MATLAB Simulink simulation results will be presented in Section 6.5.

6.2. Vector control of a cage rotor IM in DCM

Firstly, the results of a linear 4-pole cage rotor IM simulated in DCM with an indirect rotor field orientation (IRFO) vector control scheme will be presented. As the simulation is of a linear iron motor, the relative permeability of all reluctance elements of type 'linear iron' is fixed in which $\mu_r = 1350$. In order to utilise the *s*-plane current and speed loop controllers of Section 5.4.1 in the DCM simulation, the PI controllers are transformed into the discrete z-plane using the Bilinear Transform (Franklin *et. al*, 1998) in which $s = (2/t_{samp})(z-1/z+1)$. The current loop sampling time t_{samp-i} is chosen to be 100μs and the speed loop sampling time $t_{samp-\omega}$ is 2ms. In the simulation, a step rotor speed reference ω_r^* of 1500rpm was applied to the speed control loop at 3s with a load torque equal to 90% of the rated torque T_{rated} given at 4s. An external load having inertia equal to the rotor inertia of 0.0713kgm^2 as well as a linear friction of $0.1\,T_{rated}$ at 1500 rpm was also applied throughout the simulation. The maximum simulation time step is 50μs with a Newton Raphson error tolerance set to 1x10^{-6} and a maximum of 15 iterations per time step. The linear equations solver error tolerance is 1x10^{-7} with a maximum of 200 iterations and a maximum threshold of 1x10^{-5}.

Time	Event	Throughout simulation (0-5s)
0	i_{sd}^{M*} = 4.90A applied (to build up main flux)	external load inertia = 0.0713kgm^2 and linear friction of $0.1\,T_{rated}$ at 1500 rpm applied
3s	ω_r^* = 1500rpm applied	
4s	90% of T_{rated} applied	

Table 6.1: Sequence of events occurring in the simulation of the vector controlled 4-pole cage rotor motor.

Figure 6.1(a) shows the speed variation of the IRFO vector controlled motor. The rotor reaches within 5% of the 1500rpm reference speed in 0.23s from the moment ω_r^* was applied (i.e. at 3s). The speed control maintains the speed at 1500rpm after the load torque is applied. The corresponding torque variation is shown in Figure 6.1(b). From the moment the rotor starts to rotate (3s onwards), the torque was observed to

experience an oscillation of 900Hz (as shown in the inset graph of Figure 6.1(b)). This oscillating behaviour is also observed in all the vector control simulation results reported in this chapter (Section 6.2 and 6.4). Therefore, when referring to the value of the vector controlled quantities obtained from the simulations the average value of the oscillating waveform is taken which is obtained by numerical integration. These oscillations are not understood.

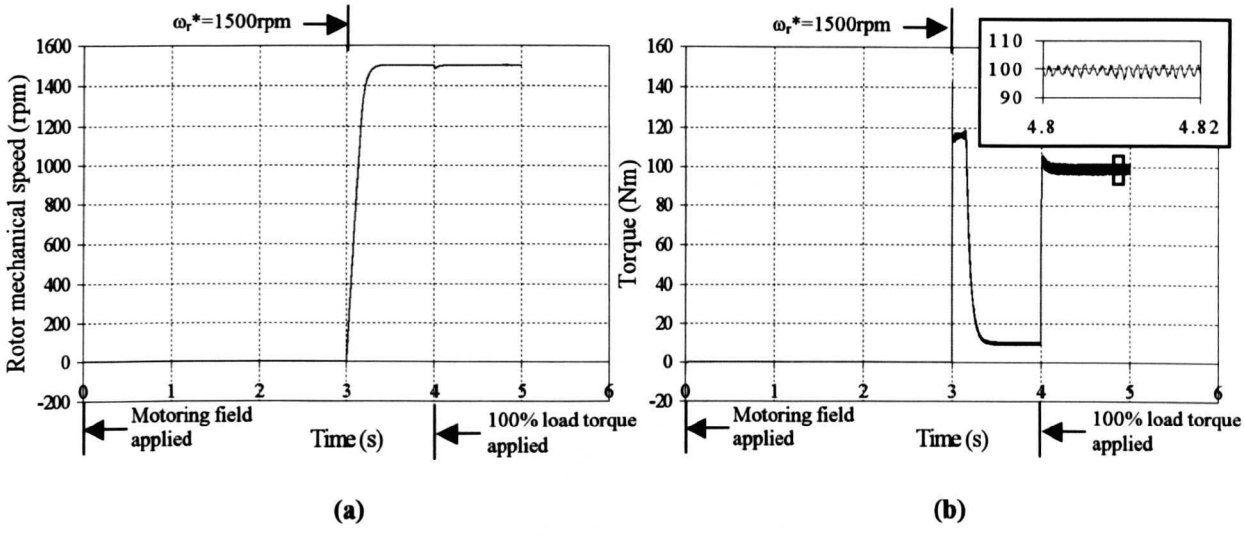

Figure 6.1: (a) speed and (b) torque variation with time of the IRFO vector controlled 4-pole cage rotor IM.

The stator currents i_{sd} and i_{sq} are presented in Figures 6.2(a) and (b). In both figures, i_{sd} and i_{sq} (shown as the darker set of lines in Figure 6.2), are obtained by transforming the αβ- axis stator currents using the IRFO controller orientation angle $\hat{\theta}_r$. These are compared with the stator currents obtained from 'direct' orientation (shown as the lighter set of lines in Figure 6.2) in which the angle of the peak rotor flux in the motor, θ_r^{DFT} is used in the transformation. In the simulation, θ_r^{DFT} is obtained from carrying out a spatial discrete Fourier transform (DFT) of the actual rotor flux density flowing in each inner rotor tooth element, as depicted in Figure 6.3, using equation (6.1)

$$X(k) = \frac{2}{N}\sum_{n=0}^{N-1} x_n \exp\left(\mathrm{j}\frac{2\pi \mathrm{kn}}{\mathrm{N}}\right) \tag{6.1}$$

where k is the index of the DFT, x_n is the flux density flowing in the inner reluctance element of rotor tooth n and N is the total number of rotor teeth in the motor.

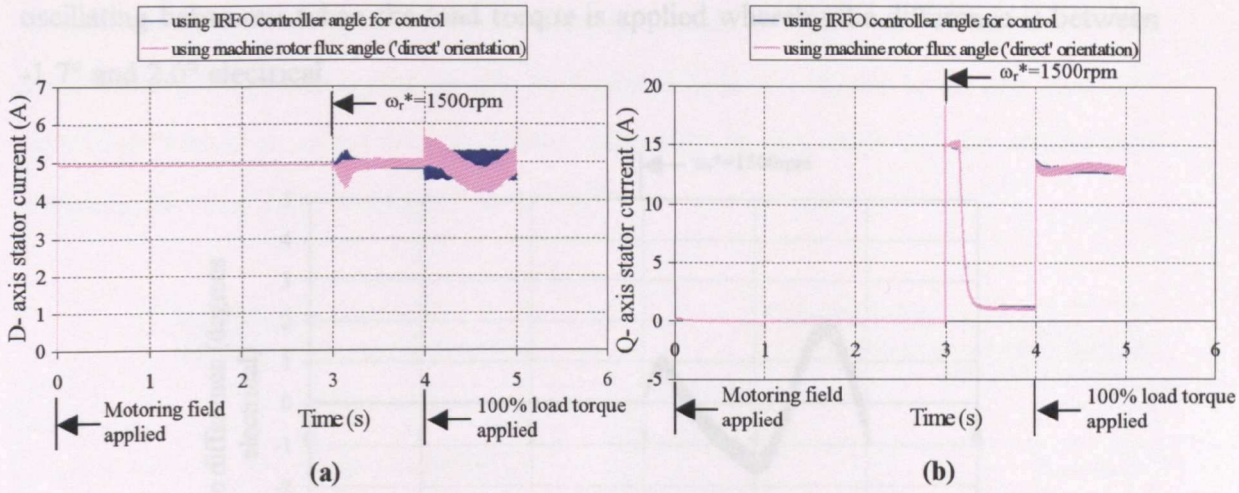

Figure 6.2: Stator current variation with time of the IRFO vector controlled 4-pole cage rotor IM: (a) d- axis (b) q- axis.

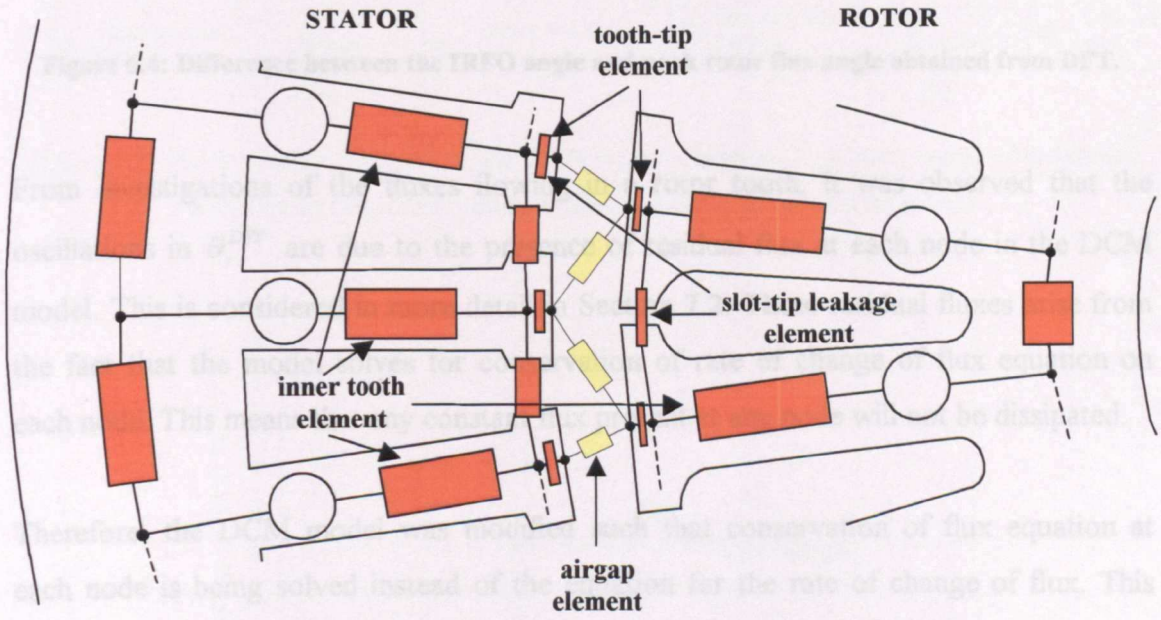

Figure 6.3: The inner, tooth-tip and airgap reluctance elements

As observed in Figure 6.2, i_{sd} and i_{sq} (obtained using $\hat{\theta}_r$) are similar to the currents obtained from 'direct' orientation in the time region of 0 to 4s, indicating that the IRFO orientation angle $\hat{\theta}_r$ is able to track the exact position of the peak rotor field in steady state conditions. However, when load is applied at 4s, the 'direct' orientation dq- axis stator currents experiences an oscillation, which is found to be at slip frequency. The discrepancy between $\hat{\theta}_r$ and θ_r^{DFT} is shown in Figure 6.4 which illustrates the variation of the difference between the two angles. This angle difference also exhibits the

oscillating behaviour when the load torque is applied whereby the difference is between -1.7° and 2.0° electrical.

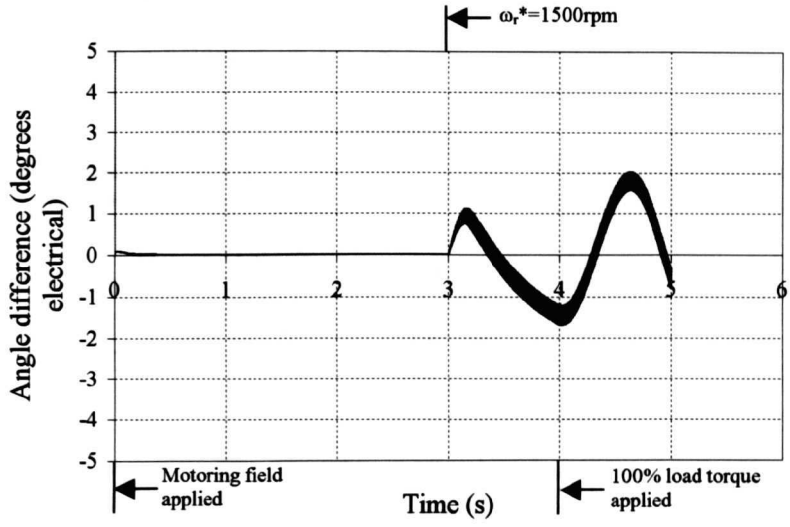

Figure 6.4: Difference between the IRFO angle and peak rotor flux angle obtained from DFT.

From investigations of the fluxes flowing in a rotor tooth, it was observed that the oscillations in θ_r^{DFT} are due to the presence of residual flux at each node in the DCM model. This is considered in more detail in Section 7.2. These residual fluxes arise from the fact that the model solves for conservation of rate of change of flux equation on each node. This means that any constant flux present at any node will not be dissipated.

Therefore, the DCM model was modified such that conservation of flux equation at each node is being solved instead of the equation for the rate of change of flux. This ensures that no constant flux exists at any node. The changes required for enforcing flux conservation at each node are described in Section 2.5(b). Henceforth, all simulations in this chapter are based on solving for flux conservation equation at each node of the DCM model.

For this reason, the rotor flux oriented vector control of the cage rotor IM was repeated with the model solving for conservation of flux equation at each node. It was observed that the speed and torque variation against time are similar to those obtained previously when solving for conservation of rate of change of flux equation at each node. However, i_{sd} and i_{sq} in the motor obtained from the IRFO controller angle $\hat{\theta}_r$ and from

'direct orientation' using θ_r^{DFT} are now in agreement as observed in Figure 6.5. The error between the two angles, shown in Figure 6.6, is also found to be less than 0.9° electrical, which is acceptable. A further reduction in this error can be obtained by reducing the rotor time constant $\tau_r = L_r^M / R_r^M$.

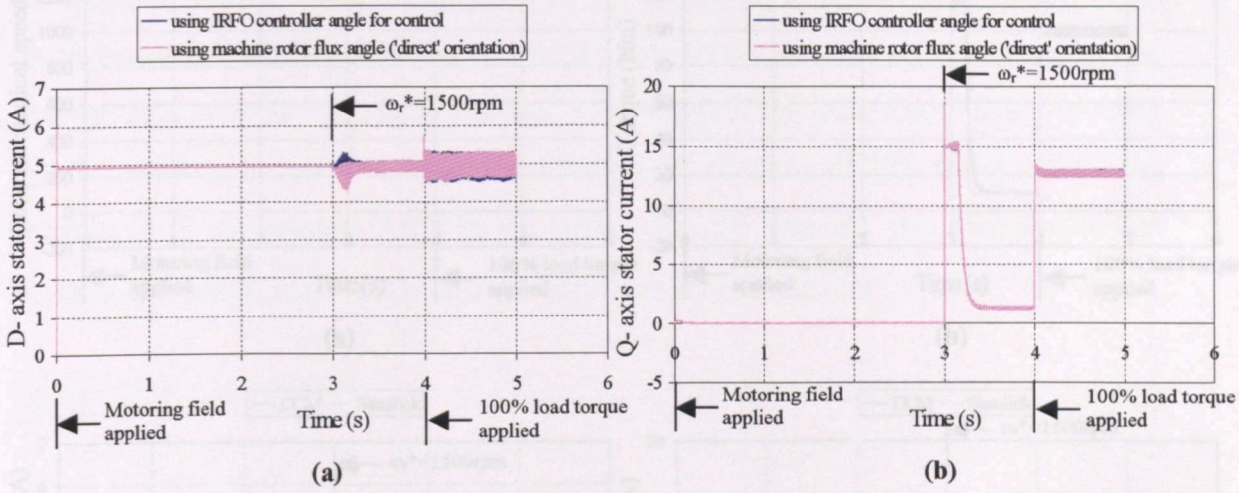

Figure 6.5: Stator current variation of the IRFO vector controlled cage rotor motor with solution based on solving conservation of flux equations: (a) d- axis (b) q- axis.

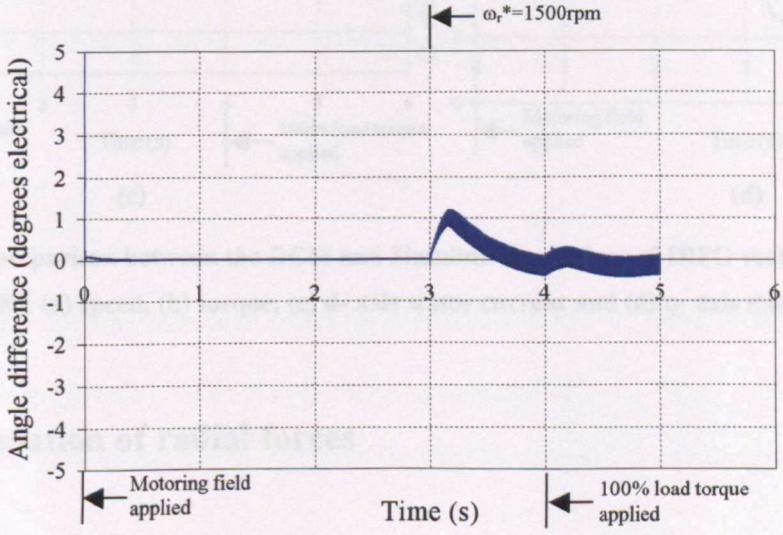

Figure 6.6: Difference between the IRFO angle and peak rotor flux angle obtained from DFT in DCM model solving for conservation of flux equations.

Finally, the results from the DCM simulation were compared with the results obtained from a two-axis lumped parameter model simulation of the same IRFO vector controlled 4-pole cage rotor IM carried out in MATLAB Simulink. It is observed that

the speed, torque and dq- axis stator current variations of the two simulation methods exhibit very close agreement as indicated by Figures 6.7(a)-(d).

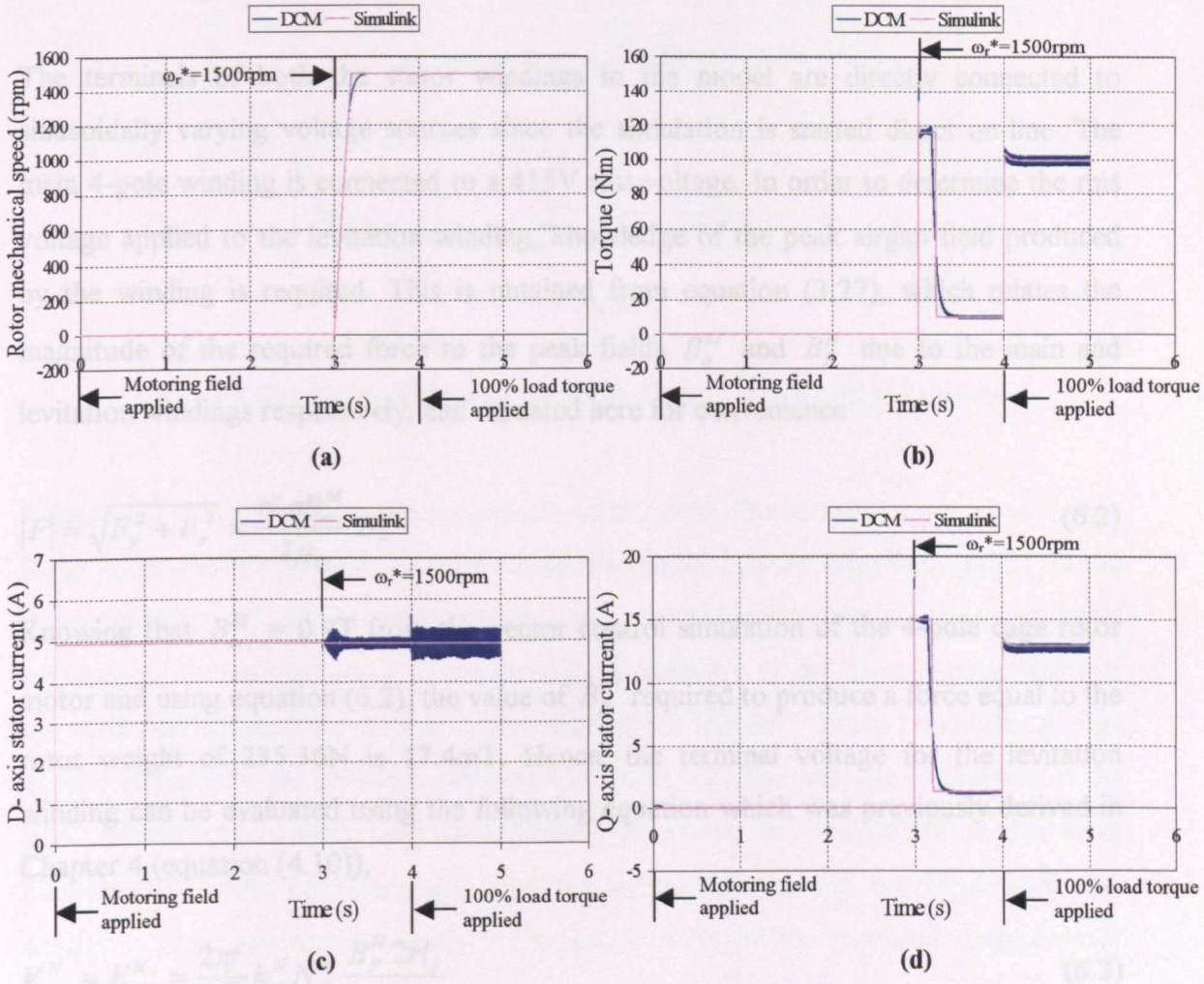

Figure 6.7: Comparison between the DCM and Simulink simulations of IRFO vector controlled cage rotor IM: (a) speed, (b) torque, (c) d- axis stator current and (d) q- axis stator current.

6.3. Simulation of radial forces

In this section, the results of the DCM modelled 4+2 pole linear cage rotor IM simulated under direct on-line (DOL) start condition are given. The motor is based on the 4-pole cage rotor motor with a 48/40 stator-rotor slot combination, introduced in Chapter 5, onto which the 2-pole levitation stator winding designed in Section 5.3 is incorporated. All reluctance elements in the DCM mesh of the motor were chosen to be of type 'linear iron' with $\mu_r = 1350$ except for the elements connecting each stator and

rotor tooth, which are of type 'air' to model the semi-closed stator and rotor slots. The motor was also modelled with only one rotor axial skew section with a skew angle of 15° electrical.

The terminals of both the stator windings in the model are directly connected to sinusoidally varying voltage sources since the simulation is started direct on-line. The main 4-pole winding is connected to a 415V rms voltage. In order to determine the rms voltage applied to the levitation winding, knowledge of the peak airgap field produced by the winding is required. This is obtained from equation (3.27), which relates the magnitude of the required force to the peak fields B_o^M and B_F^N due to the main and levitation windings respectively, and repeated here for convenience

$$|F| = \sqrt{F_y^2 + F_x^2} = \frac{rL\pi B_o^M}{2\mu_0} B_F^N \tag{6.2}$$

Knowing that B_o^M = 0.9T from the vector control simulation of the 4-pole cage rotor motor and using equation (6.2), the value of B_F^N required to produce a force equal to the rotor weight of 235.36N is 17.4mT. Hence, the terminal voltage for the levitation winding can be evaluated using the following equation which was previously derived in Chapter 4 (equation (4.10)),

$$V_{rms}^N \approx E_{rms}^N = \frac{2\pi f}{\sqrt{2}} k_{ws}^N N_{ts}^N \frac{B_F^N 2rl_z}{N} \tag{6.3}$$

where f =50 Hz and the values of the 2-pole winding factor k_{ws}^N and total series turn per phase N_{ts}^N are as given in Table 5.4(a). With a required B_F^N = 17.4mT , the rms terminal voltage of the 2-pole levitation winding applied in the simulation calculates to be 4.20V.

The magnitude of force obtained from the simulation is shown in Figure 6.8 at no load. It can be observed that at steady state the force magnitude produced is only 46.59N. This is 80.2% less than the expected force of 235.36N. To investigate the force discrepancy, the actual 4- and 2-pole field values in the DCM model are evaluated.

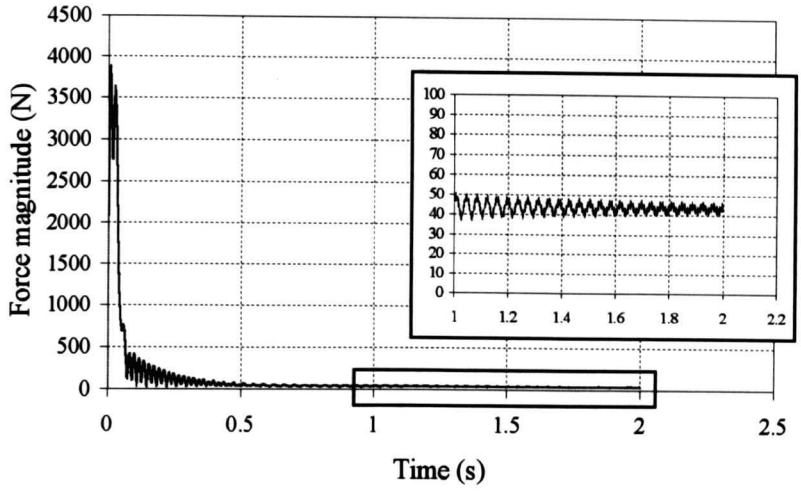

Figure 6.8: Force magnitude produced by the linear 4+2 pole cage rotor motor.

Figures 6.9 and 6.10 show the magnitude of the peak fundamental 4-pole and 2-pole fields in the motor, obtained by performing a Discrete Fourier transform (DFT) on the flux densities of the rotor-tooth-tip and stator-tooth-tip reluctance elements, respectively, around the rotor circumference. A summary of the average magnitudes of the peak fundamental 4-pole and 2-pole fields from the DFT of the two different flux density samples in the motor is presented in Table 6.2. The average magnitude of the peak fundamental 4-pole field is expected. However, the magnitude of the peak fundamental 2-pole field obtained from the rotor-tooth-tip and stator-tooth-tip flux density samples are approximately 9.2% and 19.54% of the expected magnitude of 17.4mT, respectively.

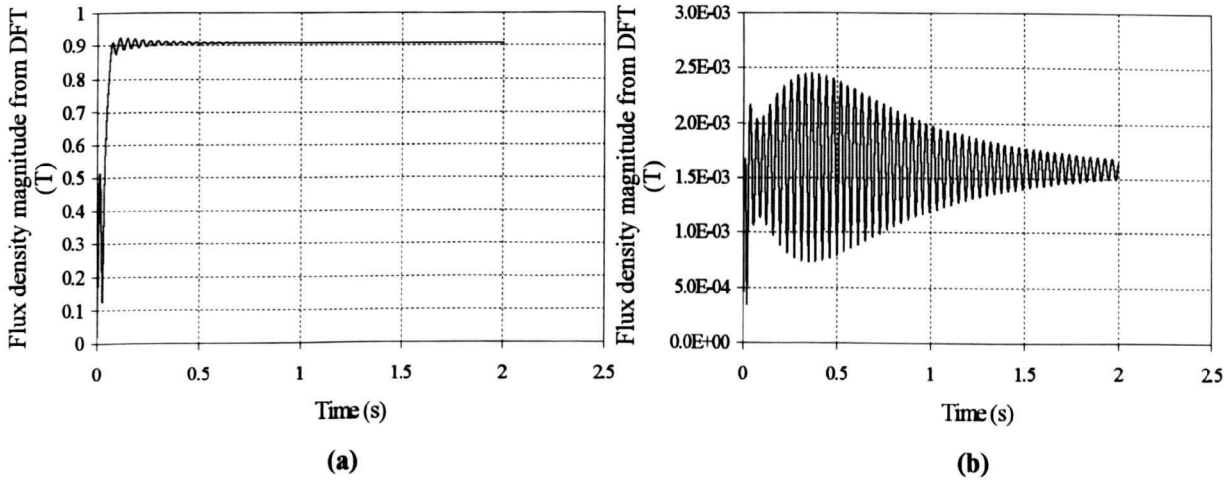

Figure 6.9: Peak magnitudes of (a) 4-pole and (b) 2-pole fields from DFT of rotor-tooth-tip flux density samples.

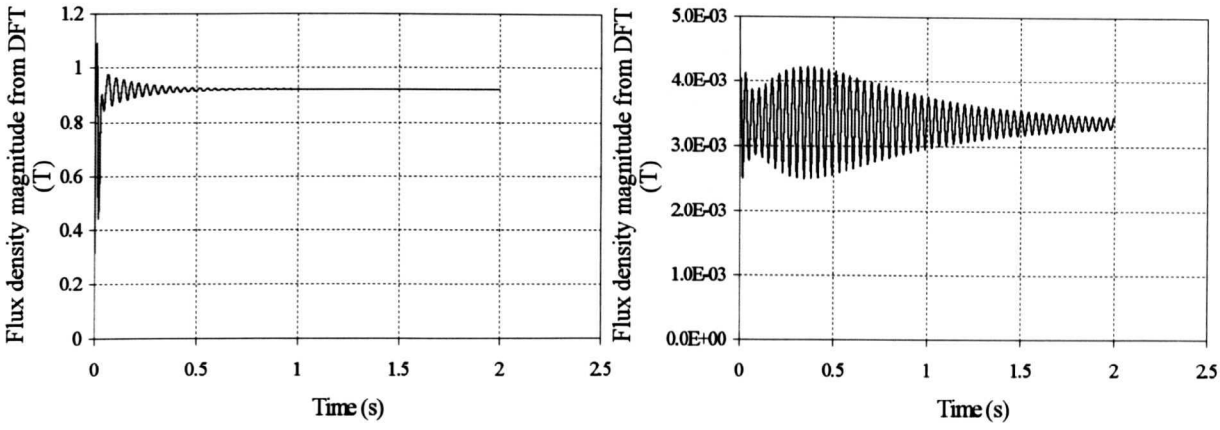

Figure 6.10: Peak magnitudes of (a) 4-pole and (b) 2-pole fields from DFT of stator-tooth-tip flux density samples.

	Using rotor-tooth-tip samples	Using stator-tooth-tip samples
Average magnitude of peak 2-pole field, $\left\|B_2^{DFT}\right\|$	1.6mT	3.4mT
Average magnitude of peak 4-pole field, $\left\|B_4^{DFT}\right\|$	0.91T	0.92T

Table 6.2: Summary of peak fundamental 4-pole and 2-pole field average magnitudes obtained from DFT.

By substituting the values of $\left|B_4^{DFT}\right|$ and $\left|B_2^{DFT}\right|$ obtained from the rotor-tooth-tip flux density samples for B_o^M and B_F^N, respectively in equation (6.2), the force obtained from the fundamental fields is 21.78N. This gives an error of 53.25% when compared to the force magnitude obtained from the simulation. Similarly, the force obtained from the fundamental fields is 46.86N when the values of $\left|B_4^{DFT}\right|$ and $\left|B_2^{DFT}\right|$ obtained from the stator-tooth-tip flux density samples is used in equation (6.2), which is comparable with the force magnitude shown in Figure 6.8.

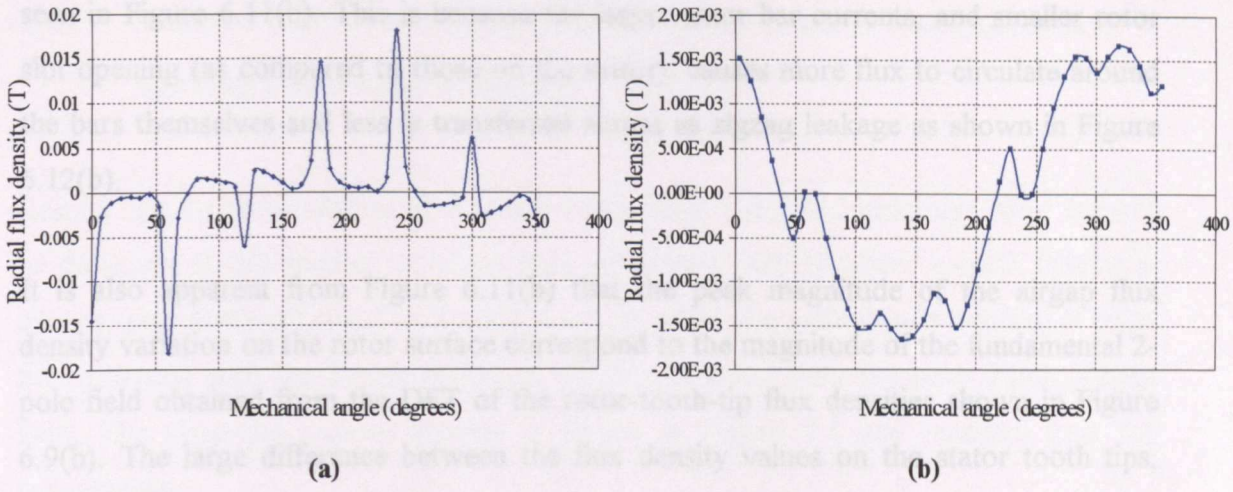

Figure 6.11: 2-pole airgap flux density variation around the circumference of the cage rotor IM at time 2s taken on (a) stator side and (b) rotor side.

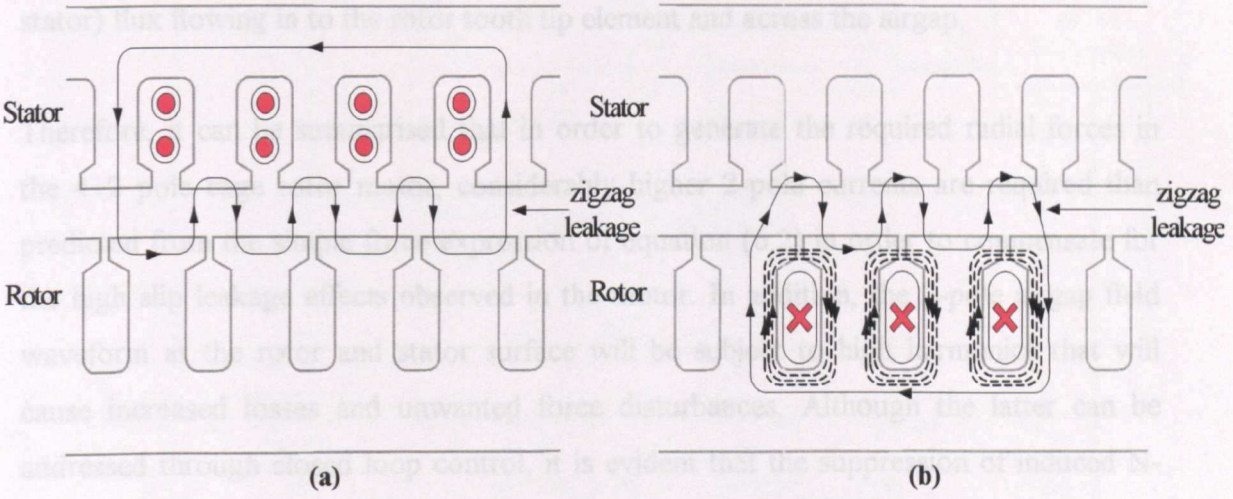

Figure 6.12: Leakage paths of the airgap flux in the 4+2 pole cage rotor IM on (a) stator side and (b) rotor side.

The reduction of the 2-pole airgap field observed in the cage rotor motor is thought to be due to relatively large leakage fluxes introduced by the large slip (25Hz at no load when connected to a 50Hz supply) experienced by the 2-pole field. This is clearly seen in Figure 6.11(a) showing the 2-pole airgap field variation (at the stator tooth surface) around the circumference with the 4-pole field de-activated and with a rotor speed of 1500rpm. The stator currents cause the flux from the stator to zigzag across the airgap and back into the stator tooth next to it, as illustrated in Figure 6.12(a). This causes the flux density to increase at certain stator tooth tips and decrease in others. At the surface of the rotor teeth however, the airgap field variation around the cage rotor circumference is more sinusoidal, although the effect of zigzag leakage is still present as

seen in Figure 6.11(b). This is because the larger rotor bar currents, and smaller rotor slot opening (as compared to those on the stator), causes more flux to circulate around the bars themselves and less is transferred across as zigzag leakage as shown in Figure 6.12(b).

It is also apparent from Figure 6.11(b) that the peak magnitude of the airgap flux density variation on the rotor surface correspond to the magnitude of the fundamental 2-pole field obtained from the DFT of the rotor-tooth-tip flux densities shown in Figure 6.9(b). The large difference between the flux density values on the stator tooth tips, compared to the rotor tooth tips at the cage surface, is due to the fact that the flux density variation is calculated on the tooth tip elements, and in the rotor most of the flux is diverted into the slot opening reluctance element with less (in comparison with the stator) flux flowing in to the rotor tooth tip element and across the airgap.

Therefore, it can be summarised that in order to generate the required radial forces in the 4+2 pole cage rotor motor, considerably higher 2-pole currents are required than predicted from the simple force expression of equation (6.2) in order to compensate for the high slip leakage effects observed in the motor. In addition, the 2-pole airgap field waveform at the rotor and stator surface will be subject to high harmonics that will cause increased losses and unwanted force disturbances. Although the latter can be addressed through closed loop control, it is evident that the suppression of induced N-pole currents, due to the N-pole levitation winding, in the rotor is possibly a desirable characteristic for radial force production that will be examined in Chapter 7.

Hitherto, the radial force is directed in an arbitrary direction. In order to control the direction in which the force is produced, the magnitude and phase of the 2-pole field must be controlled. Even though the DOL simulation has shown that the force produced in the cage rotor motor is affected by the high slip leakage and high harmonics of the 2-pole field, it is believed that the fundamental 2-pole field is sufficient to produce the required levitation force under vector control conditions.

6.4. Mixed Field Orientation (MFO) vector control simulation of a bearing relief cage rotor IM

Results of a DCM simulation of the vector controlled linear 4+2 pole cage rotor IM will be discussed in this section. A mixed field orientation (MFO) vector control scheme is chosen, previously proposed in Section 4.3.3, in which the main 4-pole winding is rotor field oriented with the 2-pole levitation winding oriented onto the peak 4-pole airgap field. The proposed control scheme is shown in Figure 4.4 and repeated here for convenience:

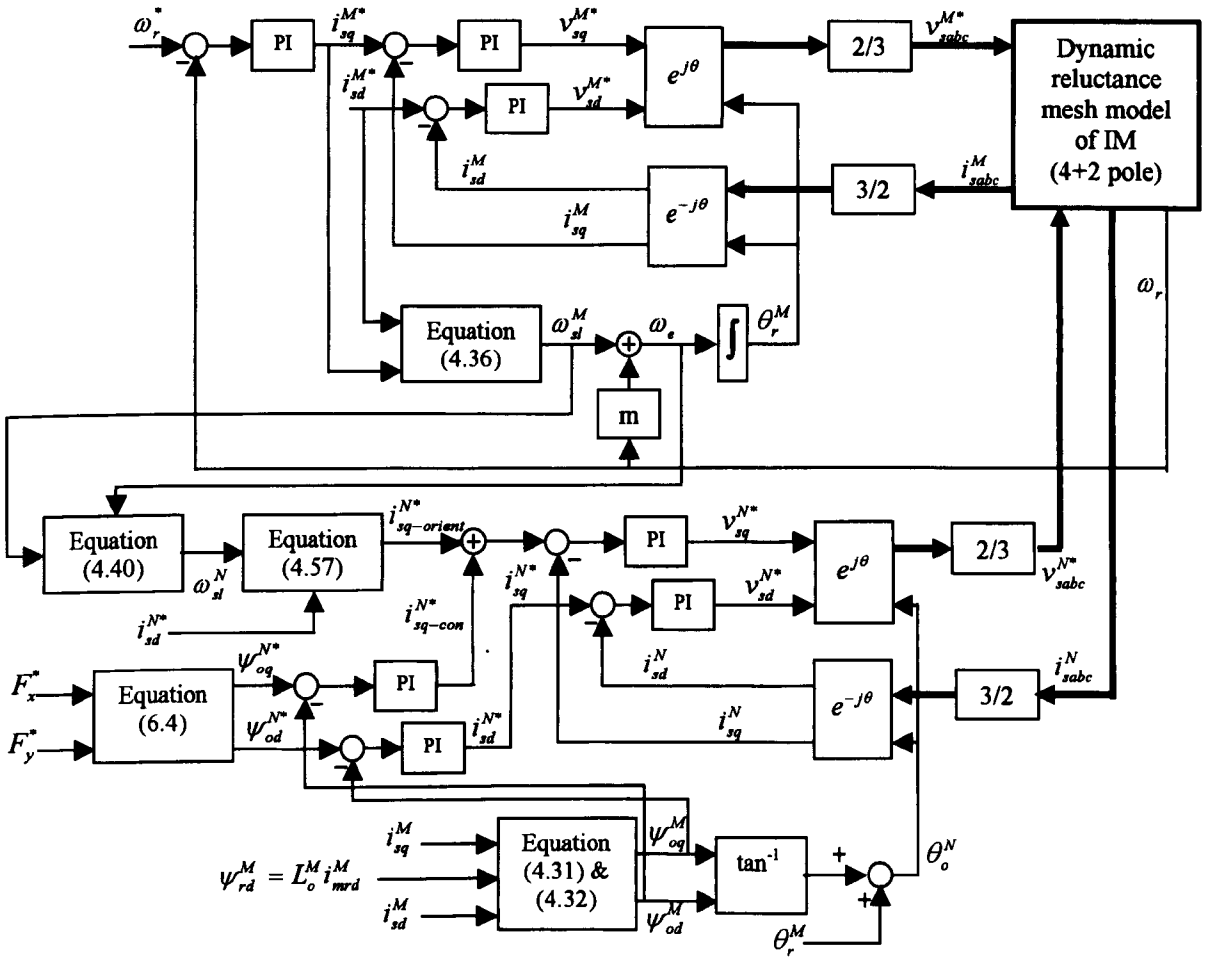

Figure 6.13: Mixed field orientation (MFO) vector control scheme for a bearingless cage rotor IM.

In the simulation, an external load having inertia equal to the motor inertia of 0.0713kgm^2 and a linear friction of $0.1T_{rated}$ at 1500 rpm is applied from the start. The current controllers for the 4 and 2-pole systems in this vector control scheme, designed in Chapter 5, both have a natural frequency of 400Hz and a damping factor of 0.8. The

speed controller, also designed in Chapter 5, has a natural frequency of 5Hz. As in Section 6.2, these controllers are then transformed into the discrete z-plane using the Bilinear transformation and implemented in the simulation with a sampling time of 100μs for the current control and 2ms for the speed control. The main 4-pole field is given time to establish by applying i_{sd}^{M*} of value 4.90A from the start of simulation. The 2-pole levitation winding current references i_{sd}^{N*} and i_{sq-con}^{N*}, responsible for controlling the forces F_y and F_x produced by the motor, are obtained from flux loop controllers previously designed in Chapter 5 with a natural frequency of 9Hz and damping factor of 0.8. In the DCM simulation, the flux linkage references ψ_{od}^{N*} and ψ_{oq}^{N*} are applied to the flux control loops at 2s and the values are obtained from equation (4.21) which is repeated here for convenience

$$\begin{bmatrix} \psi_{od}^{N*} \\ \psi_{oq}^{N*} \end{bmatrix} = \frac{2\sqrt{2}\mu_o k_{ws}^N N_{ts}^N}{\pi B_o^M n} \begin{bmatrix} F_y^* \\ F_x^* \end{bmatrix} \tag{6.4}$$

with the required forces F_y^* = 235.36N, i.e. equal to the rotor weight, and F_x^* = 0N. A speed reference of 1500rpm was given at 3s and a load of 89.55Nm, which is equal to 90% of the rated torque T_{rated}, was applied at 4s. The torque current is limited to 116% of the rated i_{sq}^M.

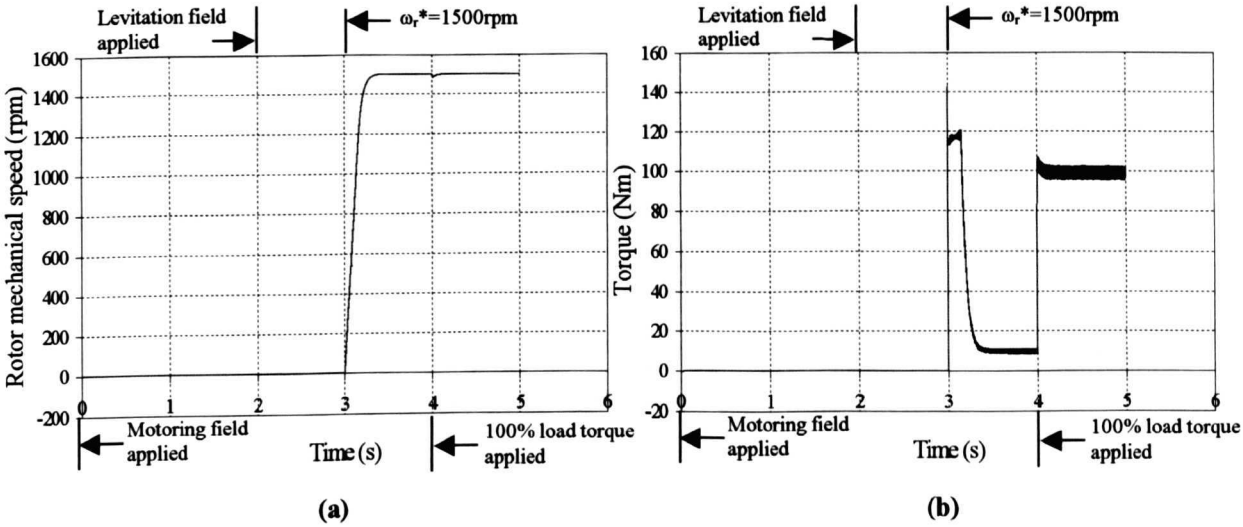

Figure 6.14: (a) speed and (b) torque variation with time of the vector controlled 4-pole cage rotor bearing relief IM.

Figure 6.14 illustrates the speed and torque variation of the simulated bearing relief induction motor. The motor is able to accelerate to the required speed of 1500rpm within 0.3s of applying the step change in speed. Under full load condition (i.e. from 4s onwards), the rotor experience a drop in speed to 1483rpm but this is restored by the speed controller within 0.1s. As the rotor speed reaches the required 1500rpm, a torque of approximately 9Nm develops, as expected, due to the 10% of rated torque friction applied.

The currents i_{sd}^{M} and i_{sq}^{M} of the main 4-pole winding as well as i_{sd}^{N} and i_{sq}^{N} of the 2-pole levitation winding are as shown in Figure 6.15. As seen in Figure 6.15(a), i_{sd}^{M} of the 4-pole motoring winding is maintained at its reference value of 4.90A throughout the simulation by the current controller. As expected, no q- axis current i_{sq}^{M} was available from 0 to 3s since rotor is still stationary. During rotor acceleration, the current reaches its limit of 15A before dropping to approximately 0.95A during steady state conditions. When the load torque is applied i_{sq}^{M} settles at 12.4A.

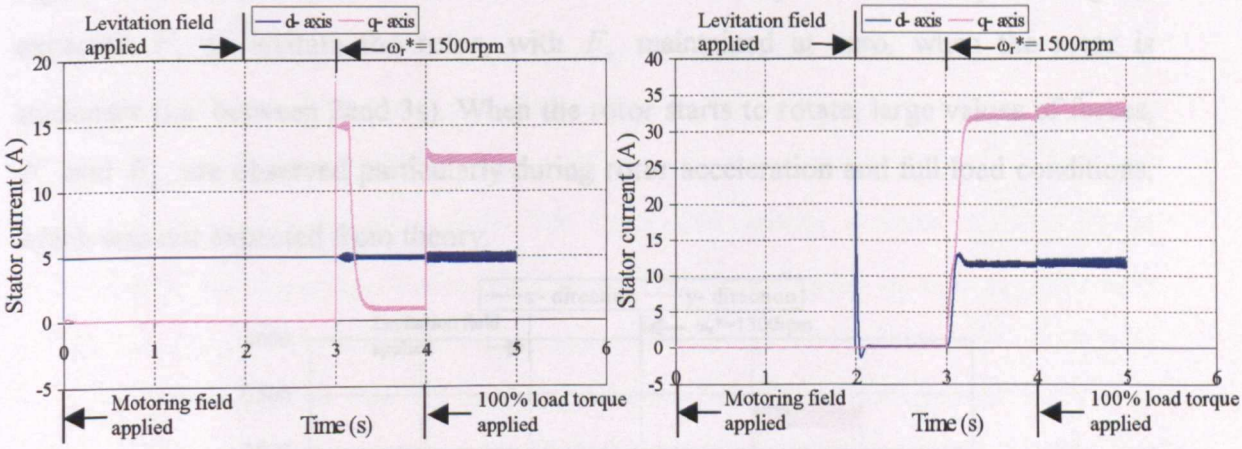

Figure 6.15: Stator current variation with time of the vector controlled 4-pole cage rotor bearing relief IM: (a) 4-pole winding (b) 2-pole winding.

The 2-pole levitation current i_{sq}^{N} obtained from the simulation, as shown in Figure 6.15(b), is maintained at zero when the rotor is stationary but increases to approximately

33A when the rotor is rotating and subjected to full load, which is expected. This is because i_{sq}^{N*}, applied to the 2-pole current control loop, is made up of two components

$$i_{sq}^{N*} = i_{sq-orient}^{N*} + i_{sq-con}^{N*} \tag{6.5}$$

in which $i_{sq-orient}^{N*}$ is the current responsible for maintaining the orientation between 2-pole field and the 4-pole field whereas i_{sq-con}^{N*} is responsible for creating F_x. In the simulation, i_{sq-con}^{N*} is zero at all times since F_x^* = 0N is demanded at all times by way of the ψ_{oq}^{N} control loop. However, $i_{sq-orient}^{N*}$ is very large since it is proportional to the slip frequency of the 2-pole field, which is very high (i.e. 25Hz in the motor of 50Hz supply frequency if 50Hz), as given by equation (4.57) and repeated here:

$$i_{sq-orient}^{N} = \frac{\omega_{sl}^{N} \cdot \left[\frac{L_r}{L_o} \psi_{od} - (L_r - L_o) i_{sd} \right]}{R_r + (L_r - L_o)s}$$

Figure 6.16 shows that the vector controlled motor is only successful in producing the expected F_y to levitate the rotor, with F_x maintained at zero, when the rotor is stationary (i.e. between 2and 3s). When the rotor starts to rotate, large values of forces, F_y and F_x, are observed particularly during rotor acceleration and full load conditions, which was not expected from theory.

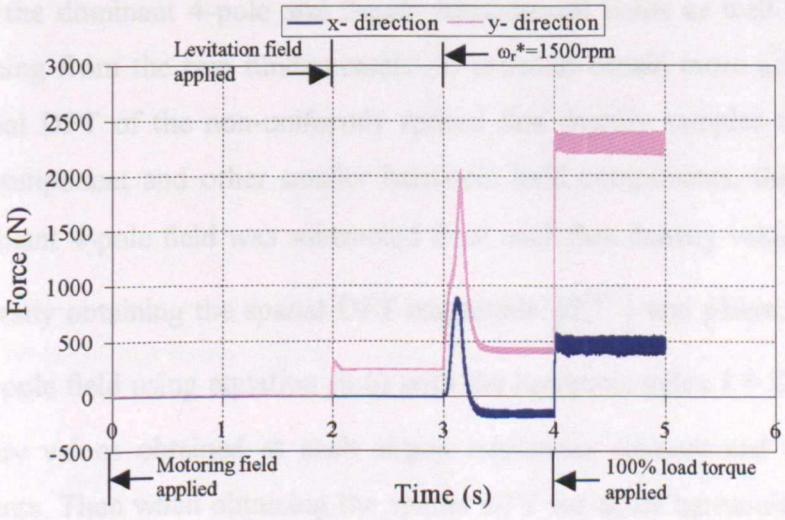

Figure 6.16: Vector controlled forces in the x- and y- direction produced by the cage rotor motor.

Even when the 2-pole levitation winding is 'directly' oriented (i.e. by using the actual peak 4-pole airgap field position, θ_o^{air} obtained from the spatial DFT of the non-uniformly spaced airgap reluctance elements flux density samples), the forces produced by the motor is similar to that shown in Figure 6.16. The spatial DFT on the flux densities of the non-uniformly spaced airgap reluctance elements is performed using equation (6.6)

$$X(k)=\frac{1}{\pi}\int_0^{2\pi} x_i(\cos k\theta_i + j\sin k\theta_i)\, d\theta \tag{6.6}$$

where x_i and θ_i are the flux density and mechanical angular position of each airgap reluctance element i respectively. The integration was carried out numerically in the DCM simulation using the trapezoidal rule. In the above equation, k represents the index for the DFT. When k = 2, the above equation will give the magnitude and electrical angular position θ_o^{air} of the peak 4-pole airgap flux density which is used in the 'direct' orientation of the 2-pole levitation winding.

In order to investigate the large force values obtained in the vector controlled bearing relief motor, the actual 4- and 2-pole field values in the DCM model is required. These field values are obtained by performing a DFT on the non-uniformly spaced airgap flux density samples using equation (6.6). The airgap flux density samples x_i, used in the DFT, contain the dominant 4-pole and 2-pole fundamental fields as well as other field harmonics arising from the two fundamentals. In order to obtain more accurate results from the spatial DFT of the non-uniformly spaced flux density samples for the 2-pole fundamental component and other smaller harmonic field components, the contribution from the dominant 4-pole field was subtracted from each flux density value x_i. This was achieved by firstly obtaining the spatial DFT magnitude $\left|B_4^{DFT}\right|$ and phase angle $\angle B_4^{DFT}$ of the peak 4-pole field using equation (6.6) with the harmonic index k = 2 and x_i being the flux density values obtained at each airgap reluctance element and containing all field components. Then when obtaining the spatial DFT for other harmonic index values ($k \neq 2$), the flux density values x_i' used in equation (6.6) are obtained from equation

(6.7) in which the 4-pole field component is subtracted from the original flux density values x_i as

$$x_i' = x_i - \left|B_4^{DFT}\right| \cos\left(2\theta_i - \angle B_4^{DFT}\right) \tag{6.7}$$

where θ_i is mechanical angular position of each airgap reluctance element i. This procedure is implemented every time the spatial DFT of the airgap reluctance element flux densities is applied to the uncontrolled or vector controlled 4+2 pole cage rotor motor. However, it has to be noted that the results from the spatial DFT of the non-uniformly spaced airgap elements for harmonic index values $k \neq 2$, are susceptible to numerical errors due to inaccuracies in equation (6.7). This is because any residual 4-pole field component present in x_i' will affect the magnitude and angle of the DFT results when $k \neq 2$.

Figure 6.17 shows the fundamental peak 4-pole and 2-pole fields obtain from the DFT of the non-uniformly spaced airgap flux density samples.

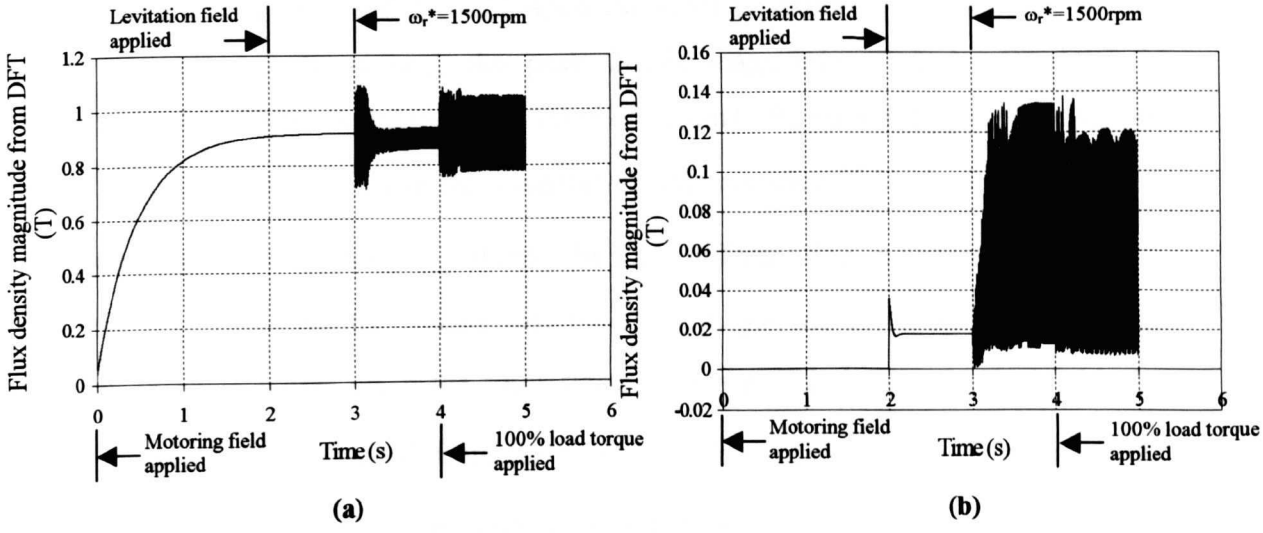

Figure 6.17: Peak fundamental magnitudes obtained from the DFT of airgap reluctance elements of the vector controlled linear cage rotor motor: (a) 4-pole field and (b) 2-pole field.

The average magnitudes of the peak fundamental 4-pole and 2-pole fields obtained from the DFT of the airgap flux densities in the vector controlled cage rotor motor during the time intervals 2-3s (when rotor is stationary), 3-4s (rotor is accelerating and reaches

steady state speed) and 4-5s (when full load torque is applied) are as summarised in Table 6.3.

	Average magnitude of peak 2-pole field, $\lvert B_2^{DFT} \rvert$	Average magnitude of peak 4-pole field, $\lvert B_4^{DFT} \rvert$	Fundamental force magnitude, $\lvert F_{2-4} \rvert$	Simulation force magnitude, $\lvert F \rvert = \sqrt{F_x^2 + F_y^2}$
2-3s	17.3mT	0.91T	237.46N	241.86N
3-4s	50.7mT	0.90T	684.47N	647.67N
4-5s	56.4mT	0.91T	771.25N	2333.6N

Table 6.3: Summary of peak fundamental 4-pole and 2-pole field average magnitudes obtained from DFT of airgap element flux densities.

The average magnitude of the peak 4-pole field are as expected, which is in the region of 0.9T. On the other hand, the peak 2-pole field magnitude obtained from the DFT is only similar to the expected 17.4mT when the rotor is stationary, between 2 and 3s. When the rotor is in motion, the peak 2-pole magnitude given by the DFT is approximately 3.08 times the expected value of 17.4mT. By substituting these values of $\lvert B_4^{DFT} \rvert$ and $\lvert B_2^{DFT} \rvert$ for B_o^M and B_F^N, respectively into equation (6.2), the forces obtained from the fundamental fields $\lvert F_{2-4} \rvert$ during the three different time instances are as shown in Table 6.3. These results indicate that the force magnitude given by the DFT force analysis $\lvert F_{2-4} \rvert$ increases when the rotor starts to rotate. This is in agreement with the force magnitude $\lvert F \rvert$ obtained from the virtual work principle of the airgap elements (shown in Figure 6.16). However, during rotor acceleration and under load, $\lvert F_{2-4} \rvert$ does not agree with the force $\lvert F \rvert$.

At this point the reason for the anomalies in the forces F_y and F_x observed during rotor rotation, as shown in Figure 6.16, are unknown and is a possible subject for future investigations into the study of bearing relief cage rotor induction motors.

6.5. Comparison with Simulink results

The results presented in the previous section can be compared with the results presented in Section 5.4.4 of a two-axis lumped parameter model simulation of the same MFO vector controlled bearing relief cage rotor motor carried out in MATLAB Simulink. Both the 4-pole currents i_{sd}^{M} and i_{sq}^{M} and the 2-pole currents i_{sd}^{N} and i_{sq}^{N} were found to be similar for both simulations, Simulink and DCM. This is shown in Figures 5.6(c), 5.12(a) and 6.15. As observed in Figure 5.15, the Simulink simulation shows that the vector controlled motor is able to produce successful levitation force to compensate for the rotor weight even when the rotor is rotating and subjected to full load. This is at variance to the results obtained from the DCM simulation, shown in Figure 6.16, in which it was found that the 235.36N levitation force is produced when the rotor is stationary but the force values increased when the rotor started to rotate. As presented previously, the fundamental force analysis carried out from the DCM simulation results shows agreement in the trend that the force in the motor will increase when the rotor is in rotation, which the two-axis lumped parameter model was unable to predict.

6.6. Chapter summary

This chapter presents an investigation of a linear 4+2 pole bearing relief cage rotor IM. The results of a DCM simulation of the motor under direct on-line start and MFO vector control conditions were discussed. From the direct on-line start simulation of the motor, it was found that the motor only produced a force magnitude of approximately 20% of the expected 235.36N. This reduction in force is felt to be due to zigzag leakages observed in the motor due to the high slip experienced by the 2-pole field. In order to generate the required radial forces in the motor, considerably higher 2-pole currents are required than predicted from the force expression of equation (6.2). This is in order to compensate for the high slip leakage effects present in the motor due to the large slip experienced by the 2-pole field (25Hz at no load when connected to a 50Hz supply). The possibility of reducing the high slip leakage effects through the suppression of induced N-pole currents in the rotor will be examined in Chapter 7. This will use a

wound rotor instead of a cage one. The variation in radial force produced by the motor compared to the reference force value due to the rotor inducing not only 4-pole but also 2-pole currents are in agreement with findings by Cai and Henneberger (2001) and Chiba *et al.* (1996). Both Cai and Henneberger (2001) and Chiba *et al.* (1996) suggest the use of a rotor that does not allow any levitation 2-pole rotor currents to flow in the bearingless induction motor.

In the vector controlled simulation of the cage rotor motor, it was observed that the motor only produces the predicted levitation force when the rotor was stationary. Once the rotor started to accelerate and rotate, the force produced was much higher. As explained in Section 6.4, the magnitude of force obtained from the simulation during rotor rotation was not explainable from the DFT analysis of the fields in the motor, even though the DFT force analysis showed that the force magnitude does increase when the rotor rotates. Further investigations into the reason for this force behaviour were not carried out in this thesis. It is a possible subject for future studies although it is not clear how a high quality (small) N-pole field can be obtained when high slip frequency N-pole currents are induced in the rotor. It is known that leakage effects of high slip rotor currents severely compromise the sinusoidal nature of the surface airgap field. It is for this reason that the remaining studies consider wound rotors where N-pole currents at high slip are not induced.

Chapter 7

Dynamic circuit modelling (DCM) of a bearing relief wound rotor induction motor

7.1. Introduction

The results presented in Chapter 6 showed that a vector controlled bearing relief cage rotor IM produces levitation forces that are consistent with theory when the rotor is stationary but further studies into the force behaviour during rotor rotation is required. Furthermore, the direct on-line start investigations of the cage rotor motor indicates that the reduction of high slip leakage effects occurring in the motor could be eliminated through the suppression of induced N-pole levitation currents in the rotor. Therefore, in this chapter, studies on a bearing relief motor with a wound rotor that suppress any N-pole rotor currents are presented. The 2-pole levitation winding required to create a bearingless 4+2 pole wound rotor IM is identical to that in the cage rotor type motor. The design of the PI controllers required for vector control was carried out in the Chapter 5. This enabled the vector control schemes proposed in Chapter 4 for the wound rotor type motor to be simulated using MATLAB Simulink, showing that the mixed field oriented vector control was the most suitable vector control scheme for this bearingless induction motor type. However, the MATLAB simulation was performed based on a simplified dq representation of the 4+2 pole wound rotor bearingless IM.

In this chapter, simulations of the same 4+2 pole wound rotor induction motor under bearing relief conditions carried out using the DCM technique, introduced in Chapter 2, are presented. In Section 7.4, the DCM simulation is performed on a linear iron type bearing relief motor. Non-linearity effects on the system performance are reported in

Section 7.5.2. A comparison between the DCM simulation results and the MATLAB Simulink simulation results is presented in Section 7.6.

Before the vector controlled simulation of the wound rotor bearingless motor is presented, this chapter will firstly present simulation results of a DCM modelled indirect rotor field oriented (IRFO) vector controlled 4-pole wound rotor induction motor without the presence of 2-pole levitation winding. An appraisal of the airgap flux vector position and orientation will also be presented as this vector position is crucial in the vector control scheme of the bearing relief wound rotor induction motor. It will be shown that an error of less than 5° between the controller airgap flux vector position and the actual machine airgap flux position can cause a significant F_x to be produced.

Secondly, an uncontrolled simulation of the linear iron 4+2 pole wound rotor induction motor will be discussed in Section 7.3. As the motor is uncontrolled, i.e. it is started directly on-line, the force produced will be acting in no particular direction. Hence, only the force magnitude will be of primary concern. The effects of non-linear iron on the direct on-line start of the 4+2 pole wound rotor motor will also be presented in Section 7.5.1. The iron non-linearity was found to introduce large harmonic forces which interfered with the fundamental force acting on the rotor when compared to that obtained using the linear iron. These harmonic forces were due to the interaction between other $M \pm N = 2$ pole combinations. Of these, the harmonic force from interaction of the third harmonic of the 2-pole field, which has a 6-pole variation, with the fundamental 4-pole field is large. Therefore, an uncontrolled simulation of a 4+6 pole wound rotor induction motor was also carried out in Section 7.5.3 as theoretically this pole combination of main and levitation winding would not create any harmonic fields capable of interacting with the 4-pole or 6-pole fundamental fields based on the $M \pm N = 2$ pole relationship.

7.2. Vector control of a wound rotor IM in DCM

A 4-pole wound rotor IM with only the 4-pole main winding is first simulated in DCM with an indirect rotor field orientation (IRFO) vector control scheme. In order to utilise the *s*-plane current and speed loop controllers (Section 5.4.1) in the DCM simulation,

the PI controllers are transformed into the discrete z-plane using the Bilinear Transform (Franklin *et al.*, 1998), $s = 2(z-1)/(t_{samp}(z+1))$. The sampling time is chosen such that the sampling frequency ratio (i.e. f_{samp} / controller bandwidth) exceeds 15. Therefore, the current loop sampling time t_{samp-i} was set to 100μs whereas the speed loop sampling time $t_{samp-\omega}$ was chosen to be 2ms.

In all the simulations of this chapter, a step speed reference ω_r^* of 1500rpm is applied to the speed control loop at 3s with a load torque equal to 90% of the rated torque T_{rated} (as listed in Table 5.1) given at 4s. An external load having inertia equal to the rotor inertia of 0.0713kgm^2 as well as a linear friction of $0.1T_{rated}$ at 1500 rpm is also applied throughout the simulation. The maximum simulation time step was set to 50μs with a Newton Raphson error tolerance set to 1x10^{-6} and a maximum of 15 iterations per time step. The linear equations solver error tolerance was set to 1x10^{-7} with a maximum of 200 iterations and a maximum threshold of 1x10^{-5}.

Figures 7.1 to 7.5 were obtained from the linear iron ($\mu_r = 1350$) DCM simulation of the IRFO vector controlled 4-pole wound rotor induction motor. As seen in Figure 7.1(a), the PI speed control produced a ramped response to the step speed reference of 1500rpm applied at 3s. The speed control was also able to maintain the speed at 1500rpm even after the load torque was applied at 4s. The corresponding torque variation is shown in Figure 7.1(b). As shown in the inset graph of Figure 7.1(b), the torque is observed to experience an oscillation of 300Hz from the moment the rotor starts to rotate (3s onwards). This oscillating frequency is equal to the main 4-pole stator winding phase belt passing frequency as observed by the rotating field in the motor. The term phase belt is the name given to the stator winding coil group and in the 4-pole motor there are 6 phase belts per pole pair since the main winding has 3 phases. Therefore, the 50Hz rotating field sees the 6 phase belts passing at 300Hz. This oscillating behaviour is also observed in all the vector control simulation results reported in this chapter (Sections 7.2 and 7.4). Therefore, when referring to the vector controlled quantities, the average value of the oscillating waveform is taken which is obtained by numerical integration. A similar oscillation, but at 900Hz, was observed in the vector control simulations of the cage rotor (Sections 6.2 and 6.4). However, unlike

the wound rotor, no possible explanation for the 900Hz could be found for the cage rotor motor.

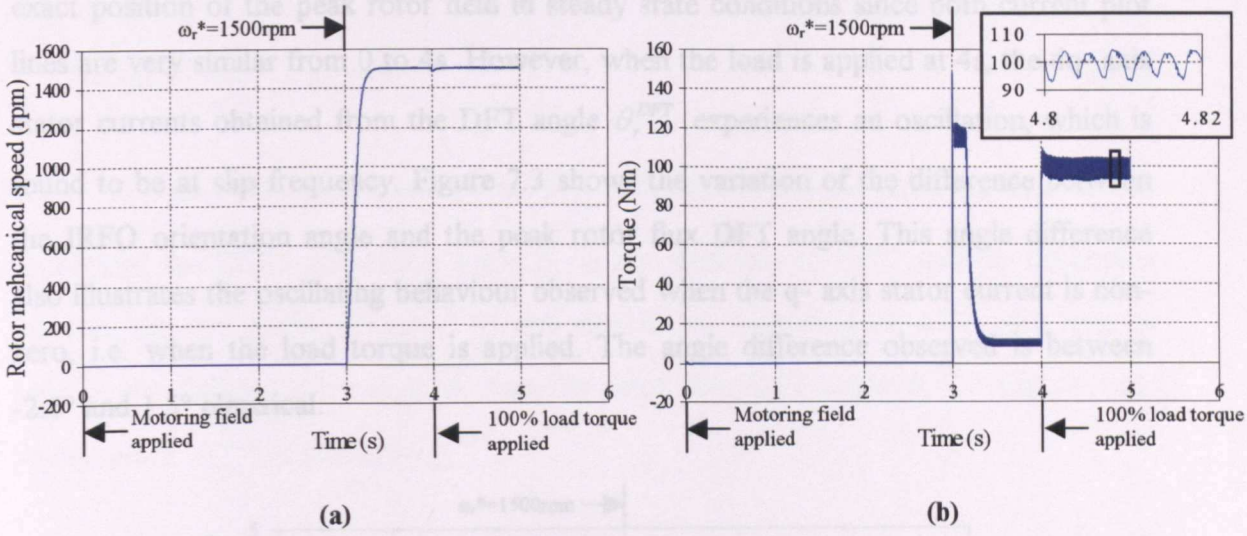

Figure 7.1: (a) speed and (b) torque variation of the IRFO vector controlled 4-pole wound rotor IM.

The currents i_{sd} and i_{sq} obtained from the simulation are shown in Figures 7.2(a) and (b). The darker set of lines in the current variations were obtained by transforming the αβ- axis stator currents using the controller IRFO orientation angle $\hat{\theta}_r$ whereas the currents plotted with the lighter set of lines use the angle of the peak rotor flux in the motor, θ_r^{DFT} ('direct' orientation). θ_r^{DFT} is found from a carrying out a spatial discrete Fourier transform (DFT) of the actual rotor flux flowing in each rotor tooth, using equation (6.1).

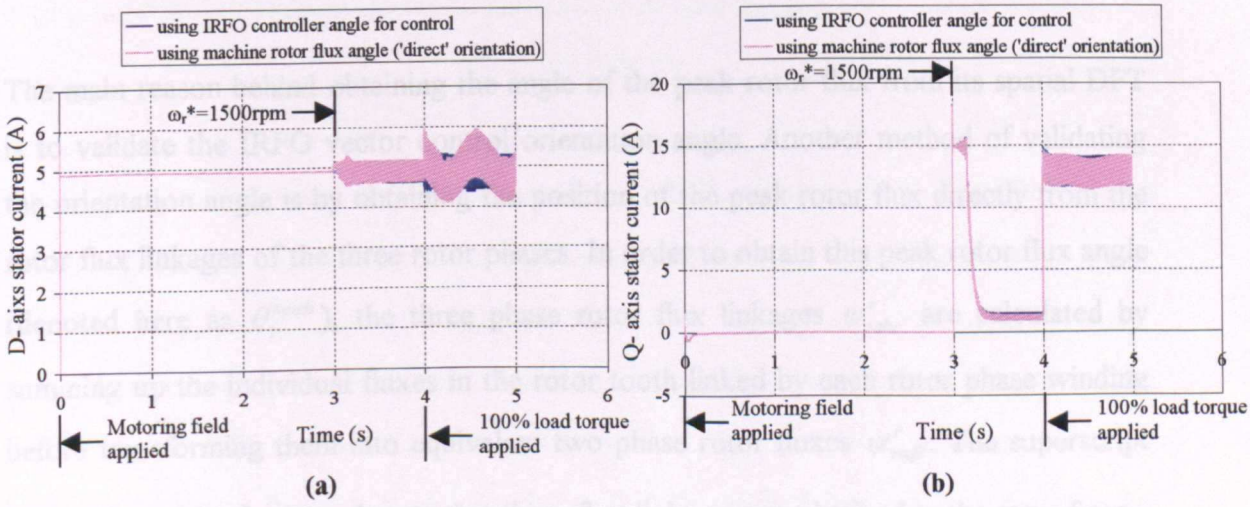

Figure 7.2: Stator current variation of the IRFO vector controlled 4-pole wound rotor IM: (a) d-axis (b) q- axis.

It is clearly seen from Figure 7.2 that the IRFO orientation angle is able to track the exact position of the peak rotor field in steady state conditions since both current plot lines are very similar from 0 to 4s. However, when the load is applied at 4s, the dq- axis stator currents obtained from the DFT angle θ_r^{DFT} experiences an oscillation, which is found to be at slip frequency. Figure 7.3 shows the variation of the difference between the IRFO orientation angle and the peak rotor flux DFT angle. This angle difference also illustrates the oscillating behaviour observed when the q- axis stator current is non-zero, i.e. when the load torque is applied. The angle difference observed is between -2.6° and 1.5° electrical.

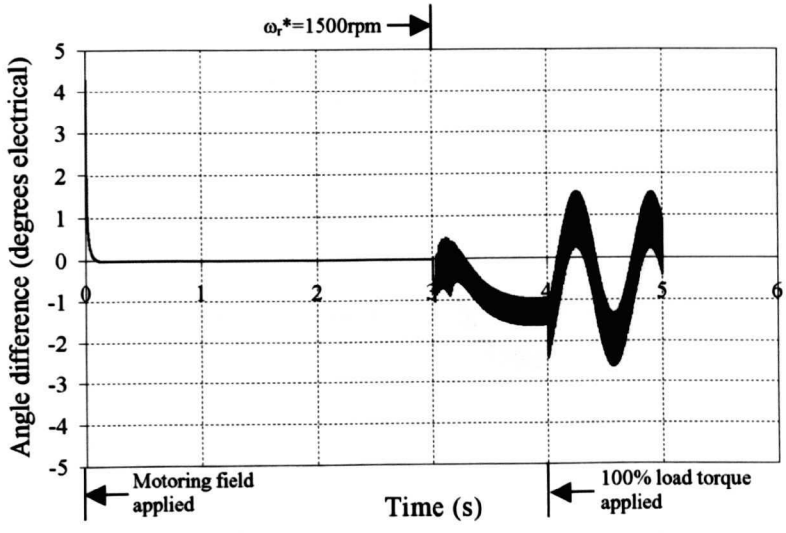

Figure 7.3: Difference between the IRFO angle and peak rotor flux angle θ_r^{DFT} obtained from DFT.

The main reason behind obtaining the angle of the peak rotor flux from its spatial DFT is to validate the IRFO vector control orientation angle. Another method of validating the orientation angle is by obtaining the position of the peak rotor flux directly from the rotor flux linkages of the three rotor phases. In order to obtain this peak rotor flux angle (denoted here as θ_r^{mach}), the three phase rotor flux linkages ψ_{rabc}^r are calculated by summing up the individual fluxes in the rotor tooth linked by each rotor phase winding before transforming them into equivalent two phase rotor fluxes $\psi_{r\alpha\beta}^r$. The superscript 'r' in ψ_{rabc}^r and $\psi_{r\alpha\beta}^r$ is to denote that these flux linkages are obtained in the rotor frame,

which is rotating with an electrical speed ω_r. Therefore, the peak rotor flux angle is given by

$$\theta_r^{mach} = \tan^{-1}\left(\frac{\psi^r_{r\beta}}{\psi^r_{r\alpha}}\right) + \omega_r + \gamma \tag{7.1}$$

where γ is an offset angle between the first stator tooth and the reference axis. It was found that the IRFO orientation angle $\hat{\theta}_r$ is also different to θ_r^{mach} and the difference between the two angles (Figure 7.4) also exhibits an oscillating variation with time as seen in the difference between $\hat{\theta}_r$ and the rotor flux DFT angle θ_r^{DFT} (Figure 7.3). Furthermore, θ_r^{mach} is similar to θ_r^{DFT}.

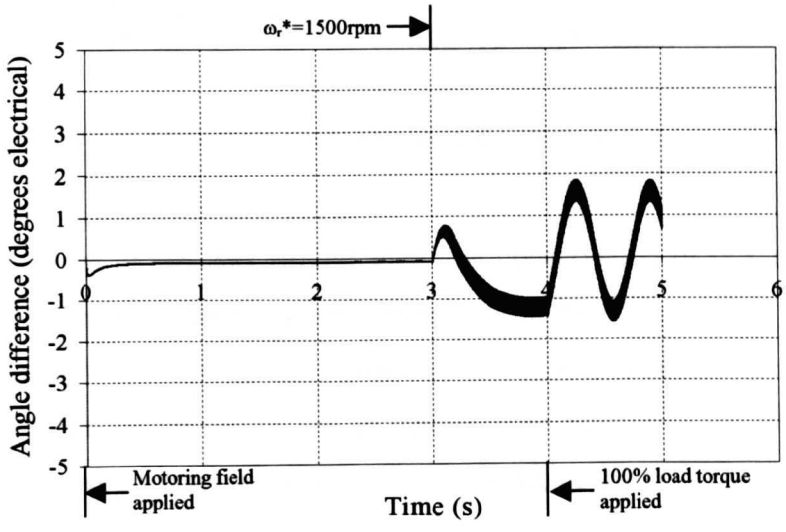

Figure 7.4: Difference between the IRFO angle and peak rotor flux angle θ_r^{mach} obtained from rotor phase flux linkages.

It was found that the oscillations in the angles of θ_r^{mach}, obtained from equation (7.1), is due to DC offsets observed in all the three phases of the rotor flux linkages ψ^r_{rabc} when load was applied to the motor as shown in Figure 7.5. The offsets in the individual rotor phase flux linkages were found to be due to residual flux present at each node in the DCM model. θ_r^{DFT} is also affected by the residual flux since it is obtained from the DFT of the fluxes flowing in each rotor tooth. The residual flux on each node in the model arises from the fact that the model solves for conservation of rate of change of

flux equation on each node. This means that any constant flux present at any node will not be dissipated, which in turn gives rise to the offsets in the flux linkages observed when the fluxes are added up.

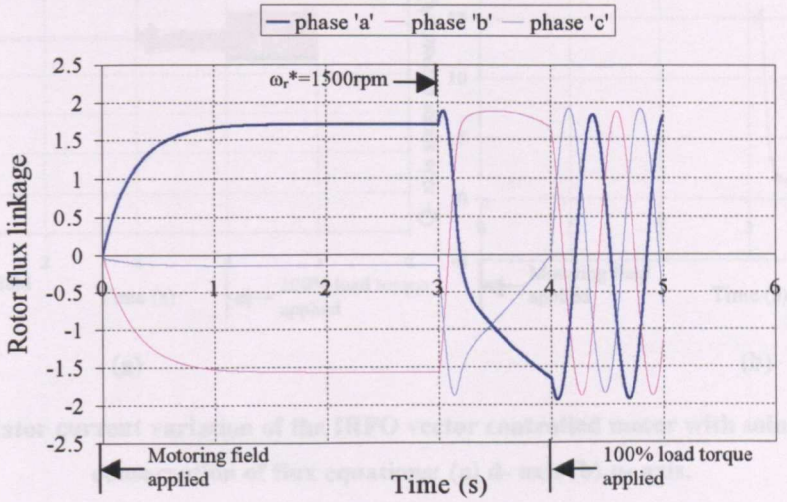

Figure 7.5: Rotor three phase flux linkage variations in rotor frame.

Therefore, the DCM model was altered such that conservation of flux equation (given by equation (2.8)) at each node is solved instead of equations for rate of change of flux. This ensures that no constant flux exists in any node. The changes required for enforcing nodal flux conservation are as described in Section 2.5(b). Henceforth, all simulations are based on flux conservation on each node of the DCM model.

For this reason, the rotor flux oriented vector control of the wound rotor induction motor was repeated with the model solving for conservation of flux equation at each node. Without any change to the mechanical equations, the speed and torque variation against time were found to be similar to those obtained previously when solving for conservation of rate of change of flux equation at each node. However, the dq- axis stator currents in the motor obtained from $\hat{\theta}_r$, represented by the darker set of lines, and θ_r^{DFT}, represented by the lighter set of lines, are now in agreement as seen in Figure 7.6. The error between the two angles, shown in Figure 7.7, was also found to be less than 0.93° electrical on average, which is acceptable. However, this error can be reduced further by altering the rotor time constant $\tau_r = L_r^M / R_r^M$.

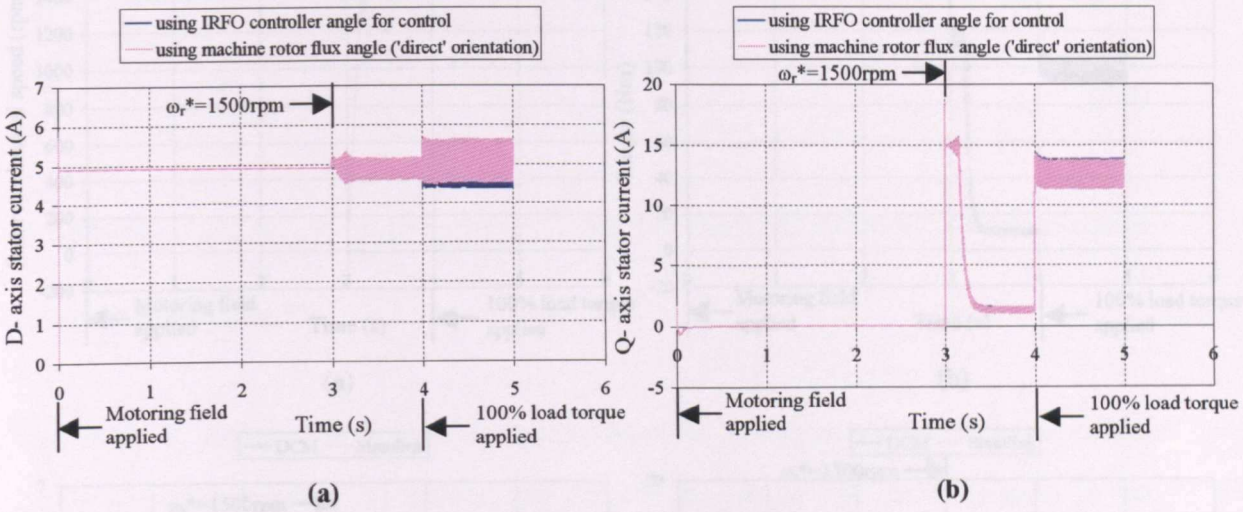

Figure 7.6: Stator current variation of the IRFO vector controlled motor with solution based on conservation of flux equations: (a) d- axis (b) q- axis.

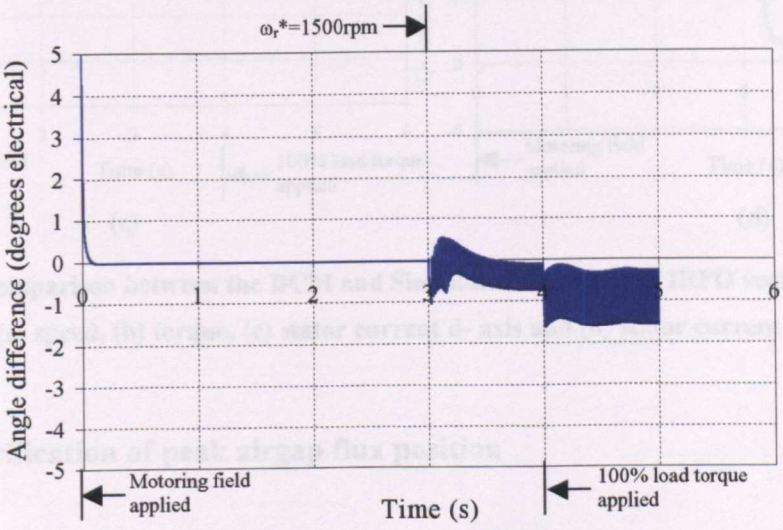

Figure 7.7: Difference between the IRFO angle and peak rotor flux angle obtained from DFT with solution based on conservation of flux equations.

These results were then compared with the results obtained from a Simulink simulation of the same IRFO vector controlled 4-pole wound rotor induction motor. It is observed that the speed, torque and dq- axis stator current variations exhibits very close agreement between the two simulation methods as indicated by Figures 7.8(a)-(d).

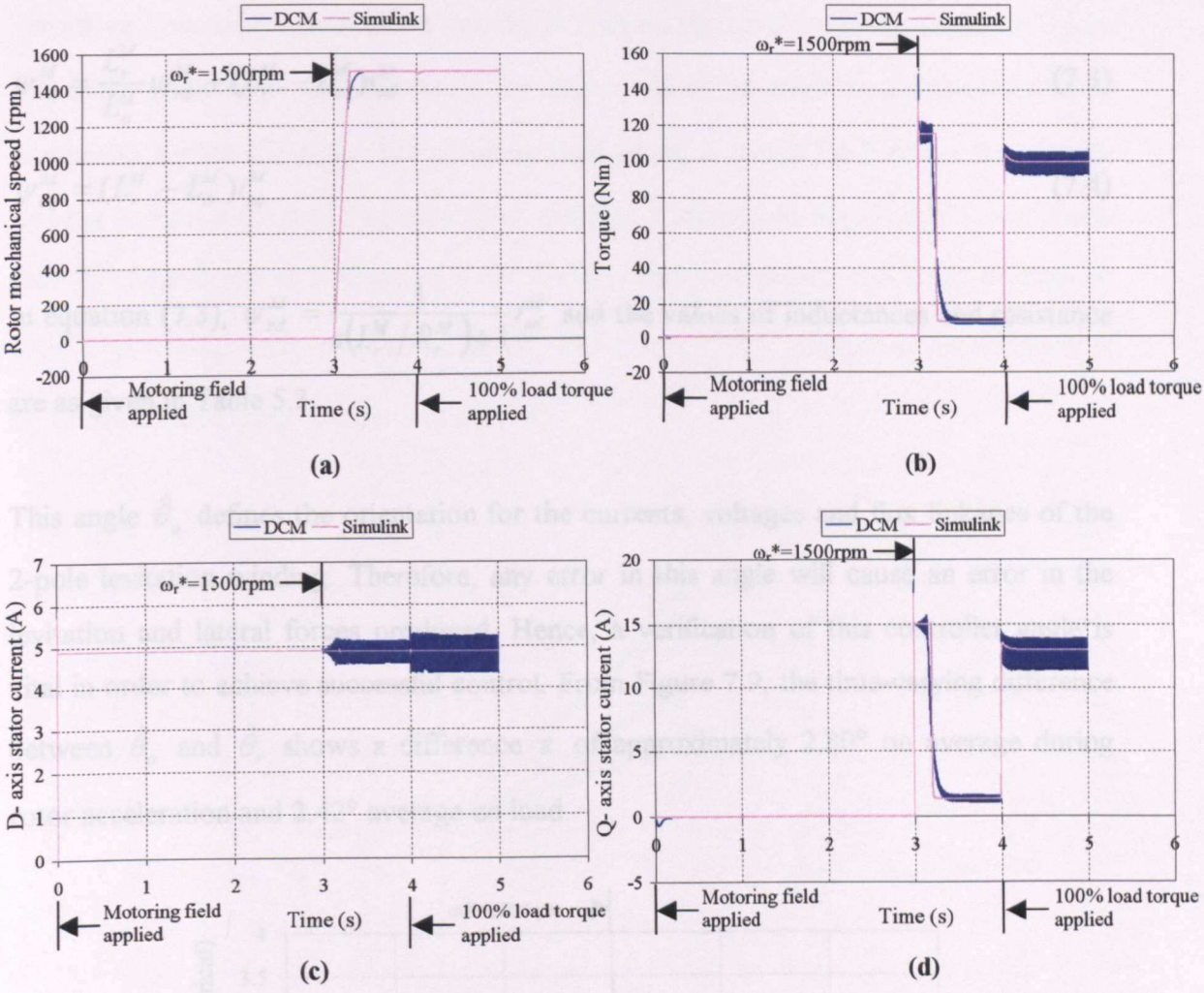

Figure 7.8: Comparison between the DCM and Simulink simulations of IRFO vector controlled motor: (a) speed, (b) torque, (c) stator current d- axis and (d) stator current q- axis.

7.2.1. Verification of peak airgap flux position

The position of the peak 4-pole airgap flux is crucial in the mixed field orientation (MFO) vector control scheme proposed for the bearingless wound rotor IM. In the MFO vector control scheme, the position of the controller peak 4-pole airgap flux $\hat{\theta}_o$ is obtained indirectly from the controller peak rotor flux angle $\hat{\theta}_r$ and the flux linkages ψ_{od}^M and ψ_{oq}^M (defined in the rotor flux frame) as given by:

$$\hat{\theta}_o = \hat{\theta}_r + tan^{-1}\left(\frac{\psi_{oq}^M}{\psi_{od}^M}\right) = \hat{\theta}_r + \varepsilon \tag{7.2}$$

where

$$\psi_{od}^{M} = \frac{L_r^M}{L_o^M}\psi_{rd}^{M} + (L_r^M - L_o^M)i_{sd}^{M} \tag{7.3}$$

$$\psi_{oq}^{M} = (L_r^M - L_o^M)i_{sq}^{M} \tag{7.4}$$

In equation (7.3), $\psi_{rd}^{M} = \frac{1}{s(L_r^M / R_r^M)+1} i_{sd}^{M}$ and the values of inductances and resistance are as given in Table 5.3.

This angle $\hat{\theta}_o$ defines the orientation for the currents, voltages and flux linkages of the 2-pole levitation winding. Therefore, any error in this angle will cause an error in the levitation and lateral forces produced. Hence, a verification of this controller angle is vital in order to achieve successful control. From Figure 7.9, the time-varying difference between $\hat{\theta}_o$ and $\hat{\theta}_r$ shows a difference ε of approximately 2.80° on average during rotor acceleration and 2.42° average on load.

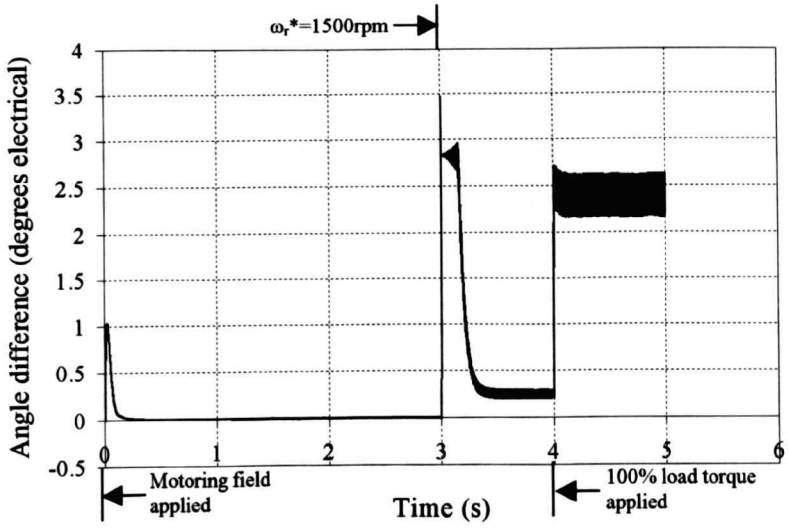

Figure 7.9: Difference between the controller peak airgap flux angle $\hat{\theta}_o$ and controller peak rotor flux angle $\hat{\theta}_r$.

In the previous section, the IRFO orientation angle $\hat{\theta}_r$ was verified by comparing it with the angle θ_r^{DFT} obtained from performing a spatial discrete Fourier transform (DFT) of the flux density flowing in each inner rotor tooth reluctance element.

Therefore, assuming that the flux density flowing in the rotor tooth-tip (refer to Figure 6.3) is the same as the flux density in the airgap, use of the angle $\hat{\theta}_o$ can be justified by comparing it with the angle θ_o^{tip} given by performing a spatial DFT of the flux density flowing in each rotor tooth tip reluctance element. Referring to Figure 7.10 it was found that θ_o^{tip} lags $\hat{\theta}_o$ by an average of 2.47° during rotor acceleration and 1.45° average on load. This implies that θ_o^{tip} is closer to $\hat{\theta}_r$, with ($\hat{\theta}_r = \theta_r^{DFT}$). Therefore, the accuracy of $\hat{\theta}_o$ is not verified from comparison with θ_o^{tip}.

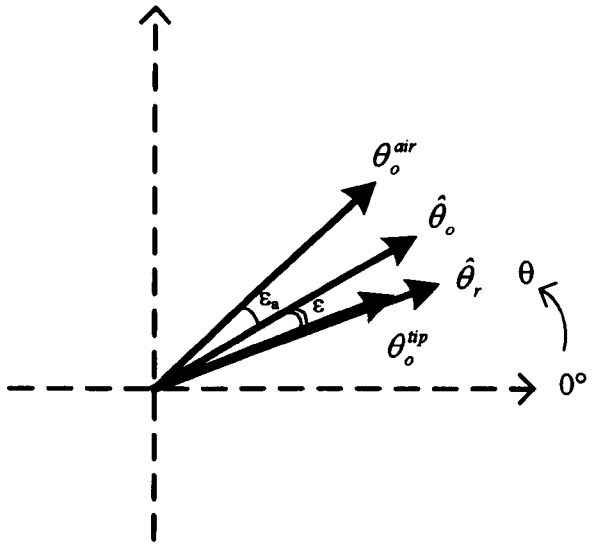

Figure 7.10: Graphical representation of the peak rotor and peak airgap flux positions obtained from controller and DFT of flux densities in the rotor tooth-tip and airgap reluctance elements.

Alternatively, one can verify $\hat{\theta}_o$ by carrying out the spatial DFT on the flux densities in the actual airgap reluctance elements. This is denoted as θ_o^{air}. However, due to the fact that the airgap elements are non-uniformly spaced around the airgap circumference, a non-uniform spatial direct Fourier transform (DFT) was utilized. Equation (6.6) was used to perform the non-uniform spatial DFT, which is repeated here:

$$X(k) = \frac{1}{\pi} \int_0^{2\pi} x_i (\cos k\theta_i + j \sin k\theta_i)\, d\theta \tag{7.6}$$

where x_i and θ_i are the flux density and mechanical angular position of each airgap reluctance element i respectively. When k = 2, the above equation will give the magnitude and electrical angular position θ_o^{air} of the peak 4-pole airgap flux density in

the 4-pole wound rotor motor. It is expected that this angle will be used to verify the controller angle $\hat{\theta}_o$. From the simulation, it was found that θ_o^{air} leads $\hat{\theta}_o$ by approximately ε_a = 4° during rotor acceleration and ε_a = 4.15° on load.

Hence, there exists a difference between θ_o^{air} and $\hat{\theta}_o$. However, this difference decreased to approximately 0° when the simulation was repeated with the controller value of $l_r^{M'}$, the equivalent circuit's referred rotor leakage inductance, increased to approximately 3 times its original value of 4.37mH and the mutual inductance L_o^M maintained at 235.36mH. This result indicates that the controller angle $\hat{\theta}_o$ obtained using equation (7.3) could not accurately predict the actual position of the peak airgap flux when using the equivalent circuit parameters of the motor derived in Chapter 5. This could be due to the assumption of equal leakage reactance split on the stator and rotor side used in the equivalent circuit parameter calculations of the 4-pole winding based on the no load and locked rotor tests. Furthermore, the mesh employed to model the stator and rotor teeth used in the parameter derivation tests can be considered to be crude since it only has 1 slot leakage element modelling only the slot tip leakages. In order to obtain much better results from the locked rotor test, which determines the leakage inductances in the motor, more slot leakage elements would have to be included across the middle of the stator and rotor slots as shown in Figure 7.11.

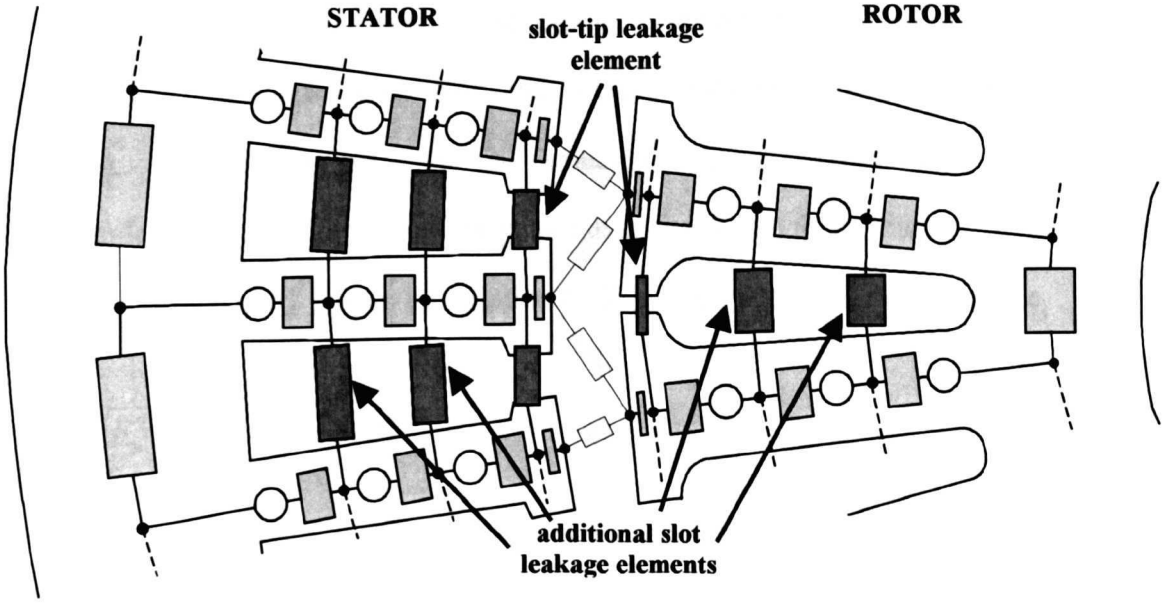

Figure 7.11: Possible improvements to the reluctance mesh model for better slot leakage modelling.

7.3. Simulation of radial forces

This section discusses an uncontrolled DCM simulation of normal forces produced by the bearing relief wound rotor IM. This simulation is comparable to that performed for the cage motor in Section 6.3 since the stator for both motors consists of a 4-pole main winding as well as an additional 2-pole levitation winding on the stator. The only exception is the 4-pole wound rotor replacing the cage rotor of Section 6.3. In the DCM model, all reluctance elements were chosen to be of type 'linear iron' having a $\mu_r = 1350$ with the exception of the slot tip leakage elements, which were chosen to be of type 'air', due to the semi-closed slots on both stator and rotor side. The motor was modelled with only one rotor axial skew section with a skew angle of 15° electrical.

As the motor is uncontrolled, the terminals of both stator windings are directly connected to sinusoidally varying voltage sources. A 415V rms voltage was applied to the 4-pole main windings. Similar to the cage rotor simulation, the applied voltage of the 2-pole levitation winding is determined from (refer equation (4.12)):

$$V_{rms}^N \approx E_{rms}^N = \frac{2\pi f}{\sqrt{2}} k_{ws}^N N_{ts}^N \frac{B_F^N 2rL}{N} \tag{7.7}$$

where f =50 Hz and the values of the 2-pole winding factor k_{ws}^N and total series turn N_{ts}^N are given in Table 5.4(a). However, a value of the peak field due to the levitation winding, B_F^N, is required. This is evaluated from the relationship between the magnitude of required force and the peak fields due to the main winding, B_o^M, and the levitation winding, B_F^N, given by equation (3.27), repeated here for convenience,

$$|F| = \sqrt{F_y^2 + F_x^2} = \frac{rL\pi B_o^M}{2\mu_0} B_F^N \tag{7.8}$$

From the vector control simulation of the 4-pole induction machine carried out in the previous section, the peak of the main 4-pole field B_o^M was found to be 0.9T. To produce a force magnitude of 235.36N, to compensate for the rotor weight, a peak

2-pole flux density B_F^N of 17.4mT is needed. Hence, by substituting B_F^N of 17.4mT into equation (7.7), a terminal voltage of 4.20V rms is required for the 2-pole levitation winding, which is exactly the same as that applied for the cage type motor. As with the cage rotor motor simulation, a load torque equal to the motor rated torque of 99.5Nm was also applied after 1s of the simulation.

Figure 7.12 shows the force magnitude obtained from the direct on-line simulation of the wound rotor IM. It is observed that in steady state at no load, the motor produces a radial force magnitude of 235.97N, which is 0.26% more than expected. When the load is applied, the force magnitude drops to 228.77N which is 3.1% of the no load force acting on the rotor. This is due to the fields in the motor not being kept constant.

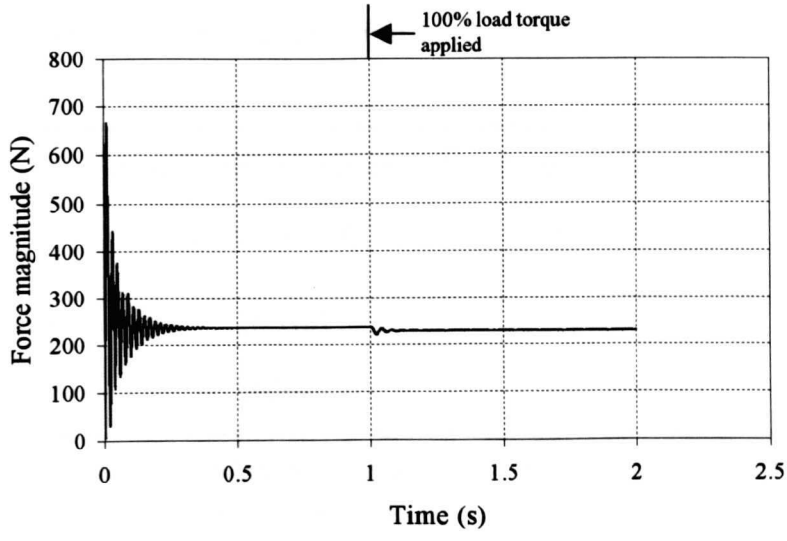

Figure 7.12: Force magnitude obtained from a direct on-line start of a bearing relief wound rotor induction motor.

In order to verify the force magnitude obtained from the simulation, the actual peak 4- and 2-pole field values are evaluated by performing a spatial discrete Fourier transform (DFT) on the flux densities of the non-uniformly spaced airgap reluctance elements around the rotor circumference using equation (7.6). As mentioned in Section 6.4, in order to obtain more accurate results from the spatial DFT of the non-uniformly spaced flux density samples for the 2-pole fundamental component and other smaller harmonic field components ($k \neq 2$ in equation (7.6)), the contribution of the dominant 4-pole field in each flux density sample x_i was subtracted to obtain x_i' using the following equation:

$$x_i' = x_i - \left|B_4^{DFT}\right| \cos\left(2\theta_i - \angle B_4^{DFT}\right) \tag{7.9}$$

where $\left|B_4^{DFT}\right|$ and $\angle B_4^{DFT}$ are the magnitude and phase angle of the dominant 4-pole field, obtained from equation (7.6) when $k = 2$, and θ_i is mechanical angular position of each airgap reluctance element i. This procedure is implemented every time the spatial DFT of the airgap reluctance element flux densities is applied to the uncontrolled or vector controlled 4+2 pole wound rotor motor. However, it has to be noted that the results from the spatial DFT of the non-uniformly spaced airgap elements for harmonic index values $k \neq 2$, are susceptible to numerical errors due to inaccuracies in equation (7.9). This is because any residual 4-pole field component present in x_i' will affect the magnitude and angle of the DFT results when $k \neq 2$.

	Average magnitude of peak 2-pole field, $\left\|B_2^{DFT}\right\|$	Average magnitude of peak 4-pole field, $\left\|B_4^{DFT}\right\|$
No load	16.1mT	0.91T
Full load	14.2mT	0.92T

Table 7.1: Summary of peak fundamental 4-pole and 2-pole field average magnitudes obtained from DFT of airgap element flux densities.

Figure 7.13 shows the magnitude of the peak fundamental 4-pole and 2-pole fields in the motor, obtained from the spatial DFT of the airgap reluctance element flux density samples. The average magnitudes of the peak fundamental fields under no load and full load conditions are as summarised in Table 7.1. The average magnitude of the peak 4-pole field are, as expected, in the region of 0.9T. On the other hand, at no load, the peak 2-pole field magnitude is 7.5% less than the expected 17.4mT. By substituting these values of $\left|B_4^{DFT}\right|$ and $\left|B_2^{DFT}\right|$ for B_o^M and B_F^N, respectively into equation (7.8), the force obtained from the fundamental fields during no load and full load conditions can be calculated as 219.12N and 195.25N respectively which corresponds to a difference of 7.3% and 14.7% from the force obtained from the simulation. These differences in

force magnitude could be due to numerical errors associated with the non-uniform DFT results for the peak 2-pole filed magnitude mentioned above. Even so, these results indicate that the forces obtained from the DFT peak magnitudes are in broad agreement with the force obtained from the virtual work principle of the airgap elements.

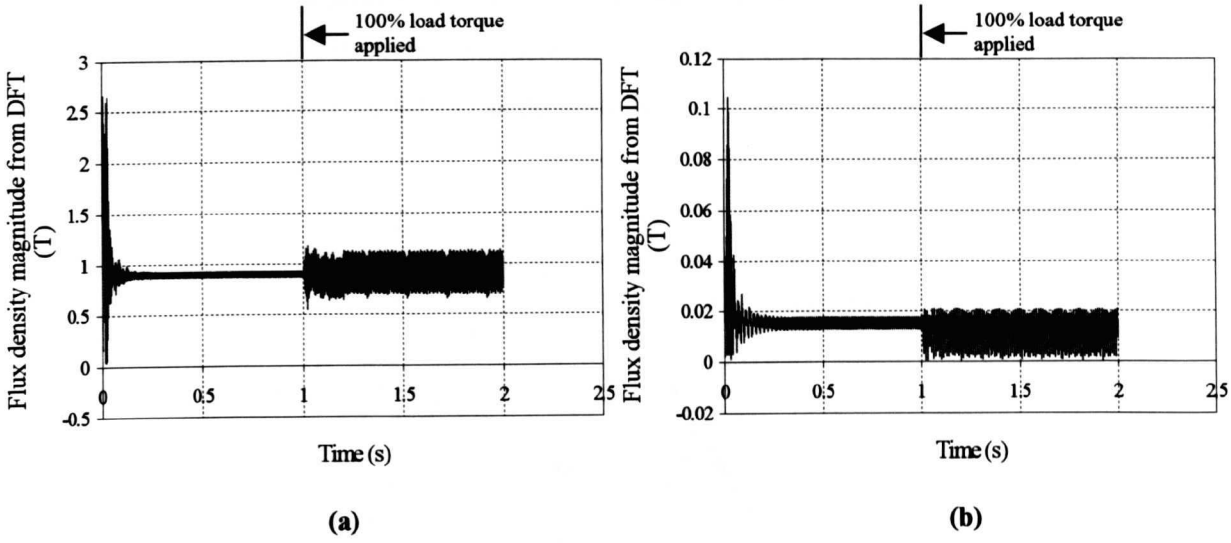

Figure 7.13: Magnitude of the fundamental fields of the wound rotor bearing relief induction motor at direct on-line start: (a) 4-pole and (b) 2-pole.

The results indicate that the wound rotor bearing relief IM produces the constant force magnitude of 235.36N required to levitate the rotor in comparison to the 46.59N force obtained from the cage rotor motor shown in Figure 6.8. As discussed in Section 6.3, the cage rotor was unable to generate the required radial forces due to the high slip leakage effects introduced in the rotor by the 2-pole field which meant that considerably higher 2-pole currents are required than predicted from the simple force expressions of equation (7.8). In addition, the 2-pole airgap field waveform at the cage rotor surface will be subject to high harmonics that will cause increased losses and unwanted force disturbances. However, in the 4-pole wound rotor motor, the induced 2-pole rotor current is suppressed. Therefore, the wound rotor does not exhibit any high slip leakage effects as observed in the cage rotor type motor. This is evident in the 2-pole airgap flux density variation around the circumference of the wound rotor motor as calculated at the tooth-tips on the stator and rotor shown in Figure 7.14. This was obtained using the same method as that for the squirrel cage machine, that is by running the direct on-line simulation at steady state and deactivating the 4-pole field by setting the main stator winding stator phase resistance to be very large. Figure 7.14 clearly illustrates that the

airgap flux density in the wound rotor machine is sinusoidal in shape and does not exhibit the zigzag leakage effects seen in the squirrel cage machine (Figure 6.11). The peak magnitude also corresponds with the magnitude of the fundamental 2-pole field of Figure 7.13(b). The reason for these good waveforms is that the wound rotor machine has no 2-pole induced currents flowing at large slips. Therefore, the suppression of the 2-pole rotor current is a desirable characteristic for radial force production and thus the wound rotor was selected for further control studies.

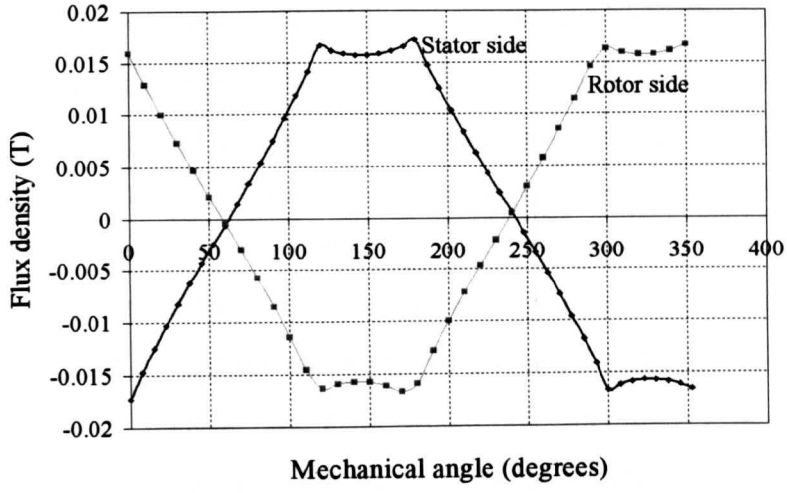

Figure 7.14: 2-pole airgap flux density distribution around the circumference of the wound rotor motor at time 0.8s taken on the stator and rotor side.

Hitherto, the radial force is directed in an arbitrary direction. In order to control the direction in which the force is produced, the peak magnitude and phase of the 2-pole field B_F^N must to be controlled such that it is aligned with the peak of the main 4-pole field B_o^M. This is achieved through a vector control scheme, which was previously designed for a bearing relief wound rotor induction machine in Section 4.4. Even though three vector control schemes were proposed for the wound rotor bearingless induction motor, the mixed field orientation (MFO) vector control scheme was chosen, as summarised in Chapter 5, due to its simpler main winding control and airgap field oriented vector control of the levitation winding which was able to produce the required levitation force as observed from the MATLAB Simulink simulation results presented in Section 5.4.4.

7.4. Mixed field orientation (MFO) vector control simulation

In this section, a DCM simulation of a vector controlled linear 4+2 pole wound rotor induction motor with short-circuited 4-pole wound rotor will be presented. The vector control scheme considered is a mixed field orientation (MFO) scheme, in which the main 4-pole winding is rotor field oriented whereas the 2-pole levitation winding is oriented onto the 4-pole airgap field, previously proposed in Section 4.4 for motors with levitation N-pole rotor current suppression (refer to Figure 4.7). An external load having inertia equal to the motor inertia of 0.0713kgm^2 as well as a linear friction of 0.1 T_{rated} at 1500 rpm was applied throughout the simulation. The current controllers for the 4- and 2-pole systems utilised in this vector control scheme was designed, in Chapter 5, with a natural frequency of 400Hz and 100Hz respectively and a damping factor of 0.8. The speed controller was also designed in Chapter 5 with a natural frequency of 5Hz. These controllers were then transformed into the discrete z-plane using the Bilinear transform and implemented in the simulation with a sampling time of 100μs for the current control and 2ms for the speed control. The main 4-pole field was given time to establish by applying i_{sd}^{M*} of value 4.90A from the start of simulation. Once the main 4-pole field had been established, the force references, F_y^* of 235.36N, which is equal to the rotor weight, and F_x^* of 0N, were applied at 2s. A speed reference of 1500rpm was given at 3s and a load of 89.55N, which is equal to 90% of the rated torque T_{rated}, was applied at 4s.

Figure 7.15 illustrates the speed and torque variation of the wound rotor type bearing relief induction motor simulated with the torque current limited to 116% of the rated i_{sq}^M. The speed variation against time clearly shows that the motor was able to accelerate to the required speed of 1500rpm within 0.3s of applying the step change in speed. As expected, the speed rises as a ramp. As the load torque is applied at 4s, the speed variation experiences a drop to 1483Nm but this was quickly restored by the speed controller within approximately 0.1s. As the rotor speed reached the required 1500rpm, the torque did not settle down to zero, as expected, due to the 10% of rated torque friction applied.

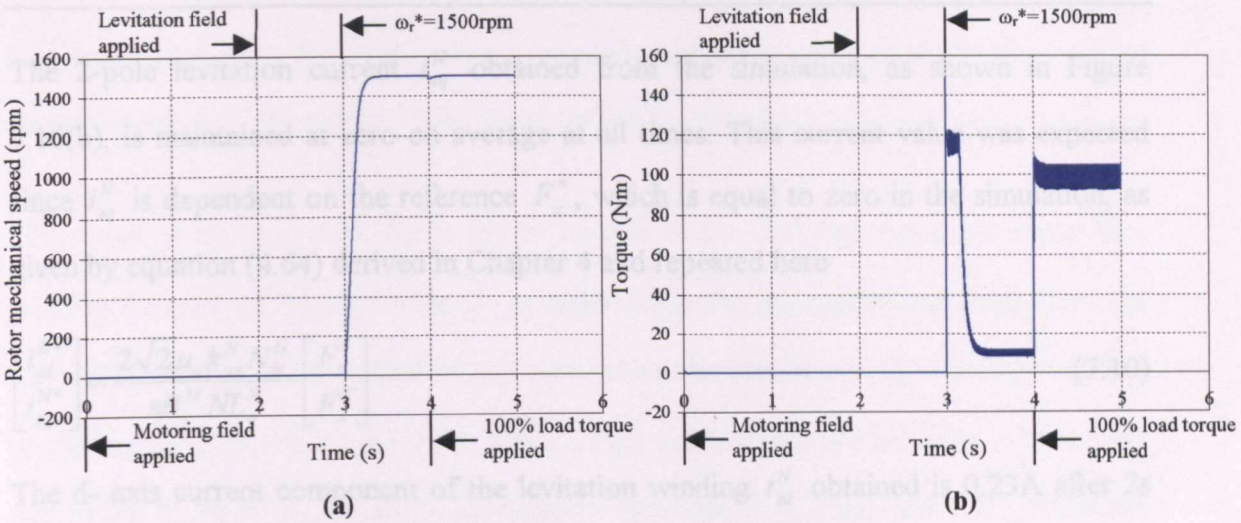

Figure 7.15: (a) speed and (b) torque variation of the vector controlled 4-pole wound rotor bearing relief IM.

The dq- axis stator currents of the main 4-pole winding and 2-pole levitation winding are as shown in Figure 7.16. As shown in Figure 7.16(a), the d- axis stator current i_{sd}^{M} of the 4-pole motoring winding is maintained at its reference value of 4.90A throughout the simulation by the current controller. As expected, no q- axis current i_{sq}^{M} is available from 0 to 3s as the rotor is still stationary. The current reaches its limit of 15A during rotor acceleration before dropping to approximately 1.25A as the rotor speed remains steady at 1500rpm and when the load torque is applied it settles at 12.7A.

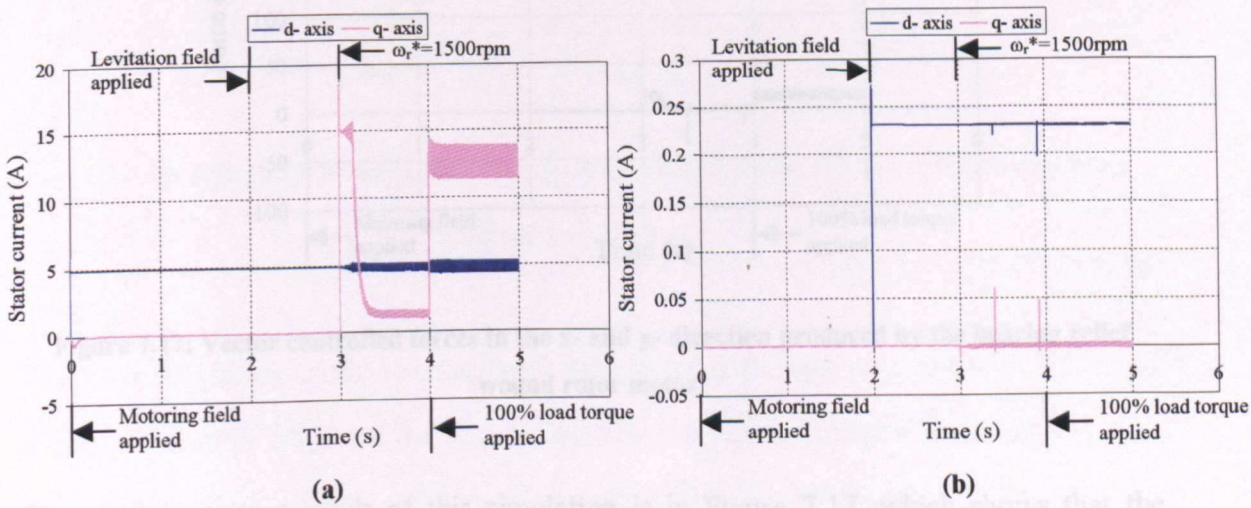

Figure 7.16: Stator current variation of the vector controlled 4-pole bearing relief IM: (a) 4-pole winding (b) 2-pole winding.

The 2-pole levitation current i_{sq}^{N} obtained from the simulation, as shown in Figure 7.16(b), is maintained at zero on average at all times. This current value was expected since i_{sq}^{N} is dependent on the reference F_x^*, which is equal to zero in the simulation, as given by equation (4.64) derived in Chapter 4 and repeated here

$$\begin{bmatrix} i_{sd}^{N*} \\ i_{sq}^{N*} \end{bmatrix} = \frac{2\sqrt{2}\mu_o k_{ws}^{N} N_{ts}^{N}}{\pi B_o^{M} N L_o^{N}} \begin{bmatrix} F_y^* \\ F_x^* \end{bmatrix} \tag{7.10}$$

The d- axis current component of the levitation winding i_{sd}^{N} obtained is 0.23A after 2s as expected. This is consistent with the value of i_{sd}^{N*} calculated using the above equation since F_y^* applied to the simulation is 235.36N at 2s. The value of the peak 4-pole fundamental field B_o^{M} used in the calculation was 0.9T with values of the 2-pole ($N = 1$) levitation winding factor k_{ws}^{N}, total number of turns per phase N_{ts}^{N}, and magnetizing inductance L_o^{N} used are given by Table 5.4.

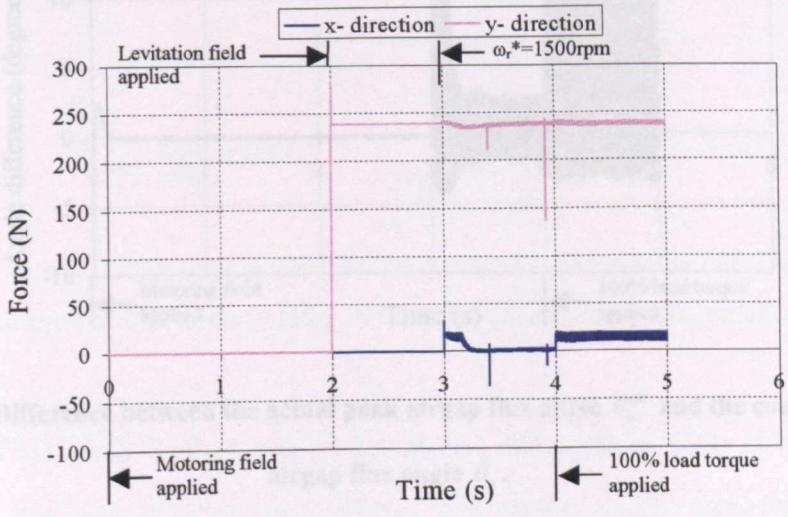

Figure 7.17: Vector controlled forces in the x- and y- direction produced by the bearing relief wound rotor motor.

The most important result of this simulation is in Figure 7.17, which shows that the machine produces the required F_y to levitate the rotor from the moment the force reference $F_y^* = 235.36\text{N}$ is applied. However, non-zero F_x is observed when the rotor

accelerates and when the load torque is applied. The mean value of F_x is found to be approximately 16.71N and 15.7N at these particular instances.

The cause of the non-zero F_x is felt to be due to the fact that the peak airgap flux position derived by the controller $\hat{\theta}_o$ is different to the peak angle obtained from the non-uniform DFT of the actual airgap reluctance element fluxes θ_o^{air} during transient conditions as shown in Figure 7.18. The average angle difference between θ_o^{air} and $\hat{\theta}_o$ was found to be 4° during rotor acceleration (between 3 to 3.2s) and 4.15° when the motor is subjected to full load. This result is identical to that observed in Section 7.2.1 for the vector control of just the 4-pole wound rotor motor since the bearing relief motor simulated here uses the same 4-pole motor for torque production.

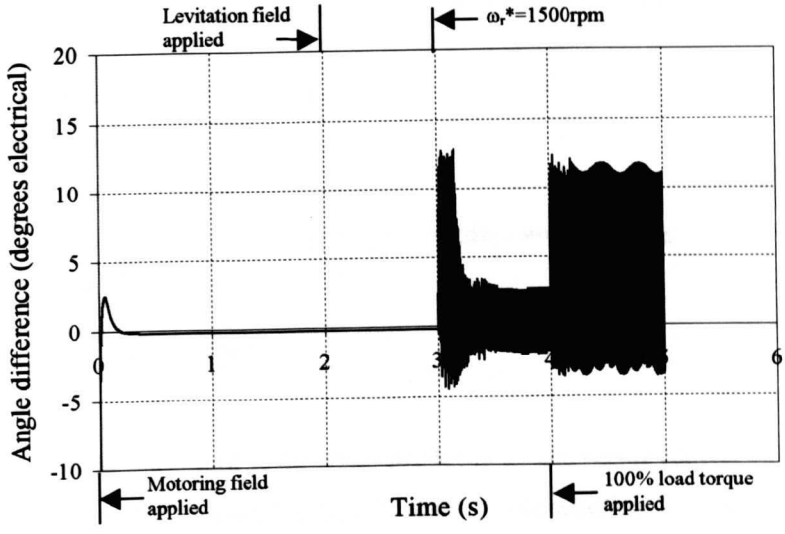

Figure 7.18: Difference between the actual peak airgap flux angle θ_o^{air} and the controller peak airgap flux angle $\hat{\theta}_o$.

When the simulation of the bearing relief wound rotor IM was repeated with θ_o^{air} used as the orientation angle of the 2-pole levitation winding voltages, currents and flux linkages (a form of 'direct' orientation) instead of the controller angle $\hat{\theta}_o$, the mean F_x obtained was found to be approximately zero even during transient conditions as shown in Figure 7.19. However, the force F_x still experienced oscillations at a frequency of 300Hz but of larger amplitude (approximately 10N) as compared to that obtained using

$\hat{\theta}_o$ observed in Figure 7.17. As mentioned in Section 7.2, this 300Hz frequency, also observed in F_y, is the main 4-pole winding phase belt passing frequency as observed by the rotating fields in the motor.

The results indicate that the controller angle $\hat{\theta}_o$ inaccurately predicts the position of the airgap flux since it is dependant on the equivalent circuit parameters of the 4-pole winding that, as discussed previously in Section 7.2.1, were obtained from the no load and locked rotor tests performed using the crude reluctance mesh which underestimated the rotor leakage occurring in the motor.

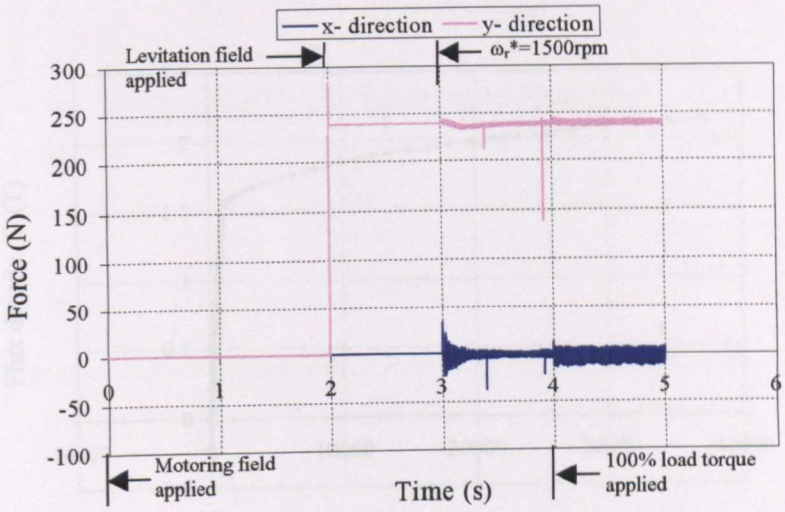

Figure 7.19: Forces in the x- and y- direction produced by the vector controlled bearing relief wound rotor motor obtained using θ_o^{air} as the 2-pole winding orientation angle.

From Figures 7.17 and 7.19, it can be concluded that a slight error in the orientation angle $\hat{\theta}_o$, in this case 4° error on average, will create an F_x force even when the reference x-direction force given was zero. The force F_y is less affected by the error in $\hat{\theta}_o$ since it is governed by a $\cos\hat{\theta}_o$ function as compared to $\sin\hat{\theta}_o$ for F_x.

The spikes observed in Figure 7.16(b), 7.17 and 7.19 are due to numerical effects of the simulation and not due to any transients occurring in the bearing relief motor.

7.5. Effects of non-linear iron on bearing relief IM performance

Thus far, all the results presented in this chapter have been obtained by simulating a DCM model of the wound rotor induction motor in which all reluctance elements were of type linear iron having a relative permeability μ_r of 1350. In this section, the effects of non-linear iron on the simulations of the 4+2 pole induction motor with a 4-pole wound rotor at direct on-line start and with a mixed field oriented vector control scheme will be presented. In the non-linear iron simulations, the permeability of each reluctance element, set to be of type 'non-linear iron', is obtained from a cubic spline interpolation of the B-H curve shown in Figure 7.20.

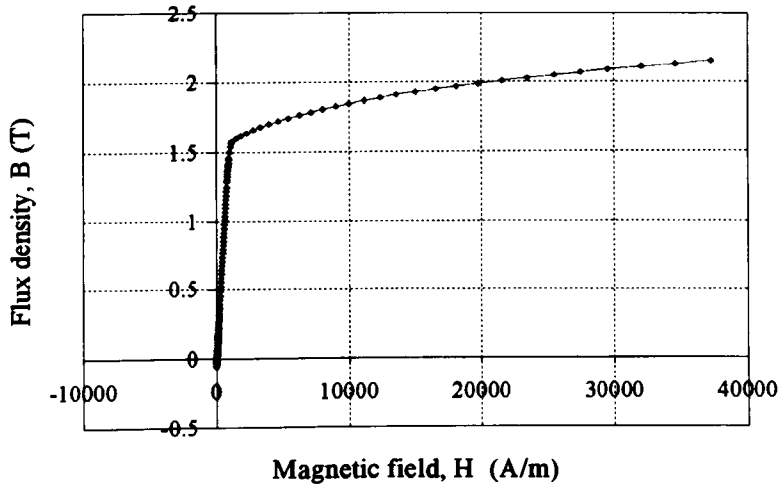

Figure 7.20: B-H curve of the non-linear iron.

7.5.1. Uncontrolled force simulation

Firstly, the effect of non-linear iron on the direct on-line simulation of the wound rotor induction machine of Section 7.3 is investigated. The same rms voltage is applied to both the 4-pole and 2-pole winding terminals, that is 415V for the former and 4.20V for the latter. After 1s, full load torque is applied to the wound rotor motor. It is found that with the introduction of non-linearity, the average no load force magnitude obtained reduces to 203.83N from the linear value of 235.97N. On load, the force magnitude drops further to 200.05N compared to the linear iron force of 228.77N. It is also noticed that the 100Hz oscillation amplitude in the non-linear force magnitude variation

increases to 67.7N peak-to-peak at full load from the linear value of 1.3N. Moreover, in addition to the higher oscillation frequency of 100Hz, a low frequency oscillation of 9.5Hz was observed when the full load torque was applied. This frequency is related to the number of rotor phase belts per pole pair, which is 6, and the slip frequency. The frequency is always the product of the two (9.5Hz = 1.6Hz x 6 at full load in Figure 7.21).

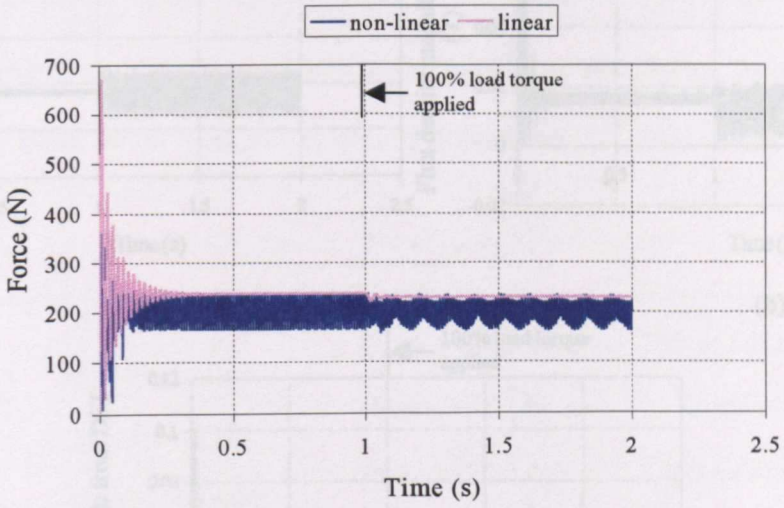

Figure 7.21: Force magnitude obtained from the direct on-line simulation of the 4+2 pole wound rotor motor under linear and non-linear iron conditions.

Figure 7.22(a) and (b) respectively show the magnitude of the peak fundamental 4-pole and 2-pole fields in the non-linear motor obtained from a DFT of the flux density flowing in all non-uniformly spaced airgap reluctance elements. The average values of the fundamental field magnitudes obtained are summarised in Table 7.2 in which it is observed that these values are very similar to that obtained in the linear iron simulation summarised in Table 7.1. However, due to the non-linearity introduced by the B-H curve, triplen field harmonics are now observed to be present in the motor. The most significant harmonic field observed is the third harmonic of the 2-pole field, having a 6-pole variation and an average magnitude of 3.6mT at no load and 5.5mT at full load, as shown in Figure 7.22(c). This 6-pole harmonic field will interact with the fundamental 4-pole field to create a harmonic force of 49.14N, on average, at no load and 74.17N, on average, at full load. This is possible since this pole combination satisfies the criterion of constant force production that is $M - N = \pm 2$. The 6-pole harmonic field was also

observed to oscillate at 100Hz with a peak-to-peak amplitude of 4.8mT at full load. It is due to this behaviour in the 6-pole harmonic that the force obtained from the simulation experiences the 67.7N peak-to-peak oscillation at the 100Hz frequency mentioned above.

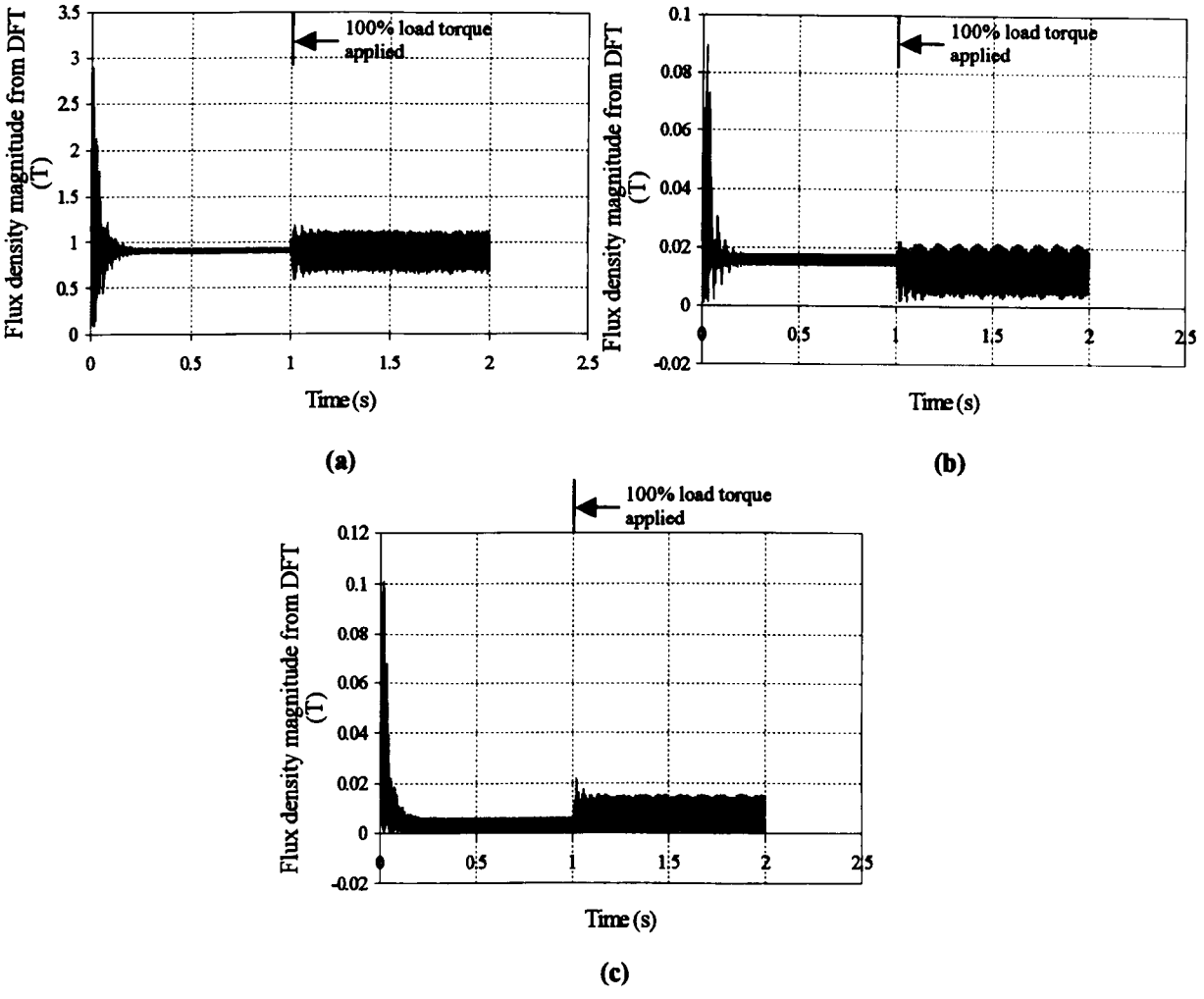

Figure 7.22: Peak fundamental and peak harmonic field magnitudes present in the non-linear bearing relief motor: (a) fundamental 4-pole field, (b) fundamental 2-pole field and (c) 3rd harmonic of the 2-pole field (i.e. 6-pole variation).

	Average magnitude of peak 2-pole field, $\lvert B_2^{DFT} \rvert$	Average magnitude of peak 4-pole field, $\lvert B_4^{DFT} \rvert$	Average magnitude of peak 3rd harmonic of 2-pole field, $\lvert B_6^{DFT} \rvert$
No load	16.5mT	0.91T	3.6mT
Full load	14.7mT	0.90T	5.5mT

Table 7.2: Summary of peak 4-pole, peak 2-pole and peak 6-pole harmonic field average magnitudes obtained from DFT of airgap element flux densities in the non-linear simulation.

In the linear iron simulation results, the magnitude of force obtained from the virtual work principle (as seen in Figure 7.21) was found to be equal to the weight of the rotor and was in broad agreement with the force calculated from the fundamental magnitudes of the 4-pole and 2-pole fields using equation (7.8). In the non-linear iron simulation, the force $|F_{2-4}|$ calculated using equation (7.8) from the DFT results for peak 4- and 2-pole fundamental magnitudes (summarised in Table 7.2) was 225.21N and 198.24N on no load and full load respectively. When $|F_{2-4}|$ is compared to the magnitude of force obtained from the virtual work principle in the non-linear simulation $|F|$, the former is more than the latter at no load but is slightly lower than $|F|$ under load as shown in Table 7.3.

	Average force magnitude from simulation, $\|F\|$ (from virtual work principle)	Fundamental force from DFT, $\|F_{2-4}\|$ (from extracted data in airgap)	Main harmonic force from DFT, $\|F_{6-4}\|$ (from extracted data in airgap)
No load	203.83N	225.21N	49.20N
Full load	200.05N	198.24N	79.34N

Table 7.3: Comparing force obtained from the simulation with the force calculated from magnitudes of the peak 4-pole and 2-pole fields given by the DFT.

Therefore, it can be observed that the drop or rise in fundamental force to create the virtual work derived force is dependent on both the magnitude and direction of the harmonic force vector created from the interaction of the third harmonic of the 2-pole field with the fundamental 4-pole field. It can be summarised that the force obtained from the virtual work principle, shown in Figure 7.21, is the resultant force obtained from the vectorial sum of fundamental and harmonic forces. In this direct on-line start simulation, no in-depth analysis of the force vectorial sum is carried out since the main objective of this simulation was to introduce the effect of non-linear iron on the force produced in the 4+2 pole wound rotor motor and to determine if the wound rotor motor produces the expected 235.36N force which was achieved in the linear iron simulation.

However, the vectorial sum force analysis will be carried out in the vector control simulation of the non-linear motor in Section 7.5.2.

As observed in the direct on-line start simulation, the iron non-linearity introduces triplen spatial harmonics of the 2-pole and 4-pole fields in the wound rotor motor which were not present in the linear iron simulation of Section 7.3. Furthermore, in this simulation, the magnitude of field harmonics originally present in the linear iron simulation, for example the 5^{th}, 7^{th}, and 11^{th}, was found to have increased due to the introduction of iron non-linearity. These harmonics have an associated pole number and if the difference between the 4-pole harmonic pole number and the 2-pole harmonic pole number is ±2, a harmonic force is created. This can either oppose or strengthen the fundamental force created from the fundamental field interactions depending on both the magnitude and direction of the harmonic force. It was observed in the direct on-line start that one of the harmonic forces is created from the interaction between the fundamental 4-pole field and the third harmonic of the 2-pole field. However, other harmonic field interactions can also create harmonic forces and some of these are shown in Table 7.4.

Pole number combination (M, N)	**4-pole harmonic index, $k_{4\text{-pole}}$**	**2-pole harmonic index, $k_{2\text{-pole}}$**
4+2	1 (fundamental)	1 (fundamental)
4+6	1 (fundamental)	3
12+10	3	5
12+14	3	7
20+18	5	9
20+22	5	11
28+26	7	13
28+30	7	15

Table 7.4: Harmonic pole number combinations in the 4+2 pole wound rotor motor.

In Table 7.4, only odd harmonics are considered to interact to create harmonic forces since it was observed in the non-linear direct on-line start simulation that even harmonics fields of both the 4-pole and 2-pole field were found to have very much

smaller magnitudes in comparison with the odd harmonics. The 4+6 pole combination is regarded as the main contributor to the harmonic forces since it involves an interaction with the dominant fundamental 4-pole field which typically has a peak magnitude of 0.9T. This 4-pole fundamental magnitude is more than 50 times that of the fundamental 2-pole field and hence is many more times larger than that of the 2-pole harmonic field magnitudes since field harmonics of larger indices typically have smaller magnitudes compared to the fundamental. Therefore, it is a valid assumption to ignore other harmonic force contributions in all the non-linear simulation force analysis carried out in this thesis. This assumption is verified from observation in the direct on-line start simulation whereby it was found that the 4+6 pole combination created a harmonic force magnitude of 49.20N at no load whereas the next pole combination in line in Table 7.4, that is the 12+10 pole, only created a harmonic force magnitude of 0.9N under the same conditions.

7.5.2. Vector controlled force simulation

The MFO vector control DCM simulation of the 4+2 pole bearingless wound rotor IM (Section 7.4) is repeated with all iron elements given a 'non-linear' type and having its permeability derived from the B-H curve shown in Figure 7.20. Since the peak airgap flux position obtained from the controller, $\hat{\theta}_o$, inaccurately predicts the position of the airgap flux in the linear iron simulation, this simulation was performed with the 2- pole winding orientation angle obtained directly from peak angle of the 4-pole airgap field θ_0^{air}.

The speed and torque variation obtained from the non-linear iron simulation simulated with the proposed controllers, designed in Chapter 5, with the torque current limited to 15A are as shown in Figure 7.23(a) and (b) respectively. It was observed that the speed variation is very similar to that obtained from the linear iron simulation. However, the torque variation experiences a low frequency oscillation of 9.5Hz during full load condition (after 4s) which is similar to that observed in the non-linear iron direct on-line simulation. As explained in Section 7.5.1, this 9.5Hz frequency is thought to be related to the electrical slip frequency since it is obtained from multiplying the slip frequency of 1.6Hz with the number of rotor phase belts per pole pair. This oscillation is also

observed in the speed-time variation and could not be eliminated even with an increase in the speed control closed loop bandwidth from 5Hz to 15Hz.

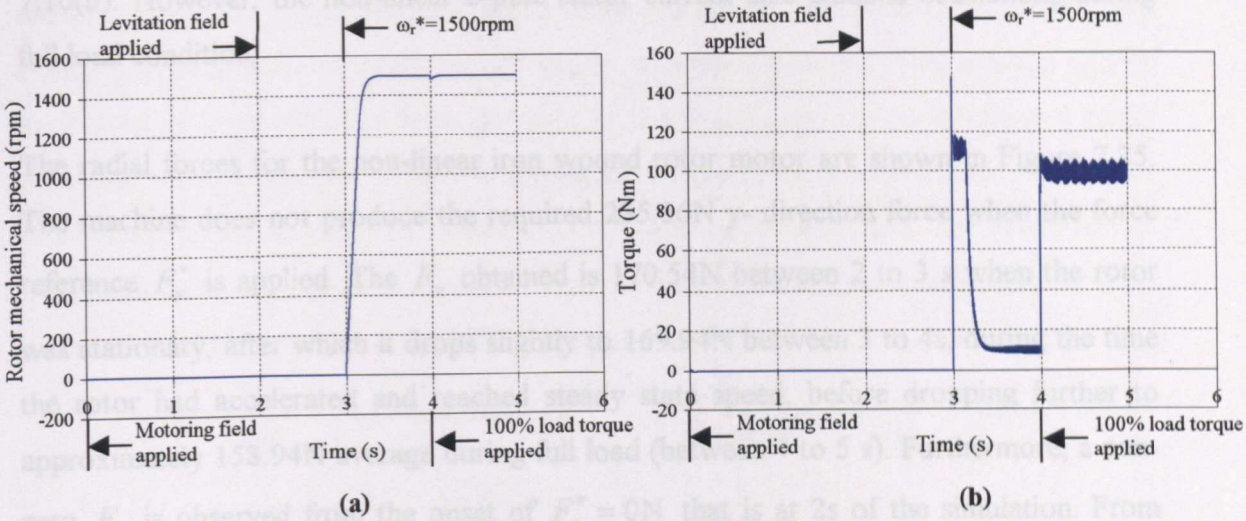

Figure 7.23: (a) speed and (b) torque variation of the vector controlled non-linear bearing relief motor.

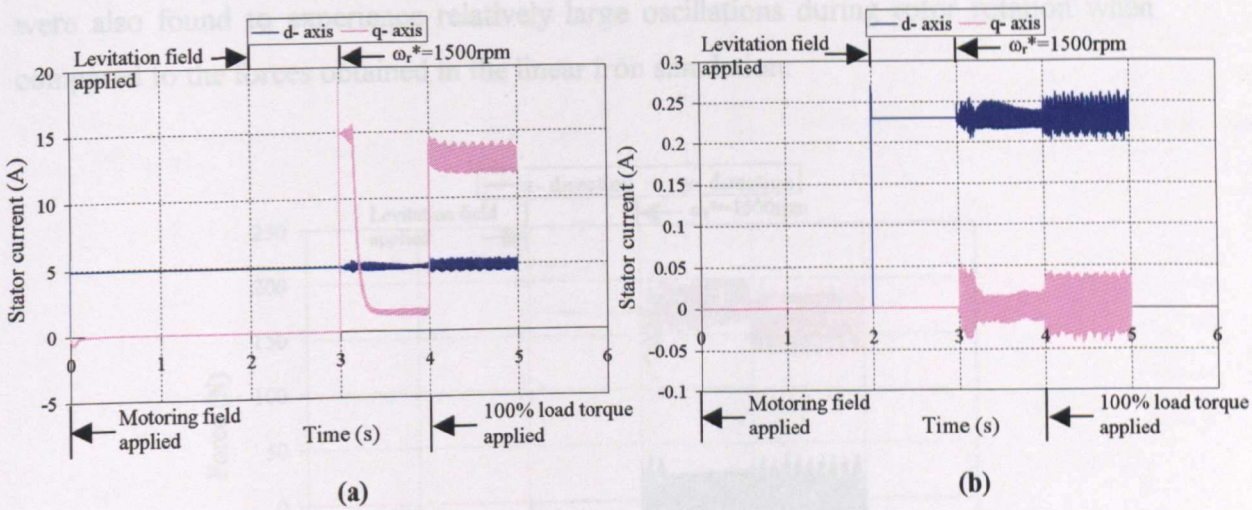

Figure 7.24: Stator current variation of the vector controlled non-linear wound rotor bearing relief IM: (a) 4-pole winding (b) 2-pole winding.

The dq- axis stator currents of the main 4-pole winding and 2-pole levitation winding are as shown in Figure 7.24. In Figure 7.24(a), the dq- axis stator currents of the 4-pole motoring winding is observed to be similar to that of the linear simulation of Figure 7.16(a) with the exception of the 9.5Hz low frequency oscillation experienced at full load. The average value of $\underline{i}_{sdq}^{M}$ in both linear and non-linear simulations is observed to

be the same. Similarly, the dq- axis stator current components of the 2-pole levitation winding shown in Figure 7.24(b) behaves in the same manner as that shown in Figure 7.16(b). However, the non-linear 2-pole stator current also exhibits oscillations during full load condition.

The radial forces for the non-linear iron wound rotor motor are shown in Figure 7.25. The machine does not produce the required 235.36N y- direction force when the force reference F_y^* is applied. The F_y obtained is 170.54N between 2 to 3 s when the rotor was stationary, after which it drops slightly to 169.94N between 3 to 4s, during the time the rotor had accelerated and reached steady state speed, before dropping further to approximately 158.94N average during full load (between 4 to 5 s). Furthermore, a non-zero F_x is observed from the onset of $F_x^* = 0\text{N}$ that is at 2s of the simulation. From Figure 7.25 it is seen that F_x has an average value of –11N, 5.76N and 4.09N during the time intervals of 2 to 3s, 3 to 4s and 4 to 5s, respectively. The forces F_y and F_x were also found to experience relatively large oscillations during rotor rotation when compared to the forces obtained in the linear iron simulation.

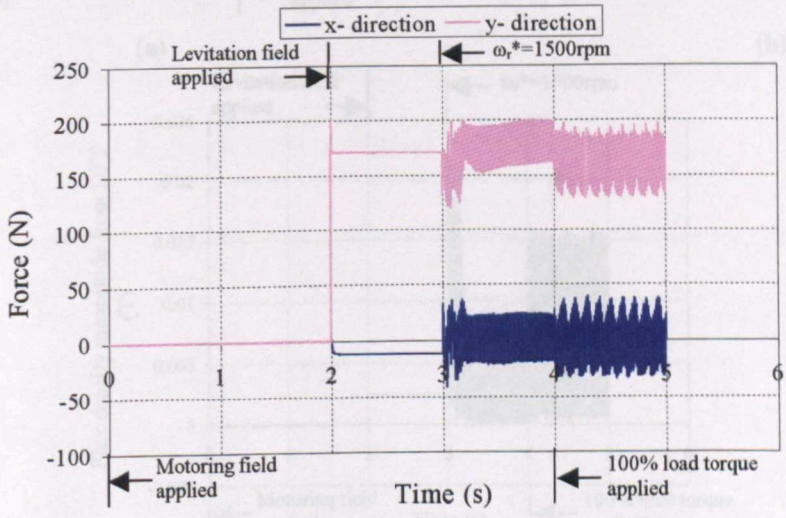

Figure 7.25: Vector controlled forces in the x- and y- direction produced by the non-linear bearing relief IM obtained using θ_o^{air}.

As observed in the direct on-line start simulation, the non-linear iron introduces larger harmonic field magnitudes in the wound rotor motor. This causes a reduction in F_y as

previously discussed. In order to analyse the forces F_y and F_x observed in Figure 7.25, a vectorial sum of the fundamental force and main harmonic force is required which is obtained from the magnitude and phase angle results of the spatial DFT of the flux densities in each non-uniformly spaced airgap reluctance element. This analysis will be performed at three different time intervals of the simulation, namely between 2 to 3s when the rotor is stationary, 3 to 4s during which the rotor is accelerated and reaches steady state condition and 4 to 5s when the full load torque is applied. The magnitude of the fundamental 4-pole field together with the fundamental 2-pole field and its third harmonic field obtained from the DFT is presented in Figure 7.26.

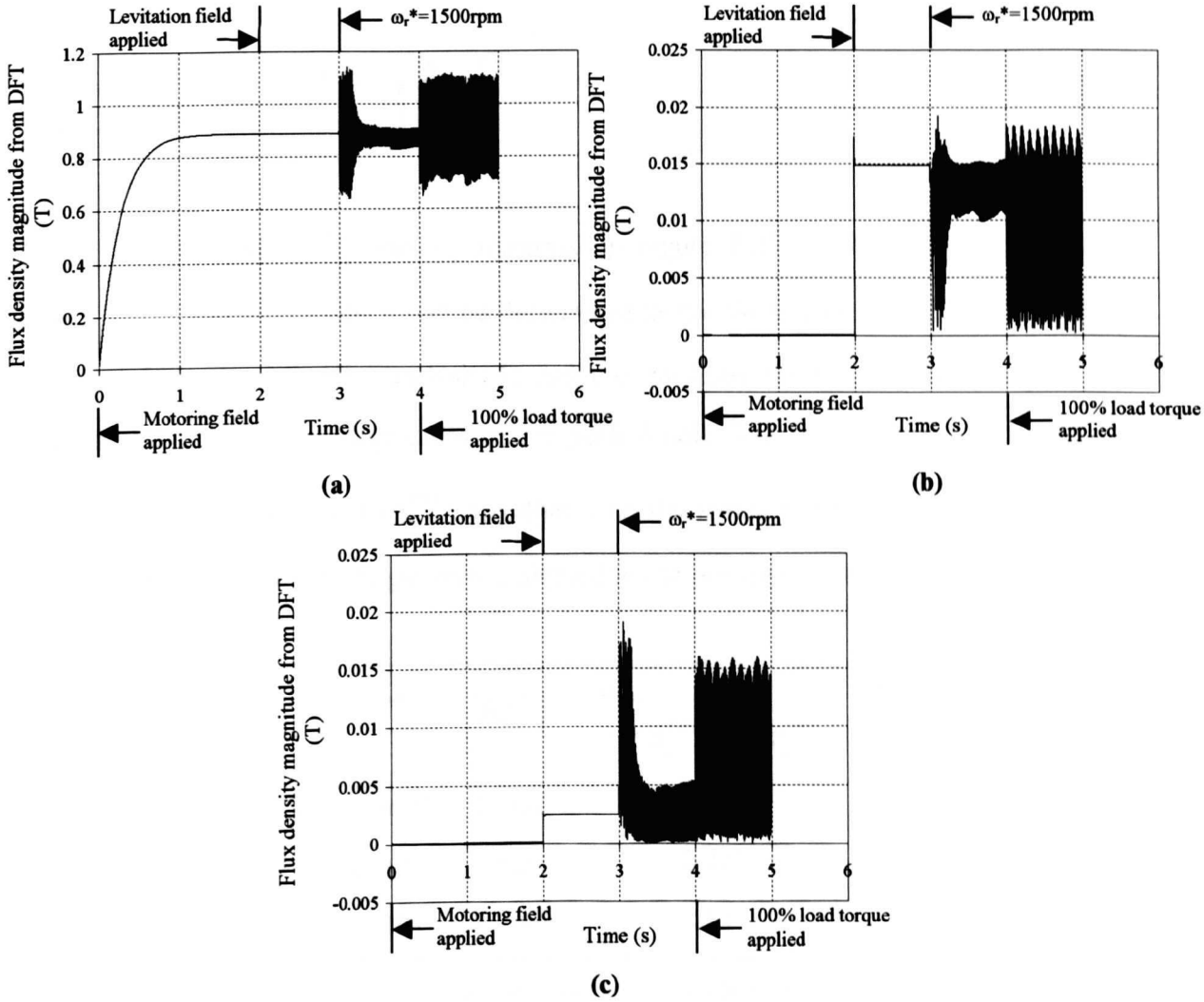

Figure 7.26: Peak fundamental and harmonic field magnitudes present in the vector controlled non-linear motor: (a) fundamental 4-pole field, (b) fundamental 2-pole field and (c) 3rd harmonic of the 2-pole field (i.e. 6-pole variation).

The magnitude of the fundamental force vector $|\underline{F}_{2-4}|$, from the interaction of the 4-pole (M = 4) and 2-pole (N = 2) fields, as well as the magnitude of the main harmonic force vector $|\underline{F}_{6-4}|$, from the interaction of the fundamental 4-pole (M = 4) and harmonic 6-pole (N = 6) fields, can be obtained using equation (7.8). The direction in which these forces are acting can be determined from the angle difference between the peak 2-pole field and the peak of the 4-pole field obtained from the DFT, ϕ_{2-4}, as well as the angle difference between the peak 6-pole harmonic and peak fundamental 4-pole fields ϕ_{6-4}, respectively stated in electrical degrees. Therefore, the resultant force magnitudes acting in the y- and x- direction is given by

$$\begin{bmatrix} F_{y-res} \\ F_{x-res} \end{bmatrix} = \begin{bmatrix} \cos\phi_{2-4} & \cos\phi_{6-4} \\ \sin\phi_{2-4} & \sin\phi_{6-4} \end{bmatrix} \begin{bmatrix} |\underline{F}_{2-4}| \\ |\underline{F}_{6-4}| \end{bmatrix} \tag{7.11}$$

Thus, the force values F_y and F_x observed in Figure 7.25 can be compared to the forces F_{y-res} and F_{x-res} which will be determined at the three time intervals of 2-3s, 3-4s and 4-5s in the following analysis. In order to facilitate the force vector analysis, a summary of the average magnitudes of the peak 4-pole field $|B_4^{DFT}|$, peak 2-pole field $|B_2^{DFT}|$ and peak 6-pole field $|B_6^{DFT}|$ together with the average values of ϕ_{2-4} and ϕ_{6-4} are presented in Table 7.5. Angle zero is aligned to the positive y- axis.

Time interval	$\lvert B_4^{DFT}\rvert$	$\lvert B_2^{DFT}\rvert$	$\lvert B_6^{DFT}\rvert$	$\phi_{2-4} = \angle B_2^{DFT} - \angle B_4^{DFT}$	$\phi_{6-4} = \angle B_6^{DFT} - \angle B_4^{DFT}$
2-3s	0.89T	14.9mT	2.5mT	0.06°	194.06°
3-4s	0.88T	13.2mT	3.3mT	-0.44°	166.79°
4-5s	0.90T	11.6mT	5.5mT	-2.53°	178.28°

Table 7.5: Summary of DFT results obtained from the airgap element flux density samples of the vector controlled bearing relief non-linear wound rotor motor.

Time interval 1: 2-3s (rotor stationary)

Figure 7.27(a) illustrates the 2, 4 and 6-pole angles obtained from the DFT. Figure 7.28(b) shows the differences ϕ_{2-4} and ϕ_{6-4}.

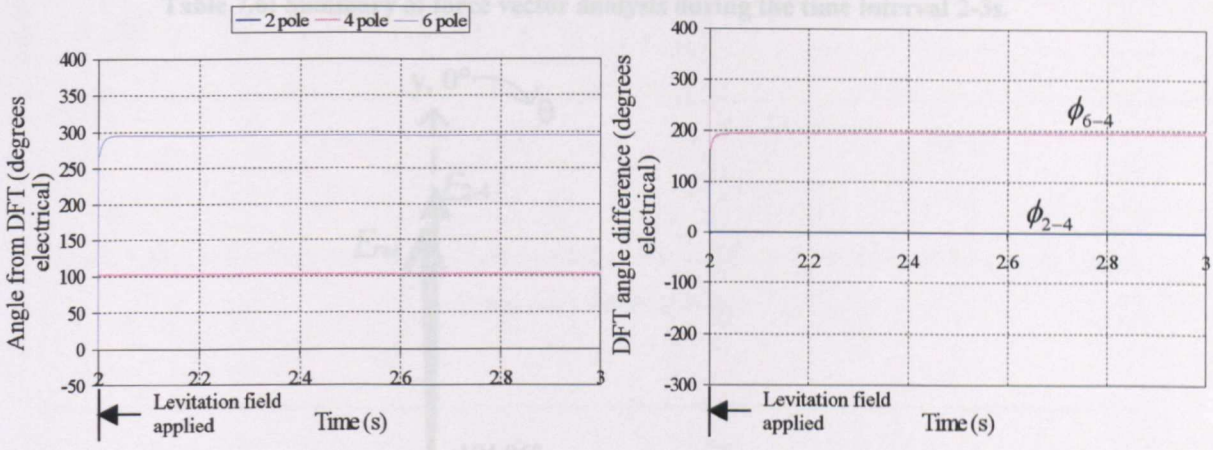

(a) (b)

Figure 7.27: (a) Angles of the peak 2, 4 and 6-pole fields and (b) difference in angles during time interval 2-3s.

With this information as well as the average magnitudes of the peak 2-pole, 4-pole and 6-pole fields given by the DFT, the fundamental force vector $\underline{F}_{2-4}$ and the main harmonic force vector $\underline{F}_{6-4}$ can be obtained. By substituting B_o^M and B_o^N of equation (7.8) with the values of $\left|B_4^{DFT}\right|$ and $\left|B_2^{DFT}\right|$ respectively from Table 7.5, $\underline{F}_{2-4}$ calculates as 197.43N$\angle$0.06°. The force vector $\underline{F}_{6-4}$ calculates to be 33.24N$\angle$194.06°. The resultant force acting on the rotor $\underline{F}_{res} = \underline{F}_{y-res} + \underline{F}_{x-res}$ is as shown in Figure 7.28 in which F_{y-res} (acting at angle 0°) and F_{x-res} (acting at angle 90°) calculates to be 165.19N and -7.87N respectively from equation (7.11). The negative sign of F_{x-res} indicates that the force is acting in the negative x- direction. These results are summarised in Table 7.6, together with F_y and F_x values obtained from the simulation during this time interval.

	F_{2-4}	F_{6-4}	F_{y-res}	F_{x-res}
Harmonic force analysis	197.43N∠0.06°	33.24N∠194.06°	165.19N	-7.87N
Simulated force	-	-	170.54N	–11.0N

Table 7.6: Summary of force vector analysis during the time interval 2-3s.

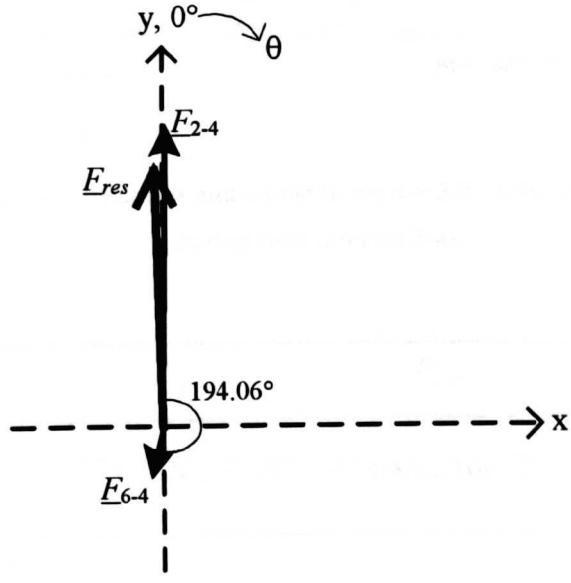

Figure 7.28: Fundamental, main harmonic and resultant force vectors acting in the non-linear bearing relief motor during the time interval of 2 to 3s.

Time interval 2: 3-4s (rotor accelerated and reaches steady state)

The angle of the peak 2-pole, 4-pole and 6-pole fields obtained from the DFT of the airgap element flux density values during the time interval 3 to 4s is partly shown in Figure 7.29(a). Figure 7.29(b) illustrates the angle differences ϕ_{2-4} and ϕ_{6-4}. For this interval $\underline{F}_{2-4}$ calculates to 174.56N∠-0.44° and $\underline{F}_{6-4}$ calculates as 43.64N∠166.79°. Hence, the resultant force acting on the rotor $\underline{F}_{res}$ for this time interval is as shown in Figure 7.30 in which F_{y-res} and F_{x-res} calculates to be 132.07N and 8.63N respectively from equation (7.11) as summarised in Table 7.7.

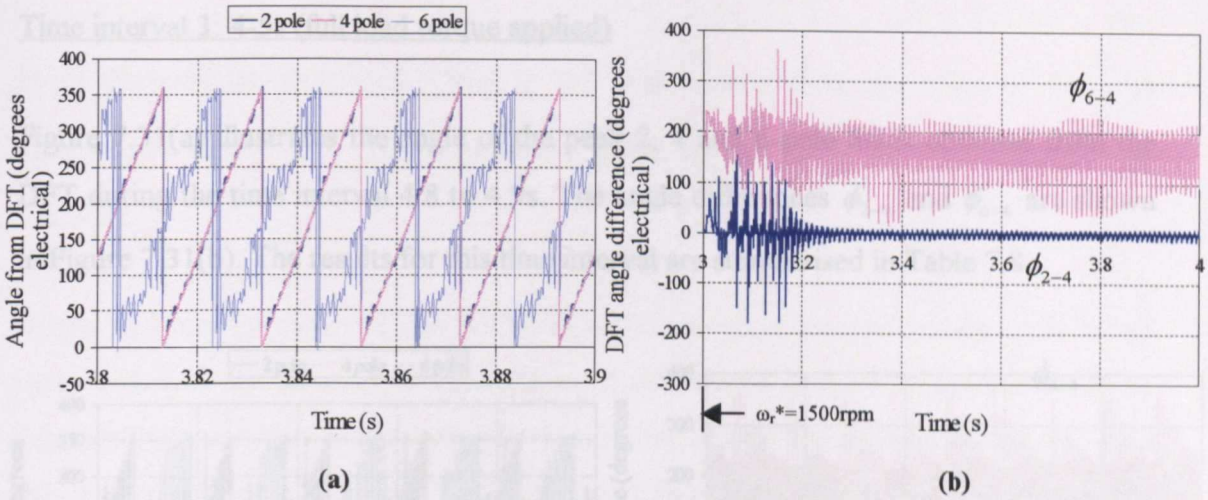

(a) (b)

Figure 7.30: (a) Position of peak 2, 4 and 6-pole fields (t = 3.8 - 3.9s) and (b) difference in angles during time interval 3-4s.

	F_{2-4}	F_{6-4}	F_{y-res}	F_{x-res}
Harmonic force analysis	174.56N∠-0.44°	43.64N∠166.79°	132.07N	8.63N
Simulated force	-	-	169.94N	5.76N

Table 7.6: Summary of force vector analysis during the time interval 3-4s.

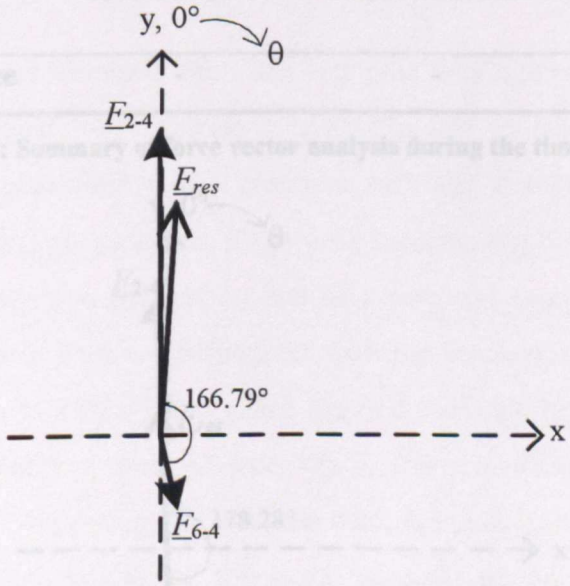

Figure 7.30: Fundamental, main harmonic and resultant force vectors acting in the bearing relief motor during the time interval of 3 to 4s.

Time interval 3: 4-5s (full load torque applied)

Figure 7.31(a) illustrates the angle of the peak 2, 4 and 6-pole fields obtained from the DFT during the time interval 4.8 to 4.9s. The angle differences ϕ_{2-4} and ϕ_{6-4} are shown in Figure 7.31(b). The results for this time interval are summarised in Table 7.8.

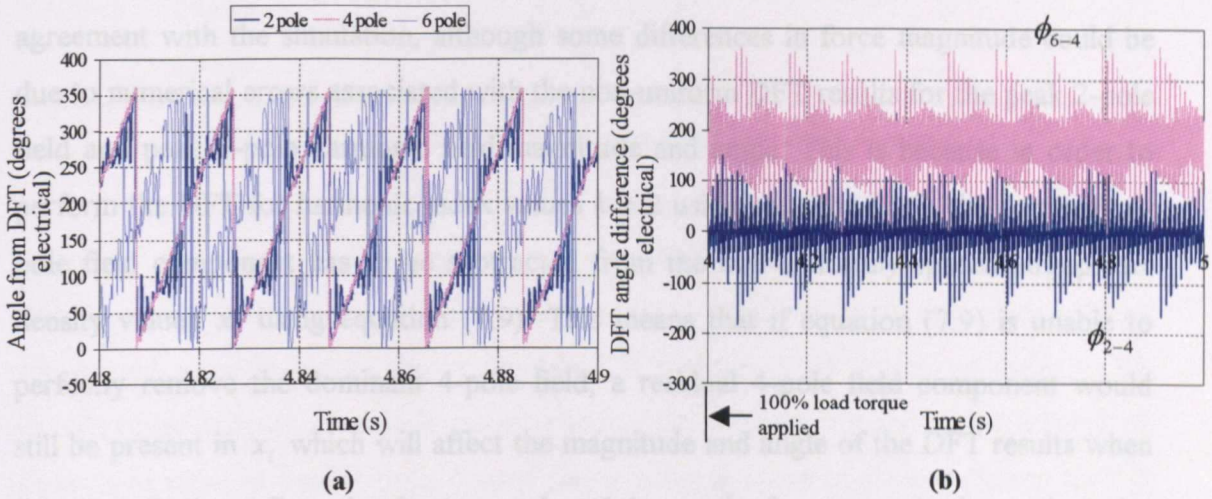

(a) (b)

Figure 7.31: (a) Angles of the peak fields from DFT (t = 4.8 – 4.9s) and (b) difference in angles during time interval 4-5s.

	F_{2-4}	F_{6-4}	F_{y-res}	F_{x-res}
Harmonic force analysis	157.02∠-2.53°	70.39N∠178.28°	86.51N	-4.82N
Simulated force	-	-	158.94N	4.09N

Table 7.8: Summary of force vector analysis during the time interval 4-5s.

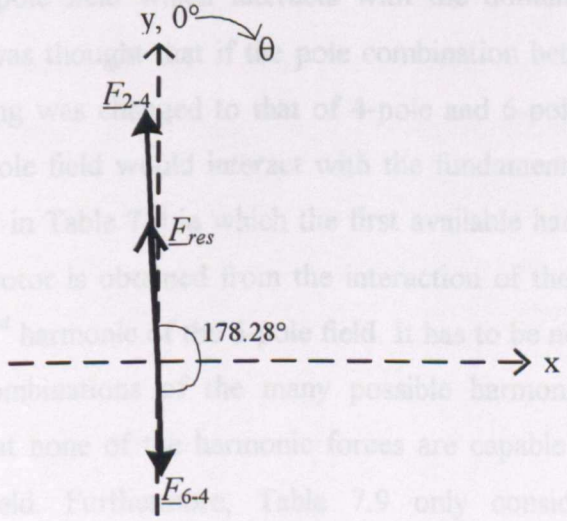

Figure 7.32: Force vectors acting in the bearing relief motor during the time interval of 4 to 5s.

From this analysis, it is shown that, in the time interval 4-5s, the value of F_{y-res} is clearly very different to the force values observed in Figure 7.25 in which F_y is 158.94N.

However, it can be observed that the harmonic force vector analysis results are in broad agreement with the simulation, although some differences in force magnitude could be due to numerical errors associated with the non-uniform DFT results for the peak 2-pole field and peak 6-pole harmonic field magnitude and angle. This is because in order to perform the DFT for harmonic index values $k \neq 2$ using equation (7.6), the dominant 4-pole field component has to be subtracted from the non-uniformly spaced airgap flux density values x_i using equation (7.9). This means that if equation (7.9) is unable to perfectly remove the dominant 4-pole field, a residual 4-pole field component would still be present in x_i' which will affect the magnitude and angle of the DFT results when $k \neq 2$ and also affect the fundamental and harmonic force magnitudes and angles calculated from the DFT results. An improvement on the DFT calculation to minimise numerical errors may yield better agreement.

7.5.3. Uncontrolled force simulation using a 6-pole levitation winding

The reduction in force obtained from the 4+2 pole bearingless wound rotor induction motor under non-linear iron conditions is mainly due to the existence of the third harmonic of the 2-pole field which interacts with the dominant fundamental 4-pole field. Therefore, it was thought that if the pole combination between the main winding and levitation winding was changed to that of 4-pole and 6-pole, respectively, then no harmonic of the 6-pole field would interact with the fundamental 4-pole field and vice versa. This is shown in Table 7.9 in which the first available harmonic force in the 4+6 pole wound rotor motor is obtained from the interaction of the 5^{th} harmonic of the 4-pole field with the 3^{rd} harmonic of the 6-pole field. It has to be noted here that Table 7.9 shows only two combinations of the many possible harmonic field interactions to illustrate the fact that none of the harmonic forces are capable of interacting with the dominant 4-pole field. Furthermore, Table 7.9 only considers the possibility of

interactions between odd harmonics to create harmonic forces as was assumed in the 4+2 pole wound rotor motor simulated in Section 7.5.1.

Pole number combination (M, N)	4-pole harmonic index, $k_{4\text{-pole}}$	6-pole harmonic index, $k_{6\text{-pole}}$
4+6	1 (fundamental)	1 (fundamental)
20+18	5	3
28+30	7	5

Table 7.9: Harmonic pole number combinations in the 4+6 pole motor.

Therefore, the direct on-line simulation under linear and non-linear iron conditions, were repeated with the new 4+6 pole stator winding combination on the existing 48/36 slot wound rotor induction motor described in Chapter 5. However, in order to be capable of inserting the 6-pole levitation winding onto the 48-slot stator, the number of phases was reduced from 3 to 2. A total series turn per phase of 96 was chosen for the 6-pole levitation winding which is double that of the original 2-pole winding of Chapter 5. This corresponds to a winding factor $k_{ws}^{N} = 0.906$ and a stator phase resistance R_s^N of 0.76Ω calculated using

$$R_s = \frac{4.19 q N_s^2 L_{ts}}{1\times 10^6 C_s} \tag{7.12}$$

obtained from Alger (1995), where $N_s = 96$ is the total 6-pole stator winding turns in series per phase, L_{ts} is the mean length of the 6-pole winding turn in centimetres and C_s is the total cross section of copper of all phases in the stator slots due to the 6-pole levitation winding stated in square centimetres. The equations used to calculate L_{ts} and C_s are

$$L_{ts} = 2L + \frac{\pi}{p} r \tag{7.13}$$

$$C_s = \left(\frac{I_{rated}}{500}\right) 2N_s \tag{7.14}$$

where p is the number of pole pairs, I_{rated} is the peak rated current flowing in the winding, and $I_{rated}/500$ represents the area occupied by a coil carrying a maximum current equal to I_{rated} based on the assumption that the current density in the induction motor is taken as $5A/mm^2$.

Another important component required to simulate the direct on-line force simulation of the 4+6 pole wound rotor motor is the rms terminal voltage applied to the levitation winding. This was calculated using equation (7.7) to give an rms voltage of 2.73V when the peak flux density produced by the 6-pole winding is chosen to be equal to that of the previous 2-pole winding, i.e. B_F^N=17.4mT. This is acceptable since B_F^N is calculated from equation (7.8) with the required force magnitude equal to 235.36N, which is assumed to also be the rotor weight of the 4+6 pole wound rotor. The rms terminal voltage applied to the main 4-pole winding is maintained at 415V. As in the simulations described previously, a load torque equal to rated torque was applied at 1s of the simulation.

The force magnitude obtained from the DCM simulation of the 4+6 pole bearingless wound rotor IM under linear iron conditions is shown in Figure 7.33. It can be observed that the force magnitude obtained in the 4+6 pole linear iron motor is 237.99N at no load and 230.93N when full load is applied. This result is comparable with that obtained in the 4+2 pole motor shown in Figure 7.12. It is also found that the force values given in Figure 7.33 under linear iron conditions are in agreement with the fundamental forces calculated from the magnitudes of the peak 4-pole and 6-pole fields given from the DFT of the non-uniformly spaced airgap reluctance elements flux density values.

Having observed that the 4+6 pole wound rotor motor produces a force equal to the rotor weight under linear conditions, as was observed in the 4+2 pole motor, a non-linear direct on-line start simulation of the 4+6 pole motor was then carried out with the same voltage applied to both the main and levitation windings as in the linear case. The result is shown in Figure 7.33.

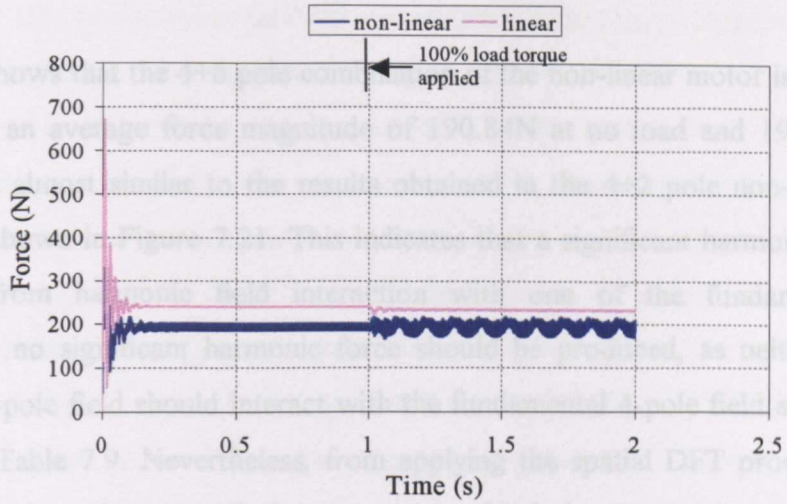

Figure 7.33: Force magnitude obtained from the linear and non-linear direct on-line simulation of the 4+6 pole motor.

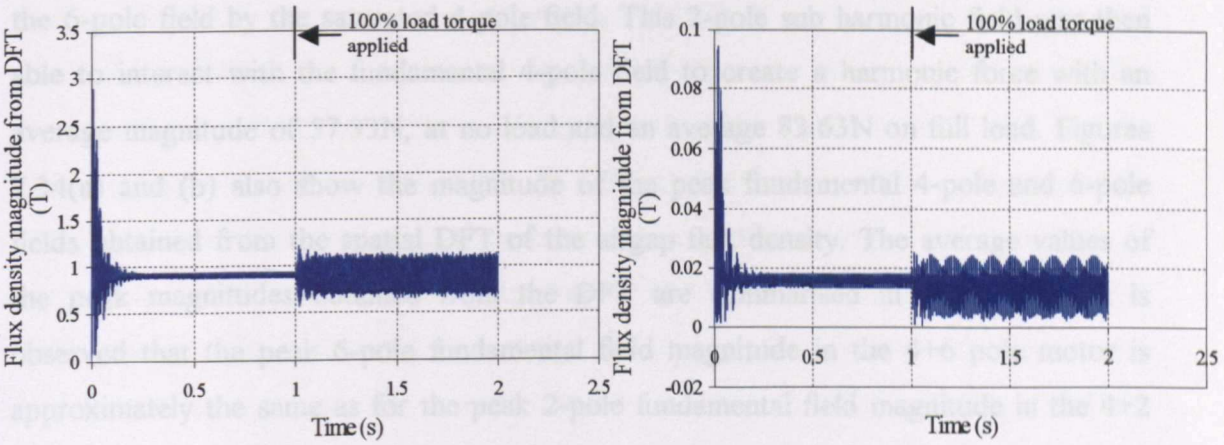

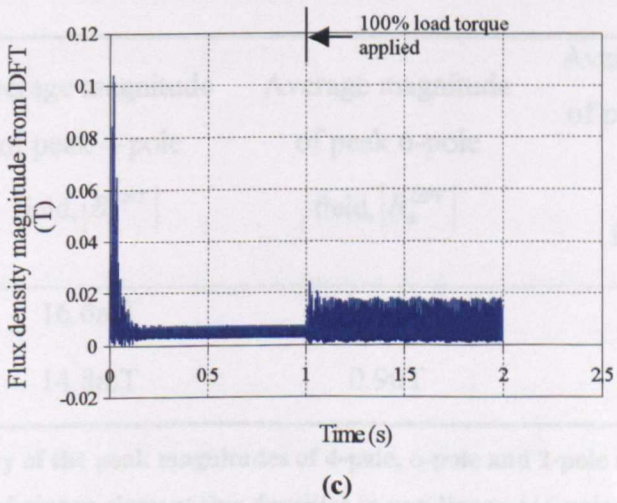

Figure 7.34: Peak fundamental and harmonic field magnitudes in the 4+6 pole motor simulated under non-linear iron conditions: a) fundamental 4-pole field, (b) fundamental 6-pole field and (c) sub harmonic 2-pole field.

Figure 7.33 shows that the 4+6 pole combination of the non-linear motor is only capable of producing an average force magnitude of 190.84N at no load and 192.47N at full load which is almost similar to the results obtained in the 4+2 pole non-linear wound rotor motor shown in Figure 7.21. This indicates that a significant harmonic force may be created from harmonic field interaction with one of the fundamental fields. Theoretically, no significant harmonic force should be produced, as neither harmonic field of the 6-pole field should interact with the fundamental 4-pole field and vice versa as shown in Table 7.9. Nevertheless, from applying the spatial DFT procedure to the airgap flux density values at each time step in the simulation, it was found that a 2-pole sub harmonic field was present in the non-linear 4+6 pole wound rotor induction motor as shown in Figure 7.34(c). The 2-pole sub harmonic field arose from the modulation of the 6-pole field by the saturated 4-pole field. This 2-pole sub harmonic field was then able to interact with the fundamental 4-pole field to create a harmonic force with an average magnitude of 57.33N, at no load and an average 83.63N on full load. Figures 7.34(a) and (b) also show the magnitude of the peak fundamental 4-pole and 6-pole fields obtained from the spatial DFT of the airgap flux density. The average values of the peak magnitudes obtained from the DFT are summarised in Table 7.10. It is observed that the peak 6-pole fundamental field magnitude in the 4+6 pole motor is approximately the same as for the peak 2-pole fundamental field magnitude in the 4+2 pole motor (Figure 7.22(b)).

	Average magnitude of peak 4-pole field, $\left\|B_4^{DFT}\right\|$	Average magnitude of peak 6-pole field, $\left\|B_6^{DFT}\right\|$	Average magnitude of peak 2-pole sub harmonic field, $\left\|B_2^{DFT}\right\|$
No load	16.6mT	0.91T	4.2mT
Full load	14.8mT	0.90T	6.2mT

Table 7.10: Summary of the peak magnitudes of 4-pole, 6-pole and 2-pole sub harmonic fields obtained from DFT of airgap element flux densities in non-linear 4+6 pole wound rotor motor.

From Table 7.10, the force calculated from the peak fundamental magnitudes of the 4-pole and 6-pole fields, using equation (7.8), was 226.58N and 199.63N respectively on no load and full load. However, the magnitude of force obtained from the virtual work principle in the non-linear case is much less than the fundamental force magnitudes stated above at no load and on load. As mentioned in Section 7.5.1, the drop or rise in fundamental force to create the virtual work principle force is dependent on both the magnitude and direction of the harmonic force vector. In this case, the harmonic force is created from the interaction of the 2-pole sub harmonic field with the fundamental 4-pole field. The force obtained from the virtual work principle in the 4+6 pole motor is the resultant force obtained from the vectorial sum of fundamental and harmonic forces.

Figure 7.33 also shows that the oscillation amplitude in the force magnitude also increases to 16.2N peak-to-peak under no load and 43.4N peak-to-peak under full load compared to 0.2N and 3.2N peak-to-peak respectively in the linear iron simulation. The force oscillation was found to have a frequency of 300Hz. Even so, it is clear that the force oscillation amplitude observed in the 4+6 pole motor is much less than that of the 4+2 pole motor, which had peak-to-peak amplitude of 68N as shown in Figure 7.21. In addition to the higher oscillation frequency of 300Hz, a low frequency oscillation of 9.5Hz, similar to that observed in the 4+2 pole motor, was also observed when the full load torque was applied. This is approximately equal to multiplying the electrical slip frequency in the induction motor of 1.6Hz with the number of rotor phase belts per pole pair, which is 6, again. It can be concluded that the 4+6 pole number combination has little effect in reducing the force magnitude reduction and oscillation under non-linear iron conditions.

The non-linear simulations of both the 4+2 pole motor and the 4+6 pole wound rotor motor results in a 9.5Hz oscillation during full load. In order to investigate if the observed low frequency oscillation relates to the choice of 48/36 slot combination of the 4+2 pole and 4+6 pole motor, which can cause the stator and rotor phase belts to be perfectly aligned at certain instances in time, the linear and non-linear direct on-line start simulations for the 4+6 pole wound rotor motor was repeated but with a different stator-rotor slot combination. A slot combination of 48/40 was chosen. The simulations

were only repeated using the 4+6 pole motor because the oscillating behaviour on load was observed to be almost identical in both machines.

The 3-phase, 4-pole main and 2-phase, 6-pole levitation stator windings in the new 48/40 slot motor are exactly the same as that of the 48/36 slot motor since the stator slot number is unchanged. However, in order to maintain the 4-pole rotor winding in the 40-slot rotor, the number of phases was reduced from 3 to 2 with each phase occupying 5 slots per pole. Therefore, the referred rotor resistance had to be recalculated using equation (5.1) to give $R_r^{M'}$ of 0.75Ω. The rms voltage of 415V and 2.73V calculated previously for the 48/36 slot motor, were applied directly to the terminals of the main and levitation windings of the 48/40 slot motor respectively.

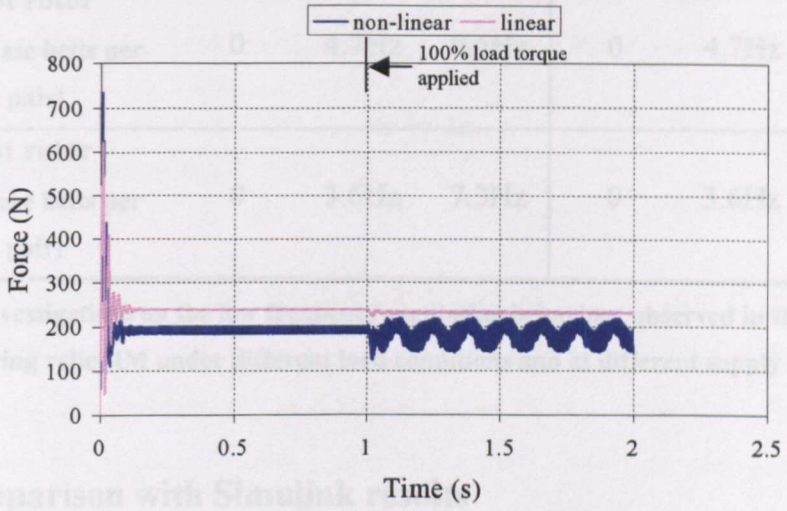

Figure 7.35: Force magnitude obtained from the linear and non-linear direct on-line simulation of the 4+6 pole motor with a 48/40 slot combination.

The force obtained from the linear and non-linear iron simulation is as shown in Figure 7.35. For linear iron, the force magnitude is 238.05N (no load) and 230.90N (full load), which are similar to that obtained in the 48/36 slot motor shown in Figure 7.33. However, when the simulation was repeated under non-linear conditions, it was found that at the force magnitude drops to 191.22N (no load) and 180.66N (full load), which is also similar to that obtained in the 48/36 slot motor shown in Figure 7.33. At full load the force for the 48/40 slot motor experiences a low frequency oscillation of

approximately 7.3Hz. This value of frequency can be approximately obtained from multiplying the electrical slip frequency of the motor (1.8Hz) with the number of rotor phase belts per pole pair, which is 4 in the 2-phase, 4-pole rotor. The exact physical understanding of this low frequency oscillation occurring under load needs to be developed but its dependency on slip and the number of rotor phase belts appear to be verified as shown in Table 7.11. It is apparent that the low frequency oscillation is independent of the supply frequency of the motor.

	Supply frequency = 25Hz			**Supply frequency = 50Hz**		
	No load	50% T_{rated}	100% T_{rated}	No load	50% T_{rated}	100% T_{rated}
36-slot rotor (6 rotor phase belts per pole pair)	0	4.7Hz	9.5Hz	0	4.7Hz	9.5Hz
40-slot rotor (4 rotor phase belts per pole pair)	0	3.6Hz	7.3Hz	0	3.6Hz	7.3Hz

Table 7.11: Investigations on the low frequency oscillating behaviour observed in the non-linear 4+6 pole bearing relief IM under different load conditions and at different supply frequencies.

7.6. Comparison with Simulink results

The results of the linear and non-linear DCM simulations of the MFO vector controlled bearing relief 4+2 pole wound rotor motor can be compared with the MATLAB Simulink results of the same motor under MFO vector control discussed in Section 5.4.4. The Simulink results were carried out with the 2-pole winding currents, voltages and fluxes being oriented onto the 4-pole airgap field using the controller angle $\hat{\theta}_o$ and it is clear from Figure 5.16 that the Simulink results show that perfect levitation can be obtained using the dq representation of the motor with no force in the x- direction. However in the DCM simulation, it was observed in Figure 7.17 that the controller angle $\hat{\theta}_o$, obtained using the same method and equivalent circuit parameters as that of

the Simulink simulation, although providing the required F_y force, also caused an unwanted F_x to be produced during rotor acceleration and on load. This was found to be due to an error occurring between the controller peak airgap field position angle $\hat{\theta}_o$ and the actual peak airgap field position angle θ_o^{air} obtained from applying a DFT on the flux density values of the airgap elements in the DCM model at every time step of the simulation. Therefore, it may be concluded that the two axis lumped parameter model may not be sufficient for fully modelling the leakage effects that influence the positioning of the airgap field.

Furthermore, the Simulink simulation of the bearing relief motor does not provide insight into the non-linear iron effects on the force production of the motor. This is because it cannot fully model a non-linear motor and does not include the capability of investigating the harmonic field interactions that affect the force production.

7.7. Chapter summary

Linear DCM simulations of the direct on-line start 4+2 pole wound rotor IM have shown that radial forces equal to the rotor weight can be achieved and that the required winding voltages and currents are as predicted from theory. However, when the direct on-line start simulation incorporated a non-linear iron, the force produced in the 4+2 pole motor is reduced compared to the linear iron motor indicating that higher 2-pole current is required to achieve the required force. This was due to introduction of a 6-pole harmonic field in the non-linear motor which interacts with the dominant 4-pole field to create an extra force. The force that is produced by the motor is a result of the fundamental force, produced from the interaction of the main 4-pole and levitation 2-pole field, and the forces due to interaction of higher field harmonics.

In the MFO vector controlled simulation of the linear 4+2 pole motor, a vertical bearing relief force to compensate the rotor weight is obtained during both steady state and transient conditions. There is no lateral force F_x as requested by the control scheme provided that the 2-pole levitation winding currents, voltages and fluxes are perfectly oriented onto the peak 4-pole airgap field. However, if there is an error in the controller

airgap flux angle $\hat{\theta}_o$, then a lateral force F_x is produced during acceleration and load conditions. Simulation with non-linear iron saw the introduction of a 6-pole harmonic field in the non-linear motor which interacts with the dominant 4-pole field and creates a large harmonic force. From the vector analysis of the fundamental and harmonic forces in the vector controlled motor it is concluded that the force produced by the simulation is indeed a resultant of the fundamental and harmonic forces. Because the harmonic force is not necessarily aligned with the 4-pole field, the harmonic force not only affects the levitation force F_y but also causes a lateral force F_x to be produced.

Because the 6-pole harmonic field present in the non-linear simulation of the 4+2 pole motor is a 3rd harmonic of the 2-pole field, it was thought that a pole number combination of 4+6 between the main and levitation winding could eliminate any possibilities of the 3rd harmonic of the levitation winding field interacting with the dominant 4-pole field. However, it was found that even though the 4+6 pole wound rotor motor produces the expected force magnitude to levitate the rotor under linear simulation, with non-linear iron there was observed a 2-pole sub harmonic field, created in the motor from the modulation of the 6-pole field by the saturated 4-pole field. Therefore, it can be concluded that in order to achieve successful forces in the non-linear bearing relief motor, compensation of the main harmonic forces produced by the motor is required. This is necessary since bearing relief is basically an open-loop process in which one has to inject a given N-pole current to yield the required force. The existence of harmonic fields must be taken into account when deriving the required N-pole current.

Apart from the harmonic forces experienced in the non-linear simulations, it was observed that under full load a low frequency oscillation of 9.5Hz is present in the force variation against time. This frequency is thought to be related to the electrical slip speed in the motor since it is approximately equal to the electrical slip speed multiplied by the number of rotor phase belts per pole pair. Is was found that this low frequency oscillation still occurs when a different stator and rotor slot combination is chosen, with its value changing according to the new values of rotor phase belts per pole pair. Further understanding is required here to find the mechanism for oscillation reduction.

Chapter 8

Dynamic circuit modelling (DCM) of a bearingless wound rotor induction motor

8.1. Introduction

As presented in Chapter 7, a vector controlled 4+2 pole wound rotor motor under bearing relief condition was simulated in which the rotor is held fixed by bearings. In this chapter, simulations of a totally bearingless motor will be presented whereby the rotor is allowed to move freely in the motor. As the objective of the simulation is to maintain the free-moving rotor at the centre, a position control loop is required which is designed in Section 8.3. However, the controller design requires the use of the force expressions for the perturbed rotor motor derived previously in Section 3.3.2. Compared to the force expression for the fixed rotor case, the rotor perturbation introduces additional terms in the force expressions which are associated with the rotor movement. Therefore, in Section 8.2, the effect of rotor displacement on the force produced in the wound rotor IM will be investigated and compared with the force expressions derived in Section 3.3.2.

In Section 8.4, the results of a linear iron simulation of the 4+2 pole MFO vector controlled bearingless wound rotor motor, incorporating the designed position controller and modifications to the DCM software to allow for the free-moving rotor, will be presented. Two different results will be presented in this section whereby in the first simulation the 2-pole levitation winding orientation angle is obtained indirectly by the controller whereas in the second simulation the orientation angle is obtained directly from the DFT of the actual airgap element's flux density values. This arises from the linear iron bearing relief simulation results presented in Section 7.4 where it was

observed that the orientation angle provided by the controller did not accurately predict the position of the peak 4-pole airgap flux onto which the 2-pole levitation winding is oriented. This causes an unwanted x- direction force to be produced. However, Section 8.4 highlights the fact that the position controllers in the bearingless induction motor are able to produce the required levitation force while maintaining the x- direction force at zero as demanded even when there is a slight error in the controllers prediction of the 2-pole levitation winding orientation angle.

A simulation of the same motor under non-linear iron conditions will also be presented in Section 8.5. This is to investigate if the non-linearity effects of the iron previously observed in the bearing relief motor could be compensated for by the incorporation of the position controllers. The main effects are namely the reduction of the y- direction force produced in the motor as well as a non-zero x- direction force due to harmonic forces and the low frequency oscillation observed when the motor was subjected to load. Finally, in Section 8.5, a comparison between the DCM simulation results of the 4+2 pole bearingless wound rotor motor and the results of the same motor simulated using a 2 axis lumped parameter model in MATLAB Simulink will be discussed.

8.2. Effect of rotor displacement on the force produced in the wound rotor IM

In this section the results of an investigation into the effect of rotor displacement on the force produced by the motor is presented. The investigation is carried out using the DCM model of the 4-pole wound rotor induction motor, introduced in Chapter 5, excited by only the 4-pole stator winding (i.e. without the presence of the 2-pole levitation winding). Figure 8.1 shows the force produced by the motor simulated using the DCM model as the rotor is displaced in the y- direction under non-rotating rotor condition at no load. It was observed that a movement in y- direction only produces force in the y- direction, i.e. no x- direction force is produced by the displacement. When the DCM simulations were repeated with the rotor rotating at rated speed and at no load, the force produced due to the rotor displacement in the y- direction was observed to be similar to that when the rotor was stationary. It was also observed that

the simulation results of the x- direction force variation with rotor displacement in the x- direction are identical to that shown in Figure 8.1.

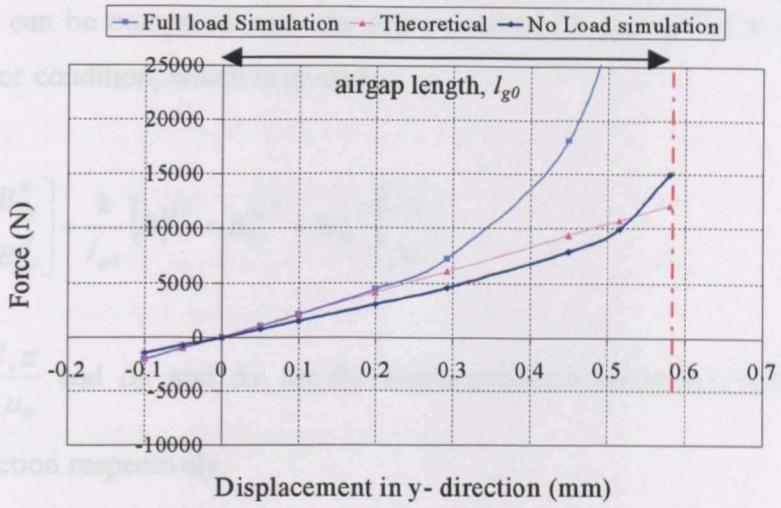

Figure 8.1: Y- direction force variation with rotor displacement obtained from the theoretical force expression and DCM simulations under no load and full load conditions.

It is clear from the simulation curve of Figure 8.1 that as the rotor moves closer towards the stator, the force produced increases in the direction of the displacement. The force produced by the displacement is termed the unbalance magnetic pull experienced by the perturbed rotor. The slope of the force-displacement variation in the linear region (less than ± 50% of the airgap length) is calculated to be 15.56×10^6 Nm^{-1}.

When the simulations are repeated but with the rotor now subjected to a full load torque of 99.5Nm, the unbalance magnetic pull force produced is larger compared to that obtained at no load as shown in Figure 8.1. The increase in unbalance magnetic force produced by the motor under full load condition is due to the fact that the induced rotor currents creates a 4-pole field which will interact with the 2-pole non-uniform airgap variation to create 6-pole and 2-pole harmonic components. These harmonic components will then interact with the main 4-pole field of the motor to create a constant force (since the difference between the poles are ± 2) that will add to the unbalance magnetic pole force. It is also evident that the unbalance magnetic pull force increases almost quadratically at full load when the rotor displacements are larger than

50% of the airgap length. However, slope of the force-displacement variation in the linear region (less than ± 50% of the airgap length) is calculated to be 23.55×10^6 Nm^{-1}.

These slopes can be compared with the force expressions derived in Section 3.3.2 for perturbed rotor condition, which is given by:

$$\begin{bmatrix} F_y' \\ F_x' \end{bmatrix} = kB_o^M \begin{bmatrix} B_{Fy}^N \\ B_{Fx}^N \end{bmatrix} + \frac{k}{l_{g0}} \left(B_o^{M\,2} + B_{Fy}^{N\,2} + B_{Fx}^{N\,2} \right) \begin{bmatrix} \Delta y \\ \Delta x \end{bmatrix} \tag{8.1}$$

where $k = \frac{rl_z\pi}{2\mu_0}$ and Δy and Δx are the displacements experienced by the rotor in the y- and x- direction respectively.

In the bearingless induction motor, $B_F^{N\,2} << B_o^{M\,2}$. Therefore, the forces acting on the perturbed rotor is approximated by:

$$\begin{bmatrix} F_y' \\ F_x' \end{bmatrix} \approx kB_o^M \begin{bmatrix} B_{Fy}^N \\ B_{Fx}^N \end{bmatrix} + \frac{k}{l_{g0}} B_o^{M\,2} \begin{bmatrix} \Delta y \\ \Delta x \end{bmatrix} \tag{8.2}$$

In the force-displacement investigation of the wound rotor motor carried out using the DCM software, the 2-pole excitation is not present, i.e. $B_{Fy}^N = B_{Fx}^N = 0$. Hence, equation (8.2) becomes:

$$\begin{bmatrix} F_y' \\ F_x' \end{bmatrix} = \frac{k}{l_{g0}} B_o^{M\,2} \begin{bmatrix} y \\ x \end{bmatrix} \tag{8.3}$$

which is the expression for the unbalance magnetic pull exerted on the perturbed rotor. Therefore, with $r = 82.26$mm, $l_z = 0.15$m, $l_{g0} = 0.58$mm and assuming $B_o^M = 0.9$T, the theoretical slope of this equation is calculated to be 20.82×10^6 Nm^{-1} which is of the same order to the slope calculated from the no load and full load simulation curves in Figure 8.1. Furthermore, the 'theoretical' force-displacement variation, calculated using equation (8.3), and shown in Figure 8.1 is observed to be close to the variation obtained

from the DCM simulations especially within the region of ± 0.1mm from the centre line of the motor.

Therefore, it can be concluded that the force expressions derived in Section 3.3.2 are justified by the DCM simulation assuming that the rotor movement can be controlled within ±50% of the airgap length when the rotor is stationary or rotating at synchronous speed before applying a load torque or a non-zero i_{sq}. Having shown that the derived force expression for the perturbed or free-moving rotor is valid, the position loop controller of the bearingless induction motor can be designed.

8.3. Radial position compensator design

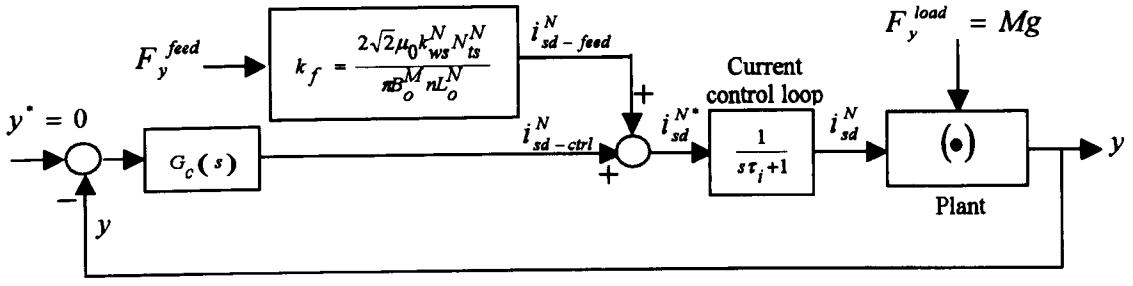

Figure 8.2: Position control loop

In the 4+2 pole bearingless wound rotor IM, the dq- axis stator current demands of the levitation 2-pole winding i_{sd}^{N*} and i_{sq}^{N*} are respectively responsible for controlling the forces F_y and F_x produced in the motor. Hence, in the vector control scheme of the bearingless wound rotor IM, i_{sdq}^{N*} are derived from the position control loops. Figure 8.2 shows the y- direction position control loop. The x- direction control loop is identical to that of Figure 8.2. The high bandwidths of the current control loops enables its closed loop dynamics to be neglected. Thus, the plant dynamics for the position control loop is dominated by the motor's equation of motion in the y- and x- direction which is given by

$$\begin{bmatrix} F_y' \\ F_x' \end{bmatrix} = M_r \begin{bmatrix} \ddot{y} \\ \ddot{x} \end{bmatrix} \tag{8.4}$$

where M_r is the mass of the rotor. The forces $F_y^{'}$ and $F_x^{'}$ in equation (8.4) are the forces acting on the free moving rotor given by equation (8.1). However, equation (8.1) can be written in terms of the 2-pole dq- currents using the relationship between B_{Fyx}^N and $\psi_{odq}^N = L_o^N i_{sdq}^N$ derived in Section 4.2.2 for the wound rotor IM, repeated here for convenience,

$$\begin{bmatrix} B_{Fy} \\ B_{Fy} \end{bmatrix} = k_1 \begin{bmatrix} \psi_{od}^N \\ \psi_{oq}^N \end{bmatrix} \tag{8.5}$$

where $k_1 = \dfrac{\sqrt{2}n}{2rlk_{ws}^N N_{ts}^N}$. Therefore, equation (8.1) is rewritten as

$$\begin{bmatrix} F_y^{'} \\ F_x^{'} \end{bmatrix} = \frac{1}{k_f} \begin{bmatrix} i_{sd}^N \\ i_{sq}^N \end{bmatrix} + k_2 B_o^{M\,2} \begin{bmatrix} y \\ x \end{bmatrix} + k_2 k_1^2 \left(i_{sd}^{N\,2} + i_{sq}^{N\,2} \right) \begin{bmatrix} y \\ x \end{bmatrix} \tag{8.6}$$

where

$$k_f = \frac{2\sqrt{2}\mu_0 k_{ws}^N N_{ts}^N}{\pi B_o^M n L_o^N} \tag{8.7}$$

and

$$k_2 = \frac{rl_z\pi}{2\mu_0 l_{g0}} \tag{8.8}$$

By substituting equation (8.6) into (8.4) and rearranging, the relationship between the input, i_{sd}^N (i_{sq}^N), and output, y (x), of the plant in Figure 8.2 is given by

$$M_r \begin{bmatrix} \ddot{y} \\ \ddot{x} \end{bmatrix} = \frac{1}{k_f} \begin{bmatrix} i_{sd}^N \\ i_{sq}^N \end{bmatrix} + k_2 B_o^{M\,2} \begin{bmatrix} y \\ x \end{bmatrix} + k_2 k_1^2 \left(i_{sd}^{N\,2} + i_{sq}^{N\,2} \right) \begin{bmatrix} y \\ x \end{bmatrix} \tag{8.9}$$

Equation (8.9) shows that the plant is non-linear since the last term in the equation is dependent on the input and output of the plant. Therefore, by considering small motions about the operating point ($x_0 = y_0 = 0$), equation (8.9) becomes

$$M_r\begin{bmatrix}\delta\ddot{y}\\ \delta\ddot{x}\end{bmatrix}=\underbrace{\frac{1}{k_f}\begin{bmatrix}\delta i_{sd}^{N}\\ \delta i_{sq}^{N}\end{bmatrix}}_{a}+\underbrace{k_2 B_o^{M^2}\begin{bmatrix}\delta y\\ \delta x\end{bmatrix}}_{b}+\underbrace{k_2k_1^2\left(i_{sd}^{N^2}+i_{sq}^{N^2}\right)\Big|_{x_0=y_0=0}\begin{bmatrix}\delta y\\ \delta x\end{bmatrix}}_{c}+\underbrace{2k_2k_1^2\left(\delta i_{sd}^{N}+\delta i_{sq}^{N}\right)\begin{bmatrix}y_0\\ x_0\end{bmatrix}}_{d} \tag{8.10}$$

At the operating point, $x_0 = y_0 = 0$. Therefore, term 'd' in equation (8.10) becomes zero. The term 'c' in the same equation can also be written as

$$k_2k_1^2\left(i_{sd}^{N^2}+i_{sq}^{N^2}\right)\Big|_{x_0=y_0=0}\begin{bmatrix}\delta y\\ \delta x\end{bmatrix}=k_2B_F^{N^2}\Big|_{x_0=y_0=0}\begin{bmatrix}\delta y\\ \delta x\end{bmatrix}$$

where $B_F^{N^2}=\left(B_{Fy}^{N^2}+B_{Fx}^{N^2}\right)$. Generally, in the bearingless IM, $B_F^{N^2} << B_o^{M^2}$. Hence term 'c' of equation (8.10) can be neglected. Thus, equation (8.10) simplifies to be

$$M_r\begin{bmatrix}\delta\ddot{y}\\ \delta\ddot{x}\end{bmatrix}=\underbrace{\frac{1}{k_f}\begin{bmatrix}\delta i_{sd}^{N}\\ \delta i_{sq}^{N}\end{bmatrix}}_{\text{i}}+\underbrace{k_2B_o^{M^2}\begin{bmatrix}\delta y\\ \delta x\end{bmatrix}}_{\text{ii}} \tag{8.11}$$

The terms on the right of equation (8.11) represents the force produced by the perturbed rotor which is similar to the findings in the previous section given by equation (8.2). In this equation, term 'i' is the force expression in the motor when the rotor is fixed at the centre whereas term 'ii' is associated with the unbalance magnetic pull experienced by the perturbed rotor investigated previously. Hence, the linearised plant transfer function in the position control design is obtained from equation (8.11) to give:

$$G_p(s)=\frac{\delta y(s)}{\delta i_{sd}^{N}(s)}=\frac{\delta x(s)}{\delta i_{sq}^{N}(s)}=\frac{1}{k_f}\cdot\frac{1}{M_rs^2-k_2B_o^{M^2}} \tag{8.12}$$

Figure 8.3 shows the linearised y- direction position control loop. The control loop for in the x- direction is identical.

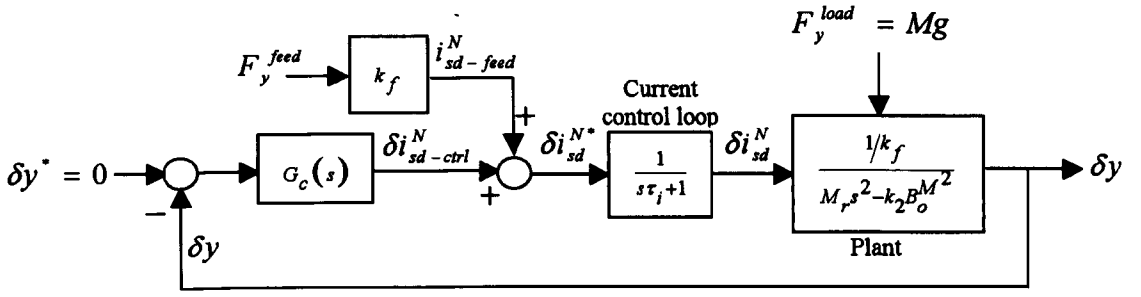

Figure 8.3: Linearised position control loop

Therefore, through substitution of (8.7) and (8.8) into (8.12), the plant transfer function for the 4+2 pole wound rotor motor is given by:

$$G_p(s) = \frac{1015.683}{24s^2 - 20.82 \times 10^6} \tag{8.13}$$

since $M_r = 24\text{kg}$, $(1/k_f) = 1015.683$, $r = 82.26\text{mm}$, $l_z = 0.15\text{m}$, $l_{g0} = 0.58\text{mm}$ and assuming $B_o^M = 0.9\text{T}$.

From equations (8.12) and (8.13), it is clear that the plant of the position control loop is of 2nd order and the plant has two poles of the same magnitude but opposite signs. One of the plant poles is unstable, i.e. on the right half of the *s*-plane, at $s = \sqrt{k_2 B_o^{M2}/M_r}$ or $s = 931.4$ in the investigated motor. Therefore, a phase lead controller was chosen in the control scheme such that it cancels the stable pole on the left half of the s-plane ($s = -931.4$). The controller was designed in the continuous *s*-plane, by way of root locus, to achieve a nominal closed loop bandwidth of 48Hz (300rad/s) and a damping factor ς of approximately 1.0 to give:

$$G_c(s) = 64.05 \times 10^3 \frac{(s + 931.4)}{(s + 2500)} \tag{8.14}$$

With this designed controller, a vector controlled totally bearingless 4+2 pole wound rotor motor could be simulated using the DCM reluctance mesh model software.

8.4. Vector control simulation of a linear iron bearingless wound rotor IM

In this section, the linear iron 4+2 pole vector controlled wound rotor motor will be simulated under bearingless conditions. In order to achieve this, the motor is modelled using the reluctance mesh model and simulated with the DCM software. However, due to the fact that the rotor in a bearingless motor is allowed to move freely, modifications to the DCM software were added to model the free-moving rotor as described in Section 2.5(g). The vector control scheme applied to the wound rotor motor is based on the mixed field orientation (MFO) scheme in which the main 4-pole winding will be rotor field oriented with the 2-pole levitation winding being oriented onto the peak 4-pole airgap field. This vector control scheme was proposed in Section 4.4 wherein the orientation of the 2-pole winding was achieved using equation (4.61) and repeated here for convenience.

$$\hat{\theta}_o = \hat{\theta}_r + \tan^{-1}\left(\frac{\psi_{oq}^{M}}{\psi_{od}^{M}}\right) \tag{8.15}$$

In this linear iron simulation, all reluctance elements were chosen to be of type 'linear iron' having a $\mu_r = 1350$ with the exception of the slot tip leakage elements, which were chosen to be of type 'air', due to the semi-closed slots on both stator and rotor side. The motor is modelled with only one rotor axial skew section with a skew angle of 15° electrical. Similar to the bearing relief simulation in Section 7.4, an external load having inertia equal to the motor inertia of 0.0713kgm^2 as well as a linear friction of $0.1\,T_{rated}$ at 1500 rpm is applied throughout the simulation. The current controllers for the 4 and 2-pole systems utilised in this vector control scheme (designed in Chapter 5) have a natural frequency of 400Hz and 100Hz respectively and a damping factor of 0.8. The speed controller employed in this scheme, also designed in Chapter Five, has a natural frequency of 5Hz. These controllers were then transformed into the discrete z-plane through a Bilinear Transform using equation (7.1) and implemented in the simulation with a sampling time of 100μs for the current control and 2ms for the speed control. The main 4-pole field is given time to establish by applying i_{sd}^{M*} of value 4.90A from the start of simulation. A speed reference of 1500rpm is then given at 3s and a

load of 89.55N, which is equal to 90% of the rated torque T_{rated}, is applied at 4s. In the bearing relief simulation, the 2-pole stator current references i_{sd}^{N*} and i_{sq}^{N*} were obtained from step references F_y^* and F_x^* in which

$$\begin{bmatrix} i_{sd}^{N*} \\ i_{sq}^{N*} \end{bmatrix} = k_f \begin{bmatrix} F_y^* \\ F_y^* \end{bmatrix} \tag{8.16}$$

However, in the bearingless motor simulation, i_{sd}^{N*} and i_{sq}^{N*} are obtained respectively from the y- and x- direction position control with the phase lead controller designed in the previous section together with feed forward signals i_{sd}^{N-feed} and i_{sq}^{N-feed} (derived from F_y^{feed} and F_x^{feed} respectively) as shown in Figure 8.3. The position controllers are also transformed into the discrete z-plane through the Bilinear Transform (Franklin *et. al*, 1998), $s = 2(z-1)/(t_{samp}(z+1))$, and implemented in the simulation with a sampling time of 100μs, which is similar to the sampling time of the 4- and 2-pole winding current controllers.

In the DCM simulation, the weight of the rotor is only assumed to act on the motor after 2s when the main 4-pole field has been established. This is achieved by either letting the mass of the rotor M_r to be very large between the time interval 0 to 2s or introducing an arbitrarily large artificial friction D which is only present during the first 2s of the simulation. Therefore, F_y^{feed} and F_x^{feed} of the position control loops are applied after 2s from the start of the simulation, in which both signals were set to be equal to the y- and x- direction load forces experienced by the motor.

In this simulation, F_y^{feed} = 235.36N, since the only load force acting in the y- direction is the rotor weight of 235.36N, and because no x- direction load force is applied to the motor, F_x^{feed} = 0N. In order to ensure that the free moving rotor does not hit the stator in the DCM simulation, an artificial spring force is also introduced which is governed by a tangent function, given by

$$\begin{aligned} F_{sp-y} &= \tan(2688.66y) \quad \text{for} -0.58 \le y \le 0.58 \\ F_{sp-x} &= \tan(2688.66x) \quad \text{for} -0.58 \le x \le 0.58 \end{aligned} \tag{8.17}$$

where y and x are the rotor displacements in the y- and x- directions respectively, as shown in Figure 8.4.

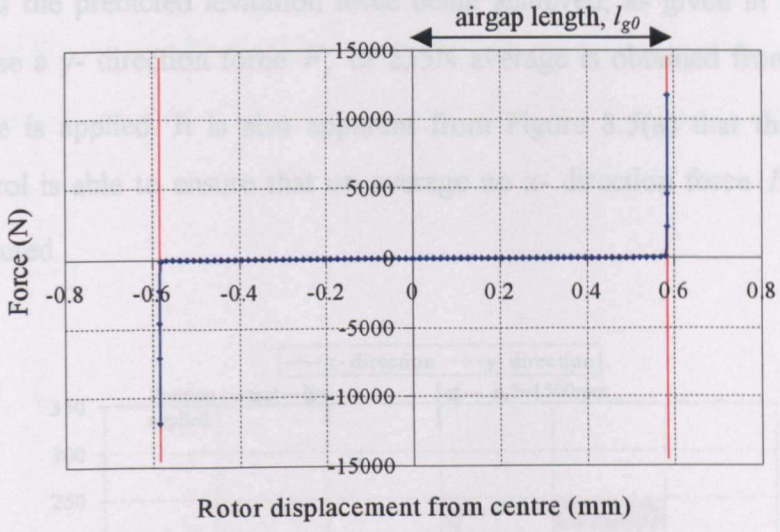

Figure 8.4: Tangent function of the artificial spring force

This function ensures that if and when the rotor experiences a displacement equal to the airgap length l_{g0} of 0.58mm, a large spring force comes into action to push the rotor back towards the centre of the motor.

The vector controlled linear bearingless motor simulated using the phase lead controller of equation (8.14) was unable to keep the rotor centred. However, when the bandwidth of the 2-pole levitation winding current controller was increased to 400Hz, i.e. similar to the bandwidth of the main 4-pole winding current control, the designed position control was able to maintain the non-rotating rotor at the centre of the motor. This is because when designing the position controller to have a bandwidth of 50Hz, the dynamics of the current controller was neglected. However, this is only true if the current controller bandwidth is much larger than the bandwidth of the position controller. Therefore, in all the simulations of the bearingless induction motor presented in this chapter, the bandwidth of 2-pole levitation current controller was increased to 400Hz. The new 2-pole current controller transfer function is

$$G_c = \frac{248.4(s+1500)}{s} \tag{8.18}$$

The result of the vector controlled linear bearingless motor simulation, with the 2-pole winding oriented by the controller angle $\hat{\theta}_o$ and a 2-pole current controller bandwidth of 400, shows the predicted levitation force being achieved, as given in Figure 8.5(a). This is because a y- direction force F_y of 235N average is obtained from the moment the load force is applied. It is also apparent from Figure 8.5(a) that the x- direction position control is able to ensure that on average no x- direction force F_x acts on the rotor, as expected.

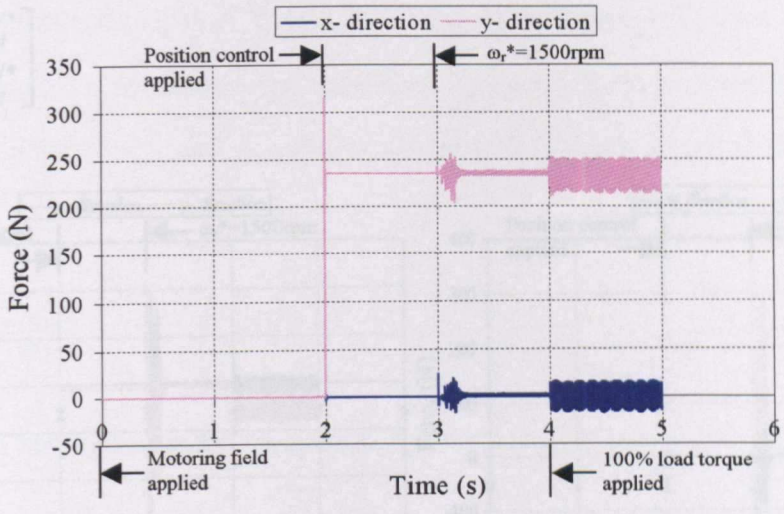

(a)

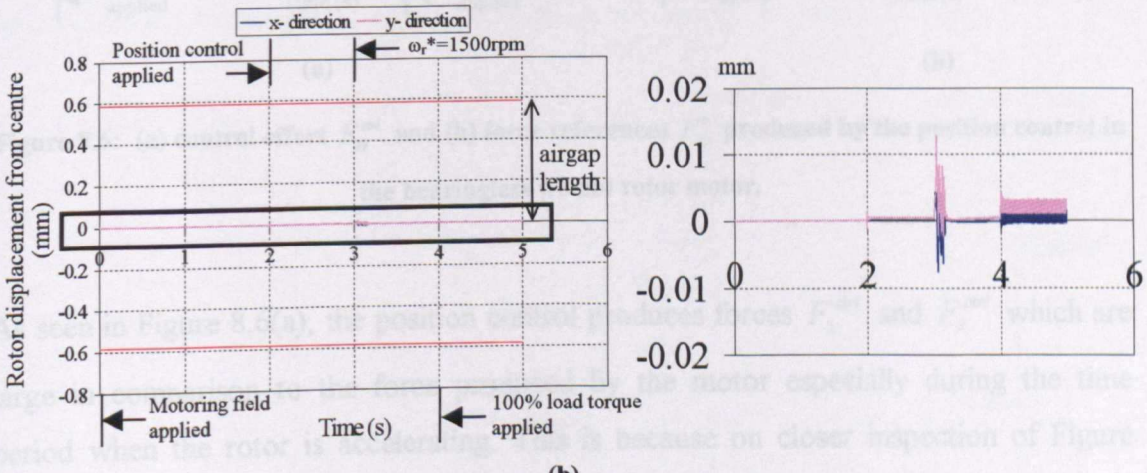

(b)

Figure 8.5: Vector controlled (a) forces and (b) rotor displacements from the centre in the x- and y-direction produced by the linear bearingless motor. For motor speed and torque see Figure 8.7.

The x- and y- direction displacements experienced by the rotor from the motor centre are as shown in Figure 8.5(b). It is clear from this figure that from 2s onwards, when the

position control is in operation, the rotor is maintained levitated at the centre of the motor even during acceleration (at 3-3.5s) and full load (after 4s) conditions. The control effort signals F_{xy}^{ctrl} and the reference forces F_{xy}^{*} obtained from the simulation are presented in Figure 8.6. These signals are obtained from the currents $i_{sdq\,ctrl}^{N}$ and i_{sdq}^{N*} shown in the position control of Figure 8.3 through the following relationships:

$$\begin{bmatrix} F_y^{ctrl} \\ F_x^{ctrl} \end{bmatrix} = \frac{1}{k_f} \begin{bmatrix} i_{sd\,ctrl}^{N} \\ i_{sq\,ctrl}^{N} \end{bmatrix} \tag{8.19}$$

$$\begin{bmatrix} F_y^{*} \\ F_x^{*} \end{bmatrix} = \frac{1}{k_f} \begin{bmatrix} i_{sd}^{N*} \\ i_{sq}^{N*} \end{bmatrix} \tag{8.20}$$

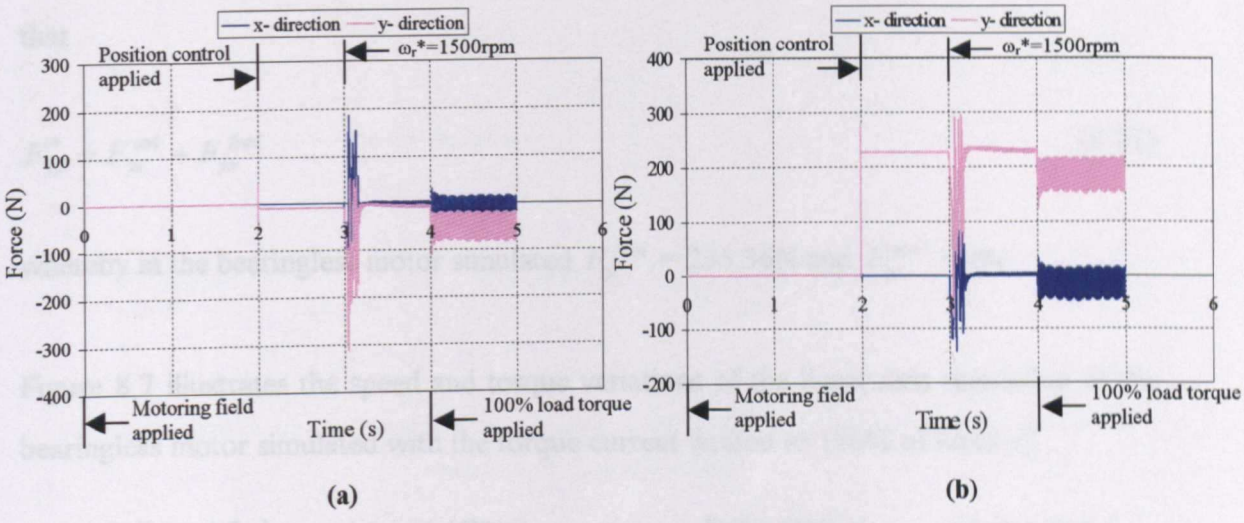

Figure 8.6: (a) control effort F_{xy}^{ctrl} and (b) force references F_{xy}^{*} produced by the position control in the bearingless wound rotor motor.

As seen in Figure 8.6(a), the position control produces forces F_y^{ctrl} and F_x^{ctrl} which are large in comparison to the force produced by the motor especially during the time period when the rotor is accelerating. This is because on closer inspection of Figure 8.5(b), it is observed that from 2s onwards, when the position control is in operation, the rotor experiences some displacements in the x- and y- direction. For example, in the time interval 3 to 3.5s coinciding with rotor acceleration, the average displacement observed in the positive y- direction is 5μm. Even though this displacement is minute, i.e. less than 0.9% of the airgap length, the associated unbalance magnetic force in the

y- direction produced by the rotor displacement, calculated using equation (8.3), is 104.1N. This force has to be counteracted by the force produced by the position controller F_y^{ctrl}. When full load is applied, the rotor experiences average displacements of 0.6μm and 2.1μm in the positive x- and y- directions respectively, which cause unbalance magnetic pull forces of 12.43N and 43.7N acting in the positive x- and y- directions. From Figure 8.6(a), the value of F_y^{ctrl} averages at -110N (negative sign indicating that the force is acting in the negative y- direction) during rotor acceleration whereas when full load is applied F_y^{ctrl} is –50.3N and F_x^{ctrl} is –14.5N. Therefore, the magnitudes and directions of F_y^{ctrl} and F_x^{ctrl} shown in Figure 8.6(a) are justified since these forces have to counteract the unbalance magnetic force produced by the rotor movement. The forces F_y^* and F_x^* shown in Figure 8.6(b) are expected due to the fact that

$$F_{yx}^* = F_{yx}^{ctrl} + F_{yx}^{feed} \tag{8.21}$$

whereby in the bearingless motor simulated $F_y^{feed} = 235.36\text{N}$ and $F_x^{feed} = 0\text{N}$.

Figure 8.7 illustrates the speed and torque variations of the linear iron simulation of the bearingless motor simulated with the torque current limited to 116% of rated i_{sq}^M.

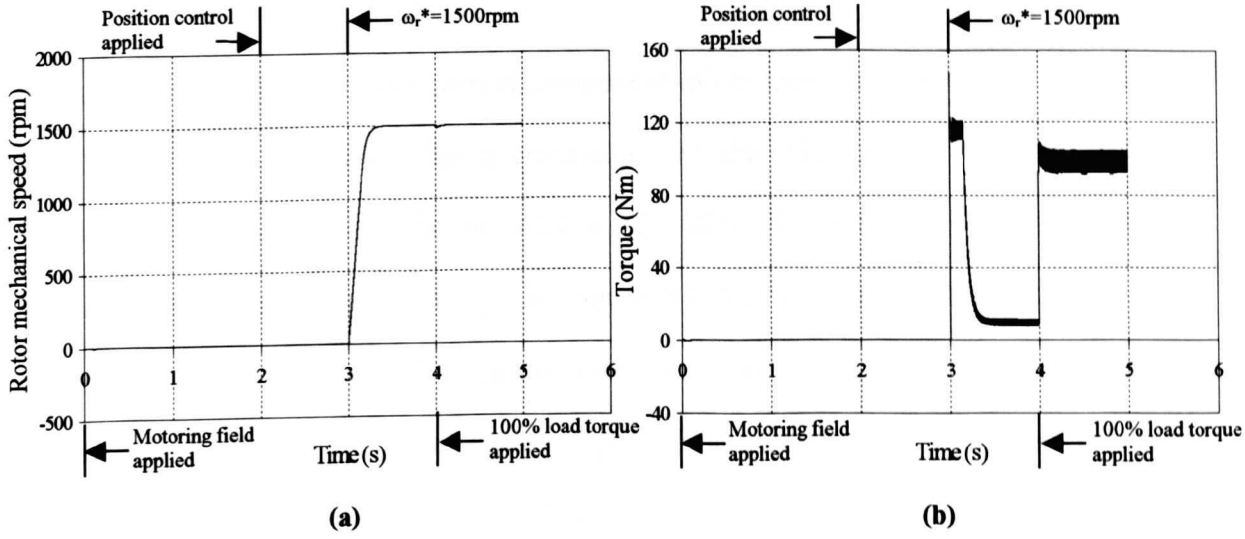

Figure 8.7: (a) speed and (b) torque variation of the vector controlled 4+2 pole wound rotor linear bearingless IM.

The dq- axis stator currents of the main 4-pole winding and 2-pole levitation winding in the motor are as shown in Figure 8.8. As observed in Figure 8.8(a), the dq- axis stator currents i_{sd}^{M} and i_{sq}^{M} of the 4-pole motoring winding are similar to that obtained in the bearing relief simulation shown in Figure 7.17(a). On the other hand, the behaviour of the 2-pole levitation currents i_{sd}^{N} and i_{sq}^{N}, oriented onto the peak 4-pole airgap field by $\hat{\theta}_o$, are slightly different to that in the bearing relief scheme since they are dependent on F_y^* and F_x^* respectively based on the relationship given by equation (8.16).

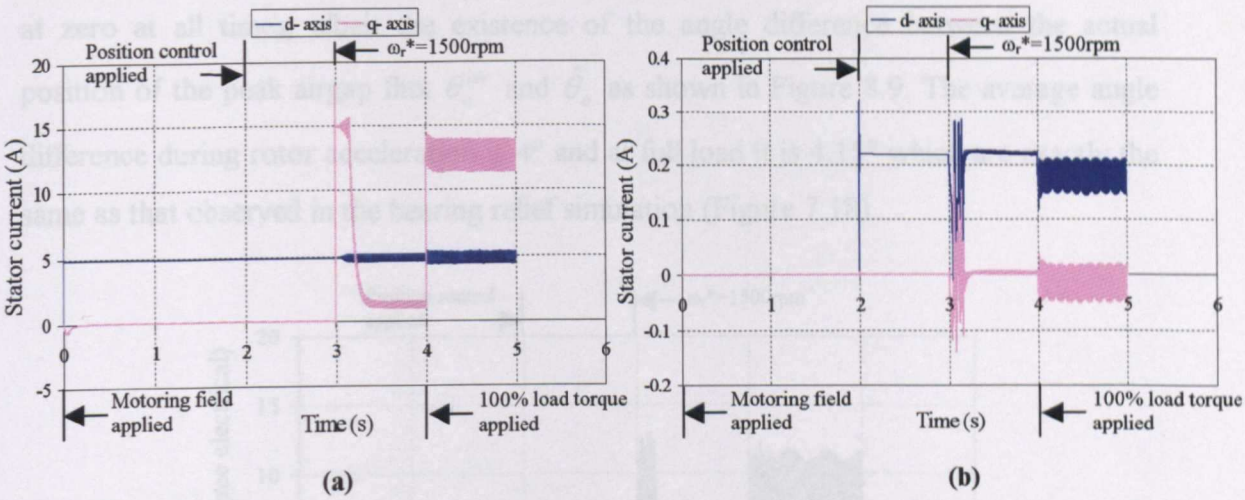

Figure 8.8: Stator current variation of the vector controlled linear bearingless IM: (a) 4-pole winding (b) 2-pole winding.

From Figure 8.8(b), the d- axis current component of the levitation winding i_{sd}^{N} obtained is 0.22A between 2s and 3s. This is consistent with the value of i_{sd}^{N*} calculated using equation (8.16) since during this time interval $F_y^* = 226.17$N, as shown in Figure 8.6(b). Similarly, the average value of i_{sq}^{N}, in Figure 8.8(b), throughout the simulation is consistent with the value of i_{sq}^{N*} calculated using the same equation with F_x^* taken from Figure 8.6(b). The value of the peak 4-pole fundamental field B_o^M used in the calculations was 0.9T with the values of the 2-pole ($N = 1$) levitation winding factor k_{ws}^{N}, total number of turns per phase N_{ts}^{N}, and magnetizing inductance L_o^N are as given by Table 5.4.

The results presented in this section are based on an MFO vector control scheme in which the 2-pole levitation winding is oriented onto the 4-pole airgap field using the angle $\hat{\theta}_o$ obtained using equation (8.15). In Section 7.2.1, it has been shown that in the simulation of the vector controlled wound rotor motor, the angle $\hat{\theta}_o$, provided by the controller, could not accurately predict the position of the peak 4-pole airgap field. This caused a non-zero F_x to be produced in the vector controlled bearing relief motor simulation (refer Section 7.4) during rotor acceleration and on load even though F_x^* is set to zero. However, with the position control present, the force F_x can be maintained at zero at all times, albeit the existence of the angle difference between the actual position of the peak airgap flux θ_o^{air} and $\hat{\theta}_o$ as shown in Figure 8.9. The average angle difference during rotor acceleration is 4° and at full load it is 4.15° which are exactly the same as that observed in the bearing relief simulation (Figure 7.18).

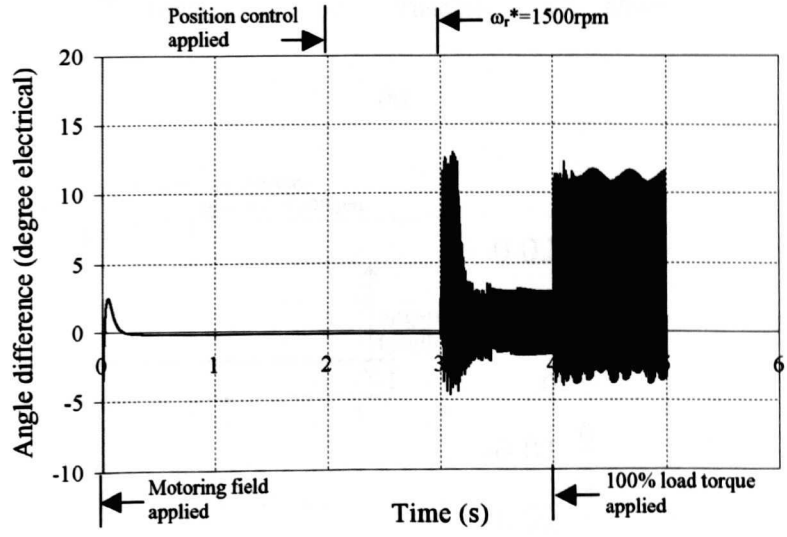

Figure 8.9: Angle difference between the actual peak airgap flux position θ_o^{air} and the position predicted by the controller $\hat{\theta}_o$ in the bearingless induction motor.

Therefore, the position controller placed in the vector control scheme of the bearingless induction motor produces the required forces to levitate the rotor as predicted by theory even though an error in the orientation angle of the 2-pole levitation winding is present. As is observed in the bearing relief simulation, the effects of error in the 2-pole winding

orientation angle is overcome by orienting the levitation winding using the actual 4-pole peak airgap flux position θ_o^{air} obtained from a spatial DFT of the flux densities of the airgap reluctance elements. Therefore, the vector controlled simulation of the bearingless motor under the same simulation conditions is repeated with the 2-pole winding currents, voltages and fluxes oriented using the angle θ_o^{air} instead of $\hat{\theta}_o$.

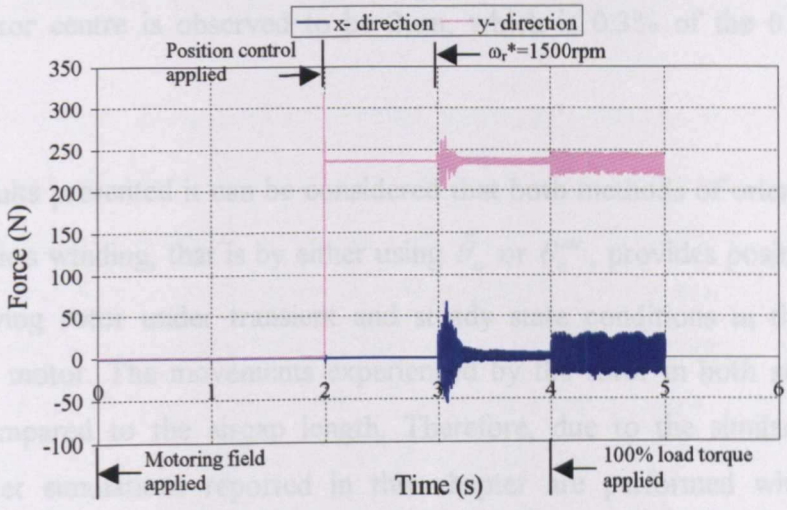

(a)

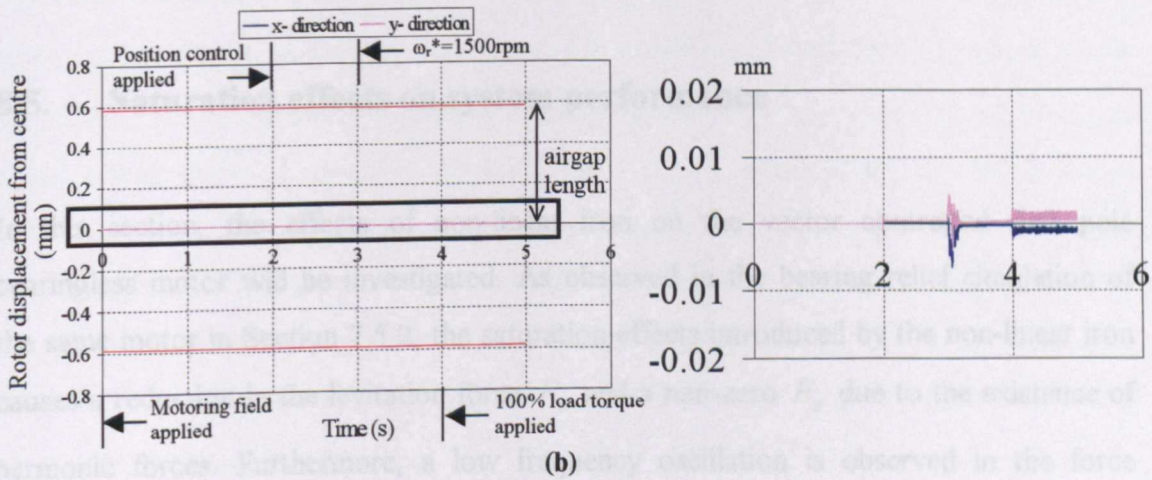

(b)

Figure 8.10: Vector controlled (a) forces and (b) rotor displacements from the centre in the x- and y- direction produced by the bearingless motor oriented using θ_o^{air}.

Figure 8.10(a) shows that the direct orientation of the bearingless motor produces the expected F_y of 235.4N and zero F_x on average. These force variations are also evidently similar to that in Figure 8.5(a), obtained when the 2-pole winding was

oriented using $\hat{\theta}_o$. The x- and y- direction displacements experienced by the rotor from the motor centre are also shown in Figure 8.10(b). The displacements shown in Figure 8.10(b) are much less compared to the displacements observed when the 2-pole winding is oriented using $\hat{\theta}_o$ shown in Figure 8.5(b). This is because θ_o^{air} ensures that the 2-pole winding currents, voltages and fluxes are more accurately aligned with the 4-pole peak airgap flux. The maximum displacement experienced by the rotor, in any direction, from the motor centre is observed to be 2μm, which is 0.3% of the 0.58mm airgap length.

From the results presented it can be considered that both methods of orientation for the 2-pole levitation winding, that is by either using $\hat{\theta}_o$ or θ_o^{air}, provides position control of the free moving rotor under transient and steady state conditions in the bearingless wound rotor motor. The movements experienced by the rotor in both simulations are negligible compared to the airgap length. Therefore, due to the similarities in these results, further simulations reported in this chapter are performed with the 2-pole levitation winding being oriented using the actual peak airgap flux position θ_o^{air} obtained from the DFT of flux densities in the airgap reluctance elements.

8.5. Saturation effects on system performance

In this section, the effects of non-linear iron on the vector controlled 4+2 pole bearingless motor will be investigated. As observed in the bearing relief simulation of the same motor in Section 7.5.2, the saturation effects introduced by the non-linear iron causes a reduction in the levitation force F_y and a non-zero F_x due to the existence of harmonic forces. Furthermore, a low frequency oscillation is observed in the force variations with time when the motor is subjected to a load torque. Therefore, it is evident that a non-linear iron simulation of the vector controlled bearingless IM should also be carried out. In the non-linear iron simulations presented in this section, the permeability of each reluctance element set to be of type 'non-linear iron' is obtained from a cubic spline interpolation of the B-H curve shown in Figure 7.21.

The non-linear iron bearingless wound rotor motor is controlled using the MFO vector control scheme whereby the main 4-pole winding is rotor field oriented and the 2-pole levitation winding being oriented onto the machine 4-pole peak airgap field position θ_o^{air}. The motor is simulated under the exact same conditions as that of Section 8.4 with the position controller designed in Section 8.3. However, it was observed that the position controller could not maintain the rotor levitated when the speed reference of 1500rpm was applied the motor at 3s, i.e. when the rotor starts accelerating.

As observed in Figure 8.1 it is observed that when motor torque is non-zero or i_{sq} is non-zero, larger unbalance magnetic pull force variation with rotor displacement is present in the motor compared to the no load variation. Furthermore, at full load the slope of the force-displacement variation is very different to the theoretical slope when the displacement is more than 50% of the airgap length. The design of the position control loop is dependent on the slope of the force-displacement variation since this slope determines the pole location of the plant in the position control loop shown in Figure 8.3. The position controller designed in Section 8.3 was based on the theoretical slope of $20.82\text{x}10^6\text{Nm}^{-1}$ and it was observed that the position controller design using this plant was unable to keep the rotor centered in the non-linear bearingless induction motor when i_{sq}^M is non-zero. Therefore, for non-linear bearingless induction motor simulation, a new position controller was designed with the plant having a force-displacement variation slope of $68.44\text{x}10^6\text{Nm}^{-1}$ which is the slope of the 'full load simulation' curve of Figure 8.1 in the rotor displacement region of 0.3 to 0.45mm. This new compensator is designed in the continuous s-plane, using the root locus technique, for the position control loop shown in Figure 8.3, to achieve a nominal closed loop bandwidth of 15Hz and a damping factor ς of 1.0. Hence, the transfer function of the designed compensator is given by

$$G_{c-nl}(s) = 207.05 \times 10^3 \frac{(s+1689)}{(s+5000)} \tag{8.22}$$

With this new controller, the simulation of the bearingless motor under non-linear iron conditions is repeated with feed forward signals $F_y^{feed} = 235.36\text{N}$ and $F_x^{feed} = 0\text{N}$ applied at 2s after the start of the simulation.

Figure 8.11 illustrates the forces produced with the new position controller as well as the displacements experienced by the free moving rotor in the x- and y- directions. It is clear that the position controller given by (8.22) is able to keep the rotor at the centre of the motor from the moment the motor experiences its rotor weight (at 2s).

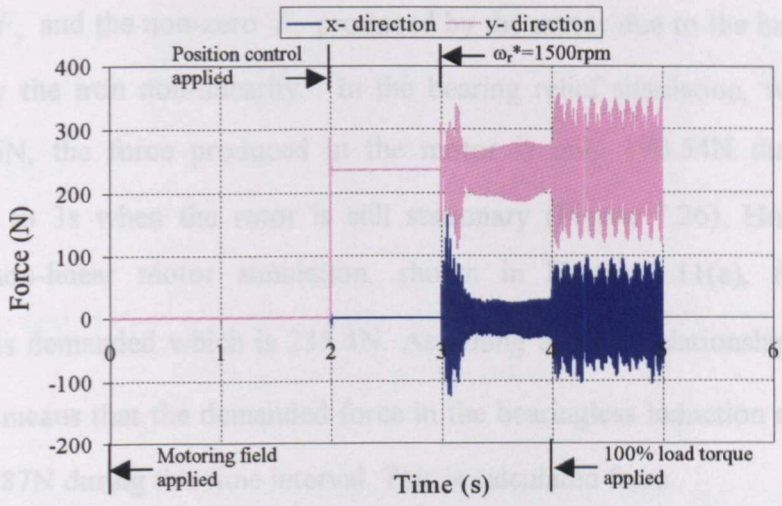

(a)

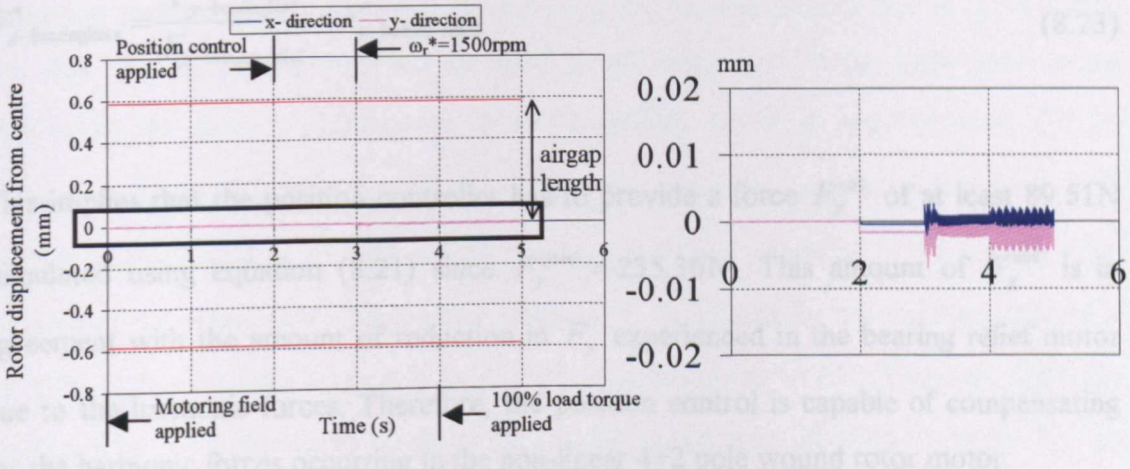

(b)

Figure 8.11: Vector controlled (a) forces and (b) rotor displacements from the centre in the x- and y- direction produced by the non-linear bearingless motor.

However, as observed in Figure 8.11, the force variations F_y and F_x as well as the rotor displacements in the y- and x- direction each experiences a low frequency oscillation of 9.5Hz during full load condition as observed previously in the bearing relief motor. The 9.5Hz oscillation may be considered as a plant disturbance. As such, the oscillations will appear in the force demands (Figure 8.12(b)) in order to counteract

the disturbance and hence keep the displacements near to their zero demands. Since the position controller bandwidth (15Hz) is higher than the disturbance frequency, the 9.5Hz position oscillation is small as seen in Figure 8.11(b) (i.e. 3μm peak-to-peak in both the y and x displacements). The position controllers are able to compensate for the reduction in F_y and the non-zero F_x produced by the motor due to the harmonic forces introduced by the iron non-linearity. In the bearing relief simulation, with a demand F_y^* of 235.36N, the force produced in the motor is only 170.54N during the time interval of 2 to 3s when the rotor is still stationary (Figure 7.26). However, in the bearingless non-linear motor simulation, shown in Figure 8.11(a), the force F_y produced is as demanded which is 235.4N. Assuming a linear relationship between F_y and F_y^*, this means that the demanded force in the bearingless induction motor F_y^* can be set as 324.87N during this time interval. This is calculated from

$$F^*_{y-\text{bearingless}} = \frac{F_{y-\text{bearingless}}}{F_{y-\text{bearing relief}}} \times F^*_{y-\text{bearing relief}} \tag{8.23}$$

This implies that the position controller has to provide a force F_y^{ctrl} of at least 89.51N calculated using equation (8.21) since $F_y^{feed} = 235.36\text{N}$. This amount of F_y^{ctrl} is in agreement with the amount of reduction in F_y experienced in the bearing relief motor due to the harmonic forces. Therefore, the position control is capable of compensating for the harmonic forces occurring in the non-linear 4+2 pole wound rotor motor.

The values of F_y^{ctrl} and F_y^* calculated above for the bearingless motor are consistent with Figure 8.12 which shows the control effort signals F_{xy}^{ctrl} and the reference forces F_{xy}^* obtained from the simulation.

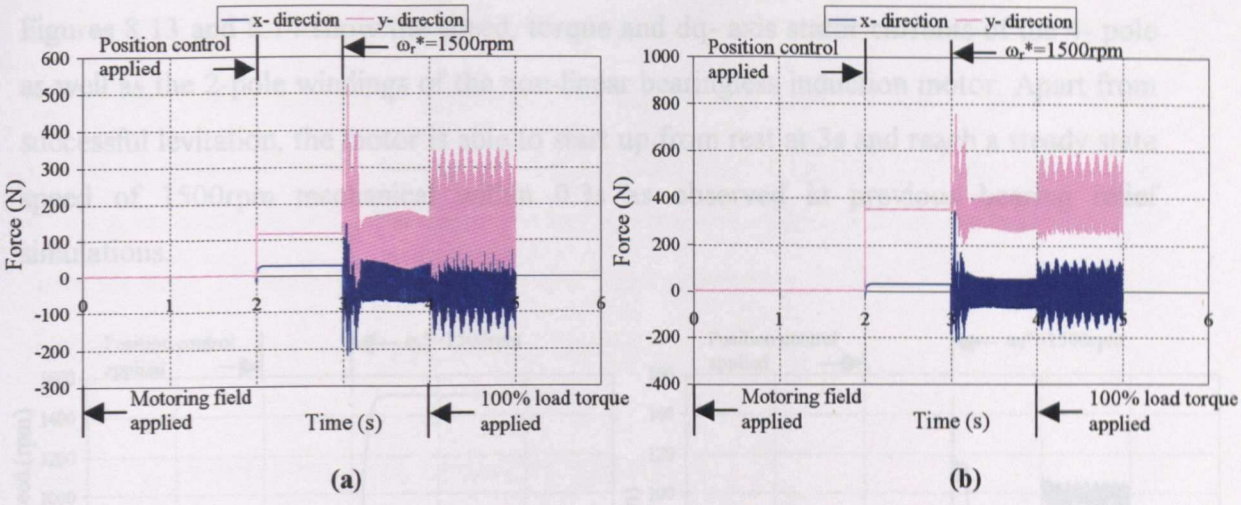

Figure 8.12: (a) control effort F_{xy}^{ctrl} and (b) force references F_{xy}^{*} produced by the position control in the non-linear bearingless motor.

Another issue encountered in the non-linear iron bearing relief simulation is the F_x present in the motor due to harmonic force even when zero reference F_x^* is applied. Referring to Figure 7.26, the force produced in the bearing relief motor is -11N during the time interval of 2 to 3s when the rotor is still stationary. In the bearingless motor simulation the force F_x produced is as demanded, which is approximately 0N on average as shown in Figure 8.11(a). Therefore, the controller must provide a force F_x^{ctrl} in the region of 11N to compensate for the negative force observed in the bearing relief simulation. In actual fact, the control effort F_x^{ctrl} produced by the position control is 28.03N during the time interval 2 to 3s as shown in Figure 8.12(b). Even so, the force produced by the motor could be maintained at 0N as required. In order to create F_x^{ctrl} of 28.03N, the rotor has to move in the negative x- direction as shown in Figure 8.12(b). However, this movement is very small, i.e. 0.4μm. The displacements experienced by the rotor are very small, in region of micrometers, even after experiencing transient conditions during rotor acceleration and load. Hence it can be said that the vector controlled bearingless induction motor with the position controller of (8.22) is successful in producing sustainable rotor levitation even under non-linear iron conditions.

Figures 8.13 and 8.14 show the speed, torque and dq- axis stator currents of the 4- pole as well as the 2-pole windings of the non-linear bearingless induction motor. Apart from successful levitation, the motor is able to start up from rest at 3s and reach a steady state speed of 1500rpm mechanical within 0.3s as observed in previous bearing relief simulations.

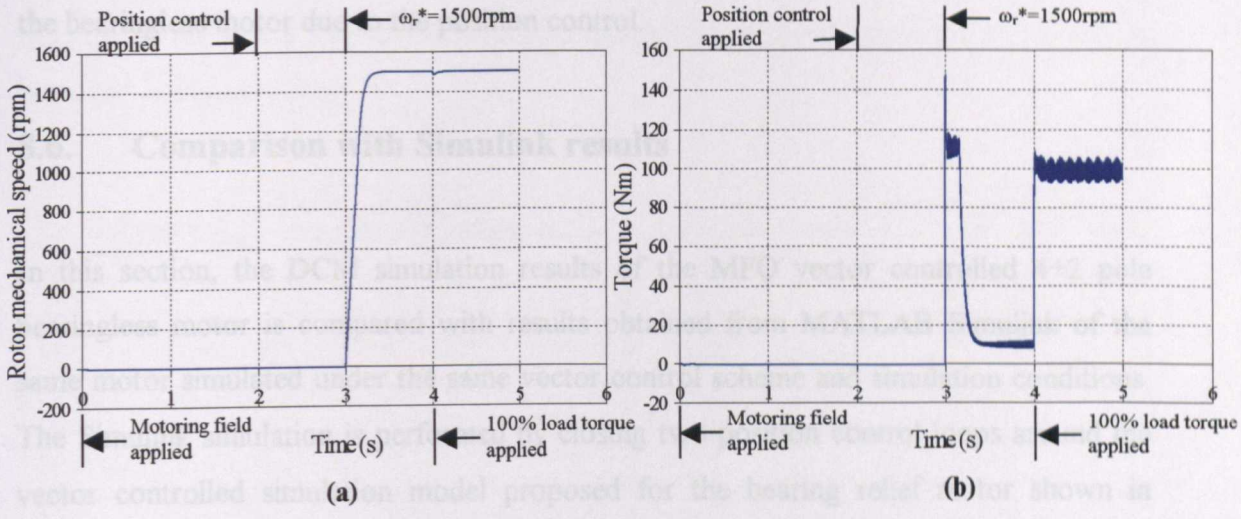

Figure 8.13: (a) speed and (b) torque variation of the vector controlled 4+2 pole bearingless non-linear motor.

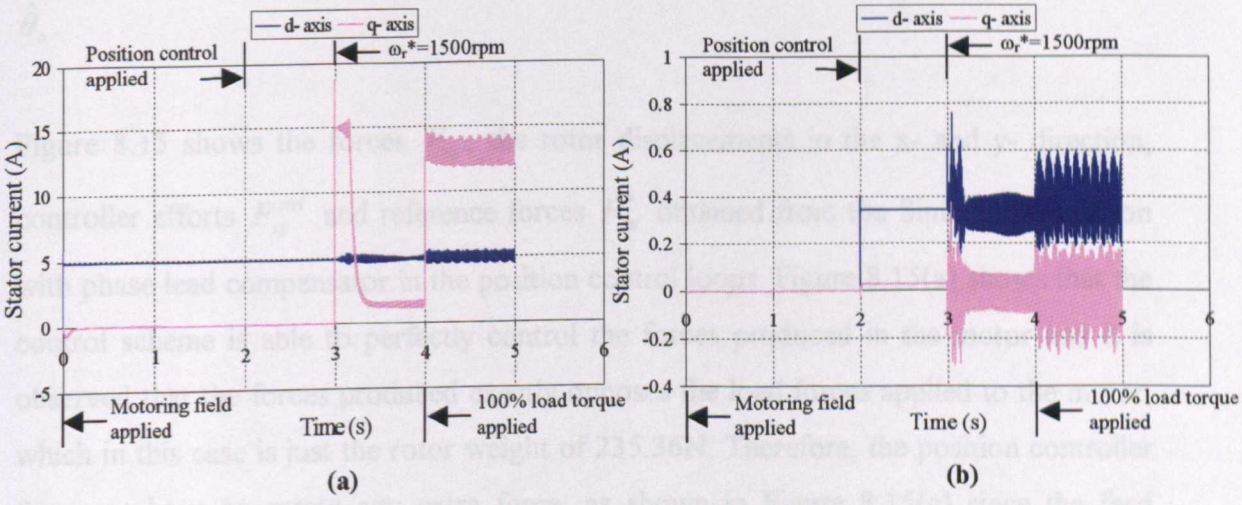

Figure 8.14: Stator current variation of the vector controlled bearingless non-linear IM: (a) 4-pole winding (b) 2-pole winding.

The bearingless motor also exhibits the 9.5Hz oscillation during full load and this is apparent in the torque variation of Figure 8.13(b). This behaviour is also present in the

dq- axis currents of the 4-pole and 2-pole winding. Figure 8.14(a) illustrates that i_{sd}^{M} and i_{sq}^{M} of the 4-pole winding is unaffected by the position control and is similar to the variations observed in the non-linear bearing relief motor (Figure 7.25(a)). The 2-pole winding currents on the other hand are expected to be different from the bearing relief currents since i_{sd}^{N} and i_{sq}^{N} are related to the force references F_y^* and F_x^* which varies in the bearingless motor due to the position control.

8.6. Comparison with Simulink results

In this section, the DCM simulation results of the MFO vector controlled 4+2 pole bearingless motor is compared with results obtained from MATLAB Simulink of the same motor simulated under the same vector control scheme and simulation conditions. The Simulink simulation is performed by closing two position control loops around the vector controlled simulation model proposed for the bearing relief motor shown in Figure 4.7. As in the Simulink bearing relief simulation presented in Section 5.4.4, the bearingless motor simulation is carried out with the 2-pole winding currents, voltages and fluxes being oriented onto the 4-pole peak airgap field using the controller angle $\hat{\theta}_o$.

Figure 8.15 shows the forces F_{xy}, the rotor displacements in the x- and y- direction, controller efforts F_{xy}^{ctrl} and reference forces F_{xy}^* obtained from the Simulink simulation with phase lead compensator in the position control loops. Figure 8.15(a) shows that the control scheme is able to perfectly control the forces produced in the motor and it is observed that the forces produced exactly opposes the load forces applied to the motor, which in this case is just the rotor weight of 235.36N. Therefore, the position controller does not have to create any extra force, as shown in Figure 8.15(c) since the feed forward signal is sufficient to create the required 2-pole levitation winding currents. This in turn means that the rotor does not experience any displacement as seen in Figure 8.15(b) implying perfect rotor levitation at the motor centre when simulated using the *dq* representation of the motor.

However, it is apparent from the DCM simulation result of the linear iron bearingless motor (Section 8.4) that this is untrue due to the fact that the force created in the motor will always include harmonic forces from harmonic field interactions. Even though the harmonic forces are small in the linear iron motor (only approximately 3N), this will always cause the force produced in the motor to be slightly more or less than the load force causing the rotor to be displaced from the centre and remain off-centre due to the inability of the phase lead compensator to eliminate any steady state errors present as observed in Figure 8.5(b).

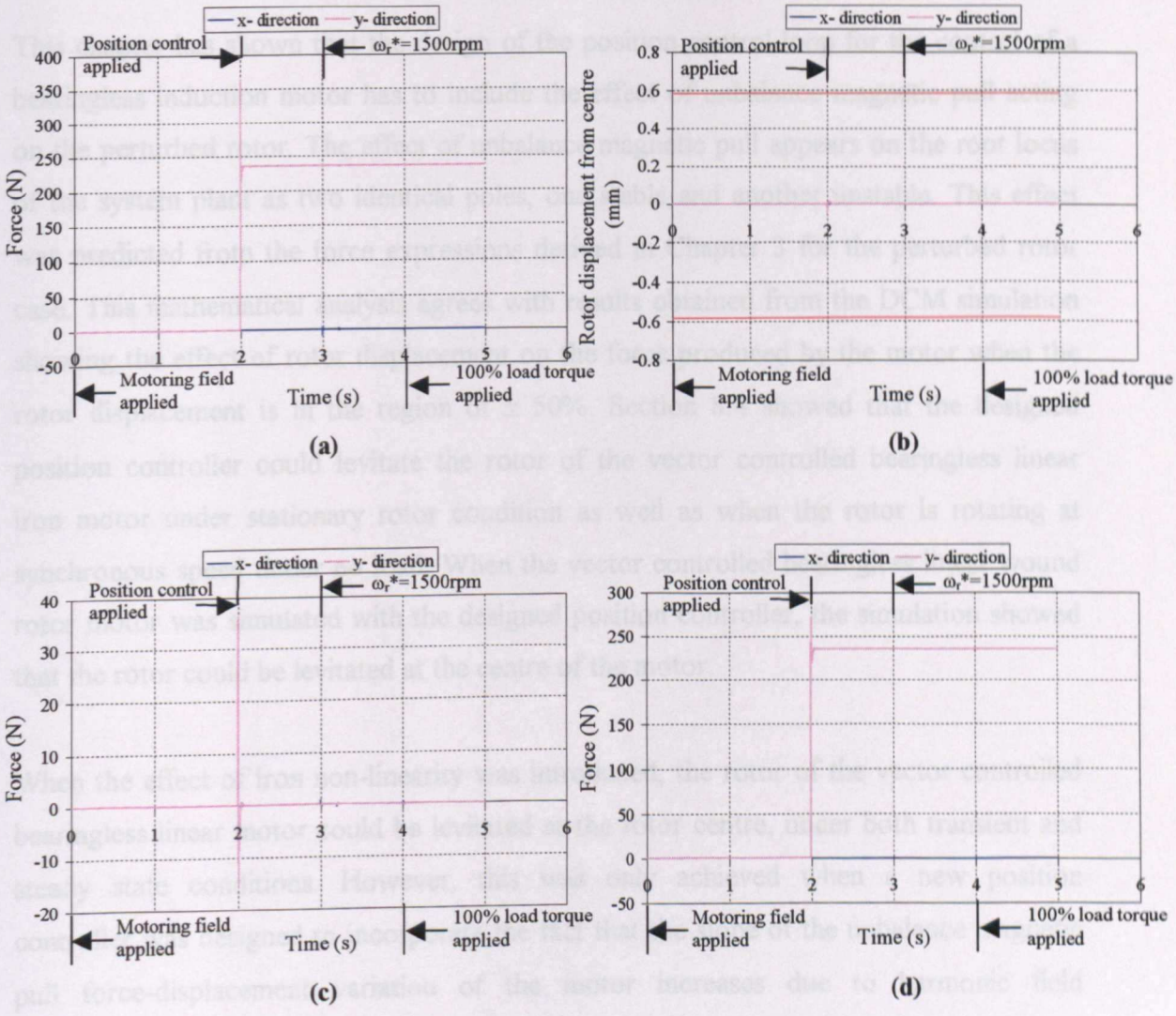

Figure 8.15: Simulink simulation results of the bearingless wound rotor motor (with phase lead compensators): (a) F_{xy}, (b) rotor displacements in x- and y- direction, (c) controller effort and (d) x- and y- direction reference forces.

This highlights the insufficiency of using the 2- axis lumped parameter model to simulate the behaviour of the bearingless motor in which effects of harmonic field interactions are significant. Moreover, because the 2- axis lumped parameter model utilised in Simulink simulation is unable to fully model a non-linear motor, no insight into the non-linear effects on the rotor levitation in the bearingless motor can be obtained.

8.7. Chapter summary

This chapter has shown that the design of the position control loop for the control of a bearingless induction motor has to include the effect of unbalance magnetic pull acting on the perturbed rotor. The effect of unbalance magnetic pull appears on the root locus of the system plant as two identical poles, one stable and another unstable. This effect was predicted from the force expressions derived in Chapter 3 for the perturbed rotor case. This mathematical analysis agrees with results obtained from the DCM simulation showing the effect of rotor displacement on the force produced by the motor when the rotor displacement is in the region of ± 50%. Section 8.4 showed that the designed position controller could levitate the rotor of the vector controlled bearingless linear iron motor under stationary rotor condition as well as when the rotor is rotating at synchronous speed under no load. When the vector controlled bearingless linear wound rotor motor was simulated with the designed position controller, the simulation showed that the rotor could be levitated at the centre of the motor.

When the effect of iron non-linearity was introduced, the rotor of the vector controlled bearingless linear motor could be levitated at the rotor centre, under both transient and steady state conditions. However, this was only achieved when a new position controller was designed to incorporate the fact that the slope of the unbalance magnetic pull force-displacement variation of the motor increases due to harmonic field components interacting with the main motoring field. This is in contrast to the bearing relief motor whereby only the linear iron motor is able to produce sufficient levitation force to compensate for the rotor weight acting on the bearings holding the rotor in place. The bearingless motor was also capable of eliminating the F_y reduction and non-

zero F_x observed in the bearing relief motor due to the incorporation of iron non-linearity. This is because the position controller produces the required force to compensate for the harmonic forces present in the non-linear iron motor. The low frequency oscillation observed during load in the non-linear iron simulation of the bearing relief motor is present in the non-linear bearingless motor simulation, but is only of marginal significance in the closed loop position control. Further investigations into the cause of this low frequency oscillation is recommended for future work into the study of bearingless induction motors.

Chapter 9

Numerical issues relating to the DCM software simulations

9.1. Introduction

The numerical solution technique used within the DCM software (refer to Section 2.4) is controlled by several parameters to ensure that convergence and accuracy is achieved. The time step control loop is determined by a user-defined maximum time step Δt_{max}. The state equations in the model are solved successfully at each time step when the residual error from the Newton Raphson linearisation is less than a user-defined tolerance, tol_{NR}. Therefore, tol_{NR} will determine how accurately the state equations are solved at each time step. The linear equation solver has two control parameters, i.e. the *threshold* and a tolerance tol_{Solver}. The *threshold* parameter determines the partial fill of the incomplete LU decomposition preconditioner. A zero or negative *threshold* value means that a complete LU decomposition is performed on the matrix, thus requiring only one iteration of the linear equation solver to obtain the solution. However, this requires a large amount of memory. Therefore, the *threshold* parameter allows for control over the trade off between memory usage and computation time. The convergence of the linear equation solver is obtained when the rms residual error is less than a tolerance value, tol_{Solver} predefined by the user. In all the simulations presented in Chapters 5, 6, 7 and 8, the following values of control parameters were used:

$\Delta t_{max} = 50\mu s$	$tol_{Solver} = 1x10^{-7}$
$tol_{NR} = 1x10^{-6}$	$threshold = 1x10^{-5}$

Table 9.1: Numerical solver control parameter values used.

In this chapter, general guidelines in choice of the numerical solver control parameters will be presented. However, the guidelines presented here might not be optimal for all applications of the DCM software but has been proven to be robust for use when modelling the bearingless induction motors considered in this thesis.

9.2. Choice of maximum time step

The DCM simulation starts with a time step value Δt equal to the user-defined maximum time step Δt_{max}. If the residual error during the Newton Raphson cycle at a particular simulation time $t + \Delta t$ increases compared to that at the previous time step t, or the linear equation solver fails to solve the linear equations within a predefined number of iterations, the time step Δt is halved. Therefore, the choice of Δt_{max} for each simulation is rather crucial. If a large value of Δt_{max} is chosen, the efficiency of the Newton Raphson linearisation is reduced. Hence, at each time step the number of iteration steps required is increased, especially in the case of a non-linear iron motor. Furthermore, a large time step can cause the predicted solution to be far from the actual solution which also increases the number of iterations required to arrive at the solution. There is also the possibility of divergence if the prediction is too far away from the actual solution. On the other hand, choosing small values of Δt_{max} ensures convergence, as the Newton Raphson linearisation of the equations becomes more efficient, thus requiring less number of iterations to achieve convergence. However, the use of small time step values will increase the total computation time of the simulation.

Investigation of the choice of Δt_{max} to achieve reasonable computation time whilst obtaining reasonable results was performed on the vector controlled simulation of the non-linear bearingless wound rotor IM presented in Section 8.5. Three Δt_{max} values were chosen, i.e. 100μs, 50μs and 25μs, with all other solver control parameters remaining unchanged as given in Table 9.1. The computation time and memory usage required to simulate the motor for 5s are summarised in Table 9.2.

Δt_{max}	Computation time	Memory usage
100μs	1hour 4 minutes	3.28MB
50μs	1 hour 35 minutes	3.28MB
25μs	2 hours 48 minutes	3.28MB

Table 9.2: Computation time and memory usage for simulations with different values of Δt_{max}.

As expected, the largest Δt_{max} considered in the investigation, i.e. 100μs, is simulated with the least computation time. However, the results obtained showed that it produces almost twice the amount of overshoot in the x- direction displacement experienced by the rotor during the start of rotor rotation (at 3s) compared to the results obtained when Δt_{max} = 50μs (refer to Figure 8.11). The difference in overshoot is approximately 42% of the actual airgap length (0.584mm) in the motor which is considered to be quite large. On the other hand, the results obtained in the simulation using Δt_{max} = 25μs were found to be very similar to that of 50μs (presented in section 8.5) with a maximum x-direction displacement overshoot difference of only 6% of the actual airgap length. However, the computation time required for the Δt_{max} = 25μs simulation is almost double the time required to simulate with a 50μs maximum time step. Hence, it can be concluded that the choice of Δt_{max} = 50μs is realistic as it is able to produce reasonably accurate results within a sensible computation time. It is observed that for all three simulations, the memory usage is unchanged at 3.28MB showing that the choice of Δt_{max} does not affect the amount of memory usage during the simulation.

9.3. Newton Raphson iteration loop tolerance parameter

The numerical accuracy of the DCM simulation results is principally determined by the tolerance value tol_{NR} set on the Newton Raphson iteration loop. In each iteration loop, the residual error from the Newton Raphson linearisation is compared with the value tol_{NR}. When the rms error is less than tol_{NR} and within the predetermined maximum number of iterations allowed, the loop is terminated and the results are output to a file. Generally, in all simulations presented in this thesis, the number of Newton Raphson

iterations required is found to be less than 10. Therefore, the choice of the maximum number of iterations for the Newton Raphson loop is rather arbitrary provided that convergence is achieved at each time step. Having chosen the maximum number of iterations allowed in the Newton Raphson loop, setting a large tolerance tol_{NR} value will mean that the state equations are not solved with sufficient accuracy. This will produce incorrect results and can lead to non-physical behaviour. If too small a value is chosen for tol_{NR}, more iterations are required to reach convergence and there is a possibility of it not being achieved at all (for example when tol_{NR} is near machine precision) due to rounding errors. Hence, the accuracy of the DCM software simulations is sensitive to the choice of tol_{NR}.

As was performed for the maximum time step control parameter, a study on the choice of tol_{NR}, keeping all other parameters unchanged, to achieve reasonable results was performed on the vector controlled simulation of the non-linear bearingless wound rotor IM presented in Section 8.5. The computation time and memory usage required to simulate the motor for 5s is summarised in Table 9.3.

tol_{NR}	Computation time	Memory usage
$1x10^{-3}$	Simulation did not converge	-
$1x10^{-4}$	1 hour 28 minutes	3.28MB
$1x10^{-6}$	1 hour 35 minutes	3.28MB
$1x10^{-9}$	1 hour 50 minutes	3.20MB

Table 9.3: Computation time and memory usage for simulations with different values of tol_{NR}.

It is shown that the largest tolerance value allowed for the bearingless motor simulation is $1x10^{-4}$ since the use of tol_{NR}= $1x10^{-3}$ resulted in a failure of the software. The computation times required to simulate all three cases are comparable with a maximum difference of 22 minutes between the tol_{NR} values of $1x10^{-4}$ and $1x10^{-9}$. Furthermore, the memory usage is constant with changes in tol_{NR}. Therefore, it can be said that the computation time and memory usage of the DCM software is insensitive to the Newton Raphson tolerance tol_{NR} parameter. It was found that the results obtained from the three

simulations having different tol_{NR} values were found to be very similar to that presented in Section 8.5 (tol_{NR} = 1x10^{-6}). Therefore, the results presented in this thesis, which used tol_{NR} of 1x10^{-6}, could have been simulated using a tolerance of 1x10^{-4} without greatly affecting the accuracy of the results.

9.4. Linear equation solver control parameters

The linear equation solver of the DCM software is controlled by two control parameters, i.e. the *threshold* and a tolerance tol_{Solver}. The general guidelines in choosing both these parameters for the bearingless induction motor model application are presented in this section.

a) *Threshold* parameter

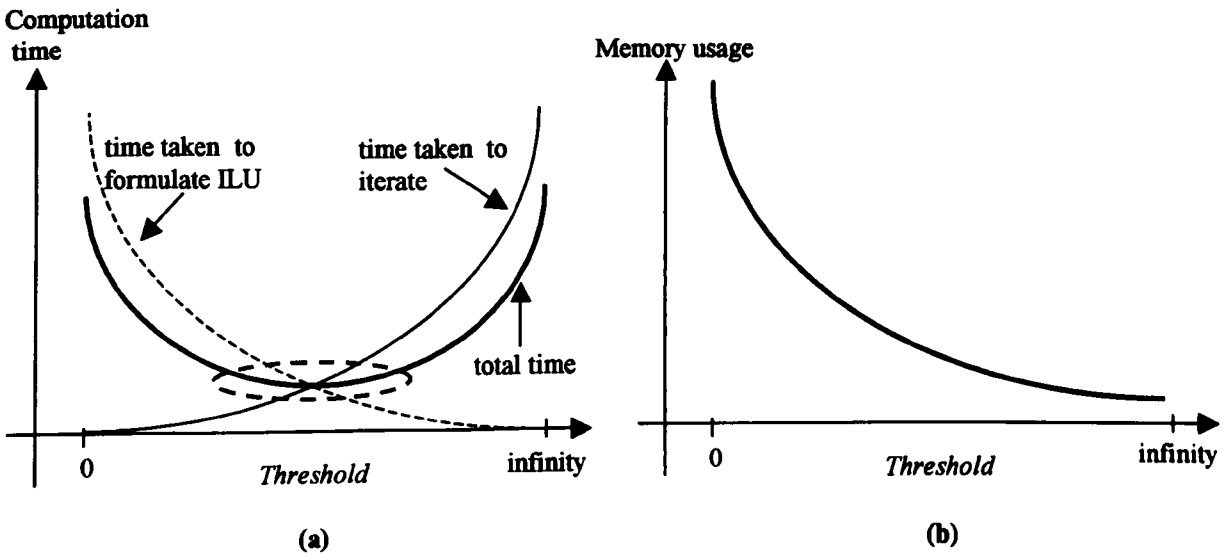

Figure 9.1: The effect of *threshold* on computation time and memory usage.

The *threshold* parameter determines the partial fill of the incomplete LU decomposition preconditioner. A zero or negative *threshold* value means a complete LU decomposition is performed on the matrix and thus subsequently requires a short iteration time since only one iteration of the linear equation solver is necessary. However, complete LU decomposition requires a long time to formulate the complete LU matrix (proportional to N^3) and a large memory usage is involved. An infinite *threshold* value on the other

hand, requires hardly any time to formulate the incomplete LU (ILU) matrix and uses minimal memory but needs a large computation time to iterate the equations. However, convergence may not be achieved in this case. Therefore, the *threshold* parameter allows for control over the trade off between memory usage and computation time based on the graphs shown in Figure 9.1. Ideally the *threshold* value is chosen to be at the minimum point of the total time curve in Figure 9.1(a) as this ensures the least amount of computation time with reasonable memory usage. However, generally the *threshold* value is chosen to be as small as possible (within the ellipse indicated in Figure 9.1(a)) to achieve convergence of the linear equation solver. In all the DCM simulations presented in this thesis, a *threshold* value of $1x10^{-5}$ was used.

b) Solver tolerance tol_{Solver}

Similar to the Newton Raphson iteration loop tolerance parameter tol_{NR}, the linear equation solver tolerance tol_{Solver} parameter controls the accuracy of the linear equations that is being solved. If a large value of tol_{Solver} is used, the results from the linear equation solver will not be solved accurately enough, causing the prediction of the next iteration to be far from the actual solutions. This can cause the number of iterations required to increase and might even cause divergence from the solution. Generally the value of tol_{Solver} should be smaller than tol_{NR} to ensure that the linear equations are solved to a higher accuracy compared to the linearisation done by the Newton Raphson. In the simulations carried out in this thesis, a general rule of choosing tol_{Solver} to be 10 times less than tol_{NR} was found to be sufficient.

Investigation of the choice of tol_{Solver} to achieve sensible computation time whilst obtaining reasonable results was performed on the vector controlled simulation of the non-linear bearingless wound rotor IM presented in Section 8.5. Three tol_{Solver} values were chosen, i.e. $1x10^{-5}$, $1x10^{-7}$ and $1x10^{-10}$, with all other solver control parameters remaining unchanged as given in Table 9.1. The computation time and memory usage required to simulate the motor for 5s is summarised in Table 9.4.

tol_{NR}	Computation time	Memory usage
$1x10^{-5}$	1 hour 24 minutes	3.28MB
$1x10^{-7}$	1 hour 35 minutes	3.28MB
$1x10^{-10}$	1 hour 30 minutes	3.28MB

Table 9.4: Computation time and memory usage for simulations with different values of tol_{Solver}.

As expected, the computation time and memory usage in the three cases are comparable indicating that they are insensitive to changes in tol_{Solver}. In addition, the results obtained from the three simulations show very close similarities indicating the simulations of the bearingless motor, carried out with $tol_{Solver} = 1x10^{-7}$, could have been performed with the tolerance set to $1x10^{-5}$.

9.5. Chapter summary

From the analysis presented in this chapter, it can be concluded that the computation time for each DCM simulation is principally affected by the maximum time step Δt_{max} parameter and the *threshold* parameter of the linear equation solver. However, the *threshold* parameter is chosen based on a trade off between the memory usage and the computation time. Therefore, having chosen the smallest *threshold* parameter value that provides robust convergence, within a reasonable amount of memory usage, the user is able to determine a suitable Δt_{max} value to provide sufficiently fast computation. Although large Δt_{max} values give a fast computation, it reduces the efficiency of the Newton Raphson linearisation and can cause poor prediction of the solutions that in turn affects the solver convergence. Therefore, there is an upper limit to the choice of Δt_{max}.

The accuracy of the equations solved by the solver is generally determined by the Newton Raphson iteration loop tolerance tol_{NR} and the linear equation solver tolerance tol_{Solver}. Generally, tol_{Solver} is chosen to be smaller than tol_{NR} (roughly 10 times less) to ensure relatively accurate solution of the linear equations. On the other hand, the choice of tol_{NR} is set by an upper limit since a large tol_{NR} will mean that the state equations are

not solved with sufficient accuracy, resulting in wrong results and the possibility of divergence in the solver. Hence, the accuracy of the DCM software simulations is most sensitive to the choice of tol_{NR} compared to tol_{Solver}. Lastly, the amount of memory usage is only determined by the *threshold* parameter and is insensitive to changes in other control parameters of the solver.

Finally, it can be concluded that the values of the control parameters used in all the DCM simulations presented in this thesis are sufficient to achieve accurate results for the investigation of bearingless induction motors.

Chapter 10

Conclusions and future work

Previous research into the induction motor type bearingless motors has shown problems related to achieving successful rotor levitation. The aim of this thesis was to utilize a modelling approach to investigate the problems associated with true bearingless induction motors and to extend existing knowledge through the new insight attained. A dynamic magnetic field model of the machine embedded in a vector-controlled system was developed using the dynamic reluctance mesh modelling technique introduced in Chapter 2. The investigations were carried out on two, model, bearingless induction motors having different rotor structures. One motor had a cage rotor structure whereas the other had a wound rotor. The wound rotor form restricts rotor currents to those associated with pole number (M) of the motoring winding. The main findings of this thesis are summarised below. Suggestions for future research work follow. An IEE journal paper on this work has been accepted for publication (Ungku Amirulddin *et al.*, 2005).

10.1. Vector control methods for levitation and lateral force production

In Chapter 3, the derived y- and x- direction forces acting on a rotor of an M-pole induction motor augmented by an additional N-pole levitation winding were found, as expected, to be dependent on the peak airgap fields due to the M-pole motoring winding and the N-pole levitation winding. The airgap fields correspond to the net airgap flux linkage vector of both windings. Hence, a field-oriented vector control scheme leads to the effective control of a levitated induction motor. Chapter 4 describes the three vector control schemes proposed for each of the bearingless motor types considered in this

thesis; namely based on indirect rotor field orientation (IRFO), indirect airgap field orientation (IAFO) and mixed field orientation (MFO).

In Chapter 5, the simulations of the vector control schemes for a 4+2 pole bearingless cage rotor IM were performed based on a two-axis lumped parameter circuit. These showed that all three schemes were able to produce the required y- direction force to compensate for the rotor weight. However, it was found that the IRFO vector controlled motor also produced an unwanted, but predicted, x- direction force. This was due to the fact that in order to have a zero x- direction force, the q- axis 2-pole airgap flux linkage ψ_{oq}^{N} must be zero. This is not the case when the 2-pole winding is rotor field oriented which leads to the conclusion that the levitation winding has to be airgap field oriented in order to produced decoupled force control. Therefore, only the IAFO and MFO vector control schemes are appropriate for the control of the cage rotor type bearingless motor. Even so, the MFO vector control scheme is at an advantage since it incorporates a simpler rotor field oriented control for the main 4-pole winding whilst still being able to produce the necessary forces via a 4-pole airgap field orientation for the 2-pole levitation winding.

Similarly, in Chapter 5, the simulation of the 4+2 pole wound rotor type motor under the IRFO, IAFO and MFO vector control schemes all showed that constant normal forces are achieved under all conditions as required by the force reference demands. However, under the IRFO vector control scheme, both the M-pole and N-pole winding currents, voltages and flux linkages are oriented onto the main M-pole rotor flux vector. This means that when the torque current i_{sq}^{M} is present, the main airgap field B_{o}^{M} will no longer be aligned with the N-pole field B_{od}^{N} and will not be in quadrature with B_{oq}^{N}. Therefore, the derived force expressions of Chapter 3 will no longer be valid as they require the peak flux densities B_{od}^{N} and B_{o}^{M} to be in alignment with each other. Hence, as for the cage rotor type motor, the IAFO and MFO vector control schemes are the only control schemes suitable for the wound rotor type motor. Nevertheless, as observed for the control of the cage rotor motor, the MFO vector control scheme is preferred for the same reason as stated for the cage rotor type motor.

10.2. Modelling of a bearing relief cage rotor IM

The results of a linear 4+2 pole bearing relief cage rotor IM modelled using the dynamic reluctance mesh modelling (DRMM) technique using the DCM software were presented in Chapter 6. The simulation results showed that under direct on-line start the motor produced lower than expected force values. This was felt to be due to the extremely high zigzag leakage fluxes observed in the motor. These substantial leakages arose from the high slip experienced by the 2-pole field. Therefore, it is concluded that in order to generate the required radial forces in the cage rotor motor, considerably higher 2-pole currents are required than predicted from the derived force expressions to compensate for the high slip effects. When the reluctance mesh modelled motor was simulated with an MFO vector control scheme, the predicted levitation force was only produced when the rotor was stationary. Once the rotor started to accelerate and rotate, the force produced was much higher. This is different to the results obtained from the simulation of the same motor modelled using the two-axis lumped parameter technique as observed in Chapter 5. The magnitude of the force obtained from the simulation of the vector controlled motor during rotor rotation was not readily explainable from the harmonic fields in the motor obtained from a DFT analysis of the airgap flux density samples of the airgap reluctance elements, even though the DFT analysis results agreed with the observation of increase in force magnitude when the rotor rotates.

10.3. Modelling of a bearing relief wound rotor IM

It is clear from the direct on-line start simulation of a cage rotor bearingless IM, presented in Chapter 6, that a high quality (small) N-pole field is difficult to achieve in the motor when high slip frequency N-pole rotor currents are induced. It is known that leakage effects of high slip rotor currents severely compromise the sinusoidal nature of the airgap magnetic field. Therefore, it can be concluded that bearingless induction motors containing rotors that do not allow N-pole currents to be induced at high slip are an advantage. For this reason, simulations of a 4+2 pole wound rotor bearingless IM modelled using the DRMM technique was presented in Chapter 7.

Linear simulations of the direct on-line start wound rotor type motor concluded that radial forces equal to the rotor weight can be achieved and that the required winding voltages and currents are as predicted from theory. When the DRMM modelled 4+2 pole motor was subject to an MFO vector control scheme, successful bearing relief compensation from the rotor weight was achieved during both steady state and transient conditions. However, it is evident from the simulation that even a small error in the controller airgap flux angle $\hat{\theta}_o$ (approximately 4° electrical), will cause a lateral force F_x to be produced during acceleration and load conditions when it is not requested. Therefore, it is concluded that in order to ensure no lateral force F_x exists unless it is requested, the 2-pole levitation winding currents, voltages and fluxes have to be perfectly oriented onto the peak 4-pole airgap field.

The inclusion of iron non-linearity into the simulations of the direct on-line and vector controlled wound rotor type motor introduced airgap field harmonics which are capable of interacting with each other to create harmonic forces. More importantly, if one of the levitation field harmonic interacts with the dominant fundamental motoring field a significantly large harmonic force is produced. This large harmonic force will either enforce or reduce the fundamental force in the motor. It was observed that the force produced by the simulation is a resultant of the fundamental and harmonic forces. Furthermore, in the vector controlled motor where the motor is required to compensate for the rotor weight acting in the negative y- direction, the large harmonic force was found to not only cause a reduction of the levitation force F_y but also to cause a lateral force F_x to be produced even when it was not requested. This is due to the fact that the levitation field harmonic is not necessarily aligned with the motoring M-pole field. Therefore, it can be concluded that in order to achieve successful forces in the non-linear bearing relief motor, compensation of the main harmonic forces produced by the motor is also required.

Apart from the harmonic forces experienced in the non-linear simulations, it was observed that under full load a low frequency oscillation of 9.5Hz (in the 4+2 pole motor) is present in the force variation against time. This frequency is thought to be related to the electrical slip speed in the motor since it is approximately equal to the

electrical slip speed multiplied by the number of rotor phase belts per pole pair. Is was found that this low frequency oscillation is still present when a different stator-rotor slot combination was chosen, with its value being dependent on the new electrical slip speed and number of rotor phase belts per pole pair. However, from the investigations carried out, the oscillation frequency was found to be independent of the supply frequency. Further understanding is required here to find the mechanism for controlling these oscillations.

Insight into the effects of non-linear iron on the performance of the bearing relief motor was not provided from the Simulink simulation of the same motor presented in Chapter 5 since the two-axis lumped parameter circuit model in Simulink was unable to fully model a non-linear motor. Furthermore, the Simulink model does not include the capability of investigating the harmonic field interactions that affect the force production. Therefore, it is concluded that the two axis lumped parameter model may not be sufficient for fully modelling the performance of the bearingless induction motor.

10.4. Modelling a vector controlled, bearingless, wound rotor IM

It is apparent in Chapter 8 that the position control design for the vector controlled bearingless induction motor must include the effect of unbalance magnetic pull caused by the perturbed rotor. The unbalance magnetic pull force expression, derived in Chapter 3 and used in the position control design, was verified from an investigation of the effect of rotor displacement on the force produced by the motor under only an M-pole excitation as shown in Section 8.2. When the designed position control loop was used in the DCM simulation of the vector controlled bearingless linear iron wound rotor IM, the control scheme was successful at keeping the rotor centred under both transient and steady state conditions. However, the choice of sampling time and bandwidth of the position controller is crucial to ensure successful control.

The effect of non-linear iron on the performance of the position control scheme of the bearingless wound rotor motor is dependent on the plant of the motor. This is because the introduction of non-linearity causes an increase in the slope of the unbalance magnetic pull force-displacement variation and hence a position controller has to be

designed to cope with this large slope. With the correct controller design, the position control incorporated in the bearingless motor was also capable of compensating for the effect of harmonic forces present due to the iron non-linearity. The low frequency oscillation observed during load in the non-linear iron simulation of the bearing relief motor is still present in the non-linear bearingless motor simulation. However, this is only of marginal significance in the closed loop position control. From comparison of the DCM simulation results of the bearingless induction motor with those of the Simulink simulation, the inadequacy of the two-axis, lumped parameter model to simulate the behaviour of the bearingless motor is further highlighted. This is because the effects of harmonic field interactions, which have been shown to be significant in the bearingless motor, are not included in the two-axis lumped parameter model. Moreover, because the two-axis lumped parameter model utilised in the Simulink simulation is unable to fully model a non-linear motor, no insight into the non-linear effects on the rotor levitation in the bearingless motor could be obtained.

Clearly, with such a complex interaction of MMF and saturation harmonics in a practical induction motor, a detailed magnetic machine model is essential for the development of effective control schemes and for the understanding of the processes of force production. Therefore, it is perhaps not surprising that no experimental results for a fully levitated induction motor rotor have yet been reported.

10.5. Recommended future work

The following areas were identified as possible extensions to the work presented in the thesis:

- An experimental validation of the effects of iron non-linearity on the performance of a bearing relief wound rotor induction motor as pointed out from the computational analysis shown in Chapter 7.

- In the modelling of the bearingless cage rotor motor, further investigations into reducing the high slip leakage effects on the force production is required possibly through higher main (M-pole) and levitation (N-pole) winding pole

number combinations in which the slot numbers can be optimised to control leakage reluctances. For such designs, bearing relief schemes for cage machines may be much more effective compared to those observed in this thesis.

- Following from the investigations carried out in Chapter 7, methods for harmonic force compensation in the non-linear bearing relief wound rotor IM could be investigated. In addition, further research into the physical understanding of the low frequency oscillations observed in the non-linear bearing relief and bearingless wound rotor IM operating under load is also required in order to find mechanisms to reduce this behaviour.

- Investigations of a three-dimensional dynamic reluctance mesh modelled vector controlled bearingless induction motor.

- The common use of fast switching semiconductor devices, such as insulated gate bipolar transistors (IGBT), in pulse-width modulation (PWM) inverter schemes for AC motor drives will introduce high frequency motor currents. These currents have a tendency to flow to earth via the motor bearings capacitively. Therefore, research into the use of bearing relief capabilities to minimise the flow of high frequency bearing currents could be worthwhile.

- Although, most research into bearingless motors has currently been centred on the permanent magnet type motor, a study on a vector controlled bearingless permanent magnet motor modelled using the dynamic reluctance mesh modelling technique may also help in the control design and operation of these devices.

Appendix A

Equations governing the behaviour of an induction motor

In this Appendix the equations governing the behaviour of an induction motor is derived in terms of the rotating dq reference frame, which is required in vector control schemes. These equations are generally written in equivalent 2-phase stator variables. The stator coils, termed the sαβ coils, are fixed in space. Therefore, the stator voltage equation can be written as

$$\underline{v}_s = \underline{i}_s R_s + \frac{d}{dt}\underline{\psi}_s \tag{A.1}$$

In (A.1), $\underline{v}_s$, $\underline{i}_s$ and $\underline{\psi}_s$ are complex vectors representing the stator voltage, current and flux linkage, and are defined by

$$\underline{v}_s = v_{s\alpha} + jv_{s\beta}$$

$$\underline{i}_s = i_{s\alpha} + ji_{s\beta}$$

$$\underline{\psi}_s = \psi_{s\alpha} + j\psi_{s\beta}$$

Similarly, the rotor is represented by its equivalent 2-phase coils, rα'β', which are fixed onto the rotor and rotates in space at the rotor speed, ω_r. The rotor voltage $\underline{v}_r$, current $\underline{i}_r$ and flux linkage $\underline{\psi}_r$ vectors are defined by:

$$\underline{v}_r = v_{r\alpha'} + jv_{r\beta'}$$

$$\underline{i}_r = i_{r\alpha'} + ji_{r\beta'}$$

$$\underline{\psi}_r = \psi_{r\alpha'} + j\psi_{r\beta'}$$

respectively. Hence, the rotor voltage equation is given by

$$\underline{v}_r = 0 = \underline{i}_r R_r + \frac{d}{dt}\underline{\psi}_r \tag{A.2}$$

where $\psi_{r\alpha'}$ and $\psi_{r\beta'}$ are the total flux linkage in the rotor coils. The rotor voltage is zero since the rotor coils are short-circuited. In order for equations (A.1) and (A.2) to be useful, both equations must be written in the same reference frame. This requires transforming from the α'β' frame to the αβ frame, which is achieved using:

$$\begin{aligned} \underline{i}_{r\alpha'\beta'} &= e^{-j\omega_r t}\underline{i}_{r\alpha\beta} \\ \underline{\psi}_{r\alpha'\beta'} &= e^{-j\omega_r t}\underline{\psi}_{r\alpha\beta} \end{aligned} \tag{A.3}$$

Hence, (A.2) can be transformed onto the stator frame thorough of substitution of (A.3) to give:

$$0 = \underline{i}_{r\alpha\beta} R_r + \frac{d}{dt}\underline{\psi}_{r\alpha\beta} - j\omega_r \underline{\psi}_{r\alpha\beta} \tag{A.4}$$

A.1. Induction machine equations in terms of $\underline{i}_s$ and $\underline{\psi}_r$

The stator and rotor flux linkage vectors, $\underline{\psi}_{s\alpha\beta}$ and $\underline{\psi}_{r\alpha\beta}$, can be represented by

$$\begin{aligned} \underline{\psi}_{s\alpha\beta} &= L_s \underline{i}_{s\alpha\beta} + L_o \underline{i}_{r\alpha\beta} \\ \underline{\psi}_{r\alpha\beta} &= L_o \underline{i}_{s\alpha\beta} + L_r \underline{i}_{r\alpha\beta} \end{aligned} \tag{A.5}$$

In order to achieve a rotor field oriented vector control scheme, the stator and rotor voltage equations have to be expressed in terms of $\underline{i}_s$ and $\underline{\psi}_r$. Therefore, by

rearranging the equations in (A.5), the terms $\underline{i}_{r\alpha\beta}$ and $\underline{\psi}_{s\alpha\beta}$ in (A.1) and (A.4) can be eliminated to yield

$$\underline{v}_{s\alpha\beta} = \underline{i}_{s\alpha\beta}R_s + \sigma L_s \frac{d}{dt}\underline{i}_{s\alpha\beta} + \frac{L_o}{L_r}\frac{d}{dt}\underline{\psi}_{r\alpha\beta} \tag{A.6}$$

$$0 = \frac{R_r}{L_r}\underline{\psi}_{r\alpha\beta} - \frac{L_o R_r}{L_r}\underline{i}_{s\alpha\beta} + \frac{d}{dt}\underline{\psi}_{r\alpha\beta} - j\omega_r \underline{\psi}_{r\alpha\beta} \tag{A.7}$$

Equations (A.6) and (A.7) are respectively the stator and rotor dynamic equations governing the behaviour of the induction motor in the fixed stator αβ frame. It has to be noted that both (A.6) and (A.7) consist of two equations each due to the real and imaginary quantities of the complex vectors.

The next step is to represent the equations in which all the stator and rotor quantities are on the rotating dq frame. The dq frame travels at a speed ω_e relative to the fixed stator αβ frame. Hence, the αβ frame quantities can be transformed into the dq frame through

$$\underline{x}_{\alpha\beta} = e^{+j\omega_e t}\underline{x}_{dq} \tag{A.8}$$

where x may be v_s, i_s or ψ_r.

Substituting this transformation into (A.6), and through differentiating by parts and simplifying, gives the stator voltage vector equation in the dq frame:

$$\underline{v}_{sdq} = \underline{i}_{sdq}R_s + \sigma L_s \frac{d}{dt}\underline{i}_{sdq} + j\omega_e \sigma L_s \underline{i}_{sdq} + \frac{L_o}{L_r}\frac{d}{dt}\underline{\psi}_{rdq} + j\omega_e \frac{L_o}{L_r}\underline{\psi}_{rdq} \tag{A.9}$$

where $\sigma L_s = \dfrac{L_s L_r - L_o^2}{L_r}$. Similarly, through (A.8), the rotor voltage equation (A.7) is transformed into the dq frame to produce

$$0 = \frac{R_r}{L_r}\underline{\psi}_{rdq} - \frac{L_o R_r}{L_r}\underline{i}_{sdq} + \frac{d}{dt}\underline{\psi}_{rdq} + j\omega_{sl}\underline{\psi}_{rdq} \tag{A.10}$$

where $\omega_{sl} = \omega_e - \omega_r$.

Finally, equations (A.9) and (A.10) can be separated into real and imaginary parts to yield the four equations governing the behaviour of the induction motor in the dq frame:

$$\underline{v}_{sd} = \underline{i}_{sd}R_s + \sigma L_s \frac{d}{dt}\underline{i}_{sd} - \omega_e \sigma L_s \underline{i}_{sq} + \frac{L_o}{L_r}\frac{d}{dt}\underline{\psi}_{rd} - \omega_e \frac{L_o}{L_r}\underline{\psi}_{rq} \tag{A.11}$$

$$\underline{v}_{sq} = \underline{i}_{sq}R_s + \sigma L_s \frac{d}{dt}\underline{i}_{sq} + \omega_e \sigma L_s \underline{i}_{sd} + \frac{L_o}{L_r}\frac{d}{dt}\underline{\psi}_{rq} + \omega_e \frac{L_o}{L_r}\underline{\psi}_{rd} \tag{A.12}$$

$$0 = \frac{R_r}{L_r}\underline{\psi}_{rd} - \frac{L_o R_r}{L_r}\underline{i}_{sd} + \frac{d}{dt}\underline{\psi}_{rd} - \omega_{sl}\underline{\psi}_{rq} \tag{A.13}$$

$$0 = \frac{R_r}{L_r}\underline{\psi}_{rq} - \frac{L_o R_r}{L_r}\underline{i}_{sq} + \frac{d}{dt}\underline{\psi}_{rq} + \omega_{sl}\underline{\psi}_{rd} \tag{A.14}$$

A.2. Induction machine equations in terms of $\underline{i}_s$ and $\underline{\psi}_o$

In order to express the dynamic equations of the induction motor in terms of $\underline{i}_{sdq}$ and $\underline{\psi}_{odq}$, the term $\underline{\psi}_{rdq}$ in equations (A.9) and (A.10) would have to be eliminated. This is achieved using the flux linkage vector equations in the dq frame where

$$\underline{\psi}_{rdq} = L_o \underline{i}_{sdq} + L_r \underline{i}_{rdq} \tag{A.15}$$

$$\underline{\psi}_{odq} = L_o \underline{i}_{sdq} + L_o \underline{i}_{rdq} \tag{A.16}$$

By rearranging (A.16), an expression for $\underline{i}_{rdq}$ is obtained which can then be substituted into (A.15) to give

$$\underline{\psi}_{rdq} = \frac{L_r}{L_o}\underline{\psi}_{odq} - (L_r - L_o)\underline{i}_{sdq} \tag{A.17}$$

Hence, by substituting (A.17) into (A.9) and (A.10):

$$\underline{v}_{sdq} = \underline{i}_{sdq}R_s + \left[\sigma L_s + \frac{L_o}{L_r}(L_r - L_o)\right]\left(\frac{d}{dt}\underline{i}_{sdq} + j\omega_e\underline{i}_{sdq}\right) + \frac{d}{dt}\underline{\psi}_{odq} + j\omega_e\underline{\psi}_{odq} \tag{A.18}$$

$$0 = \frac{R_r}{L_o}\underline{\psi}_{odq} + \frac{L_r}{L_o}\frac{d}{dt}\underline{\psi}_{odq} - R_r\underline{i}_{sdq} - (L_r - L_o)\frac{d}{dt}\underline{i}_{sdq} + j\omega_{sl}\left[\frac{L_r}{L_o}\underline{\psi}_{odq} - (L_r - L_o)\underline{i}_{sdq}\right] \tag{A.19}$$

Equations (A.18) and (A.19) are the stator and rotor equations of the induction motor in terms of $\underline{i}_{sdq}$ and $\underline{\psi}_{odq}$, which will be useful in an airgap field oriented vector control scheme. Again, both these equations can be separated into real and imaginary parts to yield another set of four equations governing the behaviour of the induction motor in the dq frame:

$$v_{sd} = R_s i_{sd} + \left[\sigma L_s - \frac{L_o}{L_r}(L_r - L_o)\right]\left(\frac{d}{dt}i_{sd} - \omega_e i_{sq}\right) + \frac{d}{dt}\psi_{od} - \omega_e\psi_{oq} \tag{A.20}$$

$$v_{sq} = R_s i_{sq} + \left[\sigma L_s - \frac{L_o}{L_r}(L_r - L_o)\right]\left(\frac{d}{dt}i_{sq} + \omega_e i_{sd}\right) + \frac{d}{dt}\psi_{oq} + \omega_e\psi_{od} \tag{A.21}$$

$$0 = \frac{R_r}{L_o}\psi_{od} + \frac{L_r}{L_o}\frac{d}{dt}\psi_{od} - R_r i_{sd} - (L_r - L_o)\frac{d}{dt}i_{sd} - \omega_{sl}\left[\frac{L_r}{L_o}\psi_{oq} - (L_r - L_o)i_{sq}\right] \tag{A.22}$$

$$0 = \frac{R_r}{L_o}\psi_{oq} + \frac{L_r}{L_o}\frac{d}{dt}\psi_{oq} - R_r i_{sq} - (L_r - L_o)\frac{d}{dt}i_{sq} + \omega_{sl}\left[\frac{L_r}{L_o}\psi_{od} - (L_r - L_o)i_{sd}\right] \tag{A.23}$$

References

Abdel-Kader (1979), *The influence of winding slots upon the airgap flux density distribution of induction machines*, PhD Thesis, University of Nottingham, U.K.

Alger, P. L. (1995), *Induction machines: their behaviour and uses*, Gordon and Breach, Basel, Switzerland.

Amin, A. A. A. (1982), *A model for the prediction of induction motor performance with detailed consideration of the air-gap magnetic field*, PhD Thesis, University of Nottingham, U.K.

Baoguo, W. and Fengxiang, W. (2001), Modelling and analysis of levitation force considering air-gap eccentricity in a bearingless induction motor, *Proceedings of the 5th International Conference on Electrical Machines and Systems (ICEMS)*, China, **2**, p934-937.

Bichsel, J. (1992), The bearingless electrical machines, *Proceedings of NASA conference on magnetic suspension technology*, p563-570.

Bleuler, H. (1992), A survey of magnetic levitation and magnetic bearing types, *JSME International Journal Series III*, **35**, 3, p335-342.

Brown, J. (1999), Bearings on the fast track, *Power Transmission Design*, **41**, 2, p33-36.

Cai, J. and Henneberger, G. (2001), Transient FEM computation of radial force and torque for bearingless wound-rotor induction motors, *International conference on electrical machines and systems (ICEMS)*, Shenyang, China, p991-994.

Chapman, S. J. (1999), *Electric machinery fundamentals*, McGraw-Hill, Boston, USA.

Chiba, A., Rahman, M. A. and Fukao, T. (1991(a)), Radial force in a bearingless reluctance motor, *IEEE Transactions on Magnetics*, **27**, 2, p786-790.

Chiba, A., Power, D. T. and Rahman, M. A. (1991(b)), Characteristics of a bearingless induction motor, *IEEE Transactions on Magnetics*, **27**, 6, p5199-5201.

Chiba, A., Deido, T., Fukao, T. and Rahman, M. A. (1994), An analysis of bearingless AC motors, *IEEE Transactions on Energy Conversion*, **9**, 1, p61-67.

Chiba, A., Power, D. T. and Rahman, M. A. (1995), Analysis of no-load characteristics of a bearingless induction motor, *IEEE Transactions on Industry Applications*, **31**, 1, p77-83.

Chiba, A., Miyatake, R., Hara, S. and Fukao, T. (1996), Transfer characteristics of radial force of induction-type bearingless motors with four-pole rotor circuits, *Fifth International Symposium on Magnetic Bearings*, Kanazawa, Japan, p319-325.

Chiba, A., Furuichi, R., Aikawa, Y., Shimada, K., Takamoto, Y. and Fukao, T. (1997), Stable operation of induction-type bearingless motors under loaded conditions, *IEEE Transactions on Industry Applications*, **33**, 4, p919-924.

Chiba, A. and Fukao, T. (1998), Optimal design of rotor circuits in induction type bearingless motors, *IEEE Transactions on Magnetics*, **34**, 4, p2108-2110.

Deng, Z., Zhang, H., Wang, X. and Yan, Y. (2002), Nonlinear decoupling control of the bearingless induction motors based on the airgap motor flux orientation, *Chinese Journal of Aeronautics*, **15**, 1, p38-43.

Dussaux, M. (1990), The industrial applications of the active magnetic bearings technology, *2nd International Symposium on Magnetic Bearing*, Tokyo, Japan, p33-38.

Fengxiang, W., Qishi, Z. and Baoguo, W. (2001), Torque and levitation force comparison of bearingless motor with different rotor structures, *5th International Conference on Electrical Machines and Systems (ICEMS)*, p1057-1060.

Franklin, G. F., Powell, J. D. and Workman, M. L. (1998), *Digital control of dynamic systems*, Addison Wesley, California, USA.

Fukao, T. (2000), The evolution of motor drive technologies: Development of bearingless motors, *Power Electronics and Motion Control Conference*, **1**, p33-38.

Khoo, S. W. K., Fittro, R. L. and Garvey, S. D. (2002), AC polyphase self-bearing motors with a bridge configured winding, *8th International Symposium on Magnetic Bearing*, Mito, Japan, p47-52.

Knospe, C. R. and Collins, E. G. (1996), Introduction to the special issue on magnetic bearing control, *IEEE Transactions on Control Systems Technology*, **4**, 5, p481-483.

Maslen, E. H., Allaire, P. E., Scott, M. A. and Hermann, P. (1988), Magnetic bearing design for a high speed rotor, *1st International Symposium on Magnetic Bearings*, p137-146.

Matsumura, F., Okada, Y., Fujita, M. and Namerikawa, T. (1997), State of the art of magnetic bearings (Overview of magnetic bearing research and applications), *JSME International Journal Series C - Mech. Systems, Machine Elements & Manufacturing*, **40**, 4, p553-560.

Mizia, J., Adamiak, K., Eastham, A. R. and Dawson, G. E. (1988), Finite element force calculation: Comparison of methods for electric machines, *IEEE Transactions on Magnetics*, **24**, 1, p447-450.

Nakamura, K., Kimura, K. and Ichinokura, O. (2005), Electromagnetic and motion coupled analysis for switched reluctance motor based on reluctance network analysis, *Journal of Magnetism and Magnetic Materials*, **290/291**, 2, p1309-1312.

Nomura, S., Chiba, A., Nakamura, F., Ikeda, K., Fukao, T. and Rahman, M. A. (1993), A radial position control of induction type bearingless motor considering phase delay caused by the rotor squirrel cage, *Power Conversion Conference*, Yokohama, Japan, p438-443.

Ohishi, T., Shimura, S. and Okada, Y. (1995), Research on synchronous type and induction type levitated rotating motor, *Electrical Engineering in Japan*, **115**, 7, p130-138.

Okada, Y., Dejima, K. and Ohishi, T. (1995), Analysis and comparison of PM synchronous motor and induction motor type magnetic bearings, *IEEE Transactions on Industry Applications*, **31**, 5, p1047-1053.

Okada, Y., Miyamoto, S. and Ohishi, T. (1996), Levitation and torque control of internal permanent magnet type bearingless motor, *IEEE Transactions on Control Systems Technology*, **4**, 5, p565-571.

Osama, M. and Lipo, T. A. (1999), A magnetic relief scheme for four pole induction motors, *Proceedings of the 6th International Conference ELECTRIMACS, Modelling and simulation of electrical machines, converters and systems*, Lisbon, Portugal, **1**, pI15-21.

Oshima, M., Miyazawa S., Deido T., Chiba, A., Nakamura, F. and Fukao, T. (1996), Characteristic of a permanent magnet type bearingless motor, *IEEE Transactions on Industry Applications*, **32**, 2, p363-369.

Ostovic', V. (1986), A method for evaluation of transient and steady state performance in saturated squirrel cage induction machines, *IEEE Transactions on Energy Conversion*, **1**, 3, p190-197.

Ostovic', V. (1988), A simplified approach to magnetic equivalent-circuit modelling of induction machines, *IEEE Transactions on Industry Applications*, **24**, 2, p308-316.

Press, W. H., Teukolsky, S. A., Vetterling, W. T. and Flannery, B. P. (2002), *Numerical recipes in C++: the art of scientific computing*, Cambridge University Press, Cambridge, U.K.

Roisse, H., Hecquet, M. and Brochet, P. (1998), Simulations of synchronous machines using a electric-magnetic coupled network model, *IEEE Transactions on Magnetics*, **34**, 5, p3656-3659.

Salazar, A. O. and Stephan, R. M. (1993), A bearingless method for induction machines, *IEEE Transactions on Magnetics*, **29**, 6, p2965-2967.

Santisteban, J. A. and Stephan, R. M. (1999), Analysis and control of a loaded bearingless machine, *IEEE Transactions on Magnetics*, **35**, 5, p3998-4000.

Schöb, R. and Bichsel, J. (1994), Vector control of the bearingless motor, *4th International Symposium on Magnetic Bearings*, Zurich, Switzerland, p327-333.

Sewell, P., Bradley, K. J., Clare, J. C., Wheeler, P. W., Ferrah, A. and Magill, R. (1999), Efficient dynamic models for induction machines, *International Journal of Numerical Modelling: Electronic Networks, Devices and Fields*, **12**, 6, p449-464.

Silvester, P. P. and Ferrari, R. L. (1996), *Finite elements for electrical engineers*, Cambridge University Press, Cambridge, U.K.

Suzuki, T., Chiba, A., Rahman, M. A. and Fukao, T. (2000), An air-gap-flux-oriented vector controller for stable operations of bearingless induction motors, *IEEE Transactions on Industry Applications*, **36**, 4, p1069-1076.

Swann, S. A. (1963), Effect of rotor eccentricity on the magnetic field in the air-gap of a non-salient pole machine, *Proceedings of the Institution of Electrical Engineers*, **110**, 5, p903-915.

Ungku Amirulddin, U. A., Asher, G. M., Sewell, P., Bradley, K. J. (2005), Dynamic field modelling of torque and radial forces in vector controlled induction machines with bearing relief, *IEE Proceeding of Electric Power Applications*, **152**, 4, p894-904.

Van der Vorst (1992), Bi-CGSTAB: A fast and smoothly converging variant of Bi-CG for the solution of non-symmetric linear systems, *SIAM Journal of Science and Statistic Computation*, **13**, p631-644.

Yahia, K. B. and Henneberger, G. (1998), Development of a bearingless induction motor, *International Conference on Motion and Vibration Control*, **3**, p1083-1088.